THE UNIVERSITY *of* EDINBURGH

The Onset of Gravitational Collapse of Colloidal gels: An Optical Microscopy Study

Xuemao Zhou

Doctor of Philosophy
The University of Edinburgh
May 2018

Abstract

Colloidal gels are ubiquitous in daily life, such as paint. A colloidal gel can support its own weight for a finite delay time in gravity. This delay time sets the shelf life of many products. Hence, understanding the gravitational stability of colloidal gels could promote their industrial application. This work presents results on the mesoscopic scale ($\sim 10^2$ µm) aiming to bridge macroscopic observations with the microscopic perspective in previous studies. In a model system of colloids + polymers, typical kinds of gel collapse were studied using fluorescence microscopy. Two collapse mechanisms are found for low and high colloidal volume fractions (φ_c), respectively. At low φ_c, denser debris falls through and breaks the gel structure. At high φ_c, solvent droplets rise to the top of a gel allowing the solvent to be expelled from the gel quickly. For gels with intermediate φ_c, these two mechanisms cooperate. Large-scale hydrodynamic remixing and recirculation are observed before the onset of gel collapse, emphasizing that hydrodynamics is crucial. The imaging results also suggest that the menisci of the samples play an important role of the gel collapse. By eliminating most of the curved meniscus, the collapse of gel can be postponed. Previous hypothesis for gel collapse is based on the competition between the yield stress of gel and gravitational stress. Our results on large and small particle gels show similar collapse behaviours both on macro- and meso-scopic scales. Considering that the yield stress varies sensitively with the size of the particle, this similarity suggests different mechanisms should be developed for the collapse of small and large particle gels.

Lay Summary

Many everyday products are powders that suspended in liquids, from foodstuff, cosmetic products to paint or cement. In most case, the solid particles are heavier than the suspending liquid so that sediment starts to form gradually at the bottom of a product soon after it is put away. One may want a product to be stable for a long time in order to have a long "shelf life"; at the same time, if needed, to flow easily with a simple squeeze. Formulating a product as a gel is a common strategy to achieve such a property. In a gel, solid particles are attractive to each other and form a porous network like a sponge so that they can support their own weight like a solid. On the other hand, such an attraction is relatively weak so that a moderate stress can turn the gel back to a liquid. However, a gel can only stand on itself for a finite time. It will eventually collapse. Therefore, in order to prolong the stable period, the collapse of the gel has been studied for many years.

Previous studies found a heavy layer of solid particles at the top of a gel. Such a layer crashes the gel leads to the collapse. Hence, the collapse of this heavy layer is one of the key processes during the collapse of a gel. On the other hand, as the solid particles settle, the suspending liquid has to rise up. Therefore, the rising of the liquid is also an important process. These two key processes are the main topics of this thesis. I try to understand how the heavy layer is formed and how the liquid is expelled from the solid network.

By directly looking at the collapse of gels under a microscope, I found that the solid particles at the vertical part of the air-gel interface fall soon after the gel is re-mixed. They accumulate around the top of the gel and form the heavy layer. Therefore, I filled a container with a gel leaving only a small air bubble, i.e. only a small air-gel interface was left in the gel. In this way, I have prolonged the stable period of the gel. This is because, by removing most of the air-gel interface, I reduced the amount of solid that available to form the heavy layer, and hence, retard the process of heavy layer crashing a gel. Also, the gel starts collapsing

around the air bubble. This observation again shows that the air-gel interface is crucial in the collapse of a gel.

I also found that the suspending liquid can form droplets which rise through the gel. As these droplets rise, they leave channels for liquid to escape more quickly. Droplets also erode the gel structure, bring debris to the top and erupt like volcanoes. This process weakens the gel and contributes to the heavy layer formation as well. Results show that droplets can be formed at the glass wall and from reservoirs left by rising air bubbles. It implies that the general formation mechanism of droplets is a nucleation and growth process.

The results of this work show that the mechanism of the gel collapse changes as the amount of solid increases. With low solid content, a gel collapses with heavy layer falling which looks like fingers poking the gel. The collapse of the gel exhibits a constant speed after the commencement of macroscopic settling. With high solid content, a gel collapse with droplets rising. The gel collapses at a decreasing speed. With intermediate solid content, these two processes cooperate, and the gel also exhibits a constant speed. Therefore, by monitoring the speed of collapse together with imaging around the meniscus microscopically, it is possible to predict the type of collapse in the early stage, even before the commencement of the macroscopic settling.

Declaration

I declare that this thesis was composed by myself, that the work contained herein is my own except where explicitly stated otherwise in the text, and that this work has not been submitted for any other degree or professional qualification except as specified.

(*Xuemao Zhou, May 2018*)

Acknowledgements

It is my pleasure to thank many people for their support and assistance in the course of my Ph.D study. First and foremost, I would like to thank my supervisor, Prof. Wilson Poon, for his guidance and profound influence on my way of thinking about physics. With his help, I challenged myself and eventually went beyond what I thought possible.

I also owe a debt of gratitude to many people in the soft matter group. In particular, I wish to thank Michiel Hermes for guidance and encouragement, Andrew Schofield for providing colloidal particles and helping me out numerous times in the lab, Joost de Graaf, Nick Koumakis and Job Thijssen for helpful discussions. I would like to acknowledge Jochen Arlt, John Royer and Ben Guy for their help with experiments.

I would like to thank Petra Schwendner, Susana Direito, Jiahong Chen, Qingshu Zheng, Yan Chen, Mattias Sachs, Veronika Afonina, Laura Sawiak, Katy Dickinson and Ana Fialho for helping me maintain my sanity. Special thanks to my best friends back in China, Qianru Hu and Ying Yin, for their continued support even when they had no idea what I was talking about.

Finally, thanks to all my family for their love and understanding.

Contents

Abstract i

Lay Summary iii

Declaration v

Acknowledgements vii

Contents ix

List of Figures xiii

List of Tables xvii

1 Introduction 1

1.1 About This Work ... 1

1.2 Colloidal System ... 2

1.2.1 Brownian Motion ... 2

1.3 Hard Sphere Colloids ... 4

1.3.1 Hard Sphere Potential ... 4

1.3.2 Sedimentation of a Single Colloid ... 4

1.4 Experimental Hard Spheres ... 5

1.4.1 Electrostatic Interactions ... 5

1.4.2 London-van der Waals Interaction ... 6

1.4.3 Hydrodynamics ... 8

1.4.4 Phase Behaviour of Hard Spheres ... 8

1.5 Introducing Attraction ... 10

2 Colloid + Polymer Mixture 13

2.1 Model System ... 13

2.2 Phase Behaviour ... 14

2.2.1 Equilibrium Phase Behaviour ... 14

2.2.2 Non-Equilibrium Behaviour ... 18

2.2.3 State Diagram 20
2.3 Formation of Colloidal Gels 20
2.4 Gel Collapse 23
2.4.1 Macroscopic Behaviours 24
2.4.2 Collapse Mechanism 26
2.5 Thesis Outline 29

3 Method 31
3.1 Macroscopic Time-lapse Imaging 31
3.1.1 Experimental Setup 31
3.1.2 Measuring the Height Profile 33
3.2 Microscopic Time-lapse Imaging 34
3.2.1 Fluorescence Microscopy 34
3.2.2 Experimental Setup 36
3.2.3 Image Processing 39
3.2.4 General Image Interpretation 43
3.2.5 Measuring Height Profile 44

4 Suspension Characterization and Gel Preparation 47
4.1 PMMA + PS Mixture 47
4.2 Gel Preparation 52
4.2.1 Determination of Colloidal Volume Fraction 52
4.2.2 Determination of Free Volume Fraction of Polymer 53
4.2.3 Approach to Composition Selection 54
4.3 Summary 54

5 Macroscopic Imaging Study 55
5.1 Introduction 55
5.2 Method 55
5.3 Categorisation of the Collapse of Gels 56
5.3.1 Large Particle Gels 56
5.3.2 Small Particle Gels 59
5.4 Conclusion 60

6 The Evolution of Collapse Mechanisms 61
6.1 Introduction 61
6.2 Method 62
6.3 Rapid Collapse Gel with Low φ_c: Gel α 63
6.4 Rapid Collapse Gel with Intermediate φ_c: Gel β 68

6.5 Rapid Collapse Gel with High φ_c: Gel γ 71
6.6 Slow Collapse Gels: Gel δ 73
6.7 Regime A gel 75
6.8 Observation of Small-Colloid Gels 76
6.9 Conclusion 81

7 Meniscus Effect 83
7.1 Introduction 83
7.2 Method 83
7.3 Rapid Collapse Gel 85
7.3.1 Meniscus Effect in Gel β 86
7.3.2 Mechanism of Rapid Collapse in Geometries 94
7.3.3 Postpone a Rapid Collapse 96
7.4 Slow Collapse Gel 98
7.4.1 Geometry $\mathbb{A}$ 98
7.4.2 Geometry $\mathbb{C}$ 98
7.4.3 Meniscus Effect in Slow Collapse Gel 101
7.5 Conclusion 102

8 The Key Features of the Onset of Collapse 105
8.1 Denser Layer 106
8.1.1 Formation of Denser Layer 106
8.1.2 Collapse of Denser Layer 113
8.2 Solvent Droplets 116
8.2.1 Spatial Distribution of Volcanoes 117
8.2.2 From Crack to Droplet 121
8.2.3 From Air Bubble to Droplet 124
8.2.4 Discussion of Solvent Droplets 127
8.3 Conclusion 130

9 Conclusion and Future Work 133

A Supplementary Observations 137
A.1 Shape of a Meniscus 137
A.2 Height Profiles from Macro- and Micro- scopic Imaging 139
A.3 The Interface Speed of Rapid Collapse 140
A.4 The Onset Height of Rapid Collapse 141
A.5 The Delay Time 143
A.6 Propagation of the Onset of Rapid Collapse 146

A.7 Verification of the Postponement of the Rapid Collapse 148
A.7.1 Geometry $\mathbb{A}$ 149
A.7.2 Geometry $\mathbb{B}$ 149
A.7.3 Geometry $\mathbb{C}$ 150
A.7.4 Geometry $\mathbb{D}$ 151
A.7.5 Summary 153
A.8 Micrographs of a Creaming Gel 153
A.9 Solvent Droplets in Laser Scanning Confocal Microscopy 155

B Rheology Study of Gel γ 159

Bibliography 163

List of Figures

(1.1) Hard sphere potential. 4
(1.2) Two ways of stabilizing colloidal particles 7
(1.3) Inter-particle potential of nearly hard sphere colloids 8
(1.4) Hard-sphere phase diagram 9
(1.5) Depletion mechanism 10
(1.6) The total potential of the hard sphere system with non-absorbing polymer. 11

(2.1) Schematic of the equilibrium phase diagram of a gel forming system. 16
(2.2) The experimental phase diagram (c_{p} vs φ_{c}) for PMMA + PS model system. 17
(2.3) Gas-liquid phase separation using common tangent construction. . 19
(2.4) Schematic state diagram related to gelation. 21
(2.5) A gold colloid cluster formed by DLCA. 22
(2.6) A confocal image of a colloidal gel formed by spinodal decomposition arrested by the glass transition. 23
(2.7) Collapse of gels in colloids + polymer model system. 25
(2.8) "Streamer" falls from the top of a rapid collapse gel. 27
(2.9) The "volcanic eruption" at the interface of a collapsing DLCA gel. 28

(3.1) The layout of the imaging module. 32
(3.2) Measure the height profile from macroscopic imaging. 33
(3.3) Stokes shift comes from the energy lost when electrons relax. . . . 35
(3.4) Principle of fluorescence microscopy. 36
(3.5) The layout of the imaging module. 37
(3.6) The wavelength characteristics of the filter cube used in the setup. 38
(3.7) Illustration of image processing. 40
(3.8) Measuring height profile from microscopic time-lapse images. . . . 44

(4.1) Viscosity of PS $M_{\mathrm{w}} = 3.1 \times 10^6$ g/mol in IM solvent. 50
(4.2) Intrinsic viscosity of PS $M_{\mathrm{w}} = 3.1 \times 10^6$ g/mol in IM solvent and the overlap concentration. 51

(5.1) Macroscopic time-lapse images 56
(5.2) State diagram $1 - b_2$ *vs.* φ_{c} for large particle samples. 57
(5.3) Typical height profiles of large particle gels from macroscopic images. 58
(5.4) Height profiles of small particle gels from macroscopic images. . . 59

(5.5) State diagram $1 - b_2$ *vs.* φ_c for small particle gels 60

(6.1) State diagram of large particle gel showing the evolution of collapse mechanisms. 62
(6.2) Height profile of a rapid collapse gel with low φ_c 63
(6.3) Micrographs of a rapid collapse gel with low φ_c, (a) - (f) 64
(6.3) Micrographs of a rapid collapse gel with low φ_c, (g) - (l) 65
(6.4) Height profile of a rapid collapse gel with intermediate φ_c. 68
(6.5) Micrographs of a rapid collapse gel with intermediate φ_c. 70
(6.6) Height profile of a rapid collapse gel with high φ_c. 71
(6.7) Micrographs of a rapid collapse gel with high φ_c. 72
(6.8) Height profile of a slow collapse gel. 73
(6.9) Micrographs of a slow collapse gel. 74
(6.10) Height profile of a regime A gel. 75
(6.11) Micrographs of a regime A gel. 76
(6.12) Height profiles of the gels formed by small PMMA colloids. . . . 77
(6.13) State diagram of small particle gel showing the evolution of collapse mechanisms. 78
(6.14) Micrographs of small-colloid gel: regime A gel. 78
(6.15) Micrographs of small-colloid gels: rapid collapse and slow collapse. 80

(7.1) Illustration of geometries. 84
(7.2) Illustration of the significance of the meniscus in rapid gel collapse. 85
(7.3) Height profiles of gel β in different geometries. 86
(7.4) Gel β in geometry $\mathbb{B}$. 87
(7.5) Gel β in geometry $\mathbb{C}$, 1× objective. 88
(7.6) Gel β in geometry $\mathbb{C}$, 2× objective. 89
(7.7) Gel β in geometry $\mathbb{D}$, 1× objective. 91
(7.8) Gel β in geometry $\mathbb{D}$, 2× objective. 92
(7.9) Height profiles of gel β in geometry $\mathbb{D}$. 93
(7.10) Gel β in geometry $\mathbb{D}$, away from air bubble with a 1× objective. 93
(7.11) Illustration of the significance of the meniscus in rapid gel collapse. 94
(7.12) Height profiles of gel β in different geometries (re-plotted). 95
(7.13) Height profiles of the gel δ in geometries $\mathbb{A}$ and $\mathbb{C}$. 98
(7.14) Micrograph of gel δ in geometry $\mathbb{C}$, first observation. 99
(7.15) Micrograph of gel δ in geometry $\mathbb{C}$, second observation. 99
(7.16) Micrograph of gel δ in geometry $\mathbb{C}$, third observation. 100

(8.1) Colloids fall from the corner of a meniscus. 106
(8.2) Mechanism of the falling of colloids from the corner of a meniscus. 108
(8.3) Finger-like clusters fall close to the wall. 108
(8.4) Mechanism of the falling of colloids around an air bubble. 110
(8.5) Gel β in a cone geometry. 111
(8.6) Top view of gel β in a cone geometry. 112
(8.7) Define the onset of the rapid collapse 114
(8.8) Top view of the volcanoes in geometry $\mathbb{D}$. 117
(8.9) Areal density of the volcanoes in geometry $\mathbb{D}$. 118

(8.10) Volcanoes at the gel interface of the creaming gel in a cuvette. . 119
(8.11) Volcanoes of the creaming gel in a bottom-cut vial. 120
(8.12) The radial distribution of volcanoes in a bottom-cut vial. 120
(8.13) Solvent droplets are generated from cracks. 123
(8.14) A solvent droplet is stuck and squeezed back into the gel. 124
(8.15) Air bubbles create wakes in slow collapse gel. 125
(8.16) A solvent droplet generated from the wake of an air bubble. . . . 126

(A.1) The shape of a meniscus. 137
(A.2) Scaled height profile of a rapid collapse gel with low φ_c 139
(A.3) The normalised interface speed of rapid collapse. 141
(A.4) The onset height (Δh_o) of rapid collapse. 142
(A.5) τ_d with varying φ_c and c_p 143
(A.6) τ_o with varying φ_c and c_p 145
(A.7) Key features in the propagation of onset of rapid collapse in geometry $\mathbb{D}$. 146
(A.8) Shape of the gel interface of gel β changes with time in geometry $\mathbb{D}$. 147
(A.9) Height profiles of a rapid collapse gel ($\varphi_c = 0.23$, $\varphi_p^{free} = 0.338$) in different geometries. 148
(A.10) Microscopic image of gel $\varphi_c = 0.23$, $\varphi_p^{free} = 0.338$ in geometry $\mathbb{A}$. 149
(A.11) Microscopic image of gel $\varphi_c = 0.23$, $\varphi_p^{free} = 0.338$ in geometry $\mathbb{B}$. 150
(A.12) Microscopic image of gel $\varphi_c = 0.23$, $\varphi_p^{free} = 0.338$ in geometry $\mathbb{C}$. 150
(A.13) Microscopic image of gel $\varphi_c = 0.23$, $\varphi_p^{free} = 0.338$ in geometry $\mathbb{D}$ at air bubble side. 151
(A.14) Microscopic image of gel $\varphi_c = 0.23$, $\varphi_p^{free} = 0.338$ in geometry $\mathbb{D}$ far away from the air bubble. 152
(A.15) Height profile of the creaming gel in a cuvette. 154
(A.16) Micrographs of the creaming gel in a cuvette (side-view). 154
(A.17) Confocal image of a solvent droplet in the creaming gel. 156
(A.18) Confocal image of volcanic eruptions in the creaming gel. 157

(B.1) Linear viscoelastic measurement for gel γ 159
(B.2) Frequency respond of gel γ 160
(B.3) Dynamic strain sweep for gel γ at $\omega = 1$, plotted against strain. . 161
(B.4) Dynamic strain sweep for gel γ at $\omega = 1$, plotted against stress. . 161
(B.5) Flow curve of gel γ 162

List of Tables

(4.1) Properties of solvents. 49
(4.2) Properties of the model system. 54

Chapter 1

Introduction

1.1 About This Work

This work is an experimental study of colloidal gels during the onset of their collapse under gravity. Some facts have been well known for decades but are still fascinating upon closer inspection. This study is mainly about exploring the collapse of gels by simply watching them on the mesoscopic scale ($\sim 10^2$ µm). Some phenomena are interpreted but with questions remaining; only tentative speculation can be offered for other observations.

Why study the collapse of gels? If thermodynamics always wins, non-equilibrium states are doomed to equilibrate to lower free energy states. It is interesting to see how nature makes sure this is done. Transient gels (especially those with short delay time) are a good system to observer this process. On the other hand, colloids can be found everywhere in daily life, such as milk, paint and cosmetic products. For many industrial products, there are two seemingly contradictory requirements. First, colloidal particles are required to be supported by their own weight for a sufficiently long time. Second, if needed, a moderate stress, like a simple squeeze, should be able to turn the product into a fluid. To fulfil these requirements, one can formulate a product as a colloidal gel which can support its own weight for a finite delay time. However, a gel with unmatched density will eventually collapse or cream. The delay time can be hours to years. Therefore, the delay time of the colloidal gel sets the shelf life of many products. Hence, understanding the collapse of gels may provide guild lines for product design.

In the following sections of this chapter, I will talk about relevant ingredients

for making a colloidal gel for this work. Then, in Chapter 2, the formation and collapse of gels will be discussed. At the end of Chapter 2, I will highlight the questions that this work aims to tackle and outline the thesis.

1.2 Colloidal System

In condensed matter physics, colloids have been the focus of interest for decades. Colloids are ubiquitous in daily life, such as solid particles in paint, fat droplets in milk, etc. The constituents of a colloidal system are colloidal particles, which are also, widely but sometimes confusingly, termed 'colloids'.[1] Colloids are microscopic solid particles or liquid droplets suspended in a solvent. Their size typically lies in the range of 1 nm $-$ 1 µm. Colloids are small enough for their dynamics to be driven by thermal energy. They are also large enough that quantum effects can be neglected and their positions and motions can be observed in real space and real time [1–3]. The system can respond strongly and non-linearly to comparatively weak stimuli [4–6]. With a mismatched density between solvent and the particles, colloids can even flow under gravity. To stabilize the colloidal systems, many industrial products are formulated as colloidal gels which can support their own weight for a finite time, such as paint and some cosmetic products. However, a colloidal gel is an out-of-equilibrium structure. It will evolve towards equilibrium states, such as a crystalline phase coexisting with a fluid phase [7–10]. Therefore, the stability of colloidal gels is one of the main concern in the industry. In this work, a model system will be used to study the effect of gravity on the long-term stability of colloidal gels.

1.2.1 Brownian Motion

Since colloidal particles are immersed in a solvent, the particles are tossed about by the thermal motion of the solvent molecules. Due to the much larger size of colloids and the stochastic nature of the motion, there will be a net imbalance force exerted on colloids. As a result, colloids move in a random walk, which means that each step of the motion is uncorrelated with the motion history. The discovery of this motion is credited to the Scottish botanist Robert Brown. Hence, this motion is also known as Brownian motion. The Brownian motion of colloidal particles can be characterized by their mean-squared displacement (MSD), which

[1] The term 'colloid' can be referred to the colloidal system or the constituents of the colloidal system as well. However, when talking about colloidal volume fraction, it is clear that, we are talking about the volume of the colloidal particles over the entire colloidal system.

is given by [11]:

$$\langle \Delta r^2(t) \rangle = 2\mathcal{N}Dt \ , \tag{1.1}$$

in $\mathcal{N}$ dimension, where D is the diffusion coefficient. For a freely diffusing colloid, the MSD is linear with time t. In this case, the free-particle diffusion coefficient D_0 of a colloid with radius R in a solvent of viscosity η_s at temperature T is given by the Stokes-Einstein relation:

$$D_0 = \frac{k_\mathrm{B}T}{6\pi\eta_\mathrm{s}R} \ , \tag{1.2}$$

where k_B is Boltzmann's constant. When the particle cannot be considered isolated, its diffusion is hindered by its neighbours; the particle dynamics is no longer straightforward. The diffusion coefficient becomes time-dependent and length-scale-dependent as well.

The Brownian time is defined as the time needed for a free colloidal particle to diffuse its own radius. Hence, in 3 dimensions, using Eq. 1.1 and Eq. 1.2, we have

$$\tau_\mathrm{B} = R^2/(6D_0) = \frac{\pi\eta_\mathrm{s}R^3}{k_\mathrm{B}T} \ . \tag{1.3}$$

It indicates how fast (or slow) an isolated particle diffuses. At room temperature, a $R \sim 1$ µm particle in water yields $\tau_\mathrm{B} \sim 1$ s ($\eta_\mathrm{s} \approx 0.001$ Pa $\cdot$ s). Also note that $\tau_\mathrm{B} \propto R^3$; in other words, size really matters.

In an optical study of a colloidal system, to suppress the Brownian motion in order to yield a good image of a single particle in real space and real time, one may want to use a larger particle. Because a larger colloidal particle diffuses slower compared to the exposure time of the imaging ($\sim 10^1$ ms), the resulting images are less distorted by the motion of the particle.

However, under gravity, quite quickly a particle will be too large to be considered as a colloid: it should be able to suspend in the solvent due to the thermal motion. For a particle, the height distribution is $\sim \exp(-mgh/k_\mathrm{B}T)$, where m is the buoyancy mass of the particle. For a large particle, the average height above the surface due to the thermal energy is $\langle h \rangle = k_\mathrm{B}T/mg = \mathcal{O}(10^{-13})$ m (consider a polymethylmethacrylate (PMMA) particle of $R = 100$ µm in water). This tells us something obvious: large particles cannot suspend in the water due to the thermal motion. Thus, we may require the size $R \lesssim \langle h \rangle$ for a particle

to be reasonably treated as a colloid. This also leads to the requirement of the gravitational Péclet number for a colloidal particle to be $\mathrm{Pe_g} = R/\langle h \rangle \lesssim 1$. We rearrange this expression, $\mathrm{Pe_g} = R/\langle h \rangle = mgR/k_\mathrm{B}T \lesssim 1$, in which mgR is the gravitational energy and $k_\mathrm{B}T$ is the thermal dynamics energy. This again reflects how we defined a colloidal system: a system in which the particles are thermally driven.

1.3 Hard Sphere Colloids

1.3.1 Hard Sphere Potential

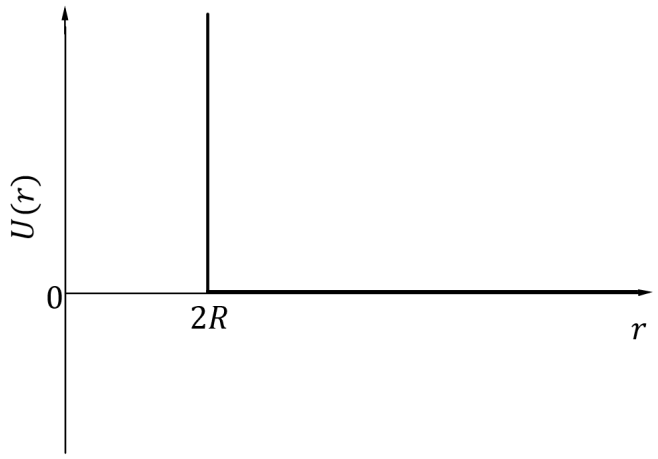

Figure 1.1 *Hard sphere potential.*

In order to introduce the inter-particle interaction in our model system, we first look at the hard spheres. The hard sphere potential is either infinite or zero depending on whether the particles overlap or not. The potential $U(r)$ between two hard spheres with a radius of R is illustrated in figure 1.1, where r is the centre-centre distance. It simply means the particle is considered to be undeformable. Because of its simplicity, the hard sphere system is an ideal model system for both more complex colloidal systems as well as many particle systems in general [12–17].

1.3.2 Sedimentation of a Single Colloid

Consider a spherical colloid with radius R in water, which sediment under the gravity. The fluid exerts a frictional, or drag, force which comes from the viscous resistance of the fluid and balances the buoyancy force. Hence, in steady state,

the colloid moves with a terminal velocity, v_s.

To estimate the drag force, a dimensionless number, so-called Reynold number, Re, is introduced. The Reynold number can be defined as:

$$\mathrm{Re} = \frac{\rho v R}{\eta_s} \ , \tag{1.4}$$

where ρ is the density of the fluid and v is the velocity of the sphere. For colloidal particles, typical sizes are in the micron range and typical velocities are $\lesssim 10^0$ µm/s. As the viscosity of the water is $\sim 10^{-3}$ Pa $\cdot$ s, the Reynold number of the colloidal system is very small (Re $\ll 1$). In this limit, the colloidal system is viscosity dominated [18]. The drag force is given by Stokes law:

$$F_s = 6\pi\eta_s R v \ , \tag{1.5}$$

where F_s is the Stokes force.

By equating the buoyancy force to the Stokes force, one can estimate the terminal velocity to be:

$$v_s = \frac{2\Delta\rho g R^2}{9\eta_s} \ , \tag{1.6}$$

where $\Delta\rho$ is the density difference between the colloidal particle and the fluid and g is the gravitational acceleration. A silica particle of ~ 1 µm radius in water yields a sedimentation speed of $v_s \sim 2 \times 10^{-1}$ µm/s ($\Delta\rho \approx 1$ g/cm^3 and $\eta_s \approx 0.001$ Pa $\cdot$ s).

1.4 Experimental Hard Spheres

It is impossible to make perfect hard spheres in reality, but they can be approximated closely. In this section, I will introduce the various colloidal interactions and I will describe how they can be minimized.

1.4.1 Electrostatic Interactions

In a polar solvent, colloids may be charged due to the ionisable groups on the surface. Consider a weak electrostatic interaction, the repulsion potential has a Yukawa form [18]:

$$U_R = A\frac{\exp(-r/\lambda_D)}{r} \ , \tag{1.7}$$

where A is the amplitude of repulsion and λ_{D} is Debye screening length. The Debye screening length characterizes the length beyond which the screening by counter-ions leads to the vanishing of electrostatic interactions, $\lambda_{\mathrm{D}} = (\frac{\varepsilon k_{\mathrm{B}} T}{2z^2 e_0^2 n_0})^{1/2}$, where ε is the dielectric constant of the medium; ze_0 is the charge of the particle; n_0 is the ionic concentration in the bulk solution.

In a polar solvent, the charge of the colloidal particle can be screened by adding salts. The counter-ions in such a system is typically produced by the dissociation of the salts. The Debye length can be reduced to several nanometres. Therefore, the charge-screened colloids can be treated as hard spheres [19].

In a non-polar solvent, although it has been shown that some charging of the colloids always occurs, the electrostatics can be neglected for small particles [19]. However, in some cases, especially for density matched polymethylmethacrylate (PMMA) based systems, colloids can acquire a charge of $z \sim 100 - 500$ due to the halogenated solvent. Also, the ionic strength is low due to the low dielectric constant of the solvent, leading to a long Debye length (up to microns). Hence, the charge on the colloid is almost unscreened. This can lead to strong long-range interactions [19]. Such long-range repulsion favours low local particle densities and changes the phase behaviour of the system [19–21].

1.4.2 London-van der Waals Interaction

Experimental colloidal particles are significantly influenced by the London-van der Waals (LvdW) interaction which is of quantum mechanical origin [22]. The LvdW force is a consequence of the fluctuating electron density of molecules. Hence, the LvdW interaction between two spherical colloids can be approximated by the integration over all pairs-wise interaction of the molecules in the colloidal particles. The LvdW interaction between two particles of the same material immersed in a fluid is always attractive [23]. The LvdW attraction strength between colloids is $\sim A/x$, when $x \ll 1$, in which $x = \Delta/2R$, Δ is the shortest distance between two colloidal surfaces and A is the Hamaker constant. The Hamaker constant is related to the polarisability of the material (equivalently, refractive index) with the dimensions of energy, and for many colloidal materials its typical value is $\sim 10^{-19}$ J (or equivalently $\sim 25 k_{\mathrm{B}} T$). If the refractive indices of the particle and the suspending solvent are equal, $A = 0$. For larger separations (say $\gtrsim 10$ nm), the LvdW potential decay quickly with the increasing centre-centre distance as r^{-7} rather than r^{-6}. It is because the electromagnetic

fields have a finite speed of propagation [18]. Therefore, the LvdW attraction between colloids is short in range but high in strength. This leads to irreversible aggregation of the colloids. Hence, colloids need to be stabilized against the LvdW attraction.

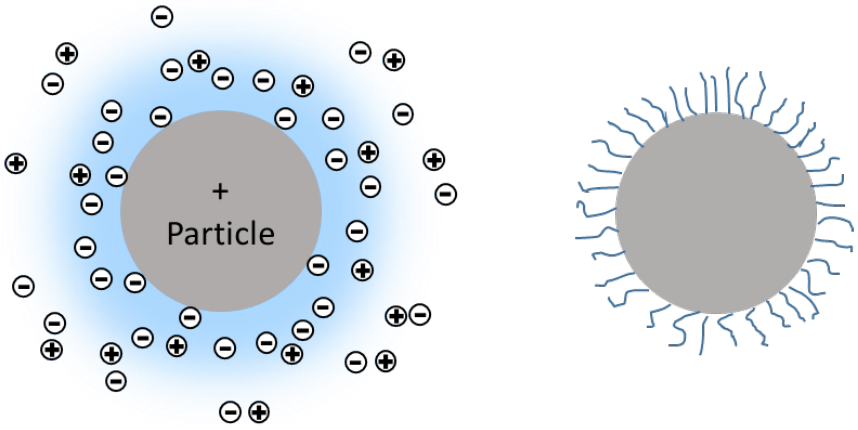

Figure 1.2 *Two ways of stabilizing colloidal particles in the suspension: (a) charge stabilization and (b) steric stabilization*

Stabilization can be achieved in two ways [22]. For colloids that contain ionisable surface groups, they are stabilized when dispersed in a polar solvent through charge stabilization. The particle is charged due to the dissociation of the ionisable group. The counter-ions form an electrostatic double layer around the particle, as illustrated in figure 1.2(a). When two particles approach, their counter-ion clouds overlap, and the particles repel each other. Usually, the charge of the particle needs to be carefully screened by adding salts, so that the hard sphere model is applicable. As mentioned in the last section, the residual charge on the particles will change the phase behaviour of the colloidal system, for example, leading to crystallisation at lower volume fraction [13].

Some colloidal particles can be stabilized by grafting a layer of polymer hairs on their surface, known as steric stabilization, as illustrated in figure 1.2(b) [24]. The length of the hairs should be longer than the range of LvdW force. Also, the polymer used should prefer solvent so that hairs readily extend outwards and repel the hairs on the other colloids when in contact. Although the hairs bring softness to the hard sphere interaction, the colloids can be considered as

nearly hard spheres if the stabilizing layer is small compared to the size of the colloid [9, 19]. The interaction between sterically stabilized colloidal particles is illustrated in figure 1.3.

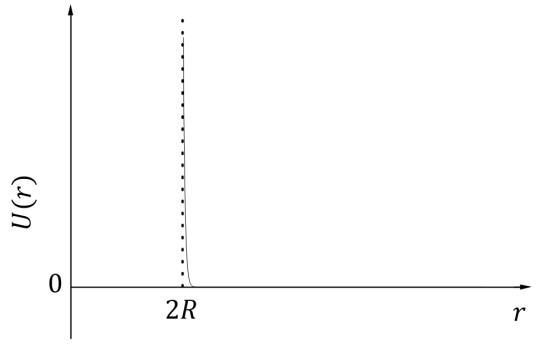

Figure 1.3 *The inter-particle potential of nearly hard sphere colloids, which are stabilized by short 'hairs'. The dotted line is the ideal hard sphere potential, as shown in figure 1.1.*

1.4.3 Hydrodynamics

The movement of a colloid disturbs the surrounding solvent. This disturbance affects the colloids in the vicinity through hydrodynamic interaction, so that the motions of separate particles are coupled. Studies have shown that the hydrodynamic interaction plays an important role in colloidal gel formation. It promotes gelation, lowering the colloidal volume fraction threshold for percolation [25, 26]. It also suppresses the formation of larger local structure [27]. On the other hand, although hydrodynamics is believed to be crucial for the gel collapse, details of the role are yet to be revealed [28, 29].

1.4.4 Phase Behaviour of Hard Spheres

The hard sphere system is an entropy-controlled system. The equilibrium states are determined by maximising the number of possible microstates for the given extensive properties of the system. The single parameter that determines the phase behaviour of a hard sphere system is φ, the volume fraction of spheres, which is given by $\varphi = NV_{\mathrm{HS}}/V_{\mathrm{tot}}$, where N is the number of spheres, $V_{\mathrm{HS}} = \frac{4}{3}\pi R^3$ is the volume of the sphere with radius R and V_{tot} is the total volume of the system.

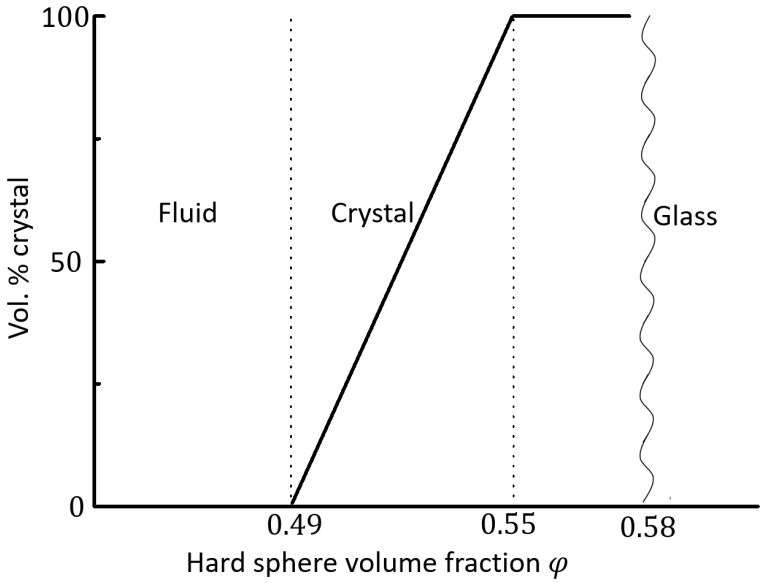

Figure 1.4 *Hard-sphere phase diagram*

The phase behaviour of the hard sphere system has been investigated for decades [9]. At low volume fraction, the hard sphere system is in a fluid state. Above $\varphi = 0.494$, crystalline phase coexists with fluid, until $\varphi = 0.545$ where the entire system is crystallised. In gravity, the colloidal crystals grown just above $\varphi = 0.494$ show a mixture of random hexagonally close-packed (h.r.c.p) planes and face-centred cubic packing; whereas in microgravity, exhibit the h.r.c.p structure alone [30]. Above $\varphi = 0.545$, the crystal becomes increasingly compact as the volume fraction is continually grown towards to $\varphi = 0.74$, at which the maximum close-packed configuration is reached. Besides those equilibrium states, non-equilibrium states can also be found in hard sphere systems. A non-equilibrium state will always evolve towards an equilibrium state, although it may take a very long time. For example, J. Zhu *et al.* reported that glass samples which crystallize fully with in two weeks in microgravity fail to crystallize after more than a year in normal gravity [30]. The non-equilibrium state can be reached by quenching fast. For instance, a hard sphere glass can be obtained by compressing particles in the centrifuge. The glass state is formed at volume fraction above $\varphi_{\mathrm{g}} = 0.58$ by arresting the crystallization into a metastable, kinetically jammed state. The glass state can persist until $\varphi = 0.64$ which corresponds to the random close-packed volume fraction (φ_{RCP}). Figure 1.4 summarises the phase behaviour of the hard sphere system [9].

1.5 Introducing Attraction

Achieving an experimental 'nearly hard sphere' system, we can continue our task on gel-making by introducing controllable attractive interactions to the system. It is a common practice to introduce attraction by adding a depletant. The depletion attraction mechanism is schematically shown in figure 1.5. An unbalanced osmotic pressure is induced by the exclusion of polymer from the region between two nearby colloidal particles. It pushes the particles together resulting in an effective attraction. Or, in other words, the depletion zone around a particle with a thickness of R_g (the radius of gyration of the polymer coil) is inaccessible for the polymer coils. Once two particles come together, their depletion zones overlap. This overlapping volume increases the free volume of polymer coils, resulting in an increase of their entropy. Therefore, the touching of the colloids is entropically favourable.

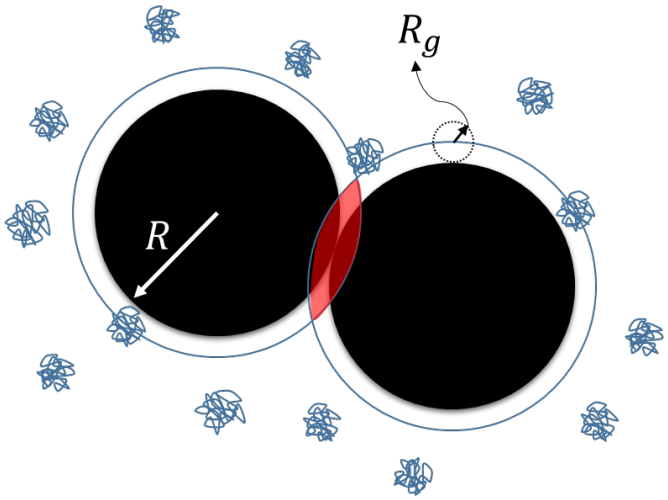

Figure 1.5 *Depletion mechanism. Colloids (black spheres) are surrounded by much smaller non-absorbing polymer coils (blue coils). When two colloids come into contact, the polymer coils exert a force equivalent to their osmotic pressure in opposite directions to keep the colloids together. Or, equivalently, the shaded zone is inaccessible to polymer coils. Once one colloid contacts another, their excluded volumes overlap to increase the free volume available to polymer coils. Hence, the entropy of polymer coils increases. Therefore, aggregation of colloids effectively increases the entropy of the system.*

This entropy driven potential U_{dep} can be estimated using statistical mechanics [18]:

$$U_{\text{dep}} = -\Pi_{\text{p}} V_{\text{overlap}} \ , \tag{1.8}$$

where

$$V_{\text{overlap}}(r) = \frac{4}{3}\pi R_{\text{g}}^3(1+\frac{1}{\xi})^3[1-\frac{3r}{4R(1+\xi)}+\frac{r^3}{16R^3(1+\xi)^3}] \ , \tag{1.9}$$

is the volume of the overlapping depletion zones between two colloids as a function of r, the centre-to-centre distance between the two colloids. $\xi = R_{\text{g}}/R$ is the ratio of the polymer radius of gyration to the colloid size.

Assuming polymer coils do not interact, the osmotic pressure Π_{p} is given by the ideal gas expression:

$$\Pi_p = n_{\text{p}} k_{\text{B}} T \ , \tag{1.10}$$

where $n_{\text{p}} = N_{\text{p}}/V_{\text{free}}$ is the number density of the polymer in the free volume (more comments on '*free volume*' V_{free} will be given in Chapter 2). Thus, we have:

$$U_{\text{dep}}(r) = \varphi_{\text{p}}^{\text{free}} k_{\text{B}} T(1+\frac{1}{\xi})^3[1-\frac{3r}{4R(1+\xi)}+\frac{r^3}{16R^3(1+\xi)^3}] \ , \tag{1.11}$$

where $\varphi_{\text{p}}^{\text{free}} = N_{\text{p}}(\frac{4}{3}\pi R_{\text{g}}^3)/V_{\text{free}}$ is the free volume fraction of the polymer. Equation 1.11 shows that, by changing the size and the volume fraction of the polymer, one can not only tune the depth of the attractive potential but also the range. For the hard sphere system with non-absorbing polymers, the total potential between two particles is shown in figure 1.6, which is given by [22]:

$$U(r) = \begin{cases} +\infty & ; for \quad r \leq 2R \\ U_{\text{dep}}(r) & ; for \quad 2R < r \leq 2R + 2R_{\text{g}} \\ 0 & ; for \quad r > 2R + 2R_{\text{g}} \end{cases} \ . \tag{1.12}$$

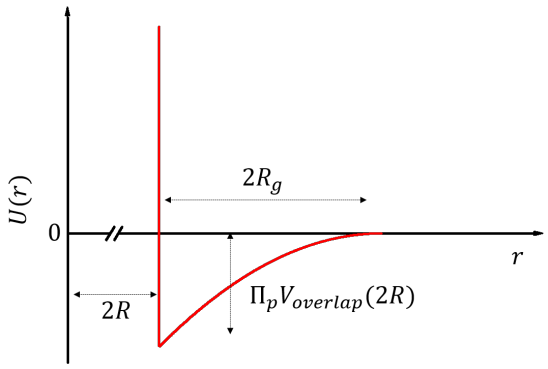

Figure 1.6 *The total potential of the hard sphere system with non-absorbing polymer.*

Chapter 2

Colloid + Polymer Mixture

Having described the constituents of a colloidal gel in the previous chapter, in this chapter I will describe how these ingredients form the model system that I will study throughout this thesis. I will describe the state diagram of this model system and explain how dynamic arrest leads to the formation of gels. Lastly I will briefly review the collapse of gels and set a direct starting point for this work.

2.1 Model System

The model system studied in this work is a mixture of polymethylmethacrylate (PMMA) particles and linear polystyrene (PS) polymer coils. The particles are dispersed in *cis*-decahydronaphthalene (*cis*-decalin) + tetrahydronaphthalene (tetralin), for closely matching the refractive index (referred to as IM solvent here). The PMMA particle is sterically stabilized by poly(12-hydroxystearic acid) (PHSA), which is $\sim$ 10 nm long [31]. The (visible light) refractive indices of PMMA and the solvent mixtures are close ($\sim$ 1.5 at 25 °C). Hence, the LvdW interaction between the particles is weak. Although the 'hair' brings softness to the inter-particle interaction, in the IM solvent mixture, the PMMA particles are expected to behave effectively as hard spheres [19, 31, 32]. The softness brought by PHSA is less significant especially for the large particles ($\sim$ 1 µm) studied in this work [19].

The non-adsorbing polymer used in this work is PS. The depletion strength is related to the free volume fraction of the polymer $\varphi_{\mathrm{p}}^{\mathrm{free}}$, as shown in Eq. 1.11. The free volume V_{free} is the volume accessible to the (centre of) polymer in the mixture, which is neither occupied by the colloids nor the depletion zones around

them (see figure 1.5). $\varphi_{\mathrm{p}}^{\mathrm{free}}$ is related to the experimental measurable quantity φ_{p}, the volume fraction of polymer in the entire volume V_{T}, by

$$\varphi_{\mathrm{p}} = \alpha\varphi_{\mathrm{p}}^{\mathrm{free}} \ , \tag{2.1}$$

where α is the free-volume fraction which has been estimated by H. Lekkerkerker *et al.* giving [10, 33–36]:

$$\alpha = (1-\varphi_{\mathrm{c}})\exp[-A\gamma - B\gamma^2 - C\gamma^3] \ , \tag{2.2}$$

where $\gamma = \varphi_{\mathrm{c}}/(1-\varphi_{\mathrm{c}})$, $A = 3\xi + 3\xi^2 + \xi^3$, $B = 9\xi^2/2 + 3\xi^3$, $C = 3\xi^3$ and φ_{c} is the colloidal volume fraction.

The IM solvent can be approximately considered as a theta solvent of PS at room temperature (see Chapter 4). Hence, in the dilute and semi-dilute solutions, the PS in IM solvent can be treated as non-interacting. The molecular weight of PS is chosen to yield small polymer-colloid size ratios ($\xi < 0.1$).

2.2 Phase Behaviour

2.2.1 Equilibrium Phase Behaviour

Having looked at the equilibrium phase diagram of hard spheres in Chapter 1, I will discuss what happens with this equilibrium phase diagram when polymers are added to the system.

At equilibrium, the average values of all state variables are constant in time. To achieve a statistical description of the equilibrium properties, we minimise the Helmholtz free energy F of the system at a fixed volume. Since the volume of the system is fixed, it is convenient to express the free energy in terms of free energy density $f = F/V$.

For our model system, the free energy density f is a function of the colloidal volume fraction φ_{c} and the polymer chemical potential μ_{p}, i.e. $f = f(\varphi_{\mathrm{c}}, \mu_{\mathrm{p}})$ [10]. On the other hand, when the temperature of the system is fixed, μ_{p} is related to the free volume fraction of the polymer $\varphi_{\mathrm{p}}^{\mathrm{free}}$ through the free-volume

number density of polymer n_p by [37]:

$$\mu_\mathrm{p} = k_\mathrm{B}T\ln(n_\mathrm{p}\lambda_\mathrm{p}^3) \ , \tag{2.3}$$

where λ_p is the de Broglie thermal wavelength for the polymer. Therefore, the free energy density f can be expressed as $f = f(\varphi_\mathrm{c}, \varphi_\mathrm{p}^\mathrm{free})$. f can be evaluated for the colloidal fluid phase and the colloidal crystal phase. For a given attraction strength, i.e. a given $\varphi_\mathrm{p}^\mathrm{free} = \varsigma$, the free energy density for each phase can be plotted as a function of φ_c, which (for low $\varphi_\mathrm{p}^\mathrm{free}$) has the form as shown in figure 2.1(a). As an example, the state point $S(\varphi_{\mathrm{c},S}, \varsigma)$ in figure 2.1(b) may phase separate into two coexisting phases, fluid phase A and solid phase B. Now, we try to predict the colloidal volume fraction of the (potentially) coexisting phases, geometrically.

Consider the equilibrium conditions for coexisting phases, i.e. equal chemical potential μ and pressure p (for colloids), we rewrite μ and p as follows:

$$\begin{aligned} \mu_\mathrm{c} &= \Big(\frac{\partial F}{\partial N}\Big)_V \\ &= \Big(\frac{\partial F}{\partial \varphi_\mathrm{c}}\Big)_V \Big(\frac{\partial \varphi_\mathrm{c}}{\partial N}\Big)_V \\ &= V_c \Big(\frac{\partial f}{\partial \varphi_\mathrm{c}}\Big)_V \ , \end{aligned} \tag{2.4}$$

where V_c is the volume of a single colloid. And,

$$\begin{aligned} -p &= \Big(\frac{\partial F}{\partial V}\Big)_N \\ &= f + V\Big(\frac{\partial f}{\partial \varphi_\mathrm{c}}\Big)_N \Big(\frac{\partial \varphi_\mathrm{c}}{\partial V}\Big)_N \\ &= f - \varphi_\mathrm{c}\Big(\frac{\partial f}{\partial \varphi_\mathrm{c}}\Big)_N \ . \end{aligned} \tag{2.5}$$

In other words, $\mu_\mathrm{c}/V_\mathrm{c}$ is the slope of $f(\varphi_\mathrm{c})$ and $-p$ the intercept. Hence, in figure 2.1(a), point A and B share a common tangent. This common tangent construction shows that, in figure 2.1(a), the initially homogeneous sample (in both branches) with colloidal volume fraction $\varphi_{\mathrm{c},S} \in (\varphi_{\mathrm{c},A}, \varphi_{\mathrm{c},B})$ can lower its free energy density by phase separating into coexisting phase of fluid phase A with $\varphi_{\mathrm{c},A}$ and solid phase B with $\varphi_{\mathrm{c},B}$. From the conservation of the number of colloids, the volume of these coexisting phase, V_A and V_B can be calculated using the *lever rule* [38]:

$$\frac{V_A}{V_B} = \frac{\varphi_{c,B} - \varphi_{c,S}}{\varphi_{c,S} - \varphi_{c,A}} \ . \tag{2.6}$$

Re-applying this process for different φ_p^{free}, we can determine the equilibrium phase behaviour of our model system as a function of φ_c and φ_p^{free} (and hence φ_p) for a certain size ratio ξ. For small ξ the phase diagram can be represented schematically as figure 2.1(b) and (c) [10, 37, 38].

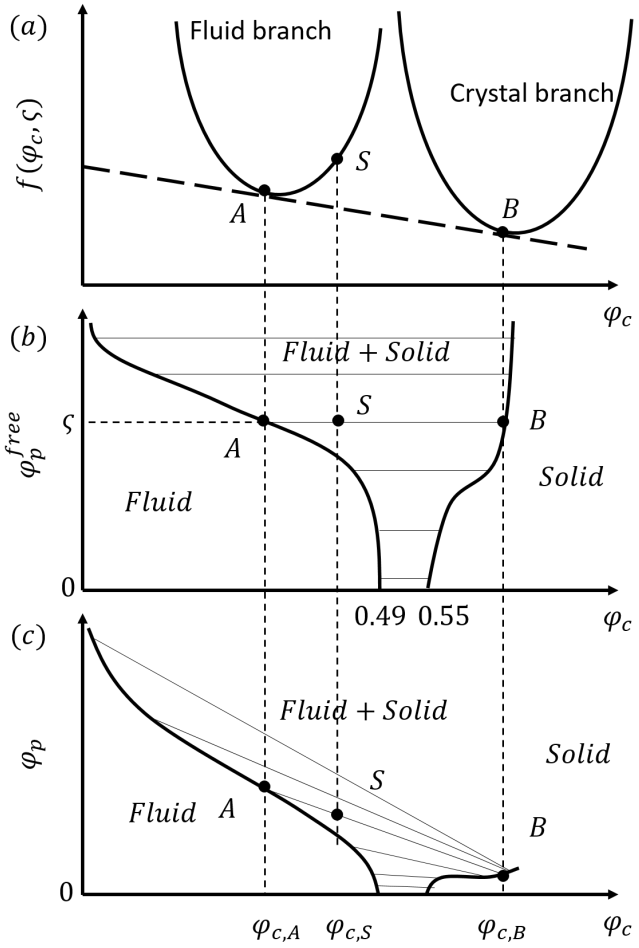

Figure 2.1 *Schematic illustration of the free energy density and the common tangent construction with low polymer concentration (a); predicted equilibrium phase diagram of PMMA+PS model system (with low ξ) in the representation of $\varphi_p^{free} \sim \varphi_c$ (b) and $\varphi_p \sim \varphi_c$ (c). For a small free-volume fraction of the polymer ς (indicated in (b)), the free energy density f for fluid and crystal branch can be plotted as a function of colloidal volume fraction φ_c, and both exhibit a single minimum. By applying the common tangent construction, the coexisting phases A and B in equilibrium state can be determined (marked in (b) and (c)). In this way, the phase boundaries can be predicted (shown as thick solid lines in (b) and (c)). The thin solid lines linking coexisting phases in (b) and (c) are tie-lines.*

To understand the difference between these two representation of phase diagram shown in figure 2.1(b) and (c), we can re-write Eq. 2.1 and Eq. 2.3 as [10]:

$$\varphi_{\rm p}^{\rm free} = \frac{\varphi_{\rm p}}{\alpha} = \frac{4}{3}\pi R_{\rm g}^3 \exp[(\mu_{\rm p} - \mu_{\rm p}^0)/k_{\rm B}T] \ , \tag{2.7}$$

where $\mu_{\rm p}^0$ is a reference chemical potential. For all coexisting phases (with different $\varphi_{\rm c}$) in equilibrium, the chemical potential $\mu_{\rm p}$ is the same, hence $\varphi_{\rm p}^{\rm free}$ is also the same (see Eq. 2.7). Therefore the tie-lines joining coexisting phases in a $\varphi_{\rm p}^{\rm free} \sim \varphi_{\rm c}$ phase diagram are horizontal (figure 2.1(b)). However, $\varphi_{\rm p} = \alpha(\varphi_{\rm c})\varphi_{\rm p}^{\rm free}$, so that the tie-lines in the $\varphi_{\rm p} \sim \varphi_{\rm c}$ representation is oblique (figure 2.1(c)).

In the predicted phase diagrams shown in figure 2.1(b) and (c), we can see that without polymer, the region of colloidal fluid-crystal coexistence is recovered for hard-sphere colloid (at $0.494 < \varphi_{\rm c} < 0.545$). With small size ratio ξ ($\lesssim 0.3$), adding polymer merely expands the range of $\varphi_{\rm c}$ at which the fluid coexists with solid (crystal), see figure 2.1(b) and (c). With larger size ratio, or equivalently longer range of attraction, colloidal liquid phase becomes stable, leading to fluid-fluid separation [37].

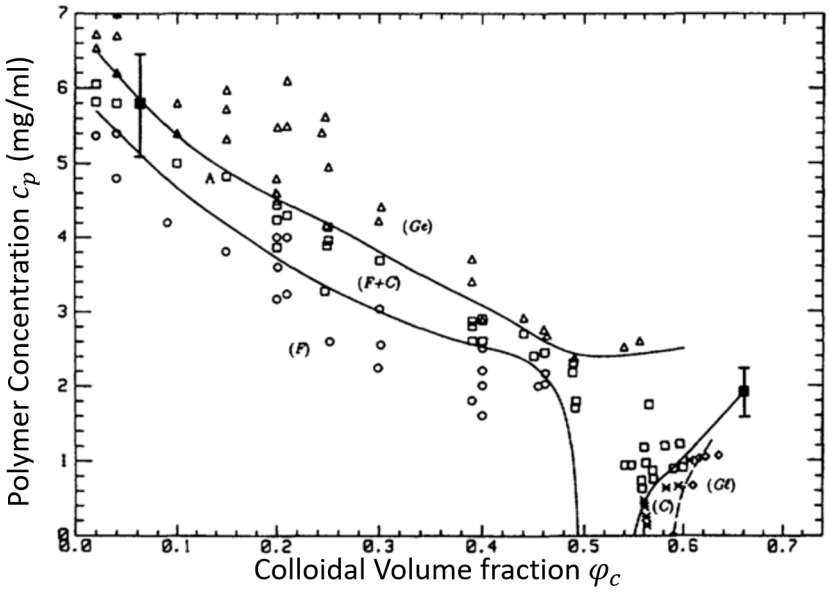

Figure 2.2 *The experimental phase diagram ($c_{\rm p}$ vs. $\varphi_{\rm c}$) for PMMA + PS model system with $\xi \approx 0.09$. ○: single phase colloidal fluid; □: fluid-crystal coexistence; △: gel; ×: fully crystalline; ◇: glass. This figure is reproduced from Ref. [39].*

In this work, the size ratio ξ is restricted to below 0.1. In this attraction range, the phase diagram of our model system has been studied experimentally by W.

Poon *et al.* as shown in figure 2.2 [39]. The phase diagram is presented in the representation of polymer concentration (calculated with respect to the entire volume of the sample) *vs.* φ_c, which is derived directly from the experiment. The radius of PMMA particle was 217 nm, the radius of gyration of the polymer was $\approx$ 19 nm, giving $\xi \approx 0.09$. At low c_p and φ_c, the sample is a single fluid phase ($\circ$ in figure 2.2). Adding more depletant to the colloidal system eventually induces phase separation, leading to fluid-crystal coexistence ($\square$ in figure 2.2). The broaden fluid-crystal coexisting region generally agrees with the theoretical prediction.

2.2.2 Non-Equilibrium Behaviour

Apart from the equilibrium phase behaviour, non-equilibrium structures are also found in the experiments. As shown in figure 2.2, colloidal glass can be formed at high φ_c with or without the presence of polymer. Further studies reveal a glass-glass transition when adding more polymer into the dense colloidal suspension [40, 41]. In the vicinity of $\varphi_c = 0.6$, all colloidal suspensions are expected to be crystalline in thermodynamic equilibrium (even if it may take a very long time) [10, 30]. Systems with $c_p = 0$ are glasses, consistent with hard sphere glass as described in Sec. 1.4.4. These glasses are formed due to the caging of the particles, and termed as 'repulsive glasses'. With a small amount of polymer, the system is completely crystallized. This suggests that φ_{glass} is shifted higher due to the existence of the depletion attraction. With this weak short-range attraction, the formation of crystals is attributed to the melting of the glass. At even higher polymer concentration, a new kind of glass can be found. This high polymer concentration glass is not caused by caging of colloids but corresponding to the long-lived bonds that stick particles to each other [11]. Therefore, these new kind of glasses are called 'attractive glasses'. The ***glass transition lines*** can be calculated from mode coupling theory (MCT) or determined by simulations [11, 29, 40, 41].

At low and intermediate φ_c, when adding even more polymer, transient gels can be formed ($\triangle$ in figure 2.2). A colloidal gel is a space spanning colloidal network that appears quiescent for a finite time; minutes or hours after re-mixing, the gel collapses (or creams) under gravity. It can even be formed at very low φ_c, if the polymer concentration is sufficiently high, i.e. the inter-particle attraction is high enough. The critical polymer concentration for gelation decreases as the colloidal volume fraction increases.

To explain this non-equilibrium behaviour, W. Poon *et al.* suggested the existence of ***gas-liquid binodal*** that is hidden inside the fluid-solid coexisting line [42]. As $\varphi_{\mathrm{p}}^{\mathrm{free}}$ increases, the free energy density curve of the fluid branch develops a second minimum, leading to the possible coexistence of two fluid phases with different colloidal volume fractions, i.e. colloidal gas (lower φ_{c}) and colloidal liquid (higher φ_{c}). The gas-liquid binodal can be formalised by applying the common tangent construction as shown in figure 2.3 [42]. A state with $\varphi_{\mathrm{c}} = \varphi_{\mathrm{i}}$ and $\varphi_{\mathrm{p}}^{\mathrm{free}} = \varsigma'$ (point i on the $f(\varphi_{\mathrm{c}}, \varsigma')$ curve) can lower the free energy of the system by phase separating into a non-equilibrium state of coexisting of a gas phase (φ_{g}) and a liquid phase (φ_{l}), as shown in figure 2.3. Of course, the equilibrium state of fluid (φ_{f}) and solid (φ_{s}) coexistence has the lowest free energy density. Hence, by applying the common tangent construction in different ways, we can derive both the equilibrium (fluid-solid coexisting) and the non-equilibrium (gas-liquid coexisting) boundaries.

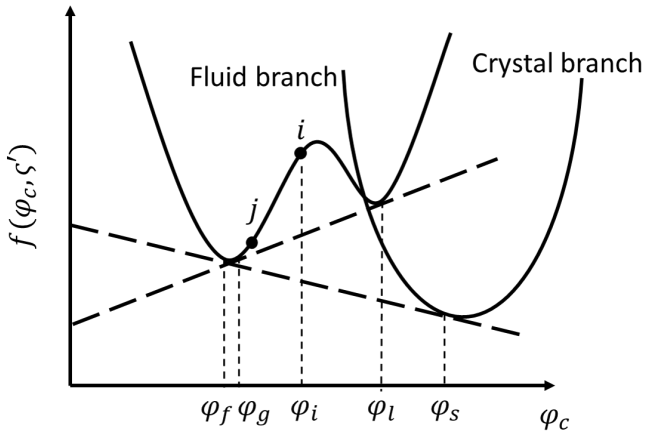

Figure 2.3 *Schematic illustration of the metastable gas-liquid phase separation using free energy plot and the common tangent construction at high polymer concentration. The fluid brunch of the $f(\varphi_{\mathrm{c}}, \varsigma')$ with high $\varphi_{\mathrm{p}}^{\mathrm{free}} = \varsigma'$ shows a 'double minimum' structure. By applying the common tangent construction, both the equilibrium fluid-solid phase boundary (φ_{f}, φ_{s}) and the non-equilibrium gas-liquid binodal (φ_{g}, φ_{l}) can be traced out.*

A closer look at point i and j in figure 2.3, we may find an important distinction: the curvature of the free energy density function $\partial^2 f / \partial \varphi_{\mathrm{c}}^2$ may be either positive (e.g. point j) or negative (e.g. point i). At φ_{i}, any small composition fluctuation may be amplified leading to a local aggregation and consequently a phase separation. This composition is unstable. By contrast to point i, at point j, the system is locally stable with respect to a small density fluctuation. Achieving the lowest free energy state (fluid-solid coexistence) is energetically costly (compared

to the unstable state). This composition is metastable. The transition point of this local stability is given by the curvature $\partial^2 f/\partial\varphi_c^2 = 0$, which is known as the ***spinodal*** line. Similarly, with varying φ_p^{free}, we can trace out the spinodal line that is embedded in the gas-liquid coexisting region, see figure 2.4. The phase-separating process that point i exhibits is known as spinodal decomposition [18]. It is related to the formation of the colloidal gel that is studied in this work. We will come back to this later.

2.2.3 State Diagram

In this section, a general way will be introduced to map the state diagram of general short-range attractive systems.

The second virial coefficient is a characterization of pair-wise interaction. For our model system, the inter-particle interaction can be simplified as pair-wise interaction $U(r)$ given by Eq. 1.12. Hence, the second virial coefficient can be defined as:

$$B_2 = \frac{1}{2}\int \Big(1 - \exp(-U(\vec{r})/k_B T\Big) d\vec{r}\,, \tag{2.8}$$

In spite of the fact that the size ratio ξ will modify the topology of the $U_{dep} \sim \varphi_c$ state diagram and shift the critical point, it is believed that any short-range attractive potential of arbitrary shape and range within a few percent of the colloidal diameter share the same phase coexistence line in the $b_2 \sim \varphi_c$ state diagram [43–45]. Here, $b_2 = B_2/B_2^{HS}$ is the normalized second virial coefficient, where $B_2^{HS} = 2\pi a^3/3$ is the second virial coefficient for hard spheres. This provides a tool to compare different experiments and simulation results.

Figure 2.4 shows a schematic state diagram presented in interaction strength ($1-b_2$ or U_{dep}) against φ_c. It summarises the equilibrium and the non-equilibrium behaviour related to gelation.

2.3 Formation of Colloidal Gels

In our model system, gels with low colloidal volume fraction are formed through a different mechanism than at high volume fraction.

At very low colloidal volume fraction and high attraction strength (shaded region in figure 2.4), a gel can be formed through diffusion-limited cluster aggregation

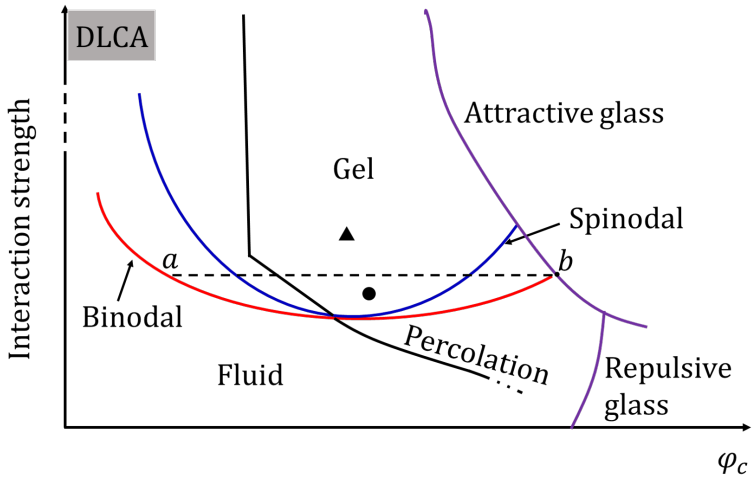

Figure 2.4 *Schematic state diagram of interaction strength against φ_c related to gelation, not to scale. Dashed line ab is the tie-line where the binodal line meets the glass transition line. State point ● is above the spinodal line but below the tie-line ab. It corresponds to the gas-liquid coexisting state. State point ▲ is above the tie-line ab. It corresponds to the gel state which is formed through the arrested spinodal decomposition, see text. Re-drawn from Ref. [11] and [29].*

(DLCA) [7]. With the existence of inter-particle attraction, two particles are considered as 'bonded' whenever they come into each other's attraction range. With a strong attraction, one can imagine a permanent and rigid bond is formed whenever two particles touch each other so that particles diffuse as a cluster. Clusters can collide and hence aggregate. Therefore, the dominating factor of the system's behaviour, and hence the morphology of the cluster, is diffusion [46]. The resulting cluster is found to be fractal, figure 2.5. Eventually, the growing clusters will reach a characteristic size and span the entire space — the system is gelled.

We can define the fractal dimension d for a fractal structure as

$$N \propto \left(\frac{R_g}{R}\right)^d , \tag{2.9}$$

where R_g is the radius of gyration of a cluster, R is the radius of the colloidal particle and N is the number of colloids. The fractal dimension d must be less than the spatial dimension $\mathcal{N}$. For $\mathcal{N} = 3$, DLCA gives $d \approx 1.8$.

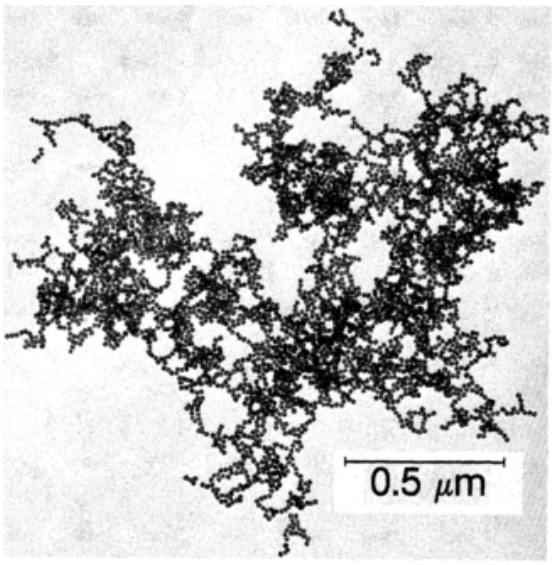

Figure 2.5 *Transmission electron micrograph of a gold colloid cluster formed by DLCA [46]. Reproduced from Ref. [47].*

Notice that, the average colloidal volume fraction of the cluster $(R/R_g)^3$ decreases as the cluster grows. Once $(R/R_g)^3$ decreases to that of the total sample (φ_c), the fractal clusters meet each other, i.e. the sample is gelled. In other words, gelation occurs when the volume fraction of clusters reaches 1. Hence, we have the characteristic size of the cluster at the gel point:

$$R_g^{gel} \sim R\varphi_c^{1/(d-\mathcal{N})} \ . \tag{2.10}$$

It can be seen that, for DLCA, the size of clusters that form a gel decreases with increasing φ_c.

With higher colloidal volume fraction, a colloidal gel is formed through spinodal decomposition that is arrested by the glass transition. With high enough φ_c, the largest colloidal clusters in the suspension will percolate, i.e. the colloidal network spans the whole space of the sample. With low attraction strength, the thermal fluctuation can constantly break and reform the bonds, so that the percolation is undetectable on the macroscopic level (the region between percolation line and binodal line in figure 2.4). Increase the attraction strength, we first look at the ● in figure 2.4 which is inside the unstable region but below the tie line *ab* at which the binodal meets the glass transition line (at *b*). The system may exhibit spinodal decomposition; however, the 'spinodal structure' cannot persist, resulting in a gas-liquid coexisting phase. Increase the attraction strength further, we now consider the point ▲. The system tries to separate into gas and liquid phases

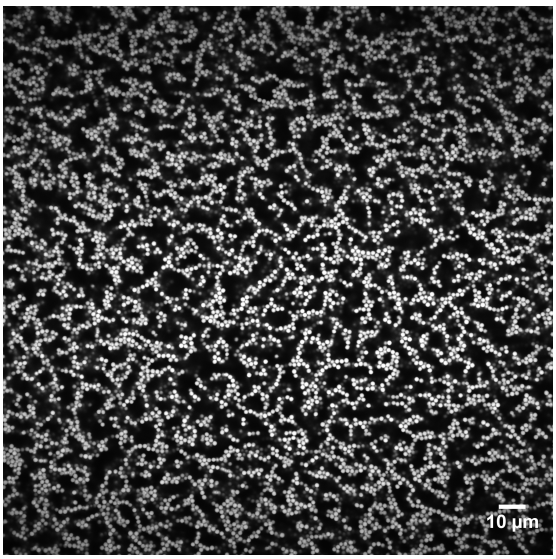

Figure 2.6 *A confocal image of a PMMA + PS colloidal gel formed through the spinodal decomposition that arrested by the glass transition. The radius of PMMA colloids is* $a = 955$ nm. *The radius of gyration of PS (the depletant) is* $R_g = 51$ nm. *The suspending solvent is a density-matched mixture of cyclohexyl bromide and cis-decalin.* $\varphi_c = 0.23$ *and* $c_p = 3$ *mg/ml.*

through spinodal decomposition, which gives rise to a bi-continuous texture. The (colloidal) liquid phase is then kinetically arrested by the glass transition, i.e. rearrangement of colloids is suppressed in the spinodal structure. Hence, the particle network is percolated and gelled. State points enclosed by the spinodal line, attractive glass line and tie line *ab* in figure 2.4 can form 'arrested spinodal gel' [11]. Figure 2.6 shows a confocal image of PMMA + PS colloidal gel. In this work, we restrict the polymer-colloid size ratio $\xi < 0.1$. In this case, the gel structure tends to be tenuous and branched, contrasted with the thick and more compact one for large ξ [48].

2.4 Gel Collapse

So far, we have been ignoring the gravity which certainly affects the non-density-matched gels. A colloidal gel is a non-equilibrium structure which is evolving (no matter how long it will take) towards the equilibrium state of coexisting fluid and crystal, see figure 2.1. Such a process is facilitated in gravity by the collapse of a gel (assuming the density of colloids is higher than that of solvent for simplicity). The sedimentation of gels has been studied macroscopically and microscopically for over three decades [49–52]. In this section, I will review the observations and perspective of the collapse of gels.

2.4.1 Macroscopic Behaviours

A colloidal gel is macroscopically quiescent after being remixed for a finite period of time (the so-called delay time). After the delay time, a gel collapses with a sharp, horizontal gel interface that separates the supernatant from the settling gel. By plotting the height of the gel interface against time, it has been shown that a gel collapses in two distinguishable ways, either with a sudden collapse of the structure followed by a much slower compaction, or *via* a slow compaction without the sudden collapse. These two classes of collapse have been related to the strength of the inter-particle attraction and the colloidal volume fraction, φ_c [29, 51–54]. For gels with low colloidal volume fraction, a sudden collapse also known as "rapid collapse" can be observed. On the other hand, at high φ_c, a gel collapses slowly with decreasing sedimentation speed in a process known as "creeping" or "slow collapse".

The collapse of colloidal gels has further been reported to depend on parameters including the range of the attractive potential, the density mismatch [55], the size of the colloids [29, 56], and even the width and height of the sample [53, 57, 58].

For our model system, R. Harich *et al.* performed an extensive study on the collapse of gels with varying φ_c and φ_p^{free} [29]. To monitor the collapse of gels, they used time-lapse imaging to record the gels. They traced the height of the gel interface and plotted the time dependence of the height of a gel as scaled height $\hat{h}(t)$:

$$\hat{h}(t) = \frac{(h(t) - h_\infty)}{(h_0 - h_\infty)} \ , \tag{2.11}$$

where h_0 is the initial height of the sample and h_∞ is the height of the final sediment. Results are summarised in the state diagram figure 2.7(a), in which the shaded region indicates the gel-forming region predicted without gravity.

They demonstrated that at high φ_c, in the regime B of the state diagram (figure 2.7(a)), a gel has a long delay time and exhibits stretched-exponential compression without sudden collapse (figure 2.7(b)). Therefore, regime B corresponds to the slow collapse. With intermediate φ_c, in regime D, the macroscopically quiescent period is followed by a rapid collapse with a constant interface speed and a final compaction of the sediment figure 2.7(c). Regime D corresponds to the rapid collapse. For regimes B and D, h_∞ was taken as $h_{RCP} = 0.64$, the height of random-close-packed sediment. At low φ_c, in regime

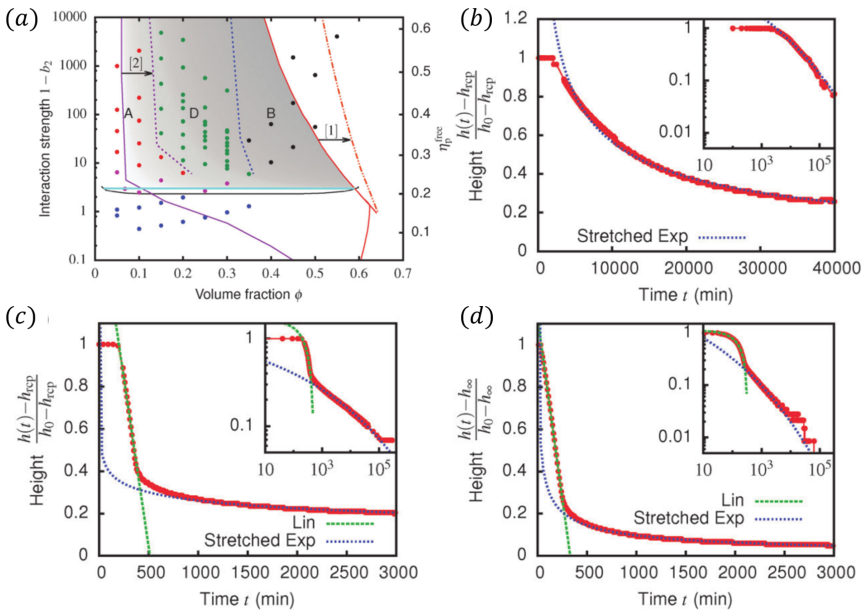

Figure 2.7 *Three different kinds of collapse in colloids + polymer model system. (a) The equilibrium and the non-equilibrium state diagram relative to gelation. The solid black line = gas-liquid binodal from computer simulations; the purple line = percolation line from simulation; the red solid line = glass transition lines calculated from MCT mapped to simulations; the cyan line = the tie line where binodal meets the glass transition line, above which the percolated system can be arrested by the glass transition. The shaded area is the gel region predicted without gravity. The real attractive glass line is likely shifted to the red dash-dotted line (arrow [1]). The gelation line in gravity should lie to the right of the percolation line (arrow [2]).* ● *= single phase,* ● *= gas-liquid coexistence,* ● *= gels with collapse behaviour A,* ● *=gels with collapse behaviour D,* ● *= gels with collapse behaviour B. (b) - (d): scaled height vs. time for typical gels in regime B (b), regime D (c) and regime A (d), respectively. Green lines = linear fits to the rapid collapse. Blue lines = stretched exponential fits to the slow sedimentation,* $\hat{h}(t) \sim e^{(t/\tau)^{\beta}}$ *with exponent* $\beta = 0.12$. *The inset in each case shows the log-log form of the main plot. Reproduced from Ref. [29].*

A, a sample collapses rapidly with little or no delay time suggesting a non-gelling structure, figure 2.7(d). Interestingly, regime A is inside the gel-forming region that is predicted without gravity. Samples in regime A are distinguishable from phase-separating samples by supernatant that is devoid of particles and the colloidal volume fraction of the final sediment. It suggests that the gelation boundary is shifted to higher colloidal volume fraction in gravity, see arrow 2 in figure 2.7(a). To understand the A - D boundary and the φ_c-dependence of the collapse, I will discuss, in the next section, the mechanism of the collapse proposed based on microscopic observations.

2.4.2 Collapse Mechanism

Microscopically, the collapse of a gel can be modelled using the poroelastic formalism pioneered by M. Biot [59] and R. Buscall *et al.* [49]. In this approach, a gel can be considered as a biphasic fluid-saturated porous continuum with a solid phase of percolated particles and a liquid phase of the solvent. As the colloids settle, the solvent is expelled from the gel structure. The back flow of the fluid through the network counteracts the compression of the gel. On the other hand, as the gel network deforms, the elasticity of the network also limits the rate of compression. Therefore, the height profile of a collapsing gel reflects the balance of the gravitational stress of the colloids with the pressure due to fluid flow and the elastic stress of the gel. In this model, a gel collapses exponentially as a poroelastic material [51, 56, 60]. Experimentally, the results of slow-collapse DLCA gels [51, 61] and slow-creaming depletion gels [56, 60] support this model. For our model system, the slow collapse can be better fitted by a stretched-exponential function, see figure 2.7(b) as an example [29, 52, 62, 63]. Hence, the kinetics of slow collapse can be captured by such poroelastic model reasonably well.

However, the sudden (rapid) collapse deviates from such (stretched-) exponential kinetics. For long-range depletion gels, combining the investigation of the micro-structure of the gel, it has been proposed that the sudden collapse can be attributed to the appearance of random micro-collapsed regions throughout the gel [54]. The picture of the collapse is then the fluid flow is driven by the formation of random compression centres within the gel and the rate at which fluid can be expelled from the gel determines the collapse of the gel. For DLCA gels, at the onset of the rapid collapse, the gel interface flattens [51]. This indicates that the sample turns into a fluid as the structure of the gel is broken. Hence, it is suggested that such deviation is the manifestation of network failure [51].

For our model system, the rapid collapse has also been associated with the network failure. L. Starrs *et al.* studied the rapid collapse using dark-field imaging (DFI) [53]. A so-called "streamer" was found falling from the top of a gel as the end of the delay period approached, see figure 2.8. Such a streamer created a strong back flow that destroyed the gel structure. Similarly, using ghost particle velocimetry, it was found that rupture in rapid collapse gels was initiated at or close to the upper meniscus [52]. The disruption of the gel structure propagated from the top of the gel with much faster local dynamics. By measuring gels

under step stresses, S. Manley *et al.* demonstrated that when a gel network was overstressed, it can take a long time to yield [51]. Hence, they suggested that the delayed rapid collapse is triggered as a result of the gravitational stress overwhelming the yield stress.

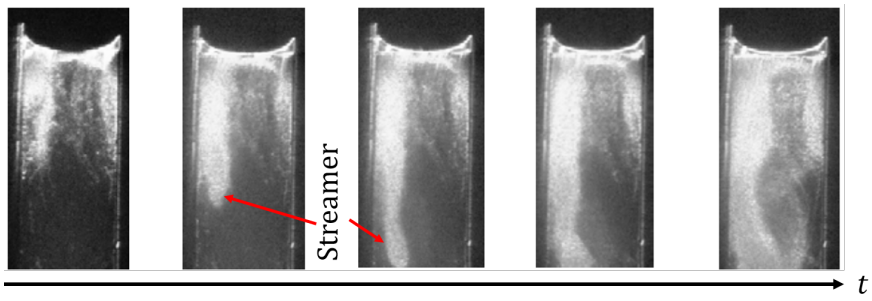

Figure 2.8 *Dark field images of a rapid collapse gel with increasing time. A "streamer" (bright patch) falls from the top of the gel and creates back flows. Reproduced from Ref. [53].*

The scenario of gel breaking due to yielding seems implausible, as pointed out by E. Secchi *et al.*, since the gravitational stress is stronger close to the cell bottom, where the structure has to sustain the entire weight of the gel [52]. Using magnetic resonance imaging (MRI), R. Harich *et al.* clarified this by showing that a layer of debris with higher local volume fraction was formed around the meniscus [29]. With intermediate φ_c, in regime D of figure 2.7(a), debris from such layer rapidly sank through the body of a gel just before the onset of the rapid collapse. Calculations suggested that it was this denser layer that forced the gel to yield and triggered the rapid collapse. However, the origin of such debris that forms the denser layer at the top is still unclear [29].

Furthermore, the yielding scenario is supported by the observations of gels with high and low colloidal volume fractions. MRI showed that at high enough φ_c, in regime B of figure 2.7(a), the gels were always strong enough to support the weight of such debris, so that the gel collapsed as a compacting poroelastic continuum [29, 49, 60, 62]. On the contrary, at low φ_c, in regime A of figure 2.7(a), calculations suggested that a sample cannot support the gravitational stress exerted by a single particle so that the gelation was suppressed by gravity [29]. Hence, the gelation boundary is shifted to higher φ_c in gravity as indicated by the arrow 2 in figure 2.7(a).

The collapse of a gel inevitably involves solvent being expelled from the gel.

This suggests that how the solvent is expelled from a gel is also an important question. In the poroelastic model, fluid flows through a compressing but intact gel network [51, 56, 60]. For long-range depletion gels, fluid is driven by the random micro-collapse throughout the gel [54]. For DLCA gels, C. Derec *et al.* reported volcanic eruptions found at the gel interface, see figure 2.9 [64]. They proposed that the eruption is caused by solvent flows through a cylindrical channel. The solvent in the channel comes from the horizontal flow of solvent in the surrounding gel. In our model system, channels were found in slowly collapsing gels. They were generated close to the wall of the container then propagated upwards. Volcanic eruptions were also observed as channels reached the gel interface [53]. It is speculated that such channels are crack apertures in the bulk of the gel [65]. However, the nature of these channels is yet to be revealed. Also, the back flow that destroys the gel structure and the volcanic eruptions imply that the hydrodynamics is crucial in the collapse of a colloidal gel.

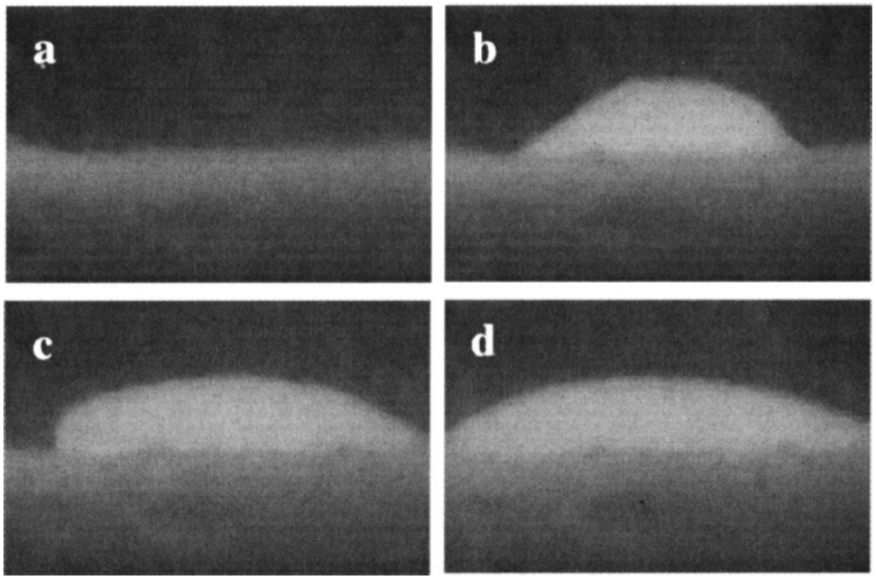

Figure 2.9 *The "volcanic eruption" at the interface of a collapsing DLCA gel. The width of the photographs corresponds to 7.5 mm and the time interval between two photographs is 4 s. Reproduced from Ref. [64].*

2.5 Thesis Outline

I highlight again the previous results mentioned in Sec. 2.4 that denser layer falling and solvent being expelled from a gel are two of the key processes during the collapse in our model system. Where does the extra mass of the denser layer come from? How is the solvent expelled from the gel? This work aims to tackle these questions.

I will show that the colloids at the vertical part of the air-gel interface are the main source of the extra mass of the denser layer. Therefore, by retarding the formation of this denser layer, I will demonstrate that the collapse of gels can be postponed. The solvent can be expelled from a gel in the form of droplets which give rise to the channels observed previously. Furthermore, an evolution of the mechanism of collapse will be presented as the colloidal volume fraction increases.

To present these results, I have talked about relevant ingredients for making a colloidal gel for this work in Chapter 1 and presented the background information of the formation and the collapse of a gel in this chapter. I will present the details of the imaging methods in Chapter 3. The model system studied in this work will be characterised and the preparation of gels will be described in Chapter 4. In Chapter 5, I will set up the starting point for the rest of the work. I will show that colloidal gels with both large and small particle sizes can be categorised into 3 regimes similar to the finding of Ref. [29]. In Chapter 6, I will present the evolution of the collapse mechanism as the colloidal volume fraction increases. Also, in Chapter 6, I will show that the vertical part of the air-gel interface is crucial for the formation of the denser layer. I confirm this in Chapter 7 by removing most of the meniscus in a gel. The result shown in Chapter 7 suggests a way to postpone the collapse of a gel. The result in Chapter 6 also shows that the solvent can be expelled from a gel as solvent droplets. The discussion on the formation of the solvent droplets as well as the denser layer will be given in Chapter 8. This thesis will be ended by attempting to bring different aspects of the observation together and raising questions for the future work in Chapter 9. Other than the main results mentioned above, interesting observations were made throughout my work. However, to keep the main storyline clear and neat, these observations will be shown in Appendix A according to their appearance in the main text. These observations serve as footnotes or lead to interesting questions of their own.

Chapter 3

Method

In this work, the onset of collapse of colloidal gels is studied using microscopic time-lapse imaging which focuses on the vicinity of the meniscus during the earlier stage of the collapse. To identify the type of collapse, long-time observation is required. Direct digital imaging can provide macroscopic observation with a long time-scale. Hence, the macroscopic imaging is used to characterise the collapse of a gel and microscopic imaging is used to study the onset of the collapse. In this chapter, I will introduce the time-lapse imaging methods that are used in this work.

3.1 Macroscopic Time-lapse Imaging

3.1.1 Experimental Setup

The macroscopic time-lapse imaging is performed in a temperature controlled incubator. The setup of the experiment is shown in figure 3.1. Experiments are performed at 23 ± 0.5 °C and 25 ± 0.5 °C. The variation of temperature does not affect the results to be presented in this thesis, see Appendix A.2. Samples are levelled up by a horizontal sample stage and illuminated by a white light. The colloidal particles in this work are dyed with nitrobenzoxadiazole (NBD) which appears yellow. The refractive indices of the solvent and the colloids are slightly mismatched so that the gel structure is turbid. A black sheet is placed behind the samples to create contrast. Images (8-bit, grey-scale) are taken using a CCD camera, which is mounted at the same height as the samples. A snapshot of the resulting image is shown in figure 3.2(a). The supernatant is transparent so that the black sheet behind the sample can be seen. The settling gel is turbid which

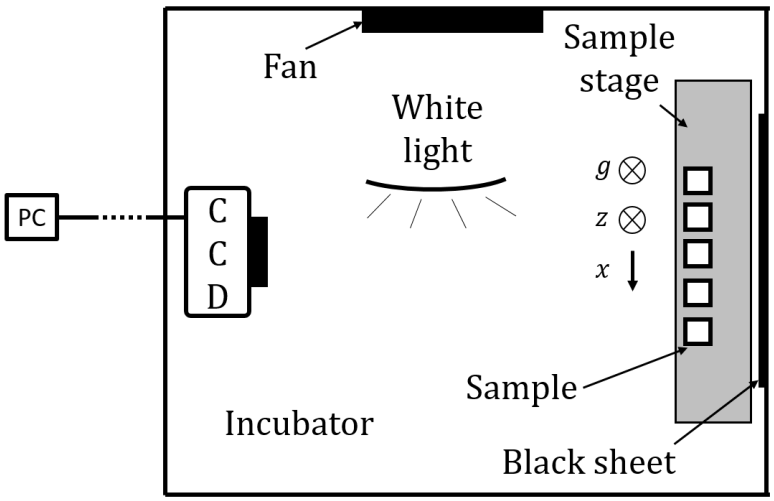

Figure 3.1 *Schematic diagram showing the setup of macroscopic time-lapse imaging.*

appears grey.

Two rulers were used to calibrate the pixel size. One was placed vertically (z-axis, gravitational direction) and the other horizontally (x direction), see figure 3.1. The pixel size in both x and z direction, p_{x} and p_{z} are equal. $p_{\mathrm{z}} = 83.33$ µm/pixel. Typically, 5 samples are imaged simultaneously.

To determine the time interval, let us consider the time resolution needed for measuring the delay time. The delay time τ_{d} of a gel is defined as the time when the gel interface detaches from the base (lowest point) of the meniscus. The time resolution Δt in the macroscopic imaging is related to the pixel size p_{z} of the image and the gel interface speed v_{i} around the meniscus:

$$\Delta t = \frac{p_{\mathrm{z}}}{v_{\mathrm{i}}} \ . \tag{3.1}$$

The gel interface needs Δt to move one pixel in the image. For rapid collapse gels, $v_{\mathrm{i}} \lesssim 1$ µm/s and $\tau_{\mathrm{d}} > 30$ min (see later), so that $\Delta t \gtrsim 1$ min/pixel. Hence, 1 min is a suitable time interval for the time-lapse imaging in these cases. The resulting uncertainty of the delay time is $\Delta\tau_{\mathrm{d}} = \Delta t/\tau_{\mathrm{d}} \approx 2\%$. For the slow collapse gel with the longest delay time ($\tau_{\mathrm{d}} = 4960$ min), $v_{\mathrm{i}} \sim 0.172$ µm/min so that $\Delta t \sim 484$ min/pixel . It gives $\Delta\tau_{\mathrm{d}} \approx 10\%$. In practice, the time interval is chosen to be between 1 min and 10 min.

Samples in a cuvette ($10 \times 10 \times 40$ mm^3, protected by lens tissues) are re-mixed

using a whirl-mixer for 40 seconds before placed on the sample stage. The interval time between the remixing of a sample and its first image is less than 20 seconds. This time is short compared to the delay time of the collapse of a gel.

3.1.2 Measuring the Height Profile

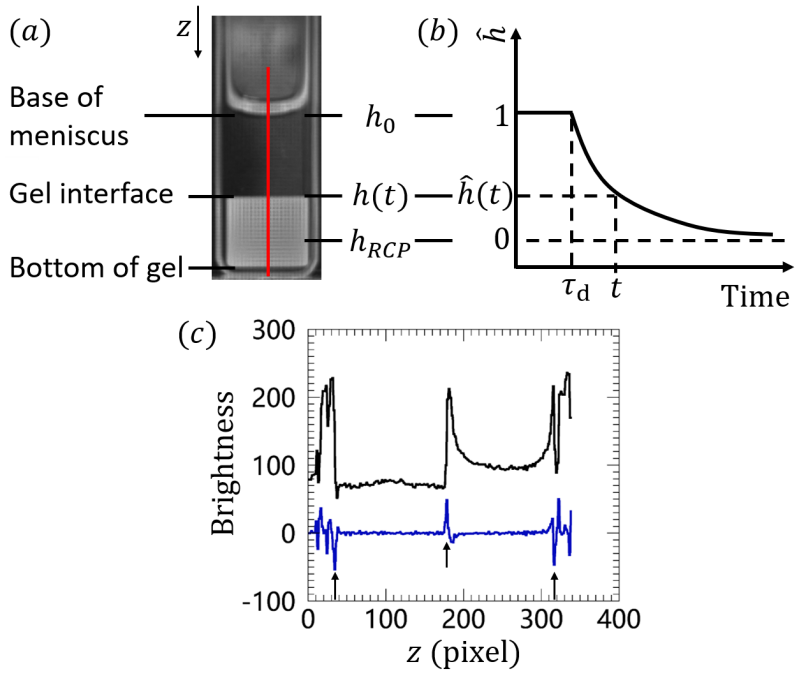

Figure 3.2 *(a) A snapshot of a settling gel from macroscopic time-lapse imaging. (c) The brightness along the centre of the sample (the red solid line) at time t is plotted as the black line. By differentiating the brightness (the blue line), the base of the meniscus, the gel interface and the bottom of the gel can be measured, see black arrows from left to right. (b) Following Ref. [29], the height profile of the gel interface is plotted as scaled height* $\hat{h}(t) = \frac{(h(t)-h_{\mathrm{RCP}})}{(h_0-h_{\mathrm{RCP}})}$ *against time (shown here schematically).*

To identify the types of collapse, height profiles of collapse processes are measured from the time-lapse images. Figure 3.2(a) shows a snapshot of a gel obtained from the macroscopic time-lapse imaging. The initial height of a gel h_0 is defined as the distance between the base of the meniscus and the bottom of the gel; and the height of the settling gel $h(t)$ is the distance between the gel interface and the bottom of the gel, figure 3.2. To measure the height, at each time t, the brightness along the centre of the sample (the red solid line in figure 3.2(a)) is differentiated. The brightness and the differentiated brightness are plotted in figure 3.2(c) as an example. By comparing to the original image, one can measure the position of the base of the meniscus, the gel interface and the bottom of the gel. The

scaled height of a gel $\hat{h}(t)$ can be calculated according to Eq. 2.11. The resulting height profile is plotted as $\hat{h}(t)$ *vs.* t following Ref. [29], as shown schematically in figure 3.2(b).

3.2 Microscopic Time-lapse Imaging

The direct way to study the collapse of a gel is to observe a gel as it collapses. Such observations have been reported in different length-scales in previous studies [29, 51, 52, 54, 64, 66]. On the length-scale of $\sim 10^2$ µm, colloid + polymer gels have been observed on the surface using direct imaging [67] and in the bulk using dark-field imaging [53]. To understand the formation of the denser layer at the top of a gel and the onset of collapse, it is necessary to re-visit the collapse of gels in the vicinity of the meniscus on the length-scale of $\sim 10^2$ µm.

However, for the model system studied in this work, poor contrast between the different regions in a gel is a considerable problem when performing an imaging study. A large difference between the refractive indices of the colloids and the solvent is required for high-contrast imaging. However, this will also lead to strong multiple scattering which limits the visible depth into the sample. The solution to the contrast problem in this work is to use fluorescence microscopy.

3.2.1 Fluorescence Microscopy

Fluorescence is the emission of photons by molecules whose electrons are excited to a higher energy state by external light source. The emission of light through the fluorescence process is almost instantaneous with the absorption of the excitation light due to a relatively short time delay ($\ll 1$ µs) between photon absorption and emission. Typically, non-fluorescent subjects of interest are labelled with a fluorescent dye or fluorophore. The sample is illuminated by an isolated excitation light. Then, the emitted light is isolated so that only the labelled subjects can be seen from the fluorescence microscopy.

The emitted light can be isolated from the excitation light thanks to the Stokes shift between the peak of excitation (or absorption) and emission spectra, see figure 3.3(a). The Stokes shift is a result of energy lost when electrons relax from the excited states back to the ground state, see the schematic Jablonski diagram shown in figure 3.3(b). As Stokes shift values increase, it becomes easier to separate the excitation and emitted light by using filters. To achieve maximum

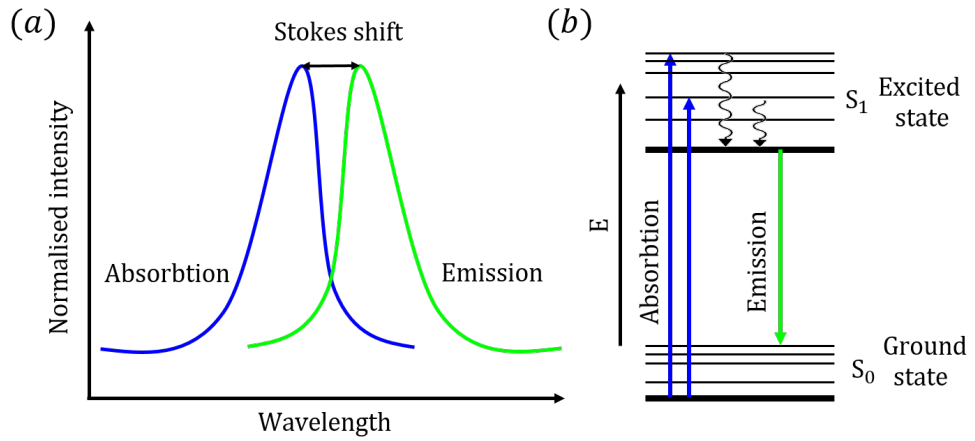

Figure 3.3 *(a) Schematic representation of the Stokes shift. (b) Schematic Jablonski diagram showing the origin of the Stokes shift. The electronic states of a molecule are arranged by energy. The vibrational ground states of each electronic state are indicated with black thick lines, the higher vibrational states with thin lines. An electron can be excited to a higher energy state (S_1) when the fluorescent molecule absorbs a photon of the appropriate wavelength (blue lines). The excited electron can release vibrational energy as heat without photon emission and relax to the vibrational ground state of the excited state (internal conversion, wavy downward pointing arrows). The molecule gives off a photon as the election collapses from the excited state (S_1) to the ground state (S_0) [68].*

fluorescence intensity, a fluorophore is usually excited at wavelengths near or at the peak of the excitation spectrum. The emitted light with the widest possible range of wavelengths that include the emission peak is filtered for detection.

Figure 3.4 shows the principle of fluorescence microscopy. For a typical arrangement, both the light source and the objective lens are positioned on the same side of the sample. In this arrangement, the lamp and light delivery assembly are called an *epi-illuminator*. Such epi-illumination is made possible by the employment of a dichroic mirror. A dichroic mirror reflects most of the excitation light and allows the emitted light to pass through. To eliminate possible background light, an extra barrier (or emission) filter is added behind the dichroic mirror. To make space for these auxiliary components in the light path, an infinity-corrected objective lens can be used. Such objective lens has an image distance that is set to infinity. Then, a tube lens is used to form a real image on the image plane of the tube lens. Between the infinity corrected objective lens and the tube lens, the rays are parallel. Components, such as filters and dichroic mirrors, can be arranged between the objective lens and the tube lens with a minimal effect on focus [68].

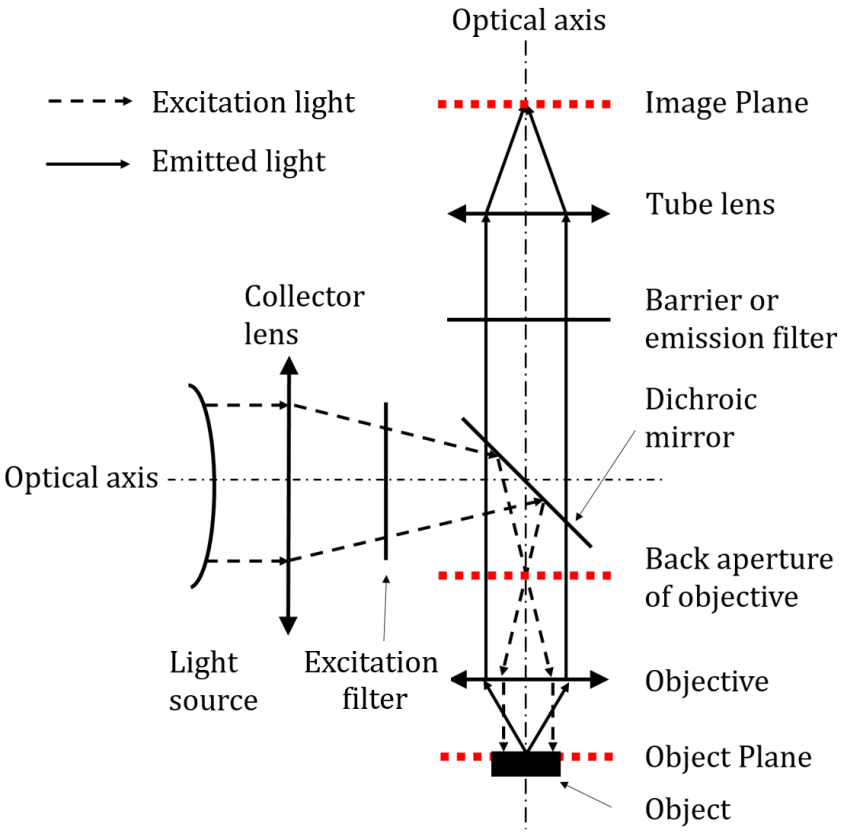

Figure 3.4 *Schematic diagram showing the principle of the fluorescence microscopy.*

The excitation light is filtered by an exciter filter to narrow the band of wavelengths and focus on the back aperture of the objective lens using a collector lens. To produce an even illumination for the specimen, the intermediate real image of the light source should fill the back aperture of the objective lens [68]. For the excitation light, the objective lens functions as a condenser lens illuminating the specimen. The light emitted by the fluorophores is collected by the objective lens and filtered by the dichroic mirror and emission filter. Finally, the tube lens collects the resulting light and forms a real image.

3.2.2 Experimental Setup

The microscopic time-lapse imaging is performed using a home-built imaging module. The layout of the module is shown in figure 3.5 schematically. The colloids in this work are fluorescently labelled with NBD, which can be excited at $\sim 488\ nm$ (blue) and emits at $\sim$ 525 nm (green). Hence, a blue LED light source is used. Both tube lens and collector lens have nominal focal length of $f = 125$ mm. The filter cube used is a Semrock single band filter set LED-FITC-

A-NQF. Its wavelength characteristics are shown in figure 3.6. The objective lens used here is a Nikon plan 1× infinity corrected objective with a numerical aperture NA=0.04. The resulting fluorescent light is focused on the CCD chip by a tube lens and forms a real image. The physical size of a (square) pixel on the CCD chip is $p_{\mathrm{CCD}} = 7.4$ µm. The dashed square highlights the adapter that connects the body of the module and the objective lens. The adapter can be mounted in different directions allowing the top-view, bottom-view and side-view of a sample can be imaged.

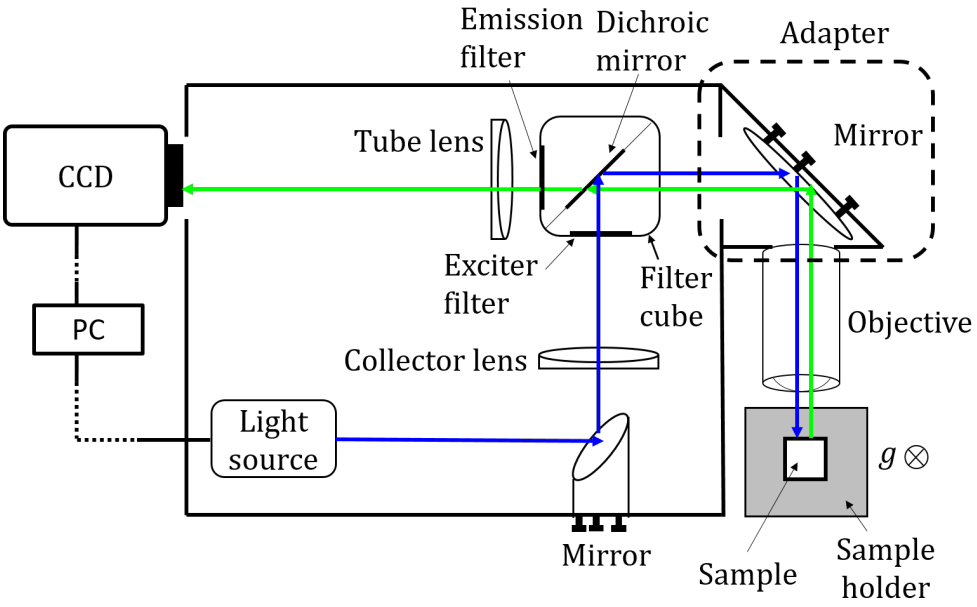

Figure 3.5 *Schematic diagram showing the layout of the imaging module.*

The typical time interval of the time-lapse imaging is 0.5 min. The experiments were performed at 23 ± 0.5 °C. A sample (protected by lens tissues) is remixed using a whirl-mixer for 40 seconds prior to the experiment. There is an inevitable delay of about 0.5 min between remixing and the commencement of imaging. Hence, the time of the first image of the time-lapse result is set to 0.5 min.

The light source is controlled using a personal computer so that the sample is illuminated only when it is imaged. This can minimise the bleaching of the fluorophore and allows long-time experiments without severely reducing the emitted light. The sample holder is horizontal and fixed. The imaging module can be adjusted in three perpendicular directions. During the experiment, the objective lens is focused on the inner wall of a cuvette (use the edge of the cuvette as a reference). Hence, the part of a sample that is close to the glass wall is imaged.

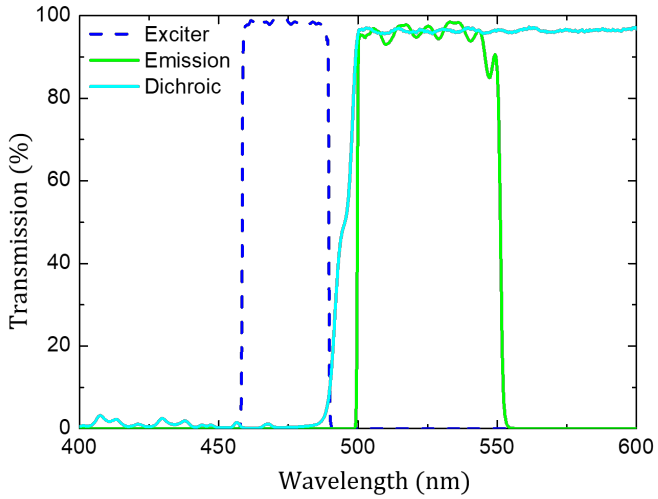

Figure 3.6 *The wavelength characteristics of the filter cube (Semrock LED-FITC-A-NQF) used in the setup, reproduced from Ref. [69].*

3.2.2.1 Depth of View

The depth of view is the depth that the objective lens can image into a gel. It depends on three aspects. The first one is the depth of field Z of the optical system. The depth of field refers to the thickness of the optical section along the optic axis within which objects in the specimen are in focus. For the $1\times$ objective lens in this setup, Z has been measured by Z. Karamanide, giving $Z = 6 \pm 1$ mm [70]. The second aspect accounts for the absorbance of the fluorophore. The intensity of excitation light decreases dramatically inside a sample due to the absorption of the fluorophore at the surface. Finally, due to the difference in refractive indices between the solvent and colloids, both the excitation light and emission light are scattered by colloids. This reduces the depth of view even further.

To estimate the depth of view, a gel with high colloidal volume fraction was imaged with constant illumination for 2 days so that the colloids at the surface were bleached. The thickness of the bleached layer is about 1 mm close to the glass wall. Notice that, this result reflects the accumulated effect of the light absorbance. Also, a low colloidal volume fraction will lead to a low concentration of fluorophore. Hence, the depth of view when imaging a gel with low φ_c can be larger than that of a high φ_c gel. Generally, the depth of view is much smaller than Z. The setup can only observe the part of a gel that is within ~ 1 mm near the glass wall.

3.2.2.2 Calibration and Spatial Resolution

In order to image the width of the whole sample using the 1× objective lens, the size of the real image on the CCD chip was adjusted (by tube lens). The module with 1× objective was calibrated using a Thorlabs calibration target. The pixel size of the image is $p_{1\times} = 9.97$ µm. Hence, the magnification of this setup is

$$M = \frac{p_{\mathrm{CCD}}}{p_{1\times}} \ , \tag{3.2}$$

giving $M = 0.74 < 1$.

The image of a self-luminous point object in a microscope is a diffraction pattern, called the Airy disk. The spatial resolution of an optical system is related to the Airy disk by the Rayleigh criterion. By this criterion, two adjacent point light sources are defined as being resolved when the central diffraction spot (Airy disk) of one point coincides with the first minimum of the other point in the image plane [68]. The limit of spatial resolution d is given by $d = 0.61\lambda/\mathrm{NA}$, where λ is the wavelength in the air and NA is the numerical aperture of the objective. For the 1× objective in this work, $d \approx 8$ µm. To maintain the maximum resolution provided by the objective, the pixel size of the CCD chip is required to be smaller than $p_{\max} = d/s$, where s is the Nyquist sample factor. For low-magnification, low-NA objective lenses, s may need to be 3 - 4 [68]. However, the CCD camera used here has a much higher p_{CCD}. Hence, the resolution provided by the objective cannot be maintained. In fact, this optical setup can observe neither single colloids nor the structure of gel network. The length-scale of the resolvable phenomenon is ≈ 30 µm, taking $s = 3$ [68].

3.2.3 Image Processing

Figure 3.7(a) shows an original image obtained from the microscopic time-lapse imaging. The brightness of the resulting images comes from the NBD-labelled PMMA colloids. NBD in the suspending solvent of a gel sample is not detectable when examining an image of a settled gel. Ideally, a homogeneous gel should produce roughly the same brightness everywhere in an image. However, uneven illumination leads to darker regions away from the centre of an image. This can be seen more obviously after adjusting the contrast globally according to the region of interest (RoI), see figure 3.7(b). The illumination is uneven because the module was not originally designed to work with such a low-magnification objective lens. To reveal more details in the micrographs, the original images are

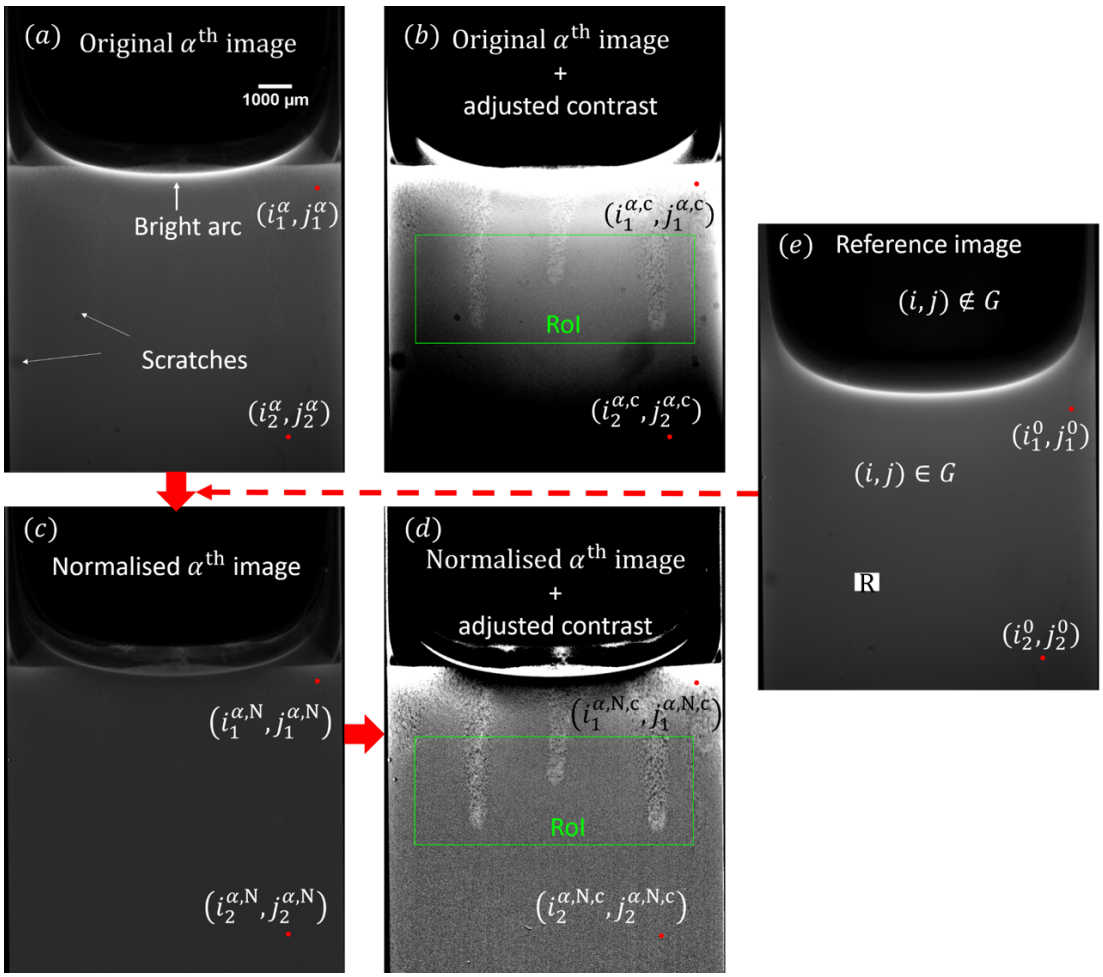

Figure 3.7 *Image processing. (a) The original α^{th} image, showing a bright arc and scratches. (b) Contrast adjusted original α^{th} image, revealing some details in the image. Also, the uneven illumination can be seen. (c) Normalised α^{th} image, using the reference image shown in (e). (d) Contrast adjusted normalised α^{th} image. More details of interest can be revealed while the corners of the meniscus are invisible. (e) The reference image in which the sample is assumed to be homogeneous. Pixel $(i, j) \in G$ corresponds to the sample in the image. Pixel $(i, j) \notin G$ corresponds to the air above meniscus or edges of the cuvette on both sides of the image. The red arrows indicate the process flow: (a) $\Rightarrow$ (c) $\Rightarrow$ (d). The green squares indicate the region of interest (RoI).*

processed so that the uneven illumination and most of the scratches on the glass wall can be eliminated. The image processing consists two parts: normalisation of brightness according to a reference image and global adjustment of the contrast according to each RoI.

3.2.3.1 Normalisation of Brightness

The process of normalisation of brightness assumes that the gel in the reference image is homogeneous on the length scale set by the resolution of our optical system ($\approx$ 30 µm). Hence, the brightness of each pixel in the reference image should be the same. The variance of brightness in later images is due to the change in the gel instead of the change of illumination. The percentage of brightness that should be attributed to the gel in the reference image can be calculated and applied to later images. In this way, in the later images, the portion of brightness that should be attributed to the gel can be evaluated.

Define $I^{\alpha}_{(i,j)}$ is the brightness of a pixel (i,j) in the α^{th} image, $\alpha = 0, 1, 2, 3, \ldots$. The micrographs in this work are 8-bit images, so $0 \leq I^{\alpha}_{(i,j)} \leq 255$. In most cases, the reference image is the first image of the time-lapse images, i.e. $\alpha = 0$ is the reference image.

Step 1: Identifying 'gel' in the reference image by setting a threshold I_{c}, so that $(i,j) \in G = \{(i,j)|I^{0}_{(i,j)} > I_{\text{c}}\}$ corresponds to the 'gel'. Then, $(i,j) \notin G$ corresponds to the cuvette or air above the meniscus. $I_{\text{c}} \sim 10$ is an experiment-dependent value that is used to truncate the cuvette and air in the reference image, see figure 3.7(e).

Step 2: Assign a uniform brightness I_{R} to each pixel $(i,j) \in G$ in the reference image, so that I_{R} is the brightness that should be attributed to an 'ideal' uniform gel. Assign $I = 0$ to $(i,j) \notin G$. Then, calculate the percentage of brightness that should be attributed to the actual gel in the reference image:

$$P^{0}_{(i,j)} = \begin{cases} I_{\text{R}}/I^{0}_{(i,j)} & ;for \quad (i,j) \in G \\ 0 & ;for \quad (i,j) \notin G \end{cases} \quad . \tag{3.3}$$

I_{R} can be the average brightness of a reference region R (figure 3.7(e), which de-emphasises scratches and air bubbles in the reference image. I will discuss the choice of I_{R} later.

Step 3: Calculate the brightness of each pixel in the α^{th} image that is attributed to the gel:

$$I^{\alpha,\text{N}}_{(i,j)} = I^{\alpha}_{(i,j)} \cdot P^{0}_{(i,j)} \ . \tag{3.4}$$

3.2.3.2 Adjustment of Contrast

The brightness and contrast of the normalised α^{th} image ($\alpha \neq 0$) is adjusted globally according to the RoI [68]. This process is performed using ImageJ (Fiji) [71]. After this step, pixels with $I^{\alpha,\text{N}}_{(i,j)} > \text{MAX}(I^{\alpha,\text{N}}_{(i,j)\in\text{RoI}})$ and $I^{\alpha,\text{N}}_{(i,j)} < \text{MIN}(I^{\alpha,\text{N}}_{(i,j)\in\text{RoI}})$ are set to 255 and 0, respectively. The resulting image $I^{\alpha,\text{N,c}}_{(i,j)}$ is the contrast adjusted normalised α^{th} image, figure 3.7(d). In this way, the contrast of the normalised image is improved so that certain features of interest are picked out. However, some information will inevitably be lost or distorted. For example, in figure 3.7(d) the corners of the meniscus are invisible after the adjustment and the base of the bright arc is over-exposed.

3.2.3.3 Discussion of Image Processing

In the reference image ($\alpha = 0$), the sample is assumed to be homogeneous. After the normalisation, $I^{0,\text{N}}_{(i,j)\in G} = I^{0}_{(i,j)\in G} \cdot P^{0}_{(i,j)\in G} = I_{\text{R}}$, as assumed. This is also why the adjustment of contrast is not applicable for the reference (0^{th}) image. Note that, if the sample is not homogeneous in the reference image, the normalisation will create artificial features in all other images. For example, air bubbles (which are much brighter) in the reference image will create black dots in all processed images.

In the processed α^{th} image figure 3.7(d), variations in brightness, i.e. the difference between $I^{\alpha,\text{N,c}}_{(i_1,j_1)\in G}$ and $I^{\alpha,\text{N,c}}_{(i_2,j_2)\in G}$, is caused by the inhomogeneity of the gel structure. This is how features of interest are picked out by the processing. Let us consider the normalised image, figure 3.7(c). If the illumination of a pixel is higher, for example (i_1, j_1), we have $P^{0}_{(i_1,j_1)} < 1$. According to Eq. 3.4, $I^{\alpha,\text{N}}_{(i_1,j_1)} < I^{\alpha}_{(i_1,j_1)}$. On the other hand, if the illumination on a pixel is lower, for example (i_2, j_2), we have $I^{\alpha,\text{N}}_{(i_2,j_2)} > I^{\alpha}_{(i_2,j_2)}$. Therefore, the uneven illumination is compensated. Most of the scratches can also be eliminated. Some scratches are too deep so that they will re-appear as the gel settles. This is because the scratches are illuminated by the gel in the cuvette.

Between frames of the normalised images, the difference of brightness ($I^{\alpha,\text{N}}_{(i,j)} - I^{\alpha-1,\text{N}}_{(i,j)}$) allows us to see features moving in the time-lapse images. For (i_2, j_2), where $P^{0}_{(i_2,j_2)} > 1$, one has $(I^{\alpha,\text{N}}_{(i_2,j_2)} - I^{\alpha-1,\text{N}}_{(i_2,j_2)}) > (I^{\alpha}_{(i_2,j_2)} - I^{\alpha-1}_{(i_2,j_2)})$. Hence, the contrast of the pixel (i_2, j_2) between frames is enhanced by $P^{0}_{(i_2,j_2)}$. Similarly, For (i_1, j_1), the contrast between frames is reduced.

Therefore, a good choice of the brightness I_{R} is crucial for the image enhancement. A high enough I_{R}, which ensures $P^{0}_{(i,j)} > 1$ and $I^{\alpha,\mathrm{N}}_{(i,j)} < 255$ (not over-exposed) for most pixels $(i, j) \in G$ at the same time, produces maximum image enhancement without losing information in the original image. Moreover, in some cases, to reveal features of interest with low contrast, I_{R} can be set higher (> 200) leaving uninteresting features over-exposed in the normalised image.

The adjustment of brightness may erase information. By changing RoI, different parts of the normalised image can be presented clearly.

3.2.4 General Image Interpretation

In figure 3.7(a), there is a part of the meniscus which is much brighter. The width of this bright arc gradually reduces as the gel interface settles. Hence, I suspect that this arc is brighter because it reflects the light from gel interface. Appendix A.1 presents a micrograph together with a 3D model to help with picturing a meniscus in a cuvette.

The gel interface is brighter. This may be because the gel interface is illuminated by extra light that comes from the uncollimated rays of excitation light and the light beams reflected by the meniscus. On the other hand, the large depth of field allows the objective lens to collect emission light that far away from the glass wall. Therefore, more illumination and large depth of field lead to a brighter interface in the image. This argument is also supported by the result from the selective plane illumination microscopy using the same setup. When a sample with high concentration of fluorophore is illuminated by a sheet of light, in the bulk, only the part near the wall can be excited due to the absorbance of the excitation light; however, the fluorophore at the interface far away from the wall can also be excited [70]. Hence, a brighter interface does not necessarily imply more colloids there. For a similar reason, the part of a sample that is close to each side of glass wall are brighter, figure 3.7. Apart from these two cases, higher brightness indicates higher local colloidal volume fraction and vice versa.

The depth of view and spatial resolution of the setup is evaluated in the previous section. Through a gel network, the time-lapse images reveal the structures with a length-scale > 30 µm that are within ~ 1 mm near the glass wall. Through a supernatant solvent, the base of the meniscus can be seen.

3.2.5 Measuring Height Profile

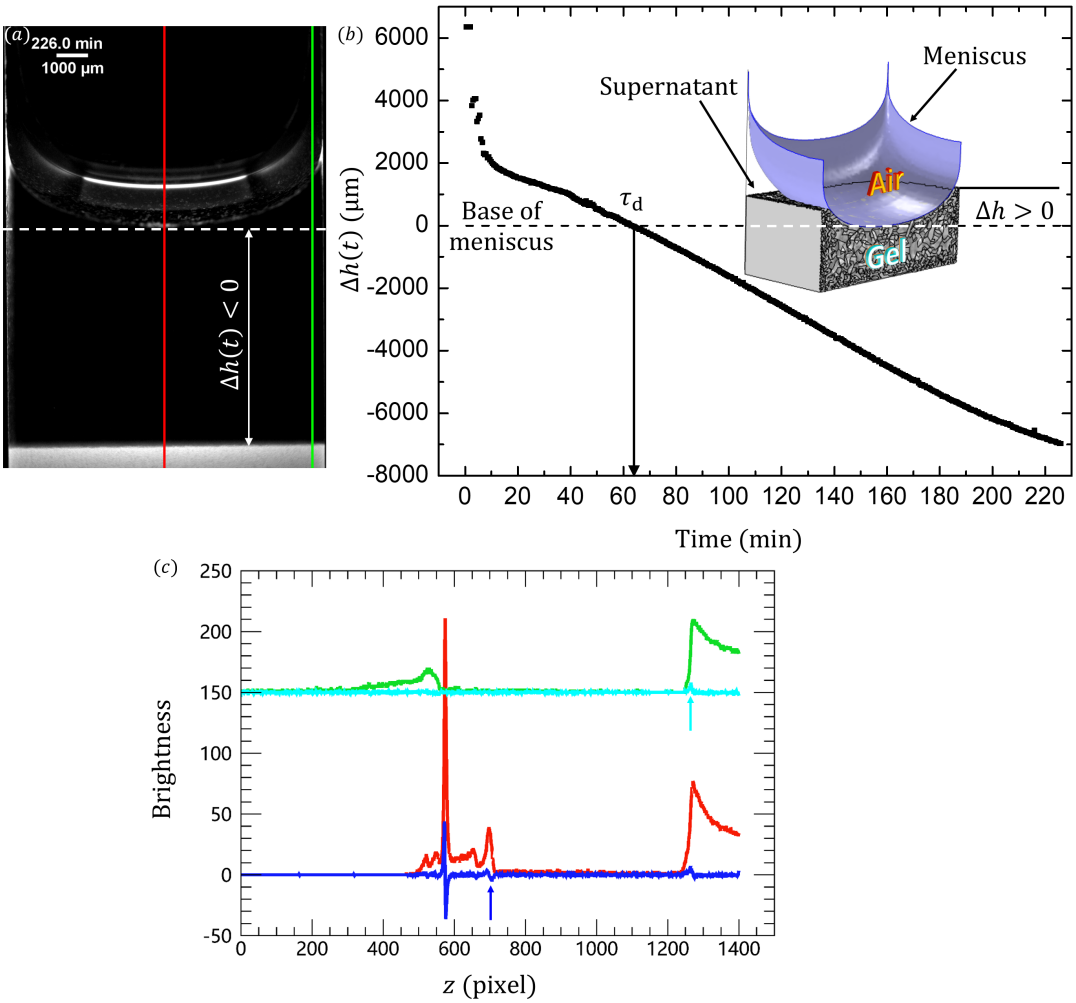

Figure 3.8 *The height profile of the gel interface is measured using the original images. (a) A snapshot of a collapsing collapse gel. The time dependence interface height $\Delta h(t)$ is as defined. (b) The resulting height profile Δh vs. t. The inset shows a 3D illustration of a collapsing gel that is still attached to the meniscus. The delay time τ_d is the beginning time of $\Delta h(t) < 0$. The horizontal dashed lines in (a) and (b) indicate the base of the meniscus. (c) To identify the position of the base of the meniscus, the brightness along the centre (the red line in (a)) is plotted as the red solid line in (c) together with its differentiated brightness (blue solid line). The blue arrow indicates the position of the base of the meniscus. To identify the gel interface, the brightness and differentiated brightness along the green line in (a) is shifted upwards by 150 and plotted as green and cyan solid lines, respectively. The cyan arrow indicates the position of the gel interface.*

The height profiles of gel collapse were measured using the original micrographs. Figure 3.8(a) shows a snapshot of a collapsing gel. The height of the gel interface is characterised by $\Delta h(t)$, the distance between the gel interface and the base (lowest point) of the meniscus. The collapse of a gel initiates at the corner of

the meniscus. Due to the curvature of the meniscus, the gel network remains attached to the meniscus during the early stage of the collapse, resulting in a positive $\Delta h(t)$ as illustrated in the inset of figure 3.8(b). When the interface is below the base of the meniscus, $\Delta h < 0$.

To identify the base of the meniscus and the gel interface, the brightness of micrographs is differentiated. The base of the meniscus is measured across the centre of the sample (the red line in figure 3.8(a)). The brightness and differentiated brightness are plotted in figure 3.8(c). Compared to the original image, the local minimum indicated by the blue arrow corresponds to the base of the meniscus. The height of the interface is measured close to the edge of the cuvette (the green line in figure 3.8(a)). The brightness and differentiated brightness are shifted upwards by 150 and plotted in figure 3.8(c), for clarity. The maximum indicated by the cyan arrow corresponds the position of the gel interface. At the very beginning, the colloids at the corner of the meniscus collapse without a well-defined interface. Hence, the height profile during this period ($t \lesssim 10$ min) is qualitative.

The height profile is plotted as $\Delta h(t)$ *vs.* t as shown in figure 3.8(b). The definition of the delay time τ_{d} is the same as in the macro-imaging. Therefore, in micro-imaging, τ_{d} is the beginning time of $\Delta h(t) < 0$. The height profile can also be plotted as scaled height $\hat{h}(t) = \frac{(h(t)-h_{\mathrm{RCP}})}{(h_0-h_{\mathrm{RCP}})}$ *vs.* t, taking the initial height of a gel h_0 from the macro-imaging result.

Chapter 4

Suspension Characterization and Gel Preparation

In this chapter, I report the characterization of the model system used in this work which is a mixture of polymethylmethacrylate (PMMA) colloids and polystyrene (PS) dispersed in a mixture of *cis*-decalin and tetralin. Then the preparation of gels will be described.

4.1 PMMA + PS Mixture

The PMMA particles used in this work were synthesised by Dr. Andrew Schofield. They are sterically-stabilised by poly(12-hydroxystearic acid) (PHSA) and dyed with nitrobenzoxadiazole (NBD). The particles were initially dispersed in dodecane. The dispersion was centrifuged until a compact sediment was collected in the bottom of the sample vial. The excess solvent was removed and replaced by mix-decahydronaphthalene (mix-decalin). The colloids were then re-dispersed in the new solvent. This procedure, known as washing, was repeated for 10 times, to remove possible monomers or other impurities. The resulting colloids were dried in a vacuum oven until the weight of the sample no longer changed.

Two different sizes of PMMA particles were used in this work. The radii of particles were measured using static light scattering (SLS) giving $a = 955$ nm and polydispersity of 3.7% for the large particles and $a = 405$ nm and polydispersity 5.0% for the small particles [72, 73].

The density measurements were performed on an Anton Parr DMA 4500 Density Meter, which was calibrated using air and ultra pure water. The error in the density measurement is $\Delta\rho = \pm 0.0001$ g/ml. To measure the density of the PMMA particle ρ_{PMMA}, 6 samples with varying mass fractions ($\varphi^{\mathrm{m}}_{\mathrm{PMMA}}$) in *cis*-decalin + cyclohexyl bromide (CHB) solvent mixture were measured at 25°C. By assuming the total volume of the suspension is the sum of the volume of colloids and the solvent, the density of PMMA particle can be calculated, giving $\rho_{\mathrm{PMMA}} = 1.1803 \pm 0.0035$ g/ml.

To confirm the result shown above, ρ_{PMMA} is also evaluated by matching the density of the solvent mixture of *cis*-decalin and CHB. The PMMA particles were suspended in such solvent mixtures with different densities. The suspensions were centrifuged (at 3000 rpm) at 25°C for 24 hours. The density of the particles is considered equal to that of the solvent in which no sedimentation is observed after centrifugation. This procedure gives $\rho_{\mathrm{PMMA}} = 1.1816 \pm 0.0001$ g/ml.

Two results above agree with each other well. Hence, the density of the PMMA particles is taken as the average value of the two results, $\rho_{\mathrm{PMMA}} = 1.181$ g/ml. Particles with different size are considered to have the same density. On the other hand, it has been reported that the PMMA particles are swelled gradually in tetralin by up to $\sim 10\%$ in volume [74, 75]. Hence, ρ_{PMMA} in IM solvent may be lower than the measured value by up to $\sim 9\%$, depending on the age of the sample.

Cis-decalin and tetralin were used as purchased (Sigma-Aldrich). The refractive index (RI) of the IM solvent mixture (*cis*-decalin : tetralin $\approx 81.5 : 18.5$) is closely matched to that of the PMMA particle ($n_{\mathrm{D}} = 1.492$). The density of the solvent is measured using the density meter. The refractive index of the solvent is measured using an Abbe refractometer. The viscosity of the solvent is measured using a rheometer TA DHR with 40 mm - 1°cone - plate geometry and at shear rate $\dot{\varepsilon}$ from 1 s^{-1} to 1000 s^{-1}. Properties are summarised in Table 4.1. In IM solvent, PMMA colloids will sediment; the density difference is $\Delta\rho = \rho_{\mathrm{PMMA}} - \rho_{\mathrm{IM}} = 0.269$ g/ml. The gravitational Péclet number $\mathrm{Pe_g} = mga/k_{\mathrm{B}}T = 4\Delta\rho g\pi a^4/3k_{\mathrm{B}}T$ is calculated to be 2.25 for the large PMMA particles and 0.07 for the small one. Therefore, the system with the large particles is more gravitationally driven.

The RI of the solvent was measured regularly, to check for evaporation. Any variation in the RI of the solvent mixture, thus its composition, was corrected

Table 4.1 *Properties of solvents.*

Solvent	Density (g/ml) at 20°C	Refractive Index at 25°C	Viscosity (cP) at 23°C
cis-Decalin	0.8964 / 0.8968[a]	1.4811(1) / 1.4793[a]	3.202(7) / 3.355[a]
IM solvent	0.9118[b]	1.4956(1)	2.445(3)

[a] Literature values, taken from Ref. [76].
[b] Measured at 23°C.

before sample preparation.

The non-absorbing polymer used in this work was linear polystyrene (PS) which was purchased from Agilent Technologies and used as purchased. For large PMMA particle, the PS used had a molecular weight of $M_\mathrm{w} = 3.1 \times 10^6$ g/mol ($M_\mathrm{w}/M_\mathrm{n} = 1.05$). G. Berry found that *cis*-decalin was a theta solvent for PS at $T_\theta = 286$ K [77]. The radius of gyration at T_θ can be estimated by $R_\mathrm{g}^\theta(\mathrm{nm}) = 0.028\sqrt{M_\mathrm{w}(\mathrm{g/mol})}$, giving $R_\mathrm{g}^\theta = 49$ nm [77]. The radius of gyration of PS ($M_\mathrm{w} = 3.1 \times 10^6$ g/mol) in IM solvent is $R_\mathrm{g} = 51$ nm, which is measured using SLS at 23°C [78]. Hence, the size ratio $\xi \approx 0.05$. The overlap concentration $c_\mathrm{p}^* = 3M_\mathrm{w}/4\pi R_\mathrm{g}^3 N_\mathrm{A}$ was calculated to be 9.34 mg/ml, where N_A is Avogadro constant. That the radius of gyration of PS in IM solvent is close to $R_\mathrm{g}^\theta = 49$ nm agrees with previous studies [29, 79, 80].

For small PMMA particles, the depletant PS has a molecular weight of $M_\mathrm{w} = 1.4 \times 10^6$ g/mol ($M_\mathrm{w}/M_\mathrm{n} = 1.04$). The radius of gyration in IM solvent was measured by SLS, giving $R_\mathrm{g} = 34$ nm. The size ratio $\xi \approx 0.08$.

PS solutions with different concentration c_p were made. For solutions with $c_\mathrm{p} > 0.6$ mg/ml, a certain amount of solid PS was dissolved in IM solvent with aimed polymer concentration c_p. The solution was mixed by slow tumbling for 24 hours to dissolve the polymer in the solvent completely. Typically, PS solution stock of 15 ml was made for each concentration. The concentration of the PS solution is calculated using

$$c_\mathrm{p} = \frac{m_\mathrm{p}}{V_\mathrm{IM} + V_\mathrm{p}} \ , \tag{4.1}$$

where m_p is the mass of the solid polystyrene, V_IM is the volume of the IM solvent, and V_p is the volume of the PS coil. The density of the PS solution $\rho_\mathrm{PS}^\mathrm{IM}$ was measured. For low polymer concentration ($c_\mathrm{p} < 10$ mg/ml), $\rho_\mathrm{PS}^\mathrm{IM} \approx \rho_\mathrm{IM} + c_\mathrm{p}$.

Hence, for low concentration solutions, $V_{\rm p}$ in Eq. 4.1 can be neglected. $V_{\rm IM} = m_{\rm IM}/\rho_{\rm IM}$, where $m_{\rm IM}$ is the mass of the IM solvent. Therefore, the uncertainty of $c_{\rm p}$ of the PS solution comes from the errors in weight and the uncertainty of $\rho_{\rm IM}$. The errors of $m_{\rm p}$ and $m_{\rm s}$ are typically ± 0.0001 g and ± 0.0001 g; the error of $\rho_{\rm IM}$ is ± 0.0001 g/ml. Hence, the error of $c_{\rm p}$ is typically $\Delta c_{\rm p} = \pm 0.025$ mg/ml. For solutions with $c_{\rm p} < 0.6$ mg/ml, the polymer solutions were made by diluting the PS solution stock with $c_{\rm p} = 5$ mg/ml. The typical error of $c_{\rm p}$ is $\Delta c_{\rm p} = \pm 0.001$ mg/ml.

In IM solvent, the viscosity $\eta_{\rm PS}$ of PS solution with different concentrations were measured using rheometer TA DHR at 23 °C. The flow curve of PS solution was measured using 40 mm - 1°cone - plate geometry with shear rate $\dot{\varepsilon}$ from 1 s^{-1} to 1000 s^{-1}. The results are plotted in figure 4.1.

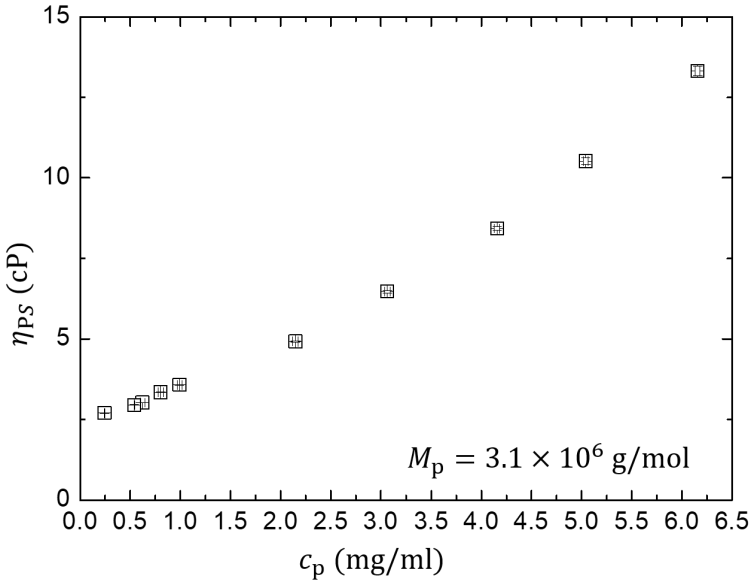

Figure 4.1 *The viscosity of polystyrene ($M_{\rm w} = 3.1 \times 10^6$ g/mol) in IM solvent. The thin lines inside each □ are the error bars.*

The viscosity of a polymer solution at low concentration is related to the intrinsic viscosity by a virial expansion of η in $c_{\rm p}$ [78]:

$$\eta = \eta_{\rm s}(1 + [\eta]c_{\rm p} + k_{\rm H}[\eta]^2 c_{\rm p}^2 + \cdots) \ , \tag{4.2}$$

where $[\eta]$ is the intrinsic viscosity, $k_{\rm H}$ is the Huggins coefficient and $\eta_{\rm s}$ is the viscosity of the solvent. The linearity at low $c_{\rm p}$ can be represented in two different

ways:

$$\frac{\eta - \eta_s}{\eta_s c_p} = [\eta] + k_H[\eta]^2 c_p \qquad \text{(Huggins)}, \tag{4.3}$$

$$\frac{\ln(\eta/\eta_s)}{c_p} = [\eta] + (k_H - \frac{1}{2})[\eta]^2 c_p \qquad \text{(Kraemer)}. \tag{4.4}$$

With low enough concentrations, these two linear plots should have the same intercept, which is $[\eta]$. The overlap concentration c_p^* can be evaluated using the measured intrinsic viscosity by $c_p^* \approx [\eta]^{-1}$ [78].

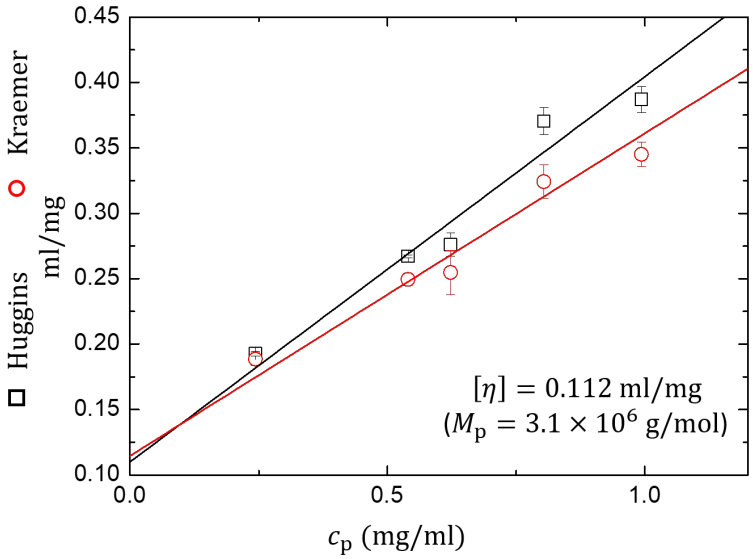

Figure 4.2 *The Huggins and Kraemer representation to evaluate the intrinsic viscosity of PS $M_w = 3.1 \times 10^6$ g/mol in IM solvent.*

The viscosity results at low polymer concentration are re-plotted as an HK plot in figure 4.2. The Kraemer plot is an increasing function. It suggests that $k_H > 0.5$, which is reasonable for a polymer with high molecular weight ($M_w > 10^6$ g/mol) [78]. The intercepts of Kraemer plot and Huggins plot give 0.114 ml/mg and 0.110 ml/mg, respectively. These two values agree with each other reasonably well. Hence, the intrinsic viscosity of the PS ($M_w = 3.1 \times 10^6$ g/mol) is taken as the average of those two values, giving $[\eta] = 0.112$ ml/mg. Therefore, the overlap concentration is $c_p^* \approx [\eta]^{-1} = 8.93$ mg/ml which is close to the value that is calculated from R_g ($c_p^* = 9.34$ mg/ml).

4.2 Gel Preparation

Gel samples were prepared by dispersing a known amount of dry PMMA colloids (by weight) in a known concentration (c_{p}) PS solution. A certain amount (m^{dry}_{PMMA}) of dry PMMA colloids was placed in a vial. Then, a certain mass of PS solution (m_{s}) was added to make a gel with the desired colloidal volume fraction. The sample vial was sealed with a lid and wrapped with parafilm and PTFE tape. The resulting samples were vigorously mixed on whirl mixer for 1 min then were slowly tumbled for 48 hours.

4.2.1 Determination of Colloidal Volume Fraction

The colloidal volume fraction φ_{c} is defined as:

$$\varphi_{\mathrm{c}} = \frac{V_{\mathrm{c}}}{V_{\mathrm{c}} + V_{\mathrm{s}}} \ , \tag{4.5}$$

where V_{s} is the volume of PS solution and V_{c} is the volume of the PMMA particles.

$$V_{\mathrm{c}} = \frac{m^{dry}_{\mathrm{PMMA}}}{\rho_{\mathrm{PMMA}}} \ , \tag{4.6}$$

m^{dry}_{PMMA} is measured as samples were prepared. The volume of the PS solution is calculated using

$$V_{\mathrm{s}} = \frac{m_{\mathrm{s}}}{\rho_{\mathrm{s}}} \ , \tag{4.7}$$

where m_{s} is the mass of the PS solution that was measured as samples were prepared. In terms of ρ_{s}, for most samples in this work, $c_{\mathrm{p}} \leq 5$ mg/ml so that $\rho_{\mathrm{s}} = \rho_{\mathrm{IM}} + c_{\mathrm{p}}$ is a good approximation; however, it is an overestimation as c_{p} approaches c^{*}_{p}.

The uncertainty of the colloidal volume fraction comes from the error in weight, the error of ρ_{s} and the variation in ρ_{PMMA}. Typically, $\Delta m^{dry}_{\mathrm{PMMA}} = \Delta m_{\mathrm{s}} = 0.0001$ g and $\Delta\rho_{\mathrm{s}} = \pm 0.0001$ g/ml. As estimated in Sec. 4.1, ρ_{PMMA} may decrease gradually up to 9% depends on the age of the sample, due to the the PMMA colloids absorbing tetralin in IM solvent. Hence, the colloidal volume fraction of the sample increases with the age of the sample up to $\Delta\varphi_{\mathrm{c}} = +0.02$. This swelling is influential. In some cases, this increment in φ_{c} over sample's age may change the collapse behaviour of a gel. It is not clear how fast the PMMA colloids swell in IM solvent. The newly made sample was transparent, because the IM solvent

is designed to closely match the RI of the PMMA particle. After about 1 day, the sample become more turbid, indicating that the PMMA particles absorb the solvent so that the RI of particle and solvent are both changes. Presumably, the PMMA colloids absorb the solvent quickly in the beginning, then gradually swell for a long time.

4.2.2 Determination of Free Volume Fraction of Polymer

To apply Eq. 2.1 and calculate the free volume fraction of the PS ($\varphi_{\mathrm{p}}^{\mathrm{free}}$), we need to calculate the volume fraction of the PS in the gel sample φ_{p} from c_{p} of the PS solution.

Similar to Eq. 4.5, the volume fraction of PS in the gel sample can be defined as:

$$\varphi_{\mathrm{p}} = \frac{V_{\mathrm{p}}}{V_{\mathrm{c}} + V_{\mathrm{s}}} \ , \tag{4.8}$$

where V_{p} is the volume of the polymer coil. The volume of the colloids V_{c} and the volume of the PS solution V_{s} are given by Eq. 4.6 and Eq. 4.7. The volume of PS V_{p} can be evaluated from the PS solution:

$$V_{\mathrm{p}} = V_{\mathrm{s}} \cdot \varphi_{\mathrm{PS}} \ . \tag{4.9}$$

The PS volume fraction in the PS solution is given by:

$$\varphi_{\mathrm{PS}} = \frac{4}{3}\pi R_{\mathrm{g}}^3 \frac{c_{\mathrm{p}} N_{\mathrm{A}}}{M_{\mathrm{w}}} \ . \tag{4.10}$$

Therefore, we can calculate φ_{p} from c_{p}. The error of φ_{p} comes from the error of V_{c}, V_{s} and c_{p}. The error on the polymer volume fraction $\Delta\varphi_{\mathrm{p}}$ is estimated to be between ± 0.06 and ± 0.12, which is a relative error of $\Delta\varphi_{\mathrm{p}} = \pm 4\%$.

By applying Eq. 2.1 and Eq. 2.2, the free volume fraction of polymer in the gel sample $\varphi_{\mathrm{p}}^{\mathrm{free}}$ can be evaluated. The error of $\varphi_{\mathrm{p}}^{\mathrm{free}}$ is evaluated to be between ± 0.006 and ± 0.06, which is a relative error of $\Delta\varphi_{\mathrm{p}}^{\mathrm{free}} = \pm 7\%$. Notice that, $\varphi_{\mathrm{p}}^{\mathrm{free}}$ is higher but close to φ_{PS}. Because, the difference between $\varphi_{\mathrm{p}}^{\mathrm{free}}$ and φ_{PS} is that $\varphi_{\mathrm{p}}^{\mathrm{free}}$ takes the depletion zone around the colloids into account.

4.2.3 Approach to Composition Selection

The composition of the sample (φ_c, c_p) was chosen according to the phase diagram in the previous study, figure 2.7(a). In this work, I will focus on the rapid collapse gel (regime D) and slow collapse gel (regime B). Therefore, For the large PMMA colloidal system, the composition of sample lies in the range of $0.10 < \varphi_c < 0.46$ and $3 < c_p < 5$ mg/ml.

Furthermore, the small PMMA colloidal system is used to draw a comparison with the key results obtained from the large one. Hence, the colloidal volume fraction of the samples also lies in the range of $0.10 < \varphi_c < 0.46$; the polymer concentration is $c_p = 5.07$ mg/ml.

4.3 Summary

In this chapter, I reported the characterisation of the model system with large and small PMMA particles. I summarise the properties of the gel system in Table 4.2.

Table 4.2 *Properties of the model system.*

	Large	Small
Radius of PMMA	$a = 955$ nm	$a = 405$ nm
Radius of gyration of PS	$R_g = 51$ nm	$R_g = 34$ nm
Size ratio	$\xi \approx 0.05$	$\xi \approx 0.08$
Density difference	$\Delta\rho \approx 0.27$ g/ml	$\Delta\rho \approx 0.27$ g/ml
Gravitational Péclet number	$\mathrm{Pe}_g \approx 2.25$	$\mathrm{Pe}_g \approx 0.07$

Chapter 5

Macroscopic Imaging Study

5.1 Introduction

As reviewed in Sec. 2.4, previous studies identified three types of collapse of gels [29, 52, 53]. In regime A, a gel collapses with little or no delay time. The sample cannot support the gravitational stress exerted by a single particle. In regime D, a gel exhibits rapid collapse before the stretched-exponential compression. During the rapid collapse, the gel interface has a constant settling speed. In regime B, a gel collapses gradually after a long delay time without the rapid collapse period. A gel in regime D is termed as a rapid collapse gel; a gel in regime B, a slow collapse gel. In this work, I want to study the mechanism of the collapse. Hence, before the detailed study of the onset of the collapse, the first step is to identify the type of the collapse in our model system.

In this chapter, I report the categorisation of the collapse of gels according to their height profiles. The long-time height profiles were measured by macroscopic time-lapse imaging. I will show that gels formed by large particles can be categorised in the same way as the small particle gels. This chapter provides the starting point for the investigation in Chapter 6 which will focus on the onset of the collapse.

5.2 Method

Samples were transferred into $10 \times 10 \times 45$ mm^3 upright glass cuvettes and thoroughly homogenized on a whirl mixer for 1 min before experiments. All samples have height ≈ 18 mm. This geometry shall be referred as the ***standard geometry*** here. We categorized the state of our samples by visual observation

using digital time-lapse imaging with time interval ranging from 1 to 10 min, see Sec. 3.1. Experiments were performed in a temperature controlled chamber at 25 ± 0.5 °C.

5.3 Categorisation of the Collapse of Gels

5.3.1 Large Particle Gels

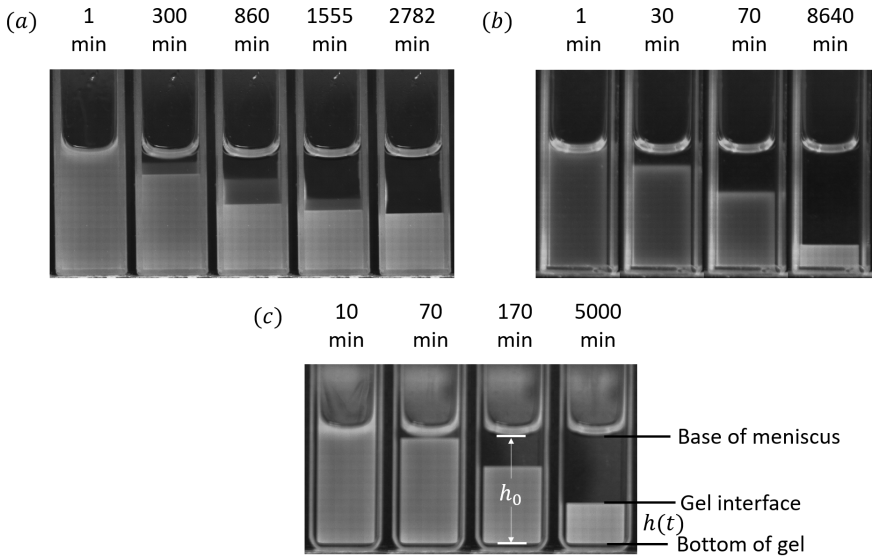

Figure 5.1 *Original macroscopic time-lapse images for samples with $\varphi_c = 0.28$ and $c_p = 1$ mg/ml (a), $\varphi_c = 0.10$ and $c_p = 5$ mg/ml (b) and $\varphi_c = 0.19$ and $c_p = 5$ mg/ml (c). The base of the meniscus, the gel interface and the bottom of the gel are indicated in (c). The definition of initial height h_0 and the height of gel $h(t)$ are also illustrated in (c).*

Figure 5.1(a) shows images of a settling sample with $\varphi_c = 0.28$ and $c_p = 1$ mg/ml. The images clearly show that the sample is phase-separating. At $t = 860$ min, the sample (under the meniscus) can be divided into three parts according to the brightness which reflects the concentration of the colloids. The dark part right beneath the meniscus is the supernatant. The brighter and fast-settling phase is the liquid phase. The phase in between is the settling gas phase. This kind of samples is categorised as liquid-gas phase separation (◇) in the state diagram figure 5.2.

Figure 5.1(b) shows images of a settling sample with $\varphi_c = 0.10$ and $c_p = 5$ mg/ml. The interface that separates the settling colloids and the supernatant can be identified. However, the interface is blurred compared to that of other gels, see

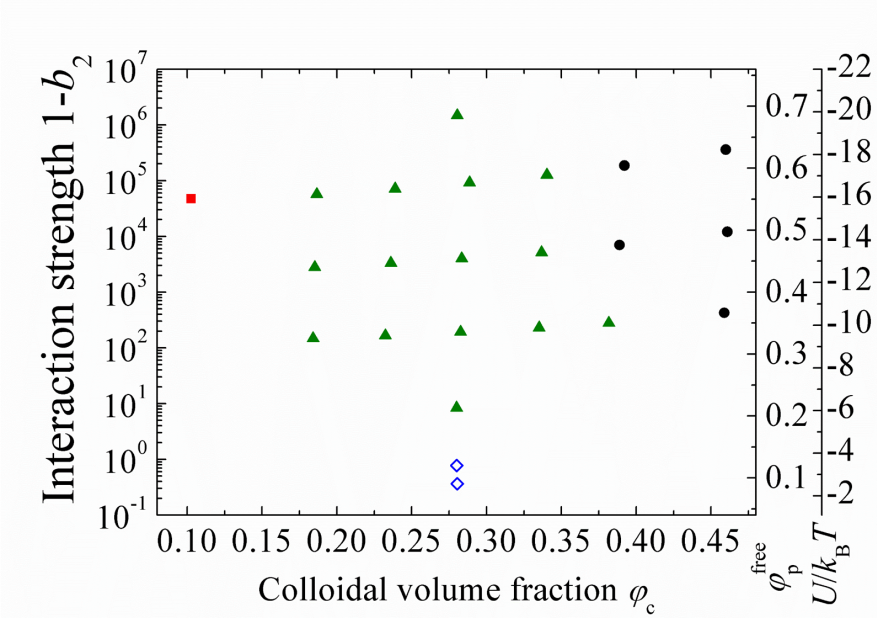

Figure 5.2 *State diagram presented as* $1 - b_2$ *vs.* φ_c*. The free volume fraction of the PS* φ_p^{free} *and the depth of the attraction potential* U/k_BT *are also given as reference.* ◇ *= liquid-gas phase separation;* ■ *= regime A: a gel collapses with little or no delay time;* ▲ *= regime D: rapid collapse gels; and* ● *= regime B: slow collapse gels.*

figure 5.1(c). The height profile is shown in figure 5.3(a). The delay time τ_d is defined as the time when the gel interface detaches from the base (= lowest point) of the meniscus. For this sample, τ_d = 15 min, which is short compared with that of other gels. This sample is categorised as gel collapse with little or no delay time (■) in the phase diagram figure 5.2. The microscopic imaging result (see Chapter 6) supports such categorisation with more details.

Figure 5.1(c) shows images of a settling sample with $\varphi_c = 0.19$ and $c_p = 5$ mg/ml. The gel interface is clear and sharp. The height profile is shown in figure 5.3(b). The delay time of this sample is about 51 min. Fast (linear) collapse can be seen, followed by gradual final compaction. Hence, this is a rapid collapse gel.

Figure 5.3(c) shows the height profile of a sample with $\varphi_c = 0.46$ and $c_p = 3$ mg/ml. The delay time of this sample is 1945 min. The gel collapses with a decreasing interface speed. Hence, this is a creeping gel or slow collapse gel.

According to the height profile of the gel collapse, the types of collapse of gels in this work are categorised into three regimes and summarised in the phase

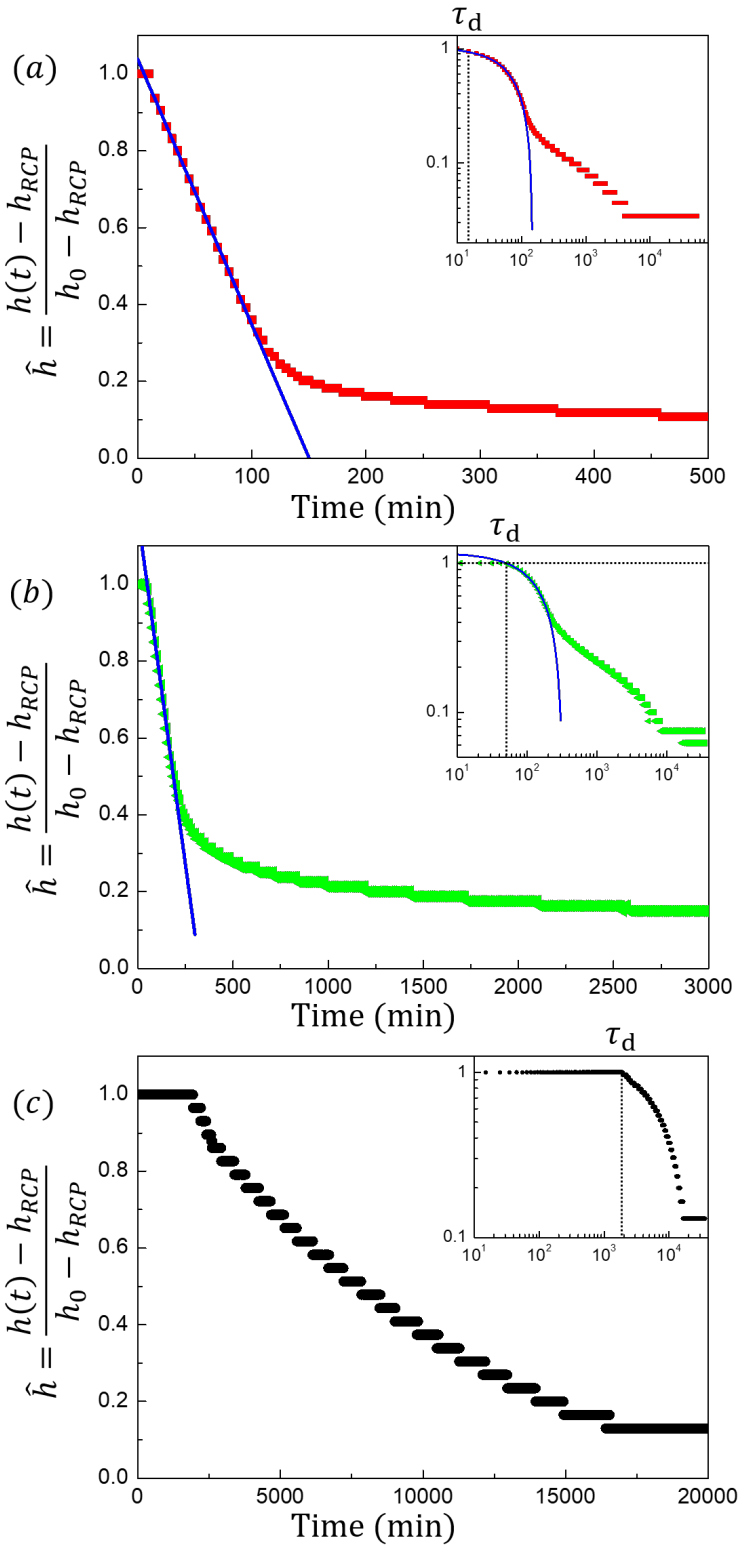

Figure 5.3 *Typical height profiles of large particle gels from macroscopic images:* $\varphi_c = 0.10$ *and* $c_p = 5$ *mg/ml (a);* $\varphi_c = 0.19$ *and* $c_p = 5$ *mg/ml (b); and* $\varphi_c = 0.46$ *and* $c_p = 3$ *mg/ml (c). The blue lines are the linear fit to the fast sedimentation. The inset in each case shows the log-log form of the main plot.*

diagram $1 - b_2$ *vs.* φ_c in figure 5.2: regime A: gel collapses with little or no delay time; regime D: rapid collapse gels; and regime B: slow collapse gels. The nomenclature here is in line with that of Ref. [29]. Regime C which corresponds to the crystallizing gel in Ref. [52] cannot be found in our system due to the high polydispersity.

5.3.2 Small Particle Gels

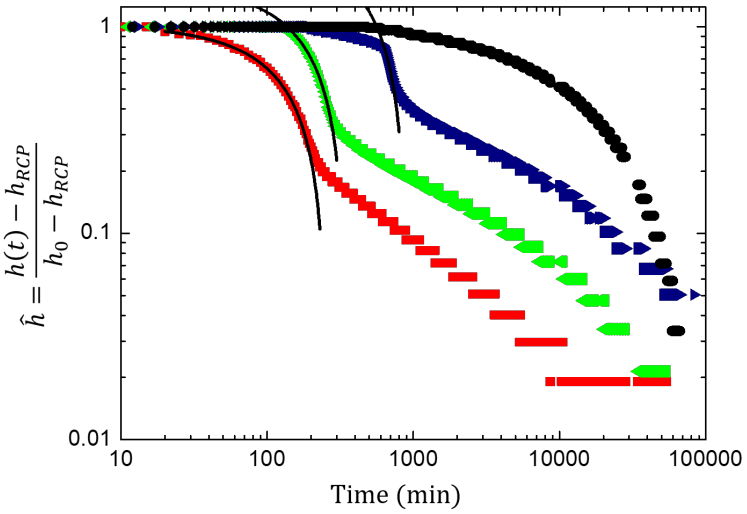

Figure 5.4 *Height profiles of small particle gels from macroscopic images.* ■*:* $\varphi_c = 0.10$, $\varphi_p^{free} = 0.366$*;* ◀*:* $\varphi_c = 0.20$, $\varphi_p^{free} = 0.387$*;* ▶*:* $\varphi_c = 0.31$, $\varphi_p^{free} = 0.409$*; and* ●*:* $\varphi_c = 0.40$, $\varphi_p^{free} = 0.441$*. The black lines are linear fit to the rapid sedimentation.*

To draw a comparison between the key results obtained from the large PMMA colloidal system (Chapter 6) and the results reported in Ref. [29], a small PMMA colloidal system close to the system used in Ref. [29] were also studied. In Ref. [29], PMMA particles with $a = 326$ nm and 7.5% polydispersity were dispersed in *cis*-decalin. The density difference was $\Delta\rho \approx 0.253$ g/ml. Depletion attraction was induced by linear PS with a radius of gyration of $R_g \approx 21$ nm. The size ratio $\xi \approx 0.064$ and the gravitational Péclet number $Pe_g \approx 0.03$. The small PMMA colloidal system used in this work is PMMA particles of $a = 405$ nm mixed with PS of $R_g \approx 34$ nm, $\Delta\rho \approx 0.27$ g/ml, $\xi \approx 0.08$ and $Pe_g \approx 0.07$. According to the state diagram (reproduced in figure 2.7(a)) reported in Ref. [29], 4 gels with the same polymer concentration and varying colloidal volume fractions are chosen for this comparative study. These 4 gels were also studied using macroscopic time-lapse imaging. Their height profiles are plotted in figure 5.4. According to the imaging results and the height profiles, the 4 samples are categorised in the same

way in the state diagram figure 5.5.

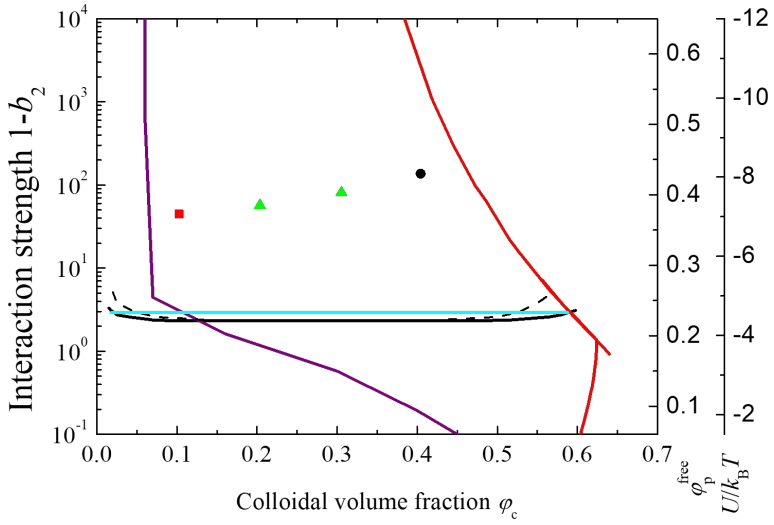

Figure 5.5 *State diagram $1 - b_2$ vs. φ_c for small particle gels. The free volume fraction of the PS φ_p^{free} and the depth of the attraction potential U/k_BT are also given as references. ■: gel collapses with little or no delay time; ▲: rapid collapse gels; and ●: slow collapse gel. For comparison, the percolation line (the purple solid line), the binodal line (the black solid line), the spinodal line (the black dashed line), the glass transition lines calculated from MCT mapped to simulations (the red solid line) and the tie line where binodal meets the glass transition line (the cyan line) are re-drawn from Ref. [29].*

For comparison, the glass transition lines, the percolation line and the tie line where binodal meets the glass line, etc, are re-drawn from Ref. [29] in the state diagram figure 5.5. In figure 2.7(a), regime A lies to the right of the percolation line and at very low φ_c (< 0.15). Regime D lies between $\varphi_c \sim 0.15$ and ~ 0.35 corresponding to rapid collapse gels. Regime B ranges from $\varphi_c \sim 0.35$ to ≈ 0.55 corresponding to slow collapse gels. Figure 5.5 shows that the types of the collapse of small particle gels in this work are consistent with the much more detailed state diagram reported in Ref. [29].

5.4 Conclusion

The state diagrams (figures 5.2 and 5.5) demonstrate that in the model system with large colloids ($Pe_g \approx 2.25 > 1$), gel collapse can also be categorised into three regimes as in the system with small colloids ($Pe_g < 1$). The categorisations are consistent with the results published in Ref. [29].

Chapter 6

The Evolution of Collapse Mechanisms

6.1 Introduction

Chapter 5 reported the categorisation of the collapse of samples using macroscopic time-lapse imaging. Their collapses are categorised into 4 regimes similar to previous studies: gel collapse with little or no delay time (regime A), slow gel collapse (regime B), liquid-gas phase separation and rapid gel collapse (regime D). The rapid collapse was previously linked to the falling of denser 'debris' at the top of a gel. Dark-field imaging [53] and preliminary mesoscopic imaging [67] provided the foundation of this scenario, suggesting the falling of the 'roof' of a gel. Recently, MRI results [29] confirmed the presence of a compact layer of debris at the top.

In this chapter, the onset of collapse will be re-visited using microscopic imaging. The imaging results show that the extra mass of the denser layer comes mainly from the corners of the meniscus (above its base). The data also show an evolution of collapse mechanisms as the colloidal volume fraction increases. Based on the state diagram figure 5.2, regime D (rapid collapse gels) can be subdivided into 3 subsections as summarised in the state diagram in the lower panel of figure 6.1. The key mechanisms are illustrated in the upper panels of figure 6.1; descriptions of each mechanism can be found in the caption. To show the evolution of collapse mechanisms, 4 gels will be discussed in detail: gel α, β, γ and δ as marked in figure 6.1. The evolution of collapse mechanism will be confirmed using a small particle model system similar to that in the Ref. [29].

In this chapter, results are presented with little discussion; I simply draw conclusions about collapse mechanisms based on visual evidence alone. In Chapter 8, I will discuss these observations in the context of other findings.

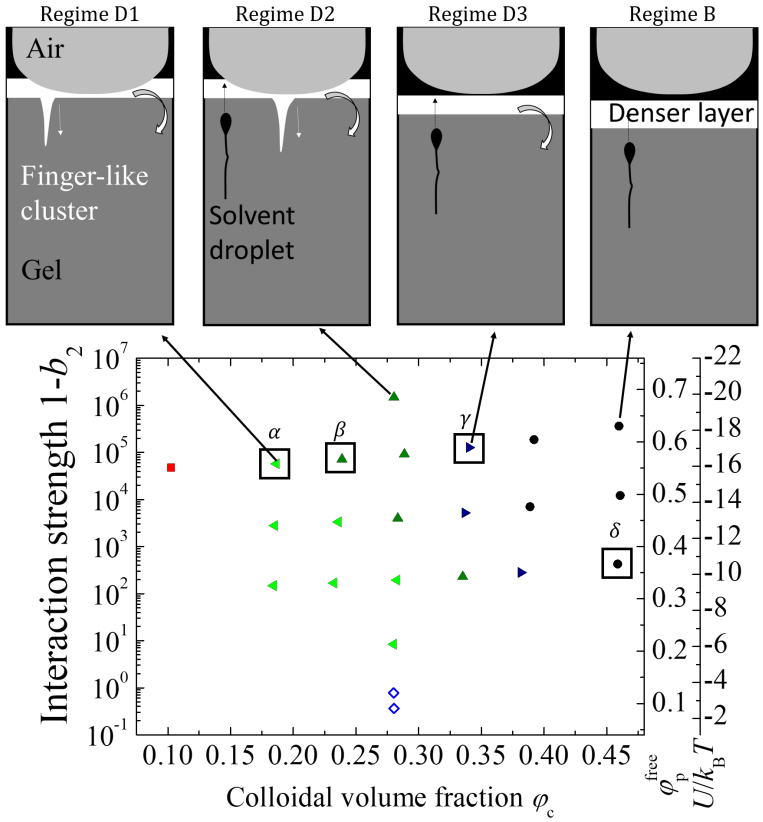

Figure 6.1 *Lower panel: State diagram re-plotted from figure 5.2; however, regime D (rapid collapse gels) is subdivided in to 3 subsections.* ◇ *= liquid-gas phase separation;* ■ *= regime A: gel collapse with little or no delay time;* ◀ *= regime D1: rapid collapse gels with finger-like clusters fall through the gel;* ▲ *= regime D2: rapid collapse gels with finger-like clusters interact with rising solvent droplets;* ▶ *= regime D3: rapid collapse gels with solvent droplets rising and denser layer falling; and* ● *= regime B: slow collapse gels with only solvent droplets rising. Gel* α, β, γ *and* δ *will be discussed in detail in this chapter. Upper panels are illustration of the key mechanisms of collapse in different regimes as indicated by the black solid arrows.*

6.2 Method

Here, I report the direct observation of the onset of collapse formed by large and small colloids in the standard geometry (as described in Sec. 5.2). The system was characterised in Chapter 4, see Table 4.2. The initial height of samples was about 1.8 cm. The micrographs were taken sideways around the meniscus using

a 1× objective such that only the top half of the sample was observed. Room temperature was 23 ± 0.5 °C. The variation of the temperature here does not affect the key conclusion in this work (see Appendix A.2). The microscopic time-lapse imaging was performed with a time interval of 0.5 min.

The experimental details were introduced in Sec. 3.2. The resulting images were processed to eliminate both the uneven illumination and most of the scratches on the cuvette. Unless otherwise specified, the brightness and contrast of the images were also adjusted. This ensured features within the gel could be clearly seen. However, this led to the regions around the meniscus becoming overexposed and turning black. Further details of the imaging process can be found in Sec. 3.2.3.

6.3 Rapid Collapse Gel with Low φ_c: Gel α

The rapid collapse gel with $\varphi_c = 0.19$, $\varphi_p^{free} = 0.557$ and $c_p = 5$ mg/ml (gel α in figure 6.1) was studied using microscopic imaging. The resulting height profile is plotted as $\Delta h(t)$ *vs.* time in figure 6.2. The height profile confirms that gel α is a rapid collapse gel. The micrographs are shown in figure 6.3(a)-(l). The time of images (c) - (l) in figure 6.3 are indicated with arrows in figure 6.2.

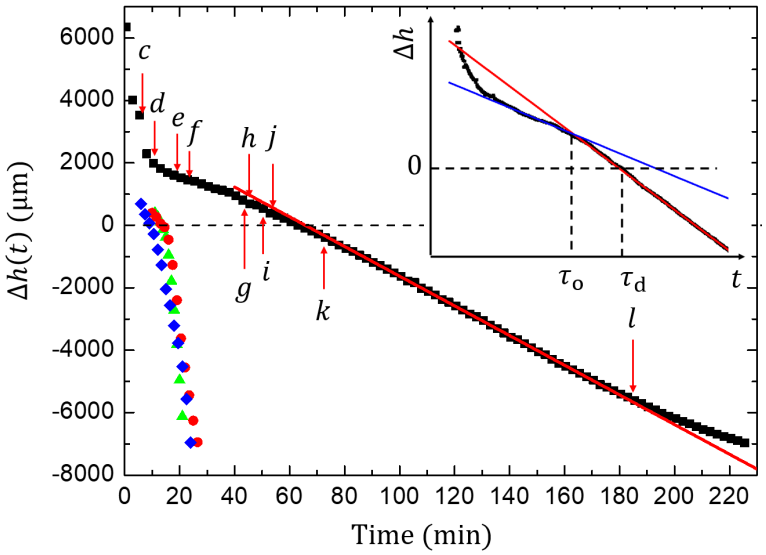

Figure 6.2 ■*: Height profile $\Delta h(t)$ vs. time of rapid collapse gel α measured from the original micrographs. Indicated by arrows are images shown in figure 6.3(c) - (l). The red solid line is the linear fit of the rapid collapse region. The black dashed line indicates the base of the meniscus.* ●, ◆ *and* ▲ *are the height profiles of finger 1, 2 and 3 denoted in figure 6.3(d). The inset illustrates the definition of the onset of rapid collapse and the delay time.*

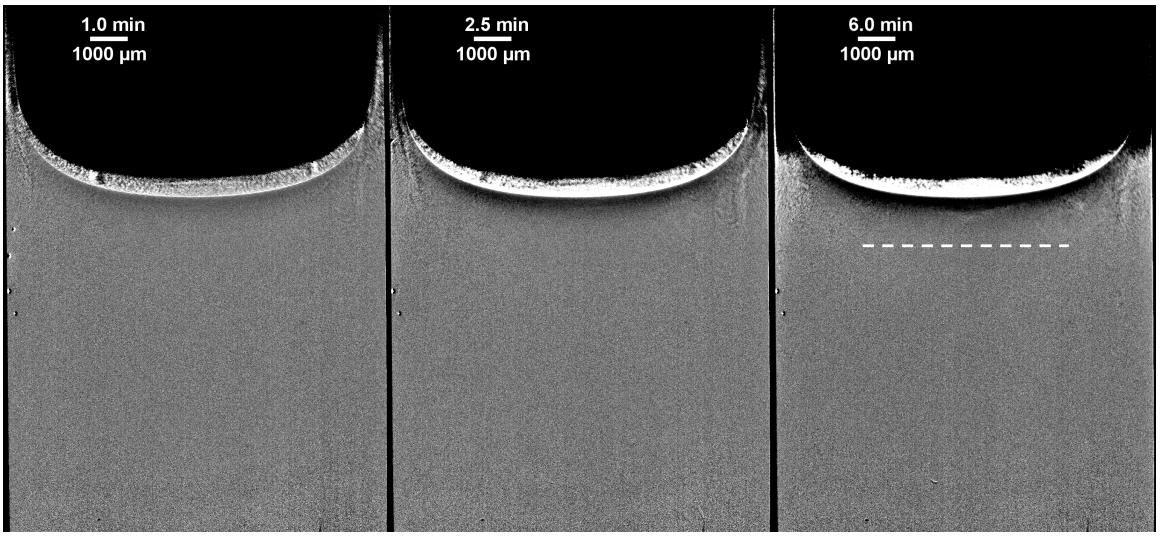

(a) *The sample is homogeneous after all visible air bubbles escape within 0.5 min. The arc at the meniscus is brighter due to reflection. The black edges on the left and right are the sides of cuvette.*

(b) *The colloids at the corner of the meniscus are falling. The meniscus becomes brighter leading to over-exposure in some part of it after being processed.*

(c) *A clear gel interface can be identified at $t = 6$ min. Also, the finger-like clusters start generating at the meniscus. The dashed line indicates the base of the meniscus (figure 6.3(l)).*

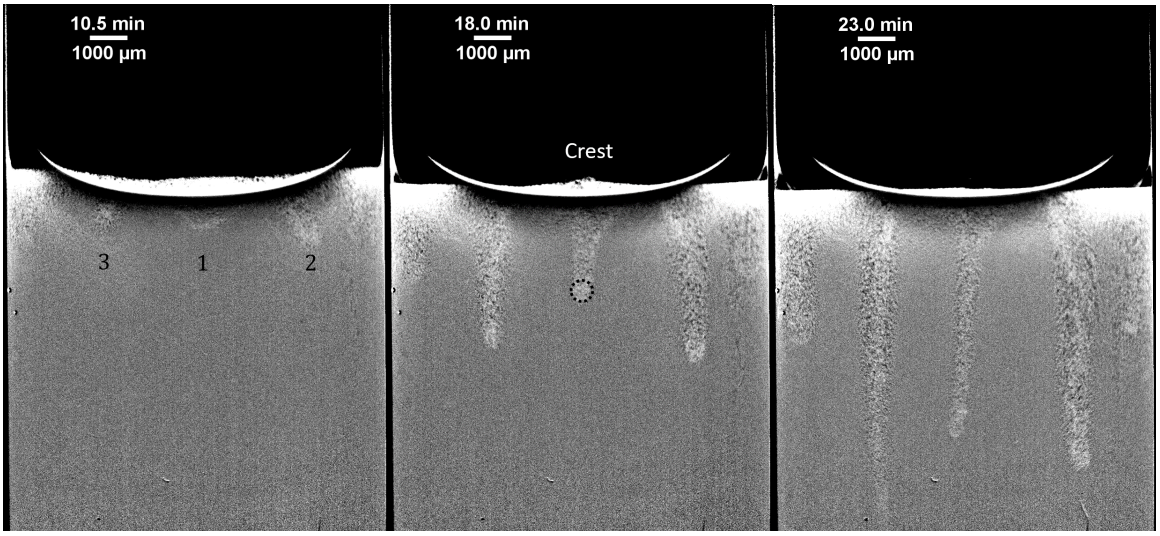

(d) *The structure around the meniscus coarsens. The bulk of the gel remains homogeneous. The interface becomes brighter and starts 'buckling', because cluster 2 and 3 grow faster than cluster 1.*

(e) *The dotted circle indicates the tip of the finger-like cluster. Clusters near the edges of the cuvette are generated from the bright coarsened layer.*

(f) *As finger 1 falls further, the colloids at the crest above it eventually collapses. The bulk of gel remains intact.*

Figure 6.3 *(a)-(l) Micrographs of the rapid collapse gel α.*

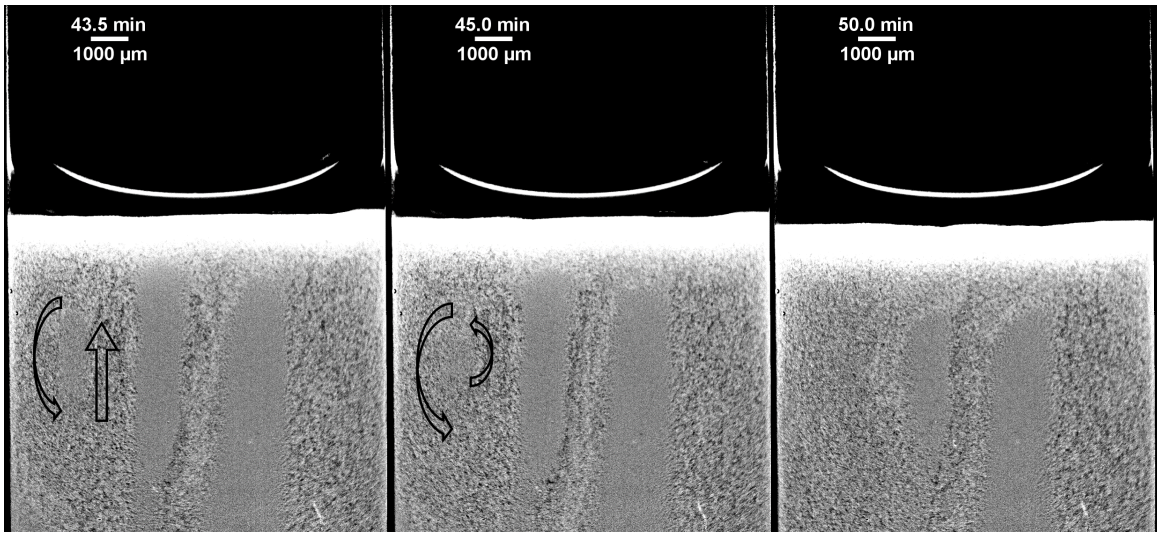

(g) *Large debris at the top falls through the gel following the fingers. A stream can be found recirculating upwards following the track of finger 3. Finger 2 merges with the one near the wall.*

(h) *The vortex on the left is closing up.*

(i) *The layer at the top (around the bright gel interface) starts to collapse from the left.*

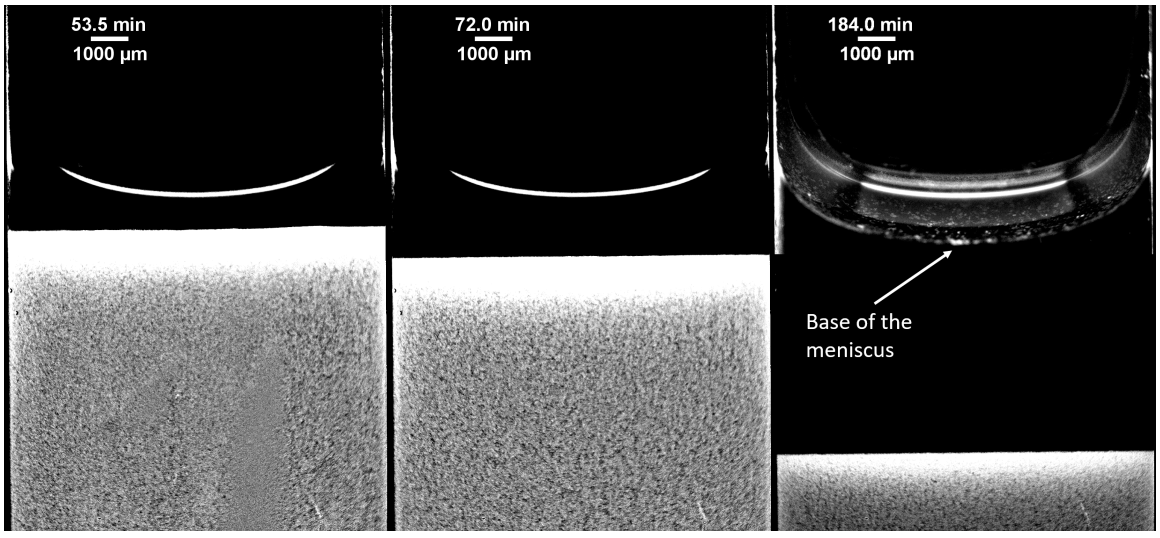

(j) *The final collapse of the layer is abrupt. At the same time, the bright gel interface buckles, indicating a massive recirculation across the whole settling gel.*

(k) *The entire gel structure has broken but appears flocculent as solvent passes through it.*

(l) *A composite image is made by combining two differently processed versions of the same micrograph. The contrast of the upper half of the image is adjusted to show the meniscus; while the lower half shows the settling gel.*

Figure 6.3 *(a)-(l) Micrographs of gel α.*

Collapse at the meniscus At $t = 0.5$ min, air bubbles are rapidly rising through the gel before being released from the gel. At $t = 1.0$ min (figure 6.3(a)), the sample is homogeneous. At $t = 2.5$ min (figure 6.3(b)), colloids at the corners of the meniscus are falling and accumulating around the meniscus. This makes the signal from the meniscus greater, causing over-exposure in some parts of it. This timescale is short compared to the delay time $\tau_{\mathrm{d}} = 63.5$ min.

Collapse of finger-like clusters At $t = 6.0$ min (figure 6.3(c)), a clear gel interface appears. Its speed decreases when it settles around the meniscus (see figure 6.2). At the same time, finger-like clusters start to form around the arc. The position of the base of the meniscus is marked as a white dashed line in figure 6.3(c) as a reference; the lower boundary of the meniscus can be seen in figure 6.3(l). As the fingers grow, the gel structure around the arc coarsens and the interface starts buckling (figure 6.3(d)-(f)). The finger in the centre of the image (finger 1) grows more slowly. The colloids above finger 1 form a crest (figure 6.3(e)). As finger 1 grows (or cluster 1 falls) further, the crest above it disappears (figure 6.3(f)). It shows that the mass source of the finger-like clusters is the crest. The three finger-like clusters in the centre of figure 6.3(d) are marked as finger 1, 2 and 3. The radii of the tips (indicated in figure 6.3(e) as the dotted black circle) of these clusters are measured manually. When $t < 16.0$ min, the tips of the fingers are broad, about 330 µm in radius. As the clusters fall, their size decreases slightly. The effective radius of the cluster is therefore averaged over the period when the size is stable ($t > 16.0$ min for all fingers) giving $R = 223 \pm 5$ µm, 265 ± 4 µm and 252 ± 5 µm, for finger 1, 2 and 3 respectively. Their height profiles, i.e. the position (in gravitational direction with respect to the base of the meniscus) *vs.* time, are plotted in figure 6.2. The falling speeds (averaged over $t > 16$ min) of finger 1, 2 and 3 are 10.2 ± 0.2 µm/s, 9.6 ± 0.4 µm/s and 17.6 ± 0.3 µm/s, respectively. At about $t = 18.0$ min, the colloids have accumulated around both sides of the edge forming two more fingers and fall (figure 6.3(e) and (f)). These two clusters are larger but distorted by the glass wall. It can be seen from figure 6.2, as the fingers form and fall, the settling of the gel slows down.

The onset of rapid collapse As the initial clusters fall down, more debris falls through the gel following the tracks of the initial fingers. At about $t = 40.0$ min, the settling of the gel interface accelerates, figure 6.2. At $t = 43.5$ min, a stream of clusters is found recirculating upwards on the left-hand side of the image forming

a vortex as indicated in figure 6.3(g) and (h). As more debris falls through, the vortex closes up (figure 6.3(h)). I suspect that the up-streaming colloids are a stream of debris brought by the solvent back flow. During this period, the gel interface is distorted frequently, due to the falling of clusters and rising of the back flow. Since the height profile is deduced from a small region of the gel interface instead of averaging over the width of the interface, it fluctuates as the interface is distorted (figure 6.2). At around $t = 50.0$ min (figure 6.3(i) and (j)), the denser layer at the top (around the bright gel interface) suddenly falls through the gel in multiple positions. The resulting strong back flow breaks the entire gel structure (figure 6.3(j) and (k)). Around this time, the collapse enters the rapid collapse stage, i.e. $\Delta h(t)$ is linear with time. The inset of figure 6.2 illustrates the definition of the onset time of rapid collapse τ_{o}. The onset (time) of rapid collapse is defined by the collapse of the gel becoming linear in combination with the denser layer falling through the gel. Technically, the determination of the onset of rapid collapse involves fitting the linear section of sedimentation during pre-collapse and rapid collapse. The x-coordinate of the intersecting point is the onset time of rapid collapse. For gel α, $\tau_{\mathrm{o}} = 50.7$ min.

During the rapid collapse period, the settling gel appears flocculated as solvent passes through it; however, the broken gel structure still exhibits a sharp, clear interface that separates the supernatant from the settling 'gel' (figure 6.3(k)). The red solid line in figure 6.2 is a linear fit of the rapid collapse period. The interface speed of the rapid collapse is $v_{\mathrm{i}} = 766 \pm 1$ nm/s which is much higher than the single particle sedimentation speed v_{s}. From Eq. 1.6, $v_{\mathrm{s}} = 56.3$ nm/s calculated with $\Delta\rho = 0.27$ mg/ml and $\eta_{\mathrm{s}} = 0.0105 \pm 0.0001$ Pa $\cdot$ s. v_{i} is much slower than the speed of fingers. It should be noted that the onset time of the rapid collapse of gel α is earlier than the delay time corresponding to the gel detaching from the base of the meniscus ($\tau_{\mathrm{d}} = 63.5$ min).

The onset of final compression From figure 6.2, the height profile deviates from the linear fit at about $t = 184.0$ min. After this time, the settling of the gel slows down gradually and starts the final compression. The image at $t = 184.0$ min was processed in two ways. The resulting images are recombined and shown in figure 6.3(l). The lower half of the image was processed in the same way as previous images. It shows no significant change of the settling gel before and after the starting of final compression. The contrast of the top portion of figure 6.3(l) was separately adjusted to highlight the meniscus. From this portion

of the image, we can see bright features that are still attached to the meniscus. These are colloids that can move along the meniscus.

Summary For a rapid collapse gel with low φ_c (regime D1, ◀ in figure 6.1), finger-like clusters are formed and fall through the gel prior to the collapse of a denser layer. The denser layer collapses at multiple sites creating back flow that breaks the gel.

6.4 Rapid Collapse Gel with Intermediate φ_c: Gel β

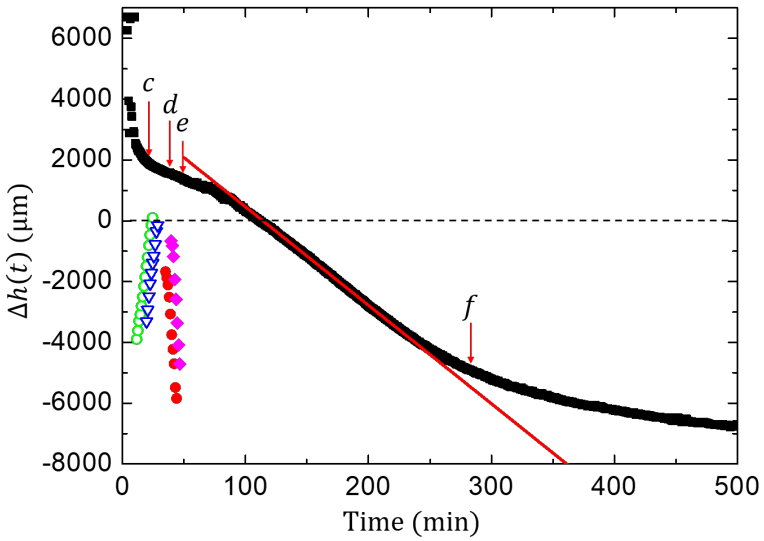

Figure 6.4 ■*: Height profile $\Delta h(t)$ vs. time of rapid collapse gel β. Arrows indicate at which time the images in figure 6.5(c) - (f) were taken. The red solid line is the linear fit of the rapid collapse. The black dashed line indicates the base of the meniscus.* ○ *and* ▽ *are the height profiles of droplets 1 and 2 denoted in figure 6.5(c).* ● *is the height profile of the finger-like cluster indicated by the dotted circle in figure 6.5(d).* ◆ *is the finger-like cluster which follows the track of droplet 1.*

With intermediate φ_c , solvent droplets can be found in addition to the finger-like clusters during the macroscopic quiescent period. The height profile of gel β (figure 6.1 $\varphi_c = 0.24$, $\varphi_p^{free} = 0.565$ and $c_p = 5$ mg/ml) is plotted as $\Delta h(t)$ *vs.* time in figure 6.4. The height profile confirms that gel β is also a rapid collapse gel. Micrographs of gel β are shown in figure 6.5. The time of images (c) - (f) in figure 6.5 are indicated with arrows in figure 6.4.

Solvent droplets rising At $t = 1.0$ min, the sample is homogeneous with the exception of some small air bubbles which can still be seen rising inside the gel, see figure 6.5(a). At $t = 2.5$ min, colloids at the corner of the meniscus fall and accumulate around the top of the gel. A solvent droplet can just be seen rising close to the edge of the cuvette, see figure 6.5(b).

At about $t = 9.0$ min, solvent droplets 1 and 2 (denoted in figure 6.5(c)) appear in the experimental window. The initial shape of the droplets is irregular. As droplets rise, tracks are left. Droplet 1 is formed by several small droplets coalescing together. The position and radius of droplet 1 and 2 are measured after they are fully formed. The height profiles of droplet 1 and 2 are plotted in figure 6.4. Their radii and rising speeds are 90 ± 1 µm, 5.2 ± 0.1 µm/s and 113 ± 2 µm, 5.9 ± 0.1 µm/s, for droplet 1 and 2, respectively. More droplets can be found rising through the gel as the gel interface approaches the base of the meniscus (figure 6.4). Some come from below the field of view, and others break away from existing tracks to make their own ones.

Collapse of finger-like clusters The finger-like cluster indicated by the dotted circle in figure 6.5(d) is generated after droplet 2 reaches the top of the gel. The cluster interacts with nearby droplets, bending their trajectories. The radius of the cluster also decreases from ≈ 500 µm at $t = 35.0$ min to ≈ 390 µm at $t = 44.0$ min. Its height profile is plotted in figure 6.4. Its average falling speed is 9.2 ± 0.2 µm/s. The second cluster is formed on the left. It falls through the gel following the track of droplet 1. As a result, it falls with an average speed of 12.1 ± 0.2 µm/s, faster than the first cluster. Its initial size is ≈ 480 µm at $t = 43.5$ min. It interacts with rising droplets and deforms as it fall through the track, figure 6.5(e).

Onset of rapid collapse As debris falls through the gel, the structure of the gel is gradually broken. At about $t = 83.0$ min, a strong recirculation can be seen from the images, suggesting that the denser layer falls around that time. Hence, $\tau_{\mathrm{o}} = 83.0$ min. The onset of rapid collapse is triggered before the gel interface leaves the base of the meniscus ($\tau_{\mathrm{d}} = 112.0$ min), figure 6.4. The red solid line in figure 6.4 is a linear fit to the rapid collapse. The interface speed of the settling gel is $v_{\mathrm{i}} = 540 \pm 1$ nm/s.

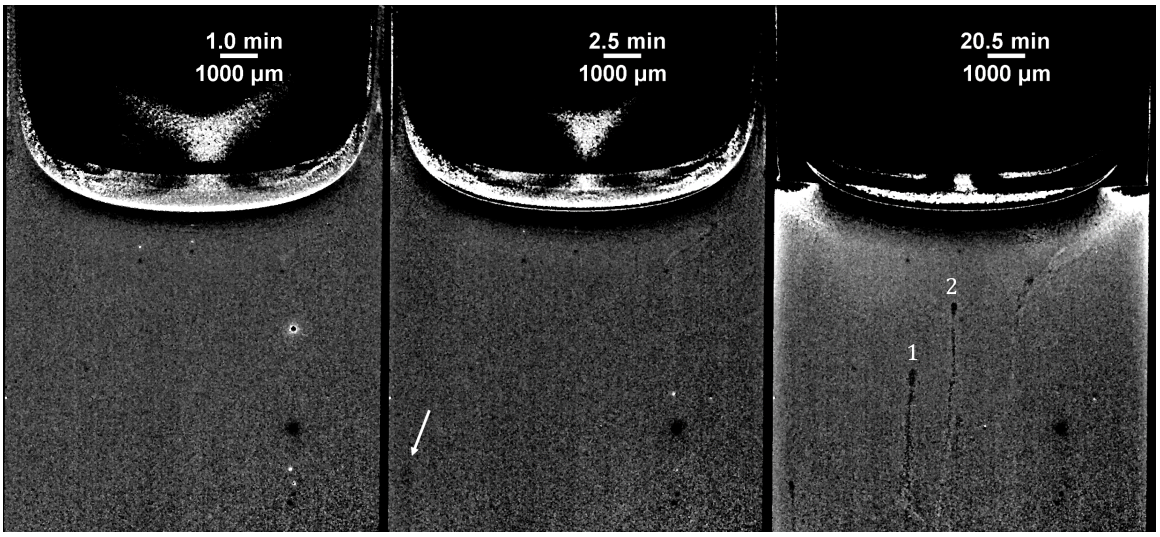

(a) *Some small air bubbles can still be seen rising inside the gel. Other than that, the sample is homogeneous. Colloids above the meniscus can be seen attached to the wall.*

(b) *The colloids both at the corner of the meniscus and attached to the wall fall down. A solvent droplet can just be seen on the bottom left of the image.*

(c) *As colloids accumulate around the meniscus, droplets rise through the gel leaving tracks allowing solvent to escape from the gel more quickly.*

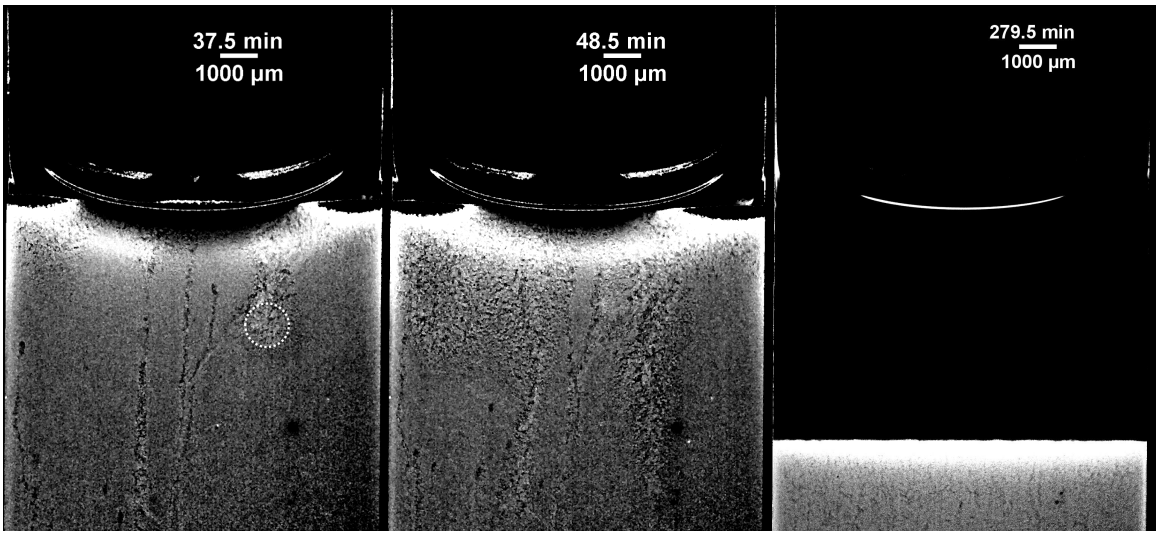

(d) *More droplets rise; first few have reached the gel interface. At the same time, finger-like clusters are formed and fall through the gel. The dotted circle indicates the tip of a cluster.*

(e) *Denser debris falls through the gel following the finger-like clusters. The clusters and droplets interact with each other.*

(f) *This image is processed without overexposing the gel interface. The settling gel appears flocculent but more compact.*

Figure 6.5 *(a)-(f) Micrographs of gel β*

Onset of final compression From figure 6.4, the height profile deviates from the linear fit at about $t = 240.0$ min. During the final compression of the sediment, the broken gel structure appears flocculated but more compact compared to that of a low φ_c gel, figures 6.5(f) and 6.3(l).

Summary In general, for a rapid collapse gel with intermediate φ_c (in regime D2, ▲ in figure 6.1), solvent droplets are found rising through the gel. Finger-like clusters interact with the rising solvent droplets, altering their sizes, speeds and trajectories as they fall. Then, falling of the denser layer triggers the rapid collapse.

6.5 Rapid Collapse Gel with High φ_c: Gel γ

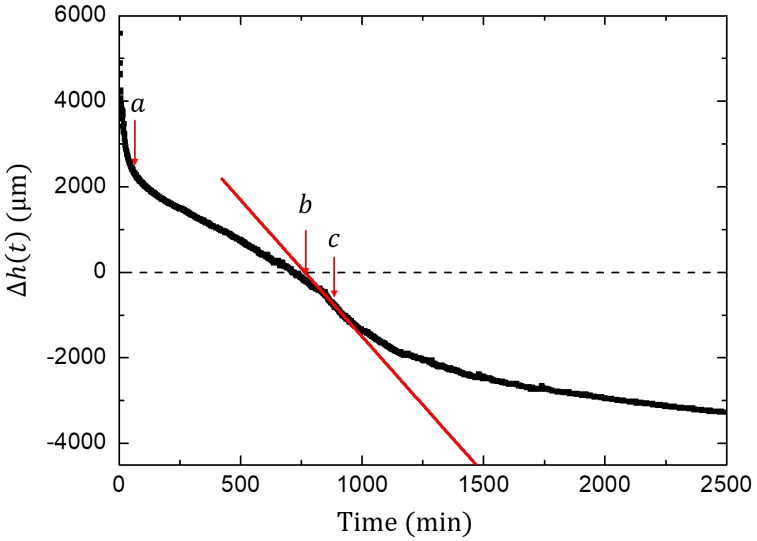

Figure 6.6 *Height profile $\Delta h(t)$ vs. time of rapid collapse gel γ. Indicated by arrows are images shown in figure 6.7(a) - (c). The red solid line is the linear fit of the rapid collapse. The black dashed line indicates the base of the meniscus.*

Micrographs of gel γ ($\varphi_c = 0.34$ and $\varphi_p^{free} = 0.586$) are shown in figure 6.7. The resulting height profile is plotted in figure 6.6. Gel γ is a rapid collapse gel with a short period of fast collapse.

Onset of rapid collapse In figure 6.7(a), the black spots with a white dot in the centre are air bubbles in the first image. No sign of finger-like clusters can be seen. However, solvent droplets are found rising through the gel; one droplet is

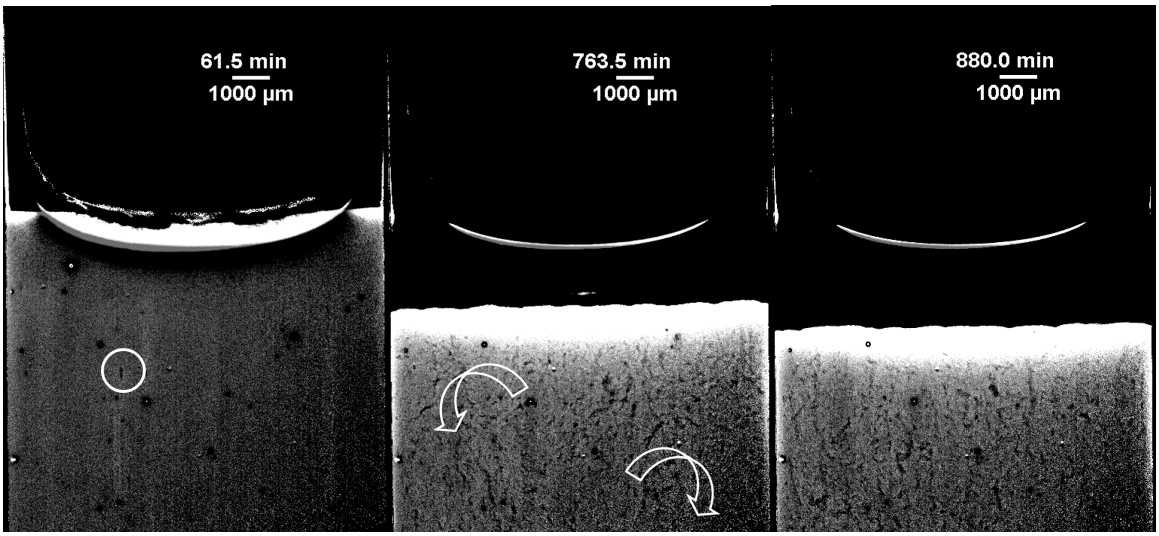

(a) *No sign of finger-like clusters can be seen. Solvent droplets are found rising in the gel (as indicated by the white circle).*

(b) *The denser layer collapse in large blocks as indicated by arrows.*

(c) *A clear, sharp interface can be identified. Volcanic craters are formed as the solvent droplets reach the interface.*

Figure 6.7 *Micrographs of gel γ*

highlighted in figure 6.7(a) as an example. At around $t = 760.0$ min, the denser layer starts collapsing as two big blocks as indicated in figure 6.7(b). This creates strong back flows that break the gel structure. The rapid collapse is triggered around this time. In figure 6.7(c), the gel interface is clear and sharp similar to that of gel α (figure 6.3) and β (figure 6.5). However, volcanic craters can be seen at the interface due to the solvent droplets reaching the interface. The interface speed of the gel γ is $v_\mathrm{i} = 96 \pm 1$ nm/s, close to the speed of single particle sedimentation $v_\mathrm{s} = 56.3$ nm/s. More results of interface speed are reported in Appendix A.3.

The onset of the rapid collapse of gel γ ($\tau_\mathrm{o} = 772.5$ min) is later than the delay time $\tau_\mathrm{d} = 715.0$ min, i.e. the gel starts rapid collapse after the gel interface detaches from the meniscus figure 6.6. However, in regime D3, for the gels with lower polymer concentration, the rapid collapse starts before the delay time. More results of the onset height and onset time of rapid collapse can be found in Appendix A.4 and A.5.

Summary At high φ_c, rapid collapse gels with high polymer concentration (in regime D3, ▶ in figure 6.1) exhibit no finger-like cluster falling but only solvent droplets rising. In these cases, the denser layer collapses as a big block instead of

multiple collapses observed in lower φ_c gels. Also, for the rapid collapse gel with highest φ_c and φ_p^{free} the onset of rapid collapse of these gels is triggered after the gel interface detaches from the meniscus.

6.6 Slow Collapse Gels: Gel δ

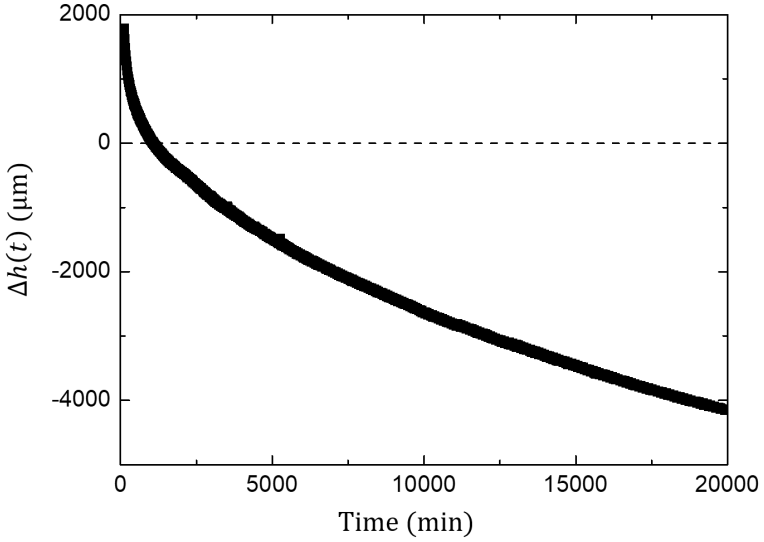

Figure 6.8 *Height profile $\Delta h(t)$ vs. time of the slow collapse gel δ (see figure 6.1) with $\varphi_c = 0.46$ and $\varphi_p^{free} = 0.382$ ($c_p = 3$ mg/ml), obtained from microscopic time-lapse imaging with a time intercal of 0.5 min.*

The slow collapse gels in this work have been identified in Chapter 5 using long-time macroscopic time-lapse imaging. Here, the microscopic imaging mainly investigates the onset of the slow collapse. The only long-time microscopic imaging was performed using gel δ ($\varphi_c = 0.46$ and $\varphi_p^{free} = 0.382$). The height profile $\Delta h(t)$ *vs.* time of gel δ measured from microscopic imaging with 0.5 min time interval is plotted in figure 6.8. It confirms that sample δ collapses non-linearly after the delay time. It shows that a slow collapse gel also starts collapsing at the corner of the meniscus right after re-stabilization. Micrographs of gel δ are shown in figure 6.9.

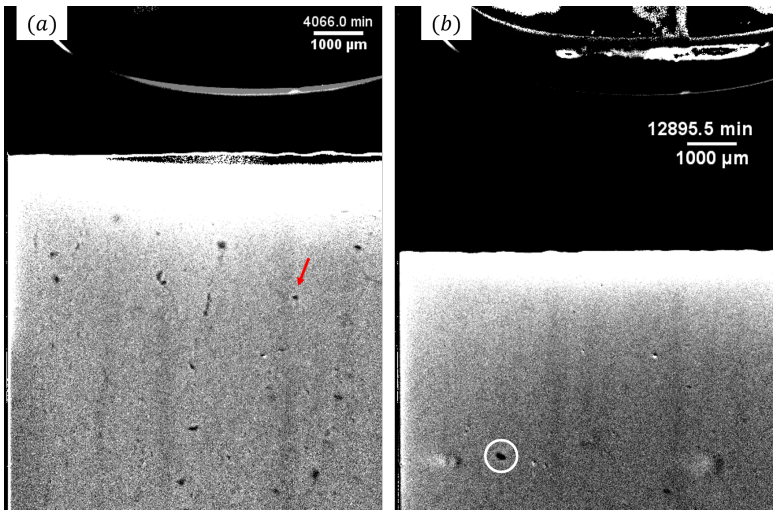

Figure 6.9 *Micrographs of gel δ. The arrow in (a) indicates a solvent droplet that is stuck until it grows big enough to rise again. The circle in (b) indicates a solvent droplet that is stuck and squeezed back into the gel.*

Solvent droplets Solvent droplets are found rising through the gel before and after the gel detaches from the meniscus, see figure 6.9. In figure 6.9(a), a solvent droplet stops rising at $t = 4066.0$ min as indicated by the arrow. This droplet continues to rise as it grows bigger. In figure 6.9(b), a solvent droplet initially rising through the gel is found stuck in the gel; however, it falls with the gel and shrinks until it disappears. These two cases imply the formation mechanism of droplets. More discussions on the solvent droplets will be given in Sec. 8.2. After about 17500 min, no solvent droplets can be seen.

As droplets reach the gel interface, volcanic eruptions can be found at the gel interface. The volcanic crater at the gel interface has been reported previously by C. Derec *et al.* [64] and D. Senis *et al.* [65] in DLCA gels formed by calcium carbonate spheres. The volcanic eruption is rare event in DLCA gels. The height profile of the collapse showed an acceleration of the interface speed when an eruption was observed. In contrast, volcanic eruption in our gels is not a rare event. When the solvent droplets (hence the volcanoes) were observed, the interface speeded up in gel γ; however, slowed down in gel δ. Therefore, in our system, the interface speed is uncorrelated with the eruption.

Summary In general, slow collapse gels are found at much higher φ_c (● in figure 6.1). For slow collapse gels, the falling of finger-like clusters or denser layers cannot be observed. However, solvent droplets are found rising through the gel, creating volcanoes as they reach the gel interface.

6.7 Regime A gel

In previous studies, it was suggested that in the gel forming region (shaded area in figure 2.7(a)), a gel cannot be formed if the gravitational stress exerted by a single particle σ_g can force the structure to yield (left to the purple dashed line in figure 2.7(a)), see Sec. 2.4. After introducing the finger-like clusters and the solvent droplets, now I present the imaging results of a regime A gel ($\varphi_c = 0.10$ and $\varphi_p^{free} = 0.551$, ■ in figure 6.1).

The height profile is plotted in figure 6.10. For comparison, the height profile of gel α is also re-plotted. The micrographs of the regime A gel are shown in figure 6.11.

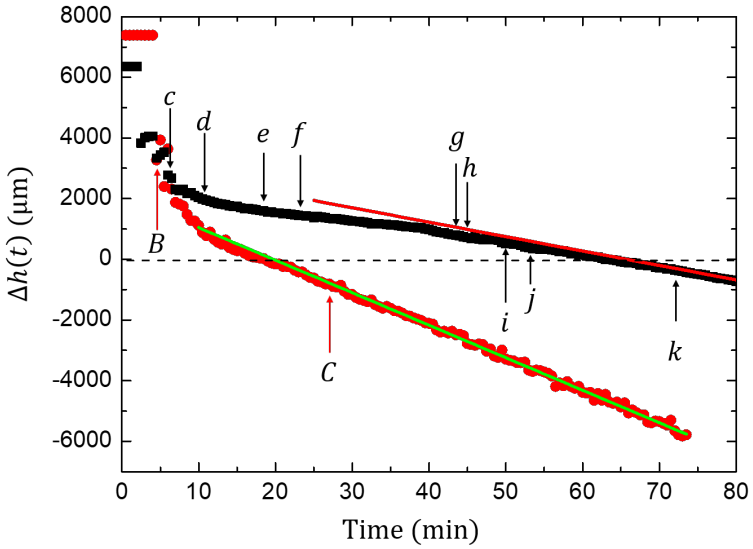

Figure 6.10 *Height profile $\Delta h(t)$ vs. time of the regime A gel (●). The green line is a linear fit to the fast sedimentation. Images figure 6.11(B) and (C) are indicated by capital letters. For comparison, the height profile of gel α is re-plotted as ■. Red line is a linear fit to the rapid collapse. Images figure 6.3(c) to (k) are indicated by lower case letters. The black dashed line indicates the base of the meniscus.*

Similarly, the regime A gel starts collapsing at the corner of the meniscus right after it is mounted. However, the sample is more granular and mobile compared to a gel. Also, neither finger-like clusters nor solvent droplets can be found in this sample, while large-scale recirculation can be found in the early stage (around 7 min). From the height profile, the settling of the regime A gel enters the fast sedimentation without delay. The interface that separates the settling colloids and the supernatant can be identified. This clearly distinguishes the regime A

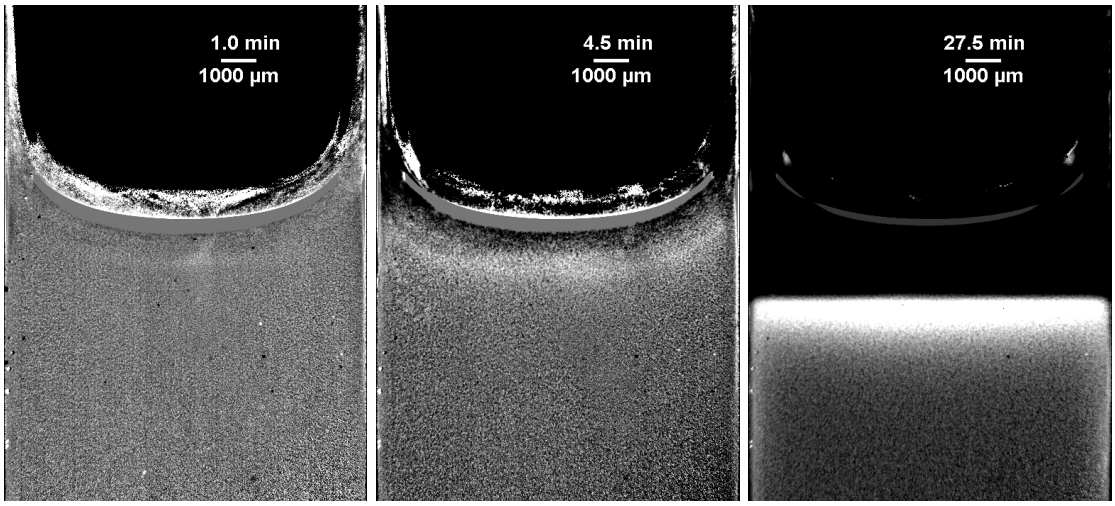

(A) *After 0.5 min, all visible air bubbles have escaped and sample is homogeneous.*

(B) *The bulk of the sample is more granular compared to that of a gel. No finger-like clusters or solvent droplets can be found. However, large-scale recirculation occurs.*

(C) *The interface separating the settling colloids and the supernatant can be identified. It is less sharp compared to that of a gel.*

Figure 6.11 *Micrographs of a regime A gel of large particle system with* $\varphi_c = 0.10$ *and* $\varphi_p^{free} = 0.551$.

gel from that undergo gas-liquid phase separation (figure 5.1(a)). However, the interface (figure 6.11(C)) is less sharp compared to that of a gel (figure 6.3). The green line in figure 6.10 is a linear fit of the fast sedimentation. The average interface speed is $v_i = 1.79 \pm 0.01$ µm/s which is much faster than the single particle sediment speed $v_s = 56.3$ nm/s. In contrast to a rich phenomena before the rapid collapse gel detaches from the meniscus, the regime A gel settles more straightforwardly, figure 6.10.

Summary For a sample in regime A, ■ in figure 6.1, no gel is formed before the collapse; neither finger-like clusters nor solvent droplets can be found.

6.8 Observation of Small-Colloid Gels

In this section, I verify the key observations of the large particle gels using a small particle system close to the one in Ref. [29]. The characterisation of the small particle model system has been reported in Chapter 4. The type of the collapse of each sample is identified in Chapter 5, see the state diagram figure 5.5.

The microscopic time-lapse imaging was performed in the same way as for the large colloid gels. Figure 6.12 is a plot of the height profiles ($\Delta h(t)$ *vs.* time) of small-colloid samples measured from micrographs. The inset is the same data as in figure 5.4 which is presented as scaled height $\hat{h}(t)$ *vs.* t. Figure 6.12 confirms the categorisation based on macroscopic imaging results.

Figure 6.14 presents the micrographs of gel $S1$, while those of gels $S2$, $S3$ and $S4$ are shown in figure 6.15. These gels were labelled in the state diagram figure 6.13. In all small particle gels, the timescale of collapse at the corner of the meniscus is much shorter than the delay time.

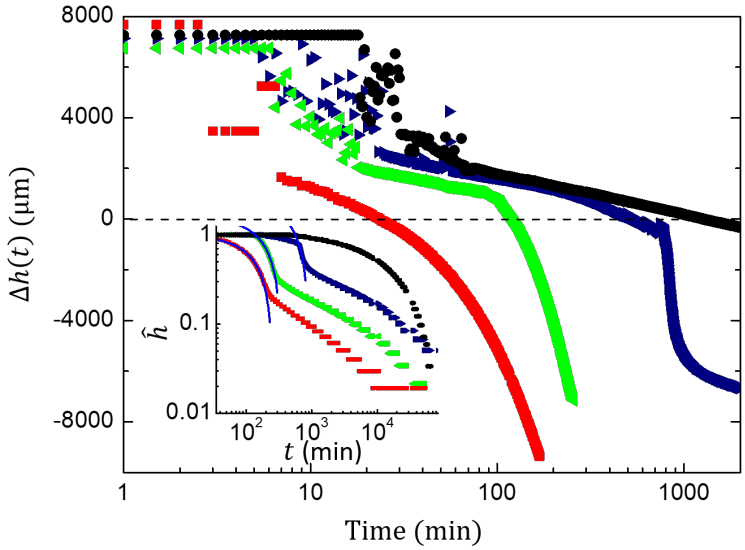

Figure 6.12 *Height profiles $\Delta h(t)$ vs. time of gels formed by small PMMA colloids. The black dashed line indicates the base of the meniscus.* ■*: $\varphi_c = 0.10$, $\varphi_p^{free} = 0.366$;* ◀*: $\varphi_c = 0.20$, $\varphi_p^{free} = 0.387$;* ▶*: $\varphi_c = 0.31$, $\varphi_p^{free} = 0.409$; and* ●*: $\varphi_c = 0.40$, $\varphi_p^{free} = 0.441$. The inset re-plots the scaled height profile from figure 5.4. The blue solid lines are linear fits to the fast sedimentation.*

Gel S1: With low colloidal volume fraction, a sample in regime A cannot form a gel before it collapses. No finger-like clusters or solvent droplets can be found in the micrographs, figure 6.14. Similar to the large-colloid counterpart (figure 6.11), the structure of the sample is more coarsened and the interface between the settling colloids and clear supernatant is blurry, as shown in figure 6.14. The linear fit of fast sedimentation yields an interface speed of $v_i = 1.052 \pm 0.001$ μm/s much faster than the single particle sedimentation speed $v_s = 10.5$ nm/s.

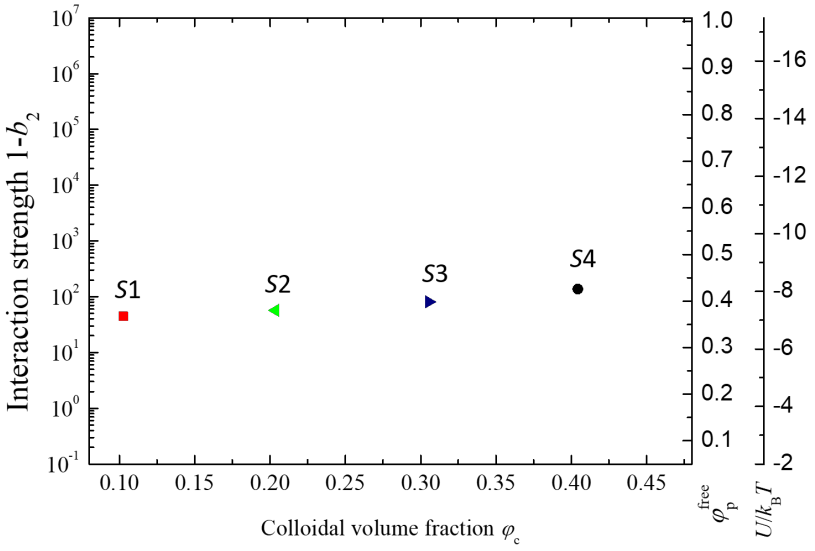

Figure 6.13 *State diagram of the small particle gel is updated from figure 5.5 showing the evolution of the collapse mechanism. The data markers are the same as those in figure 6.1. Markers are labelled by samples name above for convenience.*

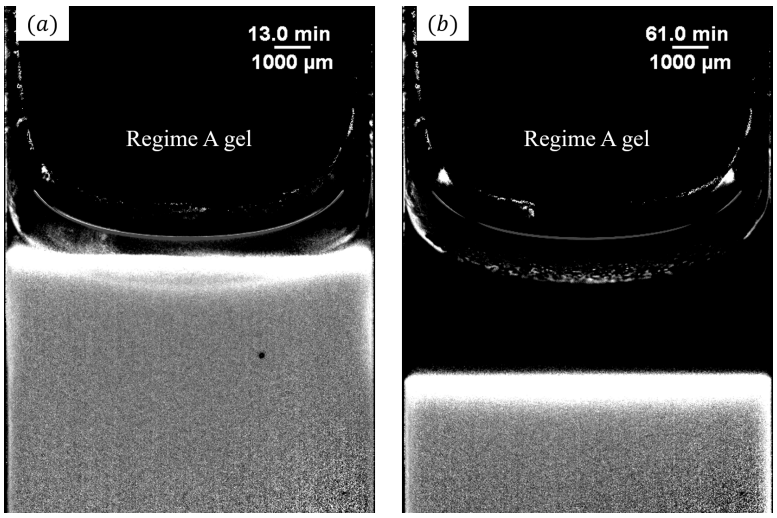

Figure 6.14 *Micrographs of small PMMA gels: regime A gel, S1. (a) Colloids collapse from the corner of the meniscus at the beginning of the experiment. Neither finger-like clusters nor solvent droplets can be found. (b) The interface separating the settling colloids and the clear supernatant is blurry. The structure of the sample is more granular.*

Gel S2: The rapid collapse gel with low colloidal volume fraction shows finger-like clusters under the corners of the meniscus, figure 6.15(a). However, no solvent droplets are observable in this gel. The denser layer collapses as indicated in figure 6.15(b) by the arrows. The onset height of rapid collapse is above the base of the meniscus, see figure 6.12. The interface speed is $v_\mathrm{i} = 0.936 \pm 0.001$ µm/s.

Gel S3: With higher φ_c, no finger-like clusters can be found. Irregularly shaped solvent droplets are found rising through the gel. The tracks left by the solvent droplets become tenuous wakes. The wakes break into shorter pieces and stretch horizontally into the centre of the image (the darker horizontal wakes can be seen on the left of figure 6.15(c)). The denser layer collapses first on the left (as indicated by the arrow in figure 6.15(c)). The resulting back flow triggers another, even stronger, massive collapse on the right, figure 6.15(d). The structure of the gel is therefore destroyed and the rapid collapse is triggered. It should be noticed that the rapid collapse is triggered after the gel interface detaches from the meniscus, similar to the large particle gel γ, figure 6.12. Also, the volcanic craters are formed as the solvent droplets reach the interface. The interface speed is $v_\mathrm{i} = 0.743 \pm 0.007$ µm/s.

Gel S4: Figures 6.15(e) and (f) present micrographs of a slow collapse gel. In figure 6.15(e), the black circles with a white dot in the centre are air bubbles in the reference image. They appear in all processed image due to the imaging process method, see Sec. 3.2. The white circles with a black dot in the centre are air bubbles in the current image. These air bubbles are released from the gel and absent in figure 6.15(f). From figure 6.15(f), the falling of finger-like clusters and the denser layer cannot be observed. The solvent droplets can be found zigzagging upwards, as indicated by the white circle. However, no volcanic eruption at the interface can be observed from these side-ways images.

Summary The imaging results shown in this section confirm the key observations from the gel collapse made from the large PMMA samples. First, a gel starts collapsing from the corner of the meniscus much earlier than the delay time. Second, in the regime A gel, no finger-like clusters or solvent droplets can be found. The sample collapses straightforwardly with a blurry but distinguishable interface. Third, the finger-like clusters are formed at the top of a rapid collapse gel with low colloidal volume fraction. Fourth, solvent droplets can be found rising through the gel with higher colloidal volume fraction. Finally, the denser

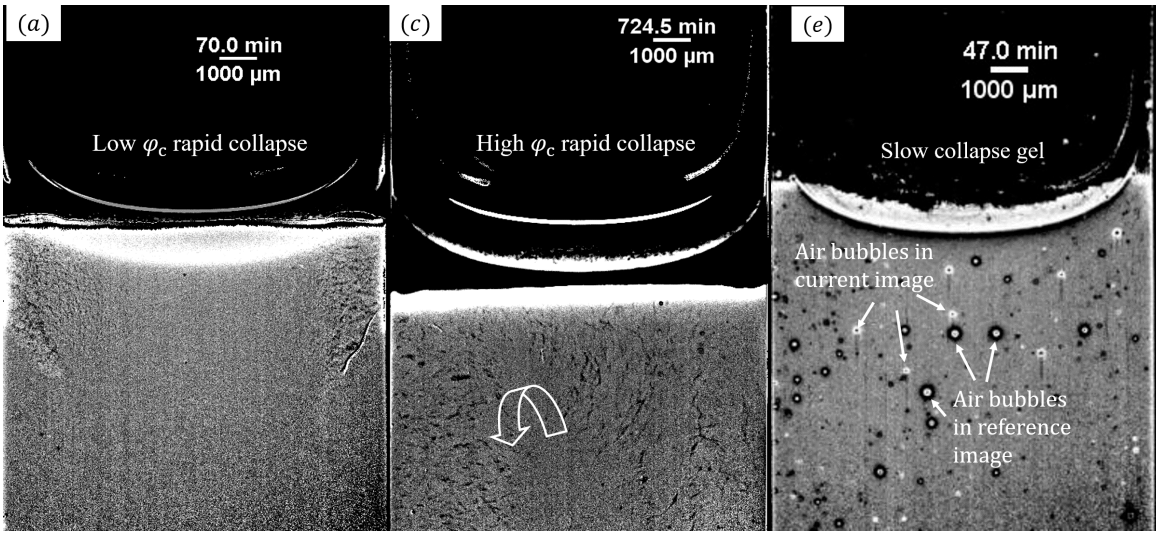

Finger-like clusters can be found on both side of the image. The meniscus and the gel interface are over-exposed.

Tracks are left by the rising solvent droplets. Dark cracks can be seen to the left of the arrow. The denser layer starts to collapse on the left-hand side as indicated by the arrow.

Air bubbles rise through the gel (see text).

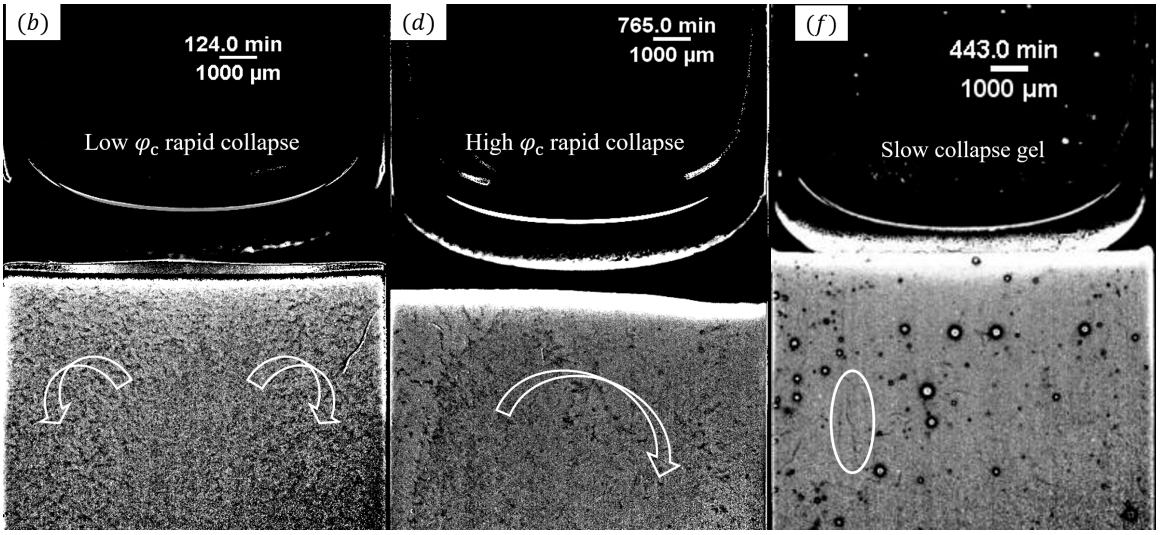

The denser layer collapses following the finger-like clusters, as indicated by the arrows.

The back flow rising from the left leads to a second massive collapse on the right. The structure of the gel is then destroyed.

Solvent droplets zigzagging upwards are found in the slow collapsing gel.

Figure 6.15 *Micrographs of small PMMA gels. Left column: S2, rapid collapse gel with low φ_c; middle column: S3, rapid collapse gel with high φ_c; and right column: S4, slow collapse gel.*

layer formed at the top of the gel falls through the bulk of a gel, destroying the gel structure.

The collapse mechanism of the rapid collapse that finger-like clusters interact with solvent droplets has not yet been observed in the small particle gel system. This could be because very few samples have been studied. Generally, the evolution of the collapse mechanism as φ_c is increased is confirmed in the model system with small gravitational Péclet number.

6.9 Conclusion

In this chapter, I reported microscopic imaging results of gels formed by large and small PMMA particles. Some valuable conclusions can be drawn directly from the observations:

1. The imaging results confirm the picture arisen from previous studies with direct observation [29, 53]. A denser layer is formed at the top of the gel. As the layer falls through the gel, the resulting back flow breaks the gel structure and the rapid collapse commences.

2. The micrographs show that finger-like clusters generated at the meniscus fall through the gel prior to the avalanche of the denser layer. Also, solvent droplets are found in intermediate and high φ_c gels rising through the gel leaving tracks behind them.

3. The result with large PMMA gels ($Pe_g > 1$) shows an evolution of collapse mechanisms as the colloidal volume fraction varies. This evolution of collapse mechanisms is verified using a small particle gel system, in which the gravitational Péclet number is much smaller than 1. This evolution is summarised in the phase diagram figure 6.1: At very low φ_c, in regime A (■), no finger-like clusters or solvent droplets can be found. At low φ_c (◀), finger-like clusters form and fall through the gel near the wall of the cuvette prior to the collapse of the denser layer. At intermediate φ_c (▲), it was observed that a gel can support the mass at the top for a longer period. Solvent droplets can be found rising through the gel before the falling of the fingers. At higher φ_c (▶), a gel can support more mass at the top, so that in the vicinity of the wall, the fingers are absent. The

denser layer collapses as large blocks. Further increase the φ_c (●) leads to a gel collapse with no fast sedimentation. The falling of the denser layer can no longer be seen. Therefore, microscopic imaging together with monitoring the interface speed can predict the types of collapse during the early stage, even before the commencement of the macroscopic collapse. This can be applied to product development and shorten its cycle.

4. The imaging results show that the collapse of a gel starts at the corner of the meniscus. The mass source that forms a denser layer is the colloids at the corner of the meniscus. Hence, it is reasonable to expect a longer delay time if the meniscus is eliminated. I will report case studies on this topic in Chapter 7.

Also, the direct observations of the collapse of gels raise some questions. I will discuss the following topics in Chapter 8:

1. The formation mechanism of the denser layer and the solvent droplet.

2. Previous studies of small particle gels interpreted the collapse of the denser layer in terms of a yielding event [29, 51, 53]. The evolution of the collapse mechanism seems to support such a picture. As φ_c increases, the yield stress of the gel increases, therefore, allowing it to support more weight at its top. For large particle gels ($Pe_g > 1$), this picture is yet to be tested.

Chapter 7

Meniscus Effect

7.1 Introduction

Results in Chapter 6 show that a gel starts to collapse from the corner of the meniscus. The falling of the accumulated denser layer then triggers the rapid collapse. Since the mass of this denser layer mainly comes from the corner of the meniscus, it is reasonable to expect that the gel collapse can be postponed by eliminating the meniscus.

In this chapter, I report studies of the meniscus effect in the collapse of large particle gels. After describing my method in Sec. 7.2, I will show in Sec. 7.3 that with and without a large air-gel interface, a rapid collapse gel settles with different mechanisms and has different onset times. The collapse mechanisms will be summarised in Sec. 7.3.2. Then, I will show that eliminating the air-gel interface is a possible way to postpone the rapid collapse in Sec. 7.3.3. I will also show a preliminary study of the meniscus effect in a slow collapse gel in Sec. 7.4. The result suggests that by reducing the area of the air-gel interface, the interface speed of a slow collapse gel can be slowed down further. Discussions on the effect of the meniscus in a slow collapse gel will be given in Sec. 7.4.3.

7.2 Method

In this chapter, large particle gels are studied in geometries with and without large menisci. Efforts have been made to eliminate the meniscus (geometries $\mathbb{C}$ and $\mathbb{D}$ in figure 7.1). The gel was transferred to a vial and remixed on a rolling band for 48 hours to release the dissolved air. Then, the gel was carefully filled

into a cuvette ($10 \times 10 \times 45$ mm^3). The sample was left alone for 1 min to release air, then sealed with a glass slice which was cut to fit the cross section of the cuvette. We find that this and all other protocols tried do not eliminate all air, and an air bubble is always left in the cuvette.

The four geometries studied in this chapter are illustrated in figure 7.1:

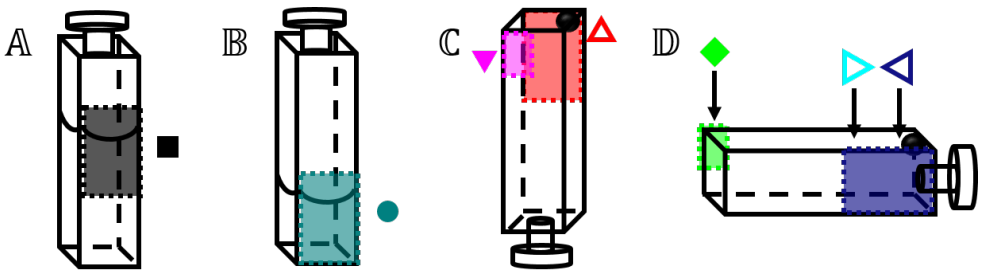

Figure 7.1 *Illustration of different geometries.*

Geometry 𝔸: upright geometry with sample height of $\sim$ 1.8 cm. This is the standard geometry that has been studied in Chapters 5 and 6. The black dashed square indicates the portion of the sample imaged by a 1$\times$ objective.

Geometry 𝔹: upright geometry with sample height of $\sim$ 1.0 cm. The dark cyan dashed square indicates the portion of the sample imaged by a 1$\times$ objective.

Geometry ℂ: complete filled up-side-down geometry except for a small air bubble (black). With this geometry, the sample was mounted on a frame, instead of being placed on a levelled sample holder. A 1$\times$ objective was used to image the air bubble side as indicated by the red dashed square. The height profile from the images of a 1$\times$ objective was measured near the air bubble. A 2$\times$ objective (Nikon, NA=0.06) was used to image the opposite side of the air bubble (magenta dashed square). The height profile was measured near the edge of the cuvette (far away from the air bubble). The images on both sides were taken simultaneously.

Geometry 𝔻: the same geometry as geometry ℂ, but with the sample lying horizontally with the small air bubble at one end of the cuvette. A 1$\times$ objective was used to image the air bubble side as indicated by the blue dashed square. From the 1$\times$ objective result, the height profiles were measured both close to the air bubble ($\triangleleft$) and away from the air bubble ($\triangleright$). A 2$\times$ objective was used to image the opposite side (green dashed square). The height profile was

measured close to the edge of the cuvette (◆). The images on both sides were taken simultaneously.

For geometries 𝔸 and 𝔹, the samples were re-mixed on a vortex-mixer for 40 seconds before each measurement. For geometries ℂ and 𝔻, a small magnet (3 mm × 3 mm × 6 mm) was added in the cuvette to help with the remixing of the settled gel. The sample was shaken vigorously by hand for about 1 min, then kept tumbling on a rotating wheel for 72 hours before each experiment. In this way, the sample is re-mixed and the air inside the sample can coalesce to form a single air bubble.

The time interval of the time-lapse imaging is 0.5 min for all experiments. At the 1× objective side, the sample was only illuminated whenever the image was taken. For geometries ℂ and 𝔻, at the 2× objective side, the sample was illuminated constantly throughout the experiment. Therefore, the dye on the colloids that facing the 2× objective was bleached heavily.

7.3 Rapid Collapse Gel

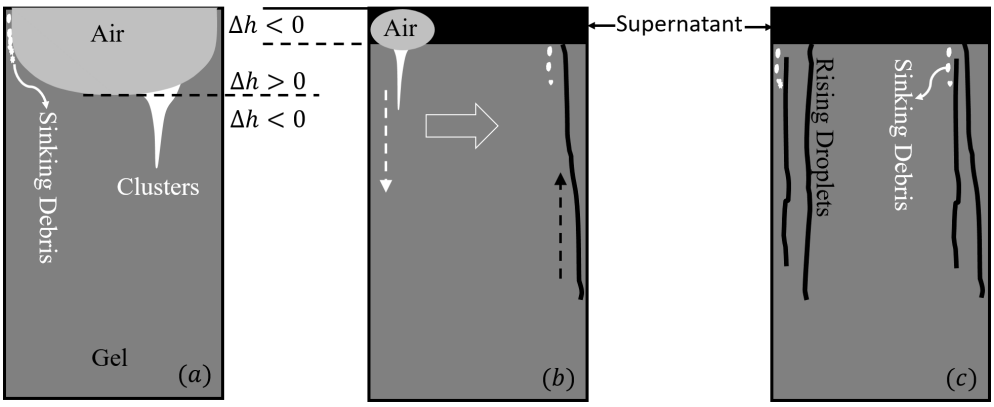

Figure 7.2 *Mechanisms of the rapid gel collapse with and without a curved air-gel interface. (a) With a large meniscus, debris falls from the vertical part of the meniscus. Finger-like clusters fall from horizontal part of the meniscus. (b) With a small air bubble, finger-like cluster falls from the air bubble and solvent droplets rise. A front of recirculation from falling clusters encroaches on the collapse due to the rising of solvent droplets. (c) Far away from any curved interface, solvent droplets rise and debris falls through the tracks left by the droplets.*

In different geometries, a rapid collapse gel settles with different mechanisms as illustrated in figure 7.2. To demonstrate this, I will report a case study of Gel

β in different geometries and show the reproducibility. Then, I will verify the general results using another rapid collapse gel. The mechanisms previewed in figure 7.2 will be discussed later.

7.3.1 Meniscus Effect in Gel β

Gel β ($\varphi_c = 0.24$, $\varphi_p^{free} = 0.565$, see figure 6.1) was studied in four geometries. The imaging results are reported in the next four subsections. The height profiles of gel β in 4 geometries are summaries in figure 7.3.

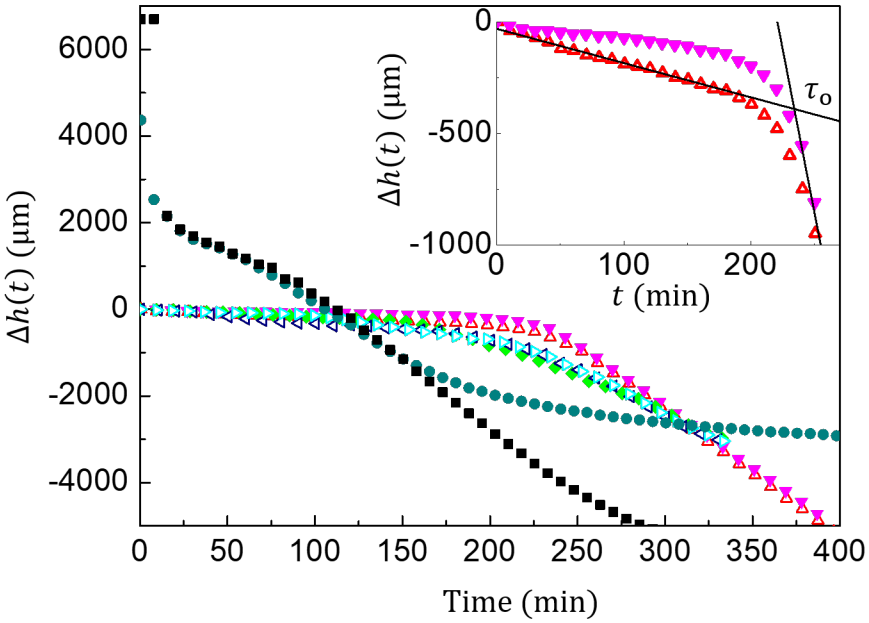

Figure 7.3 *Height profiles of gel β in geometries $\mathbb{A}$ (■), $\mathbb{B}$ (●), $\mathbb{C}$ (△ and ▼) and $\mathbb{D}$ (◁, ▷ and ◆). The symbols correspond to those used in figure 7.1 along with the illustration of the geometries. The inset exposes the details of the same data in geometry $\mathbb{C}$ to show the initial stage of the collapse.*

7.3.1.1 Geometry $\mathbb{A}$

$\mathbb{A}$

The imaging results for gel β in geometry $\mathbb{A}$ have been presented in Sec. 6.4, see figures 6.4 and 6.5. In summary, gel β is a rapid collapse gel with solvent droplets rising before the falling of finger-like clusters. The onset time of rapid collapse is $\tau_o = 83.0$ min; delay time is $\tau_d = 112.0$ min. The interface speed during the rapid collapse is $v_i = 540 \pm 1$ nm/s. The height profile is re-plotted as ■ in figure 7.3.

7.3.1.2 Geometry $\mathbb{B}$

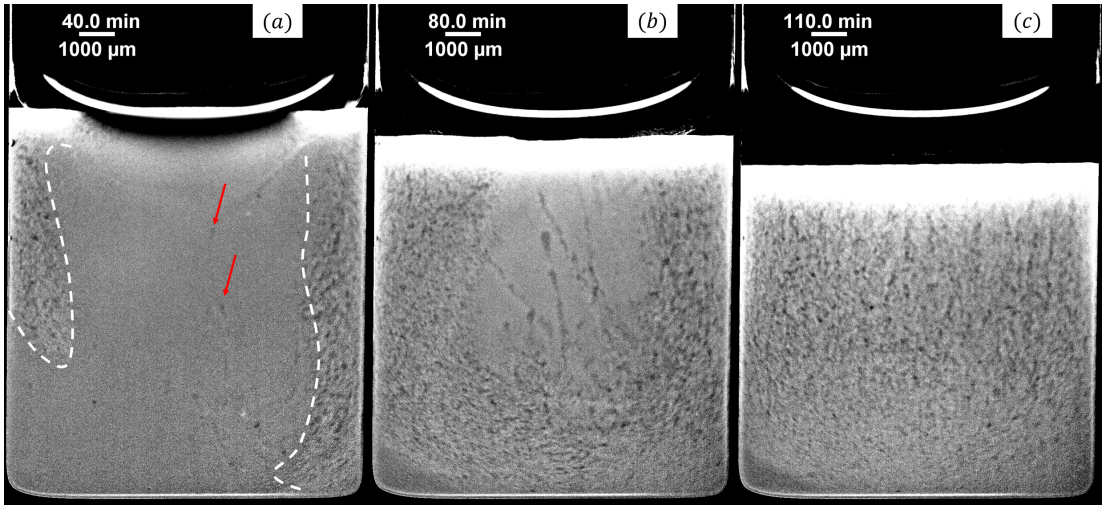

Figure 7.4 *Gel β in geometry $\mathbb{B}$. (a) Finger-like clusters (indicated by the dashed white lines) and solvent droplets (indicated by the red arrows) can be found. (b) The falling of the denser layer creates large-scale recirculation. (c) The structure of the gel is destroyed.*

Figure 7.4 shows images of gel β in geometry $\mathbb{B}$. Two finger-like clusters can be found falling along the edges of the cuvette as indicated by white dashed lines. Their shapes are distorted by the edges of the cuvette, see figure 7.4(a). Solvent droplets are found rising in the centre of the image, as indicated by red arrows in figure 7.4(a). Large-scale recirculation can be found in the gel, see figure 7.4(b). The falling of denser layer destroys the structure of the gel and triggers the rapid collapse. The settling gel appears flocculated (figure 7.4(c)).

The height profile is plotted as ● in figure 7.3. The onset time of rapid collapse is $\tau_o = 72$ min, which is about 14% shorter than that in geometry $\mathbb{A}$. Considering that the error of τ_o in geometry $\mathbb{A}$ is about 10% (see Appendix A.5), τ_o in geometry $\mathbb{B}$ is shorter but very close to that in geometry $\mathbb{A}$. The delay time $\tau_d = 107$ min, which is very close to that in geometry $\mathbb{A}$. The interface speed is $v_i = 451 \pm 2$ nm/s, which is $\sim 17\%$ slower than that in geometry $\mathbb{A}$ (540 ± 1 nm/s).

Similar to the result of geometry $\mathbb{A}$, the rapid collapse is triggered by the falling of the denser layer.

7.3.1.3 Geometry ℂ

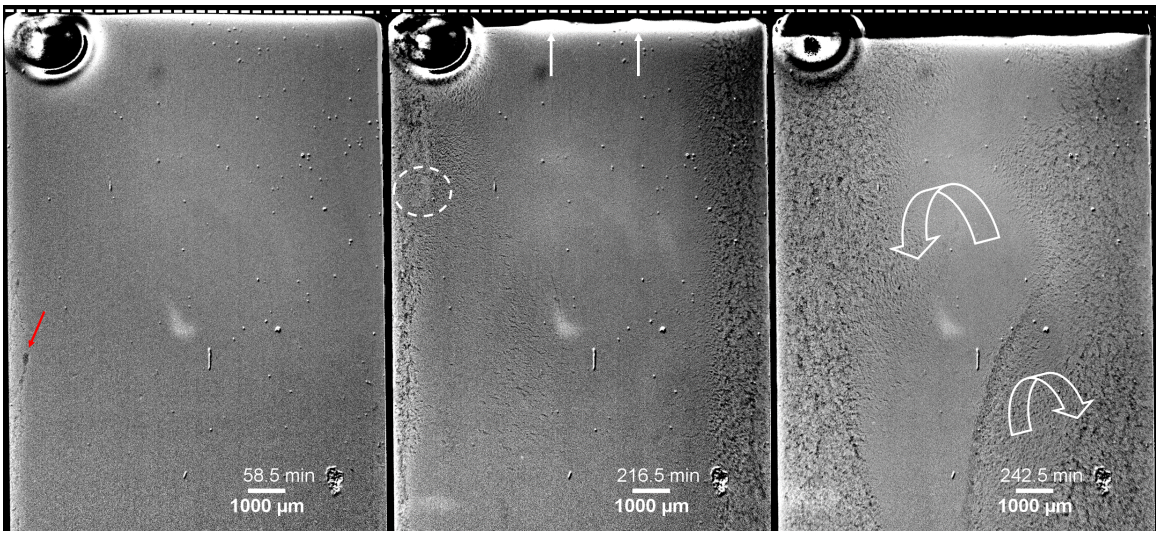

(a) *Solvent droplets (red arrow) rise along the edge of the cuvette.*

(b) *A finger-like cluster (white dashed circle) is generated from the bottom of the air bubble. Two volcanoes deep inside the gel are indicated by the white arrows.*

(c) *Large-scale recirculation can be found in the gel, as indicated by arrows.*

ℂ

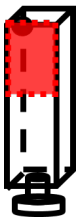

Figure 7.5 *Gel β in geometry ℂ, observed using a 1× objective. White dashed lines indicate the top of the gel.*

Near air bubble Figure 7.5 shows images of gel β in geometry ℂ at the air bubble side. The images were taken using a 1× objective, as indicated by the red dashed square in figure 7.1. The air bubble is about 2.5 mm in diameter. The gel interface detaches from the top of the cuvette from the beginning of the experiment. Colloids collapse around the air bubble and solvent droplets rise along the edge of the cuvette, figure 7.5(a). The radius of the solvent droplet indicated by the red arrow is about 70 µm. At $t \approx 210$ min, a finger-like cluster of $R \sim 360$ µm was generated at the bottom of the air bubble and fell as shown in figure 7.5(b). During this period, more solvent droplets rise along the edge of the cuvette. Also, the volcanoes in the centre of the image suggest that there are solvent droplets rising deeply inside the gel. Figure 7.5(c), as more debris falls following the finger-like cluster, large-scale recirculation is triggered. Therefore, the gel structure is destroyed.

The height profile measured close to the air bubble is plotted as △ in figure 7.3.

Initially, the gel interface settles slowly with a speed of 25.5 ± 0.1 nm/s which is slower than the single particle sedimentation speed $v_s = 56.3$ nm/s. Following the definition of the onset time of rapid collapse in geometry $\mathbb{A}$ (see figure 6.2), one can calculate $\tau_o = 231$ min, see the inset of figure 7.3. Around τ_o, the settling of the interface accelerates gradually until it reaches the constant speed of $v_i = 475 \pm 1$ nm/s which is slower than that in geometry $\mathbb{A}$ (540 ± 1 nm/s) but close to that in geometry $\mathbb{B}$ (451 ± 2 nm/s).

When the experiment was repeated on only the air bubble side (red dashed square in figure 7.1), the general phenomenon can be reproduced. Clusters were formed and fell around the air bubble; however, solvent droplets can be found not only at the edge of cuvette but also in the centre of the image. The falling of cluster created large-scale recirculation that breaks the gel. Averaged over 6 different experiments, for gel β in geometry $\mathbb{C}$, $\tau_o = 206 \pm 9$ min and $v_i = 491 \pm 7$ nm/s.

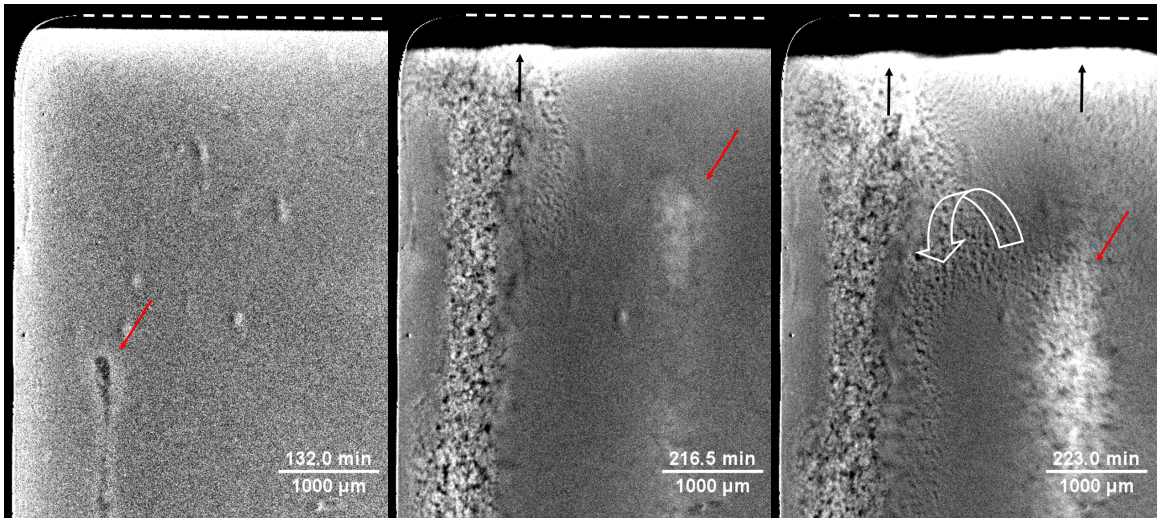

(a) *Solvent droplets (red arrow) are rising along the edge of cuvette.*

(b) *A solvent droplet is rising through the gel bringing debris up to the top.*

(c) *Local recirculation can be found at the top, as indicated by the curved white arrow.*

$\mathbb{C}$

Figure 7.6 *Gel β in geometry $\mathbb{C}$, observed using a $2\times$ objective. Red arrows indicate solvent droplets; black arrows indicate volcanoes at the interface. White dashed lines outline the top of the gel in each image.*

Far from air bubble Figure 7.6 shows images of gel β in geometry $\mathbb{C}$ at the side far away from the air bubble. The images were taken using a $2\times$ objective, as indicated by the magenta dashed square in figure 7.1. The gel at this side also detached from the top at the beginning of the experiment. Figure 7.6(a)

shows the first solvent droplet found in the images. It is about 65 µm in radius which is close to the size of the first droplet shown in figure 7.5(a). Figure 7.6(b) shows the local destruction of the gel caused by the rising solvent droplets. The volcanoes at the gel interface (indicated by black arrows in figure 7.6(b) and (c)) are much brighter than the surrounding. This is because the colloids originally in the image are heavily bleached, and appear darker. The colloids brought up with the solvent have not yet been bleached, hence, appear brighter. For the same reason, the solvent droplets indicated by the red arrows in figure 7.6(b) and (c) are brighter. This result confirms that the solvent droplets bring debris to the top as they rise through the gel. Also, these droplets appear much larger than early ones. Figure 7.6(c) shows the local recirculation as indicated by the curved whiter arrow. It shows that the debris brought up by solvent droplets can accumulate around the volcano craters and fall down through the track left by the droplets. This local collapse is consistent with the observation in geometry $\mathbb{A}$, in which multiple collapses of the denser layer was observed instead of collapsing as big blocks.

The height profile measured close to the edge of the cuvette (farthest away from the air bubble) is plotted as ▼ in figure 7.3. The initial interface speed is 13.6 ± 0.2 nm/s, which is slower than that around the air bubble. The onset time of rapid collapse is $\tau_o = 230$ min. The interface speed of rapid collapse is $v_i = 478 \pm 1$ nm/s.

7.3.1.4 Geometry $\mathbb{D}$

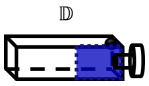

Near air bubble Figure 7.7 shows images of gel β in geometry $\mathbb{D}$ at the air bubble side. The images were taken using a 1× objective, as indicated by the royal blue dashed square in figure 7.1. At $t \approx 6$ min, a solvent droplet can be found at the bottom right corner of the cuvette. The radius of the droplet is about 55 µm. Also, the gel structure collapses around the air bubble. At about $t = 30$ min, a cluster with $R \approx 200$ µm is formed under the air bubble as indicated by the red dashed circle in figure 7.7(a). At $t \approx 70$ min, a cluster with $R \approx 400$ µm is generated at the bottom of the air bubble and falls. Figure 7.7(b) shows that more debris sinks following the big cluster. At $t = 107.5$ min, a larger cluster with $R \approx 800$ µm falls down and creates recirculation, as indicated in figure 7.7(c) by the arrow. This recirculation breaks the structure of the gel and propagates towards the left, figure 7.7(d).

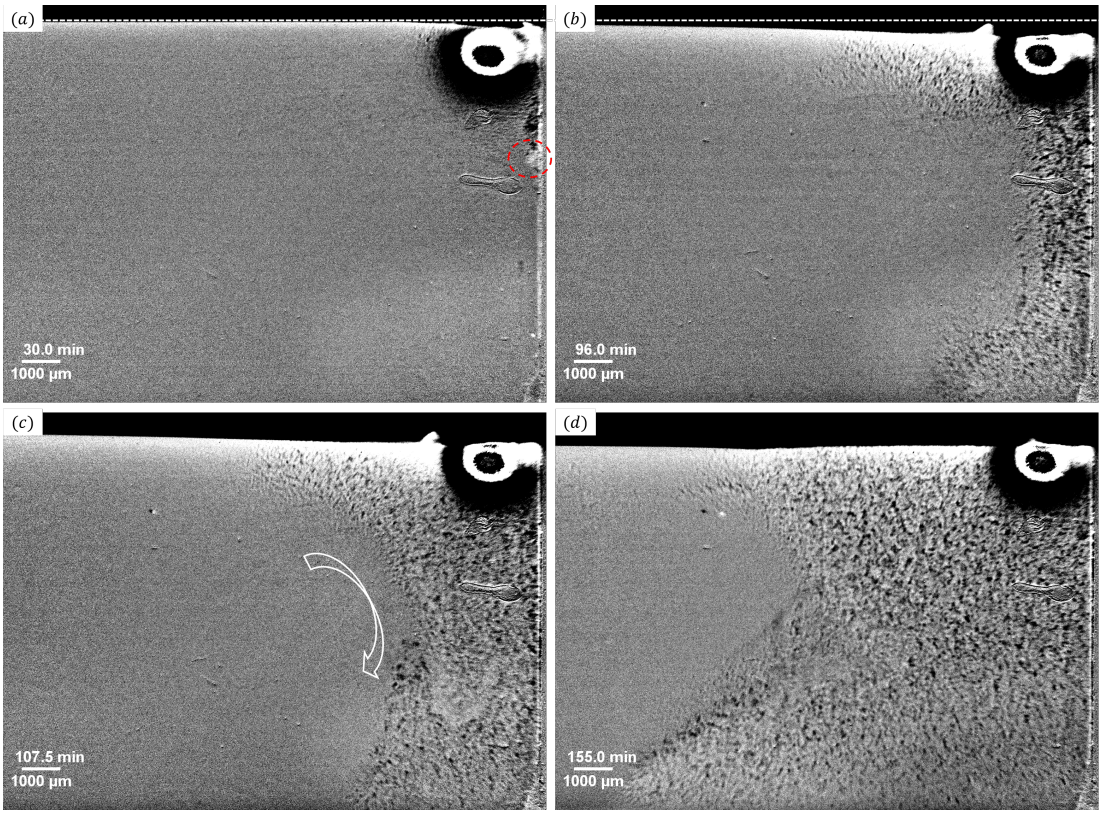

Figure 7.7 *Gel β in geometry $\mathbb{D}$. Images were taken at the air bubble side using a 1× objective. The observation position is indicated by the royal blue dashed square in figure 7.1. The white dotted lines in (a) and (b) indicate the top of the gel, i.e. the inner wall of the cuvette. The red dashed circle in (a) indicates a finger-like cluster. The arrow in (c) indicates the recirculation of the colloids.*

The height profiles measured close to the air bubble and at the other end of the image (as indicated in figure 7.1) are plotted in figures 7.3 and 7.9. From the inset of figure 7.9, the interface speed around the air bubble (◁) suddenly increases from 29 ± 1 nm/s to 86 ± 2 nm/s at about $t = 30$ min. On the left of the image (▷ in figure 7.9), the interface speed accelerates from 10.6 ± 0.9 nm/s to 104.2 ± 0.4 nm/s around $t = 96$ min.

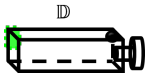

Far from air bubble On the other side of the cuvette, the top of the gel was observed simultaneously using a 2× objective, as indicated by the green dashed square in figure 7.1. The distance between the observation windows of the 1× and the 2× objective is about 24 mm. The height profile measured around the centre of the image is plotted in figures 7.3 and 7.9 as ◆. From the inset of figure 7.9, the interface speed accelerates from 31.5 ± 0.2 nm/s to 205 ± 2 nm/s around $t = 155$ min, i.e. $\tau_o = 155$ at this location. At this time, one solvent droplet could be found rising through the gel, while the surrounding gel structure

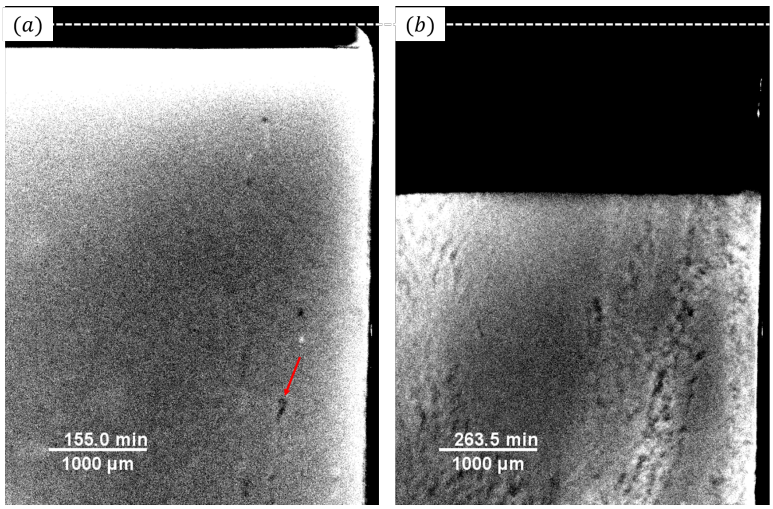

Figure 7.8 *Gel β in geometry $\mathbb{D}$. Images were taken far away from the air bubble using a 2× objective. The observation position is indicated by the green dashed square in figure 7.1.The white dotted lines in (a) and (b) indicate the top of the gel, i.e. the inner wall of the cuvette. The red arrow in (a) indicates a solvent droplet that rising through the gel.*

remained intact, see figure 7.8(a). The settling of the gel accelerates slightly again at about $t = 220$ min. At $t = 263$ min, the large-scale recirculation can be seen in the 2× objective images, figure 7.8(b). Note that, the colloids originally in the 2× objective images were bleached heavily. Hence, the bright colloids in figure 7.8(b) came from outside of the imaging window.

Similar to the definition used for discussing geometry $\mathbb{C}$, here, the time when the settling of the gel abruptly accelerates is considered to be the onset time of rapid collapse τ_o. The height profiles measured from different position clearly show a propagation process of the onset of rapid collapse. From the results shown above, the propagation of the rapid collapse is faster than that of the recirculation. In other words, the acceleration of the settling is not induced by the recirculation that breaks the gel structure. Details about this can be found in Appendix A.6. It is also worth pointing out again that after τ_o, the settling of the gel keeps accelerating, although slightly, before it slows down and starts final compression. This kind of behaviour — abrupt onset followed by slightly speeding up, is different from that found in other geometries.

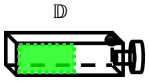

Re-investigating gel β Gel β in geometry $\mathbb{D}$ was re-investigated. The general collapse behaviour as described above can be reproduced. However, in one case, the collapse of the gel shows differences. In this new observation, only the part

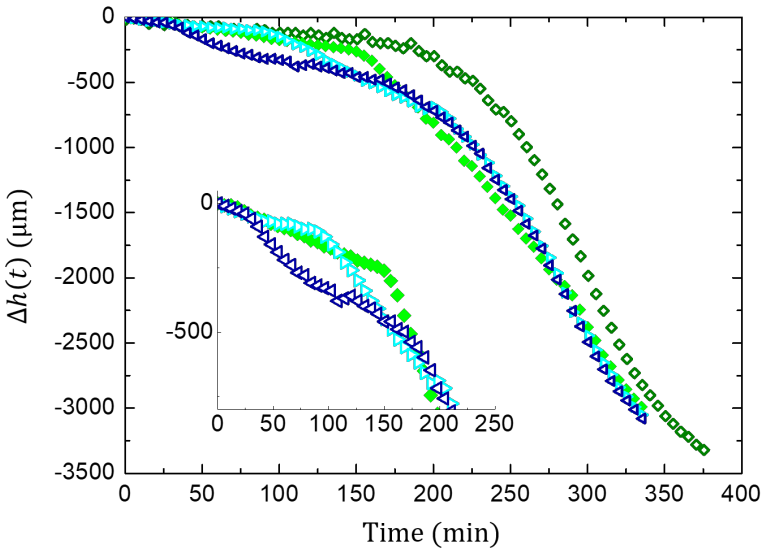

Figure 7.9 *Height profiles of gel β in geometry 𝔻. ◁, ▷ and ◆ are obtained from one set of imaging as indicated in figure 7.1 along with the illustration of the geometries 𝔻. Gel β in geometry 𝔻 was observed again at the part far away from the air bubble (the green dashed square in figure 7.1), however, with a 1× objective. The resulting height profile is plotted as ◇. The inset exposes the detail of the same data of ◁, ▷ and ◆.*

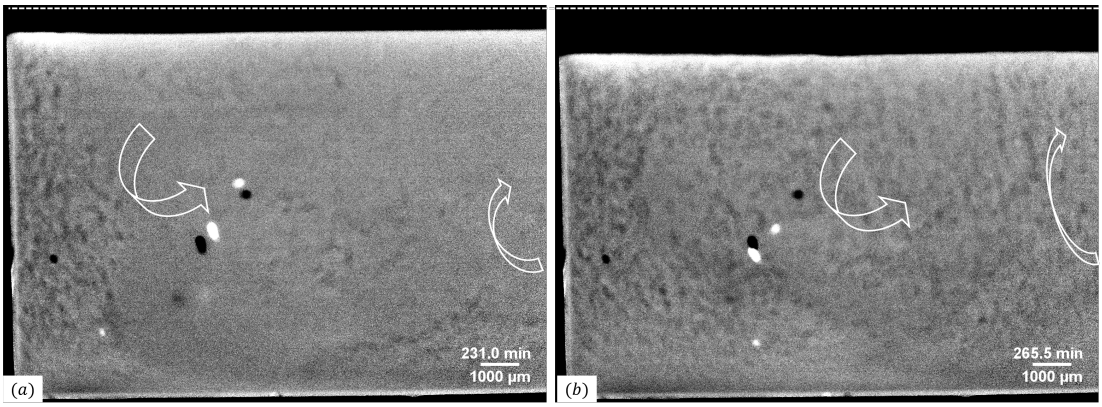

Figure 7.10 *Observe gel β in geometry 𝔻 again. Images were taken far away from the air bubble (the green dashed square in figure 7.1), however, with a 1× objective. The white dotted lines in (a) and (b) indicate the top of the gel, i.e. the inner wall of the cuvette. The white arrows indicate the recirculation in the gel. The large white dots in the images are large PMMA clusters (from synthesis). The black dots are their positions in the $t = 0$ image, which are the results of image processing.*

far away from the air bubble (the green dashed square in figure 7.1) was imaged, however, with a 1× objective. The height profile measured close to the edge of the cuvette is plotted as ◇ in figure 7.9. Compared to the previous result, the onset of rapid collapse in the second experiment appears smoother. Between

$t \approx 180$ min and 250 min, the interface speeded up gradually from 13 ± 1 nm/s to 411 ± 4 nm/s. The onset time of rapid collapse is $\tau_o = 231$ min, which is much longer than the first observation, see figure 7.9. Surprisingly, τ_o of the second experiment is the same as that in geometry $\mathbb{C}$. Also, the rapid collapse behaviour in the second experiment is more similar to that in other geometries. From imaging results, solvent droplets can be found rising close to the edge of cuvette after $t \approx 30$ min. After $t \approx 150$ min, debris can be found falling close to the edge of the gel following the tracks left by the droplets. At about 180 min, the falling of the debris creates large-scale recirculation which propagates from left to right (figure 7.10(a) and (b)). At around 231 min, another recirculation came into the image from the right, figure 7.10(a). Figure 7.10(b) shows the two vortices meet each other. The gel structure is therefore destroyed.

Two observations of gel β in geometry $\mathbb{D}$ described above show the difference in gel collapse. The first result suggests that the onset of rapid collapse is triggered around the air bubble followed by transport to the other end of the sample. The gel does not collapse uniformly. The interface speed accelerates abruptly at τ_o. After τ_o, the settling of the gel accelerates further before it starts the final compression. In the second experiment, the rapid collapse was not only triggered around the air bubble but also at far away from the air bubble. The rapid collapse away from the air bubble is triggered by the debris falling in situ. The interface motion speeds up smoothly around τ_o. The rapid collapse behaves similarly to that in other geometries. However, both results show that, with a flat top, gel β has a longer onset time of rapid collapse.

7.3.2 Mechanism of Rapid Collapse in Geometries

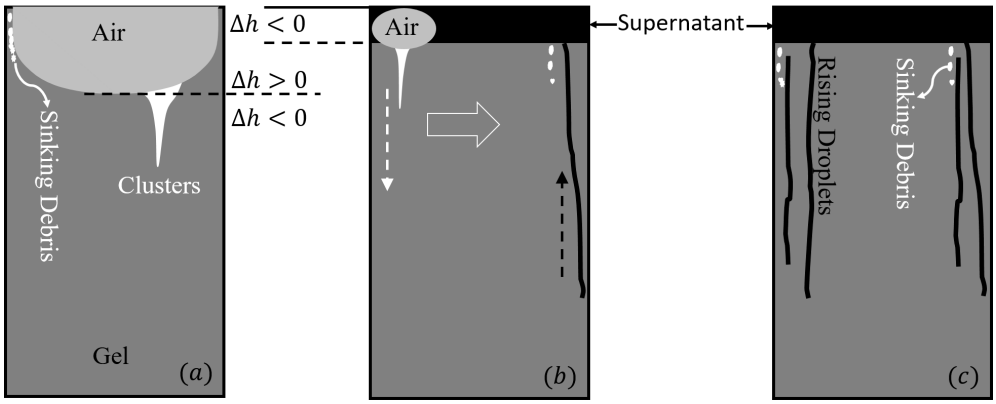

Figure 7.11 *Illustration of the significance of the meniscus in rapid gel collapse.*

Gel β ($\varphi_c = 0.24$, $\varphi_p^{free} = 0.565$ and $c_p = 5$ mg/ml, see figure 6.1) in geometries $\mathbb{A}$, $\mathbb{B}$, $\mathbb{C}$ and $\mathbb{D}$ were studied using microscopic time-lapse imaging. The height profiles of gel β in different geometries are re-plotted in figure 7.12. The schematic illustrations of the geometries are presented in figure 7.12 as insets, which are arranged according to the onset time of rapid collapse τ_o in these geometries. The key observation made from gel β is verified in Appendix A.7 using a gel with $\varphi_c = 0.23$, $\varphi_p^{free} = 0.338$. From the imaging results, the rapid collapse mechanisms can be summarised by some key processes, which are illustrated in figure 7.11 (the same cartoons are used as shown in figure 7.2).

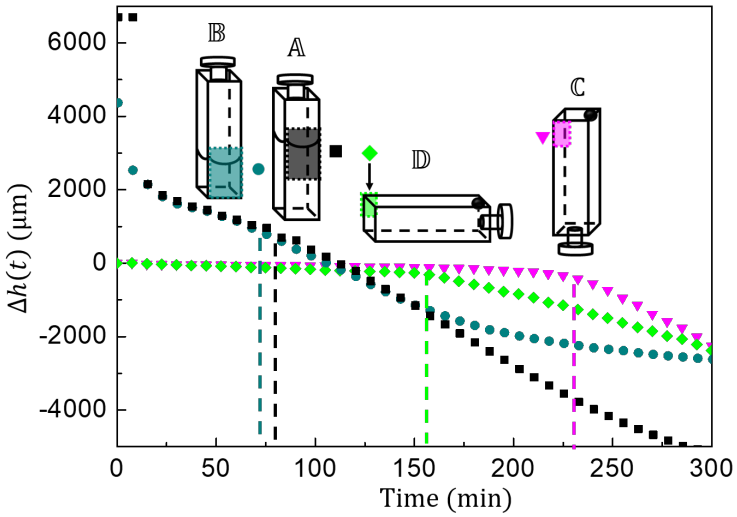

Figure 7.12 *Height profiles of gel β in geometries $\mathbb{A}$, $\mathbb{B}$, $\mathbb{C}$ and $\mathbb{D}$. The dashed lines indicate the onset time of rapid collapse τ_o in each geometry. The insets illustrate the geometries of the sample. The geometries are arranged according to τ_o in these geometries. Legend is given along with the illustration of the geometries.*

The collapse of a sample with a curved meniscus (geometries $\mathbb{A}$ and $\mathbb{B}$) starts at the corner and starts from $t = 0$, ■ and ● in figure 7.12. Debris at the corner of a meniscus accumulates at the top of a gel, forming a denser layer. Finger-like clusters are generated from the denser layer and fall through the gel. The denser layer at the top eventually collapses, creating back flow that destroys the gel structure and triggers the rapid collapse. The key processes are debris falling at the corner and finger-like clusters sinking into the bulk, figure 7.11(a).

For a sample with a nearby air bubble (ellipse, top left in figure 7.11(b)), clusters fall from air bubble while solvent droplets rise alone the edge. However, a front of recirculation from the sinking clusters encroaches on the collapse due to rising

droplets, figure 7.11(b)).

For a sample far away from any curved meniscus, gel detaches from the flat top and collapse slowly during the delay time. The sample shows a longer delay time after which the sedimentation speeds up dramatically, ▼ in figure 7.12. The rising solvent droplets bring debris to the top of a gel. As the droplets rise, they erode the gel structure locally leading to the debris at the top sinks into the bulk. The key process is solvent droplets rising, figure 7.11(c).

The first observation of gel β in geometry $\mathbb{D}$ agrees with the picture of figure 7.11(b)), see Sec. 7.3.1.4. Due to the large width of the sample, the encroaching process of the front from sinking clusters at the air bubble side can be observed clearly. However, in the second observation presented in Sec. 7.3.1.4, the rising droplets that are far away from the air bubble leads to the falling of debris and thus a large-scale recirculation. The collapse due to the sinking clusters (air bubble side) and rising droplets (opposite side) compete with each other. Their fronts meet in the middle of the sample. The latter process was also observed in the gel with $\varphi_c = 0.23$, $\varphi_p^{free} = 0.338$ (Appendix A.7). In geometries $\mathbb{C}$ and $\mathbb{D}$, never observed is the process opposite to figure 7.11(b)), in which the rapid collapse is triggered only at the flat-top side and propagates to the air bubble side. I will discuss this difference in Sec. 8.1.

7.3.3 Postpone a Rapid Collapse

Figure 7.12 shows that the onset time of rapid collapse is postponed in geometries $\mathbb{C}$ and $\mathbb{D}$. In this section, I will discuss the possible causes of this postponement.

For geometries $\mathbb{A}$ and $\mathbb{B}$, the gel collapses with the same mechanism. The onset times of rapid collapse are very close to each other. Compared to the gel in geometries $\mathbb{A}$ and $\mathbb{B}$, in geometry $\mathbb{C}$ the gel is taller and with a top that is mostly flat. In geometry $\mathbb{C}$, gel β also collapse rapidly after a slow settling period. τ_o become about 3 times longer in geometry $\mathbb{C}$. The rapid collapse is postponed.

To speculate the causes of the postponement, the effect of increased height and elimination of meniscus should be considered. L. Starrs *et al.* showed that the increment of sample height leads to either decreased or unchanged delay time [53]. There exists a characteristic stress screening (or transmission) length scale

above which the delay time is saturated [53, 81]. In their cases, the delay time is equivalent to τ_o in this work. Here, by doubling the height of the sample (from geometry $\mathbb{B}$ to $\mathbb{A}$), τ_o increases only by $\sim 14\%$. Compared to the error of τ_o which is about 10%, it suggests that the delay time is almost unchanged when the sample height is greater than 1 cm. It is reasonable to suggest that the tripled τ_o in geometry $\mathbb{C}$ may not come from the increment of the height of the sample. On the other hand, in Chapter 6, the result shows that the extra mass of the denser layer comes mainly from the colloids at the corner of the meniscus. Hence, eliminating the meniscus can retard the mass accumulation at the top of a gel, so that the rapid collapse can be postponed. Therefore, the increase of τ_o in geometry $\mathbb{C}$ can be attributed to the reduction of the area of the meniscus.

Compared to the gel in geometry $\mathbb{B}$, the gel in geometry $\mathbb{D}$ is wider and without meniscus. The sedimentation behaviour of the gel varies between experiments. However, generally speaking, τ_o of the part of a gel with a flat top is longer than that in geometries $\mathbb{A}$ and $\mathbb{B}$. According to the previous study, the increment of the width of a gel leads to either decreased or unchanged delay time [53]. Hence, the increase of τ_o can be attributed to the elimination of meniscus.

Comparing the gel in geometries $\mathbb{C}$ and $\mathbb{D}$, the collapse mechanisms are generally the same. However, the effects on τ_o are different, i.e. in geometry $\mathbb{C}$, the rapid collapse is postponed more significantly. This suggests that the height and width of the sample affect the gel collapse differently. In the direction of height, the gravity is a compressional force; in the direction of width, the gravity acts as shear. More studies are required to understand such differences.

The meniscus effect in small PMMA ($a = 301$ nm) gels has been briefly investigated by S. Meeker [67]. A rapid collapse gel with $\varphi_c = 0.2$ and $c_p^{free} = 7.22$ mg/ml yielded a delay time of ≈ 2 hrs. In a nearly filled cuvette with an air bubble of radius ~ 2 mm, it was reported that no significant change in the delay time can be observed within error. I speculate that this is because the air bubble in their experiment is too large. Also, the time resolution of the experiment is 0.5 hrs, which may be too large for possible meniscus effect to be revealed.

7.4 Slow Collapse Gel

A preliminary study of the meniscus effect in a slow collapse gel was performed using gel δ ($\varphi_c = 0.46$ and $\varphi_p^{free} = 0.382$), in geometries $\mathbb{A}$ and $\mathbb{C}$.

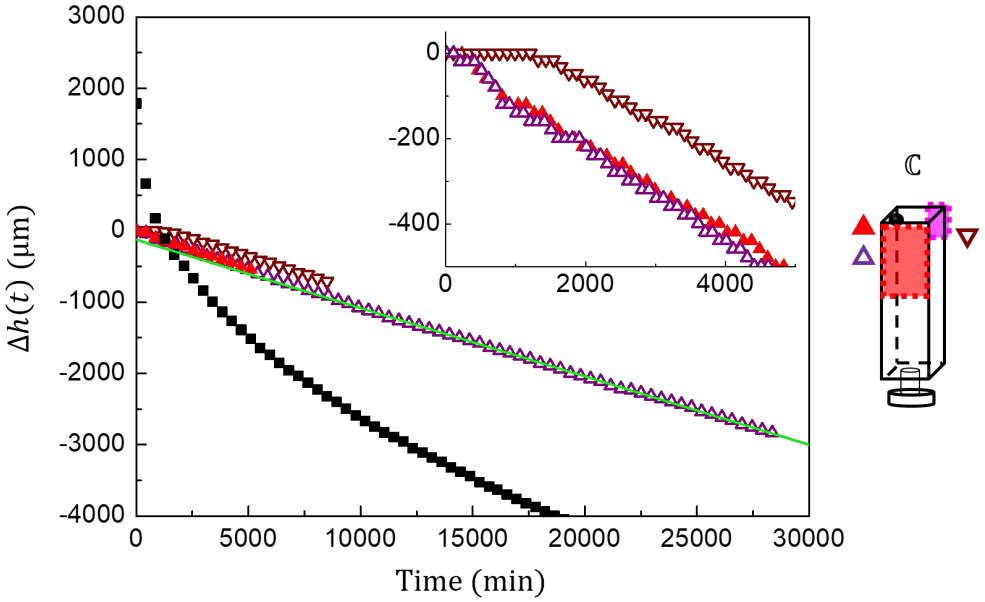

Figure 7.13 *Height profiles of the slow collapse gel δ ($\varphi_c = 0.46$ and $\varphi_p^{free} = 0.382$), in geometries $\mathbb{A}$ and $\mathbb{C}$. In geometry $\mathbb{A}$, the height profile (■) is re-plotted from figure 6.8. In geometry $\mathbb{C}$, the height profile obtained from three observations are plotted with the symbols shown along with the illustration of the geometries. The green line is linear fit to the △ data. The inset exposes the details of the same data to show the initial stage of the collapse in geometry $\mathbb{C}$.*

7.4.1 Geometry $\mathbb{A}$

Imaging results of gel δ in geometry $\mathbb{A}$ was presented in Sec. 6.6, figures 6.8 and 6.9. In summary, the gel δ in geometry $\mathbb{A}$ collapses with a decreasing interface speed. The delay time is $\tau_d = 1092$ min. Solvent droplets can be found rising through the gel. The resulting height profile is re-plotted in figure 7.13.

7.4.2 Geometry $\mathbb{C}$

In geometry $\mathbb{C}$, the air bubble left in the cuvette is about 1.8 mm in radius. Three observations were performed.

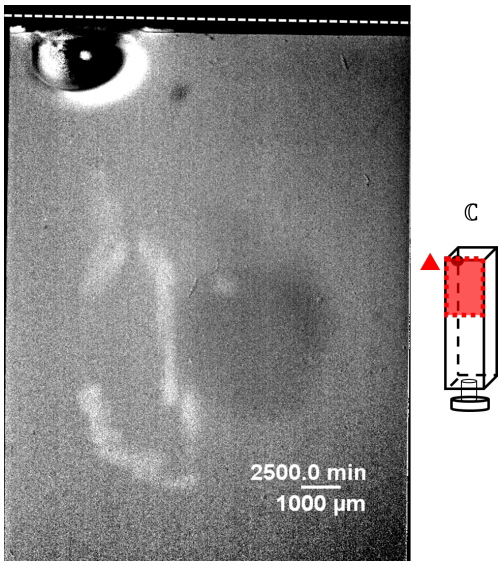

Figure 7.14 *Micrographs of gel δ in geometry ℂ, from the first observation, at the air bubble side; corresponding to ▲ data in figure 7.13. The white dashed line indicates the top of the gel.*

In the first observation, the face with the air bubble was imaged, see the illustration in figure 7.13. The imaging result is shown in figure 7.14. The imaging result shows no solvent droplets in the gel. In figure 7.13, the height profile measured around the air bubble is plotted as ▲. The gel interface detached from the top at about $\tau_d = 300$ min.

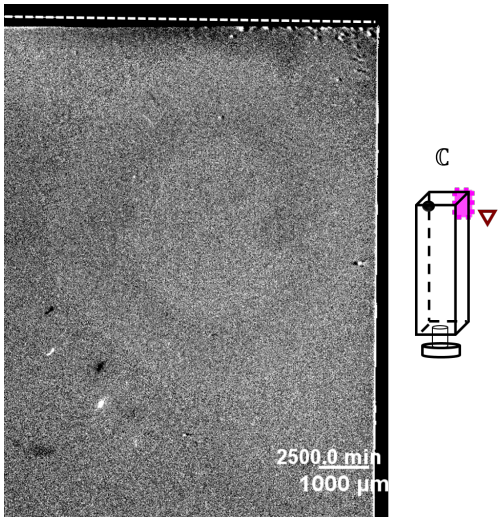

Figure 7.15 *Micrographs of gel δ in geometry ℂ, from the second observation; corresponding to ▽ data in figure 7.13. The white dashed line indicates the top of the gel.*

The second observation imaged the face far from the air bubble (the magenta

dashed square in figure 7.13), however, with a 1× objective. The imaging result is shown in figure 7.15. Also, the imaging result shows no solvent droplet in the gel. The resulting height profile is plotted as ▽. The gel interface detached from the top at about $\tau_d = 1260$ min.

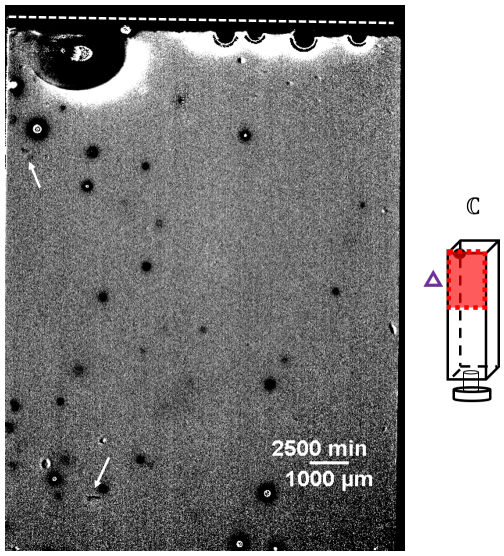

Figure 7.16 *Micrographs of gel δ in geometry ℂ, from the third observation; corresponding to △ data in figure 7.13. The black circles (some with a white dot in the centre) are the air bubbles in the first image. The white dashed line indicates the glass top of the cuvette. The white arrows indicate the solvent droplets in the gel.*

The third observation imaged the face with the air bubble (the red dashed square in figure 7.13). However, the sample was vigorously re-mixed using vortex-mixer for 1 min instead of tumbling on a rotating wheel. Hence, the original air bubble is broken down into many small bubbles. After the sample is mounted, the air bubbles rise through the gel and gradually merge to form a large one at the top. This merging process lasts until about $t = 6500$ min. Interestingly, in this observation, solvent droplets can be found rising through the gel, figure 7.16. This observation provides a hint of the formation of the solvent droplets. I will talk about this later in Sec. 8.2.3.

The resulting height profile is plotted as △ in figure 7.13. The third observation re-produces the first one well, even though the ways of re-mixing the sample are different. The initial interface speed ($t < 10000$ min) is $v_i = 1.749 \pm 0.003$ nm/s. The most striking feature is the constant interface speed at long timescale. At $t > 10000$ min, the interface speed is $v_i = 1.597 \pm 0.001$ nm/s. For comparison,

the single particle sedimentation speed of gel δ is $v_s = 88$ nm/s. On the other hand, the imaging results show no sign of recirculation or denser layer falling in the gel. This is clearly different from the behaviour of a rapid collapse gel.

7.4.3 Meniscus Effect in Slow Collapse Gel

A preliminary study on the meniscus effect in slow collapse gels has been reported above. Gel δ (see figure 6.1, $\varphi_c = 0.46$ and $\varphi_p^{free} = 0.382$)) in geometries $\mathbb{A}$ and $\mathbb{C}$ were studied.

In geometry $\mathbb{A}$, the collapse of the gel initiates from the corner of the meniscus. Similarly, in geometry $\mathbb{C}$, the gel interface around the air bubble detached from the top much earlier than that at the opposite side. This suggests again that colloids tend to start collapsing around the vertical part of an air-gel interface. Compared to the height profile in $\mathbb{A}$, reducing the area of the meniscus does not lead to longer delay time, figure 7.13. However, in geometry $\mathbb{C}$, a slow collapse gel collapses even slower. The interface speed is much slower than the single particle sediment speed. Hence, eliminating the vertical air-gel interface also postpones slow gel collapse.

The striking feature of the collapse in geometry $\mathbb{C}$ is the constant interface speed after 10000 min. To speculate the mechanism behind this observation, a gel can be modelled as a poroelastic material. In the initial stage of the collapse, as the gel network deforms, the back flow of the solvent through the network limits the rate of deformation of the gel [49, 51, 54]. By Darcy's law, the solvent flows at a velocity v within the porous gel network, leading to a local displacement of the solid of $w(z,t)$ in the z (gravitational) direction, giving:

$$-\frac{\partial P}{\partial z} = \frac{\eta_s(1-\varphi_c)}{k}(v - \frac{\partial w}{\partial t}) \ , \tag{7.1}$$

where P is the pore pressure, η_s is the viscosity of fluid and is the viscosity of the PS solution here, k is the permeability of gel. k is commonly estimated using Kozeny-Carman equation [51, 67, 82], giving

$$k = \frac{(1-\varphi_c)^3 a^2}{45\varphi_c} \ . \tag{7.2}$$

Continuity demands:

$$(1-\varphi_c)v = -\varphi_c \frac{\partial w}{\partial t} \ . \tag{7.3}$$

Therefore,

$$\frac{\partial w}{\partial t} = \frac{k}{\eta_s}\frac{\partial P}{\partial z} = \frac{(1-\varphi_c)^3 a^2}{45\varphi_c \eta_s}\frac{\partial P}{\partial z} \ . \tag{7.4}$$

Initially, the gel is not compressed and elastic stress is negligible so that $\frac{\partial P}{\partial z} = \Delta\rho g \varphi_c$. For gel δ, $\varphi_c = 0.46$, $\eta_s = 0.0065 \pm 0.0001$ Pa $\cdot$ s, giving the initial interface speed $\frac{\partial w}{\partial t} = 1.4$ nm/s. The measured initial interface speed $v_i = 1.749 \pm 0.003$ nm/s is close to the value that is evaluated by Darcy's Law. At long time-scales (after 10000 min), the interface speed $v_i = 1.597 \pm 0.001$ nm/s is also very close to $\frac{\partial w}{\partial t}$. This is even more striking. At this time-scale, the gel network is compressed so that the elastic stress is non-zero and the colloidal volume fraction is increased. This leads to an increased $\frac{\partial P}{\partial z}$. On the other hand, the increasing φ_c may lead to a decreasing permeability k, which is reasonable. Therefore, that the long-time interface speed is of the same order of magnitude as $\frac{\partial w}{\partial t}$ is not too surprising. However, the constant $\frac{\partial w}{\partial t}$ implies that $k\frac{\partial P}{\partial z}$ is a constant. This unexpected result needs to be verified with more observations. Its mechanism is unclear.

7.5 Conclusion

In this chapter, I report case studies of rapid collapse gels and a slow collapse gel with different geometries. The imaging results show that:

1. A rapid collapse gel with a reduced meniscus has a longer delay time. The postponement of the delayed collapse can be attributed to the removal of most of the meniscus. More specifically, it can be attributed to the reduction of the vertical area of an air-gel interface. This is because the extra mass of the denser layer at the top of a gel comes mainly from the corner of the meniscus. By reducing the area of the meniscus, the accumulation of mass in the denser layer can be retarded. Hence, the denser layer needs a longer time to form and trigger the rapid collapse. Hence, eliminating the meniscus is a possible way to postpone the rapid gel collapse.

2. For a rapid collapse gel with a small air bubble, a front of recirculation from the settling clusters encroaches on the collapse due to the rising droplets. This large-scale recirculation can be seen more clearly in a wide geometry, as the

recirculation propagates from the air bubble side to the opposite side. This result highlights the effect of hydrodynamics in the gel collapse.

3. For a slow collapse gel, reducing the area of the meniscus does not yield a longer delay time; however, it leads to a much slower and constant interface speed. Such interface speed is very close to the initial speed that is predicted by Darcy's law. However, the mechanism of the constant interface speed observed in the slow collapse gel with reduced meniscus is not clear.

4. The collapse of a gel can be initiated at the vertical part of an air-gel interface, i.e. the corner of a meniscus or around an air bubble. Why is the collapse of a gel more likely to be triggered at the vertical part of an air-gel interface? I will discuss this in Sec. 8.1.

Chapter 8

The Key Features of the Onset of Collapse

In Chapters 6 and 7, I have reported that the collapse of a gel is more likely to be initiated at the vertical part of an air-gel interface. This leads to mass accumulation at the bottom of the air-gel interface. The extra mass of the denser layer comes from two sources: the colloids at the vertical part of the air-gel interface and the debris brought to the top by the solvent droplets. Together with the previous studies highlighted in Sec. 2.4, the imaging result in Chapters 6 and 7 reveals details of the denser layer falling. The other key process during the collapse of a gel is that solvent is expelled from the gel. The imaging result shows that solvent is expelled in the form of droplets at the onset of collapse. The tracks created by the rising droplets allow the solvent to be released from the gel more easily. The collapse mechanism is a result of the interplay of the falling of the denser layer (or finger-like clusters) and the rising of solvent droplets as shown in Chapter 6. In this chapter, I will discuss these two key processes on the basis of more detailed observations.

In Sec. 8.1, I will discuss why the collapse of gel initiates from the corner of the meniscus. Then, I will treat a preliminary test of the yielding scenario of the denser layer, which suggests that the denser layer accumulates more mass than it needs to force a gel to yield. In Sec. 8.2, I will discuss the general formation mechanism of the solvent droplets. Since volcanic eruptions can be found as solvent droplets reach the gel interface, I will report a preliminary study of the spatial distribution of volcanoes aiming to probe the forming location of the solvent droplets. Then, I will report an observation that rising air bubbles in

the gel can generate solvent droplets. Finally, I will propose a general formation mechanism.

8.1 Denser Layer

In Sec. 8.1.1, I will discuss the formation of the denser layer. I will talk about why the collapse of a gel initiates from the corner of a meniscus or around an air bubble. The hypothesis is that a gel needs a surface to hold onto. Then, in Sec. 8.1.2, I will discuss the collapse of the denser layer which can be in the form of finger-like clusters or large blocks. I will show that the denser layer accumulates more mass than it is required to overcome the yield stress of a gel. I suspect that the friction between colloids and the wall may partially support the weight of the denser layer, explaining this result. Understanding the formation and collapse of the denser layer provides suggestions to prolong the delay time even further.

8.1.1 Formation of Denser Layer

To investigate the formation of the denser layer, the initial stage of the collapse around the meniscus was imaged using a 1 × objective. Figure 8.1 presents gel α ($\varphi_c = 0.19$, $\varphi_p^{free} = 0.557$, see figure 6.1) in geometry $\mathbb{A}$. Figures 8.1(a) and (b) show colloids fall down soon after the gel is mounted at three locations: (1) on the glass wall (in the centre of the images); (2) at the corner of the meniscus (at both side of the images and figure 8.1(c)) and (3) between two red dashed lines.

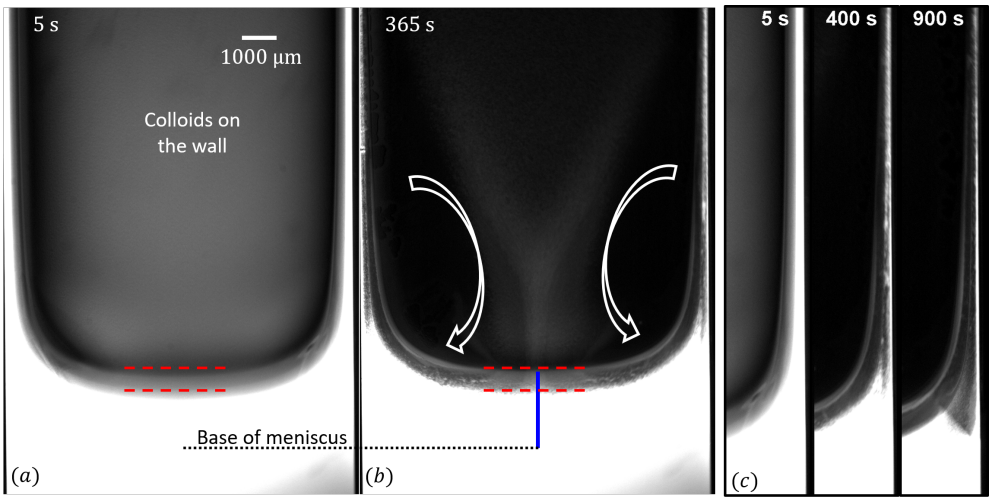

Figure 8.1 *(a) and (b) Micrographs of gel α. (c) Zoom into the corner of the meniscus. The base of the meniscus is indicated, which can be seen after the gel collapses. The blue line in (b) indicates the cross section corresponding to sketch figure 8.2(b) and the blue curve in figure 8.3.*

(1) The falling colloids on the wall is inevitable since the sample was half-filled. These colloids contribute to the denser layer formation in two ways. One is the additional mass at the top, the other is the shear-induced compaction of clusters resulted from the recirculation [83].

(2) Why does the collapse of a gel start at the corner of a meniscus? To understand this, let us consider a colloid at the meniscus. A PMMA colloid 'floats' at the meniscus as shown by the x-ray micrographs instead of being adsorbed on the meniscus [84]. Hence, a colloid is pressed towards the meniscus by a depletion force $F_{\rm d}$ as shown schematically in figure 8.2(a). The depletion potential between one colloid of radius a and a surface is

$$U(r) = -k_{\rm B}T\varphi_{\rm p}^{\rm free}\frac{1}{8R_{\rm g}^3}(4a + 2R_{\rm g} + 2r)(a + 2R_{\rm g} - r)^2 \ . \tag{8.1}$$

Hence, the depletion force between a colloid and a surface is

$$F_{\rm d} = \frac{dU(r)}{dr}\Big|_{r=a} = k_{\rm B}T\varphi_{\rm p}^{\rm free}\frac{3a}{R_{\rm g}^2} \ , \tag{8.2}$$

which is in the normal direction and is twice the inter-particle depletion force ($F_{\rm b}$), i.e. $F_{\rm d} = 2F_{\rm b}$. Compared to the buoyancy force of a single colloid,

$$F_{\rm d}/G = \frac{9k_{\rm B}T\varphi_{\rm p}^{\rm free}}{4\Delta\rho g\pi a^2 R_{\rm g}^2} \ . \tag{8.3}$$

For gel α, $F_{\rm d}/G \approx 240$. It suggests that a single colloid is kept at the meniscus. In the bulk, the weakest point in a gel branch has only a single bond, see the colloid (black circle) in figure 8.2(a). Such a colloid experiences a maximum upward force of $F_{\rm b}$. At a meniscus, the component of $F_{\rm d}$ in vertical direction ($F_{\rm d}^{\parallel}$) counteracts the buoyancy force of the colloid G. At the bottom of a meniscus, where θ (the angle between $F_{\rm d}$ and the vertical direction) is close to 0, $F_{\rm d}^{\parallel} \approx F_{\rm d} = 2F_{\rm b} \gg G$. However, $F_{\rm d}^{\parallel}$ decreases with increasing θ as a colloid approaches the corner of the meniscus. We can measure the maximum θ from figure 8.1 giving $\theta_{\rm max} \approx 89°$. Hence, at the vertical part of the meniscus, one finds $F_{\rm d}^{\parallel} = F_{\rm d}\cos(\theta) = 0.0175F_{\rm d} = 0.035F_{\rm b} \ll F_{\rm b}$. Also, compared to the frictional glass wall, at the vertical part of the frictionless meniscus, the colloids are more unstable.

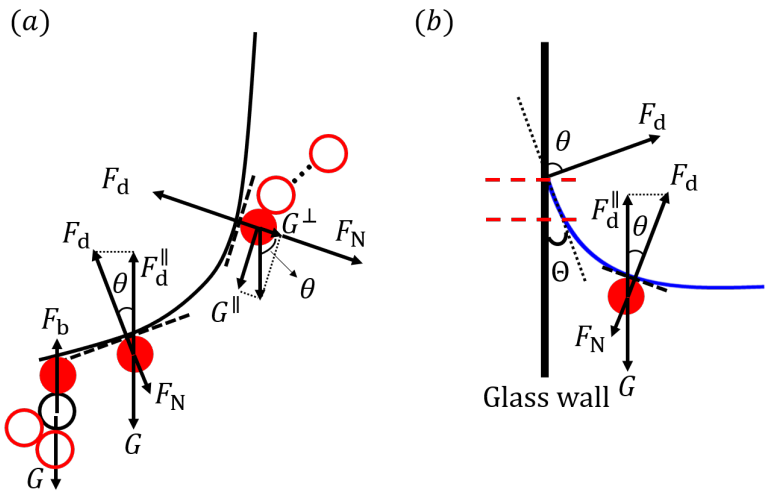

Figure 8.2 *Mechanism of the falling of colloids from the vertical part of a meniscus. The colloids (red sphere) are pressed onto the interface (black curve) by depletion forces (F_d). The gel structure is anchored to the interface through these colloids. Sketch (a) illustrates the colloids at the corner of a meniscus, see text. The black line is on the meniscus as indicated by the black curve in figure 8.3. Sketch (b) shows the cross section at the bottom of the contact line as indicated in figure 8.1 by the blue line (into the page) and in figure 8.3 as the blue curve. Red dashed lines correspond to those in figures 8.1 and 8.3. Θ is the contact angle of the gel. More description of the shape of the meniscus can be found in Appendix A.1.*

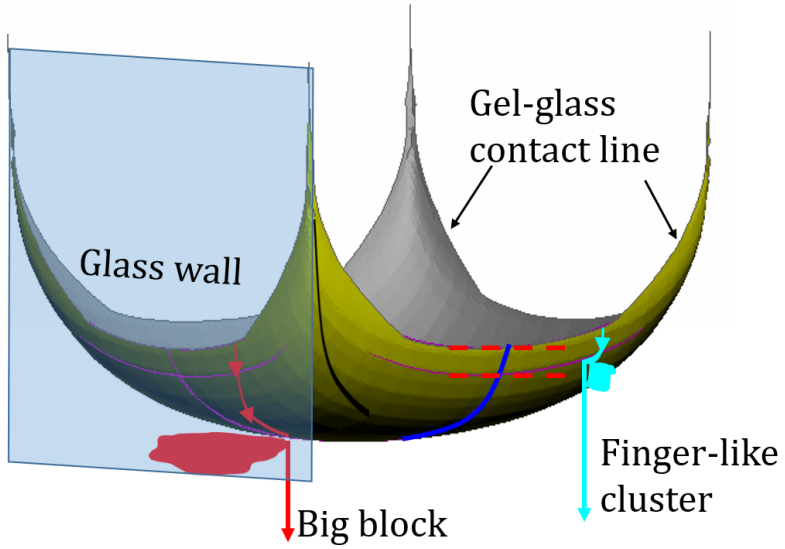

Figure 8.3 *A 3D schematic of a meniscus. Cyan trajectory: With low φ_c (regimes D1 and D2 in figure 6.1), the yield stress of a gel is low so that a cluster accumulates less mass before it can break the gel and fall as a finger-like cluster. Red trajectory: For greater φ_c (regimes D3), the yield stress is higher so that more mass is needed for a cluster to force the gel to yield. Therefore, it collapses as a big block. The black and blue curves correspond with those in figure 8.2(a) and (b), respectively. Red dashed lines correspond to those in figures 8.1 and 8.2(b).*

We notice that F_b is the maximum upward force experienced by the colloid at the weakest point rather than the averaged value (the minimum vertical component could be $\sim$ 0 N). Therefore, one can determine the range of the critical angle θ_crit above which the gel is unstable compared to the bulk. First, when $\theta > 60°$, $F_\mathrm{d}^{\parallel} < F_\mathrm{b}$. Hence, 60° is the lower limit of the range. To estimate the upper limit, let us consider the colloids between the red dashed lines in figure 8.1.

(3) For colloids between the red dashed lines in figure 8.1, let us look at the cross section at the blue line in figure 8.1(b) that intersects the meniscus into the page. This cross section is sketched in figure 8.2(b) and indicated in figure 8.3 as blue curve. Consider that the contact angle of the gel $\Theta \approx 20°$ (see Appendix A.1), the maximum θ, in this case, reaches $90° - \Theta = 70°$. Imaging results show that colloids between the red dashed lines collapse right after the gel was mounted. This suggests that θ_crit should be less than 70°. Therefore, I estimate that $60° < \theta_\mathrm{crit} < 70°$.

Generally, in terms of the stability under gravity, colloids at the bottom of a meniscus > in the bulk > at the vertical part of a meniscus where $\theta > \theta_\mathrm{crit}$. I suggest this is why a gel starts collapsing from the corner.

Figure 8.2(a) also shows how colloids collapse at the corner. The gel network is anchored to a meniscus through the colloids at the meniscus. F_d is balanced by normal component of the buoyancy force ($G^{\perp}$) and a normal force F_N. The tangent component of the buoyancy force ($G^{\parallel}$) is unbalanced and increases as the colloid approaches the vertical part of the meniscus. Therefore, these colloids are moved downwards along the meniscus. As they slide, the surrounding particles (red circles) are dragged downwards due to the inter-particle attraction or hydrodynamic interaction.

Similarly, one can understand why a gel starts collapsing around an air bubble in geometries $\mathbb{C}$ and $\mathbb{D}$. Due to the geometry of the air bubble, the unbalanced $G^{\parallel}$ is pointing downwards. Therefore, the gel between an air bubble and the top glass (blue area in figure 8.2(b)) are more unstable under gravity.

In this force balance hypothesis, the gel is assumed to be fully matured. However, from the linear viscoelastic measurement (see figure B.1), the timescale for a gel to mature can be up to 10 min. Therefore, this hypothesis is not applicable to the

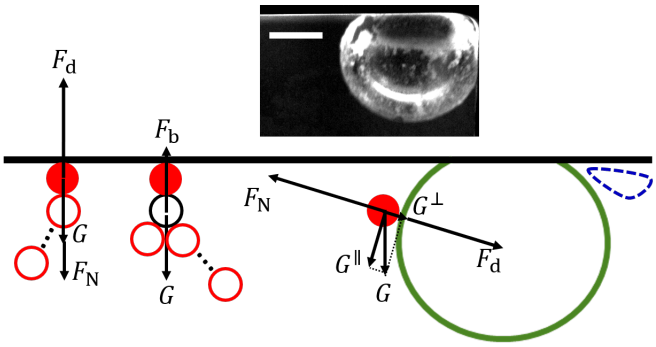

Figure 8.4 *Mechanism of the falling of colloids around an air bubble. Between an air bubble and the top glass, a colloid as shown experiences a downward-pointing $G^\parallel$. Therefore, compared to that at the top glass and in the bulk, the gel in the vicinity (as indicated by the blue dashed area) is more unstable.*

very beginning ($\lesssim 2$ min, before which $G' < G''$) of the collapse during which the Brownian motion and residual shear from re-mixing should be more important.

The gel shown in figure 8.1 has an air-gel interface whose centre of curvature is above the gel. If this centre is below a gel, based on this force balance hypothesis, one may expect the gel collapse sideways, as illustrated in figure 8.5(a). It is because the colloids at the air-gel interface slide aside along the interface, see figure 8.5(b).

Therefore, a cone geometry was designed to preliminarily test the force balance hypothesis, as presented in figure 8.5(c). A 10 µl graduated pipette tip (Star Lab) was filled with ultraviolet cured glue (Norland optical adhesive 65) so that the gel sample can be loaded on top. In this geometry, the gel forms a spherical cap, as demonstrated by the side-view micrograph in figure 8.5(d). To minimize the evaporation and hence the coffee-ring effect, the geometry is contained in an upside down cuvette whose bottom was replaced by a cover slice. Also, a paper soaked with gel was placed in the cuvette 10 min before loading the gel onto the cone. Figure 8.5(e) schematically shows the dimension of the geometry. The diameter of the bottom plane of the spherical cap is about 6.5 mm. The height of the spherical cap is 1728 ± 1 µm. Below the top of the pipette tip, there is about 1 mm thick of sample which cannot be observed.

The side-view micrographs of gel β ($\varphi_c = 0.24$, $\varphi_p^{free} = 0.565$, see figure 6.1) were taken by a 1 × objective. The sample was constantly illuminated so that the colloids in the front can be heavily bleached. Micrograph at 691.0 min shows that the air-gel interface can still be observed using fluorescent microscope after

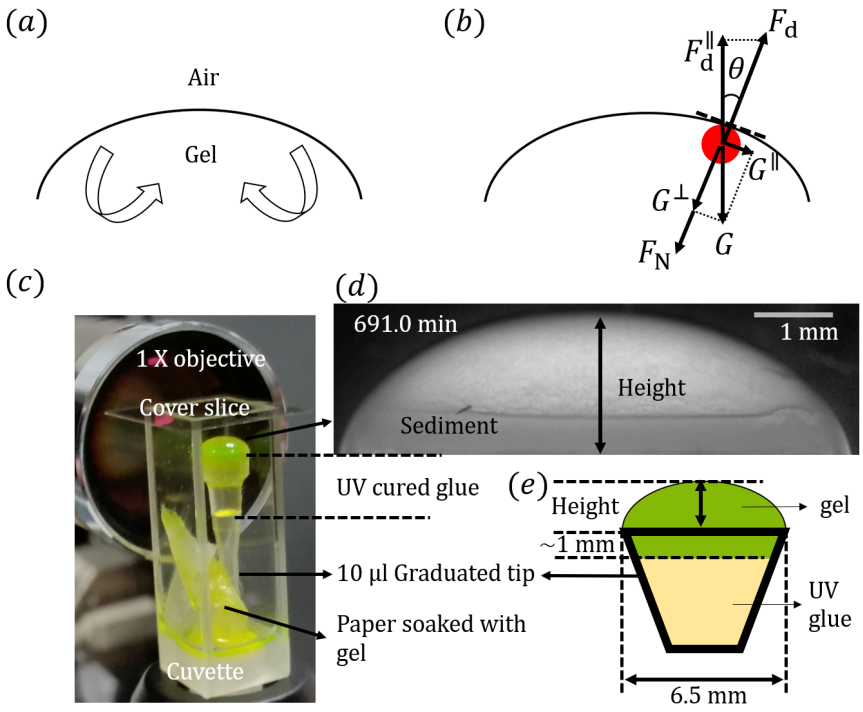

Figure 8.5 *If the centre of curvature of the air-gel interface is below the gel, the initial collapse is expected to be sideways which leads to a back flow in the centre as indicated by the arrows in (a). This is a result of colloids sliding to one side at the beginning of the collapse, see (b). To test this hypothesis, a cone geometry was designed. An images of the geometry is shown in (c). A sideways image of the gel β taken using a 1 × objective is shown in (d). The dimension of the geometry is shown in (e).*

the gel is collapsed. It suggests that some colloids were still attached to the interface. This is consistent with the result of a gel in a cuvette where colloids can be found at the meniscus after the gel is settled, see figure 6.3(l). This is also expected from the hypothesis. The height of the gel decreased by $\sim 7\%$ in 800 min. I suggest the evaporation is negligible for an experiment less than 200 min.

The top view of gel β was imaged by a 2 × objective. Figure 8.6(a) presents the micrograph at $t = 10.0$ min. The black circle indicates the bottom plane of the spherical cap, showing the location of the observation. The gel at the zenith of the spherical cap fell into the focus plane (pointing into the page) at about $t = 10.0$ min. It suggests that the gel detached from the air-gel interface, which is confirmed by a closer observation with a 20× objective (Nikon Plan Fluor ELWD, NA=0.45). It is also consistent with the observation of gel β with a flat glass top, see figure 7.3. The displacement field of clusters is measured using

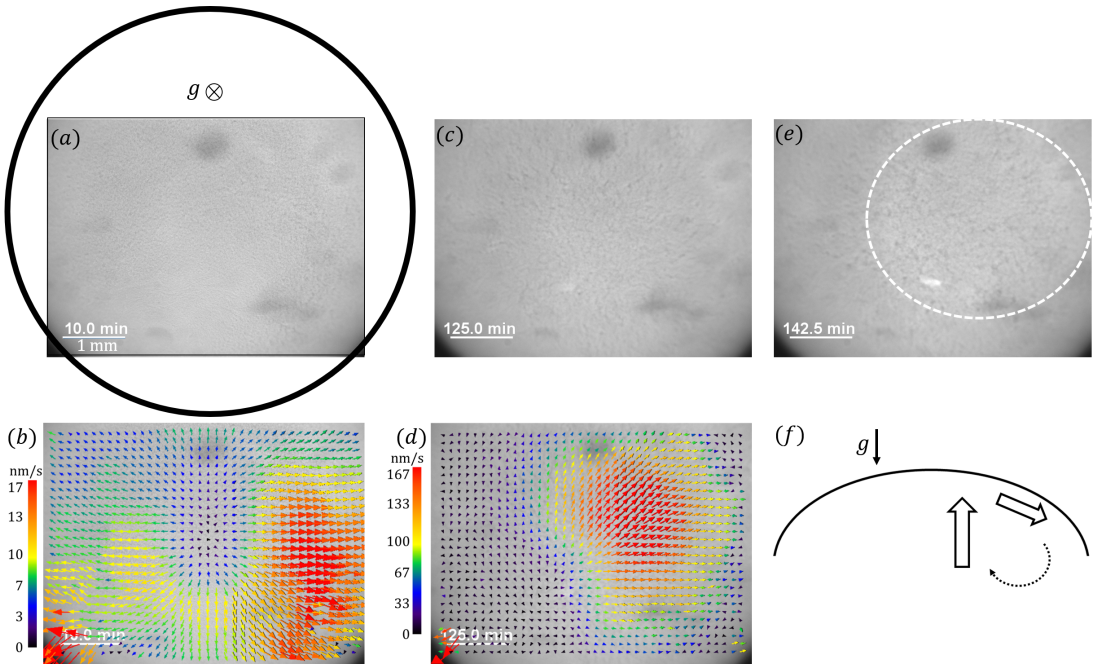

Figure 8.6 *Top view of gel β in cone geometry, imaged by a 2 × objective. (a) Micrograph at t = 10.0 min. (b) Motion of the clusters averaged between t= 10.0 and 20.0 min. (c) Micrograph at t = 125.0 min. (d) Motion of the clusters averaged between t=125.0 and 125.5 min. (e) Micrograph at t = 133.0 min showing colloids are brought by recirculation in the middle of the sample, as indicated by the white dashed circles. (f) A side view schematic showing the collapse mechanism inferred from the top-view results.*

particle image velocimetry (PIV) between 10.0 and 20.0 min [85]. The resulting velocity vector field is overlaid onto the original micrograph and presented in figure 8.6(b). Although the absolute value of the velocity is subjected to the spherical aberration due to the curvature of the air-gel interface, the direction is informative. Figure 8.6(b) shows that the gel collapses aside. Also, in the region with higher speed, volcanoes can be found after $t = 16.0$ min. At $t = 125.0$ min, a strong flow can be found in the centre of the image, see figure 8.6(c). Figure 8.6(d) presents the PIV result at $t = 125.0$ min showing that the speed is one order of magnitude higher than that at $t = 10.0$ min. Colloids brought by the up-streaming recirculation (pointing out from the page) can be found in figure 8.6(e). After the recirculation, the gel interface quickly fell out of the focus plane. The collapse mechanism of the gel in a cone geometry can be inferred from the top-view imaging results as shown in figure 8.6(f). The gel collapses aside so that the avalanche of colloids creates a back flow in the centre of the gel.

In the cone geometry, the droplet was pinned on the pipette tip. This setup is reminiscent of a drying droplet with a pinned contact line, which exhibits coffee-

ring effect [86] and Marangoni effect [87]. However, it has been demonstrated that this setup yields a slow evaporation rate in an experiment over 800 min. It is reasonable to neglect the evaporation and hence the coffee-ring effect. On the other hand, if there were a difference in surface temperature between the centre and the edge of the gel, the Marangoni effect would lead to a vortex at the surface bringing colloids back to the centre of the surface [87]. However, there was no such temperature difference and the surface showed no vortex in both top and side view results. Hence, Marangoni effect is also negligible in the cone geometry. Furthermore, a recent study showed that the coffee-ring effect in colloid + polymer gel is suppressed when the colloids are small ($\lesssim 1$ µm); however, enhanced when they are large ($\gtrsim 5$ µm) [88]. First, these results reassure that the coffee-ring effect in our case is negligible. Second, we see from Eq. 8.3 that $F_\mathrm{d}/G \sim a^{-2}$ which suggests the buoyancy force becomes more important for colloids at the surface as their size increases. Hence, the force balance hypothesis may provide a new perspective in the enhancement of coffee-ring effect for large particle colloidal gels.

Generally, the collapse of a gel in a cone geometry supports the force balance hypothesis.

8.1.2 Collapse of Denser Layer

Previous studies suggested that collapse of the denser layer is a yielding event [29, 51, 53]. In Chapter 6, I showed that the denser layer of a gel in regime D collapses in the forms of finger-like clusters (figure 6.3) or big blocks (figure 6.15(c) and (d)). Following the force balance hypothesis proposed in figure 8.2, one can understand the collapse of a denser layer.

Figure 8.3 shows a meniscus in 3D schematically. The cyan trajectory shows a possible route of a cluster at the meniscus. As the cluster moves downwards, it accumulates mass. Once it is heavy enough, it forces the gel to yield and falls through. At low φ_c (regimes D1 and D2 in figure 6.1), the yield stress is relatively low. Therefore, a cluster needs less mass to break the gel so that it collapses as a finger-like cluster from high above the base of the meniscus and close to the glass wall. For greater φ_c (regime D3 in figure 6.1), the yield stress is higher so that a cluster needs to accumulate more mass to force the gel to yield. The red trajectory in figure 8.3 shows a possible route that such a cluster takes to become part of a big block, which eventually collapses the gel. With even higher

φ_c (regime B in figure 6.1), the clusters that form the denser layer cannot force the gel to yield.

The interpretation presented above appears to agree with the yielding scenario. The yield stress increases with φ_c. Therefore, the mass that a gel can support at its top increases with φ_c. Here, I report a preliminary test of this scenario by comparing the stress exerted by part of the denser layer with the yield stress of the gel. I will show that the denser layer accumulates more mass than it needs to force a gel to yield.

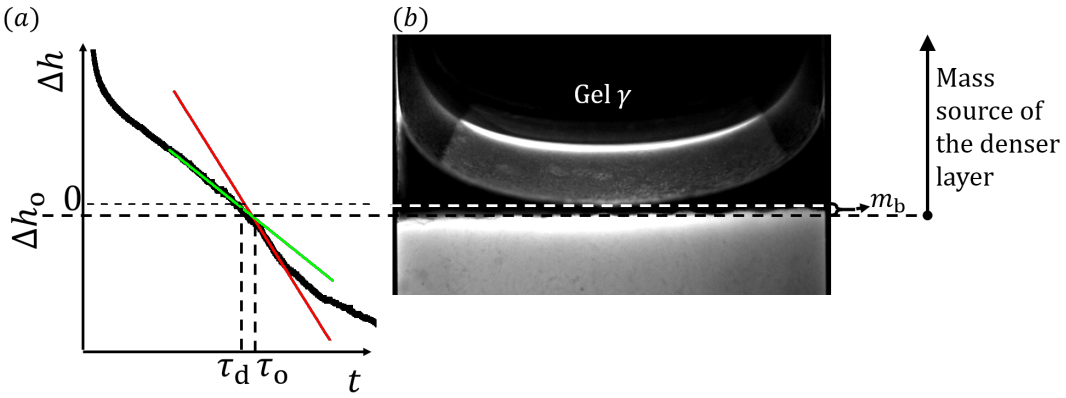

Figure 8.7 *The onset of the rapid collapse is defined as the time when the collapse enters the linear region. The dashed lines show the position of the gel interface at the onset time of the rapid collapse and the base of the meniscus, respectively. Also shown here is an image illustrating the origin of the mass of the denser layer of gel γ. For gel γ, only m_b, the mass between the base of the meniscus and the gel interface at the onset of rapid collapse, is measurable from the imaging results.*

The inset of figure 6.2 is re-plotted in figure 8.7(a). Corresponding to the onset time of rapid collapse τ_o, the onset height of rapid collapse Δh_o can be determined. Take gel γ ($\varphi_c = 0.34$ and $\varphi_p^{free} = 0.586$) as an example, at τ_o, the colloids that were originally above the gel interface are the mass source of the denser layer, as shown in figure 8.7(b). Due to the geometry of the meniscus, estimating the mass of the entire denser layer is not possible using the imaging result. Here, I estimate only part of it, i.e. the layer between the base of the meniscus and the gel interface m_b.

$$m_b = \Delta\rho|\Delta h_o|A\varphi_c \ , \tag{8.4}$$

where $A = 10 \times 10$ mm^2 is the area of the cross section of the cuvette. Hence, the

gravitational stress due to the mass of m_b is $\sigma_\mathrm{b} = \Delta\rho g|\Delta h_\mathrm{o}|\varphi_\mathrm{c} = 0.11$ Pa, where $\Delta h_\mathrm{o} = -120$ µm and $\varphi_\mathrm{c} = 0.34$.

Then, we compare this stress with the yield stress of the gel. The rheology of gel γ was studied using TA-DHR with 40 mm rough plane geometry and reported in Appendix B. The yield stress of gel γ is measured to be $\sigma_\mathrm{y} \approx 0.053$ Pa. We find that, for gel γ, σ_b is higher than σ_y. Note that, m_b is only a part of the mass of the denser layer. Therefore, the denser layer accumulates more mass than it needs to force a gel to yield.

As a remark, let us review the published data in Ref. [29]. In figure 9 of Ref. [29], a rapid collapse gel with $h_0 = 14$ mm shows a denser layer of thickness $L_\mathrm{d} \approx 0.15h_0 = 2.1$ mm. The average colloidal volume fraction of the denser layer φ_d is about 0.175, which is $\sim 1.1\varphi_\mathrm{c}$ (similar to the result reported in Ref. [53]). The density difference is $\Delta\rho = 0.253$ mg/ml. Hence, the stress exerted by the denser layer $\sigma_\mathrm{d} = m_\mathrm{d}g/A = \Delta\rho g L_\mathrm{d}\varphi_\mathrm{d} \approx 1$ Pa. σ_d is two orders of magnitude higher than the yield stress of this gel (20 mPa). Hence, in a small PMMA gel, the denser layer also accumulates more mass than it needs to force a gel to yield.

I will now speculate on the reasons behind this phenomenon, and I will argue that, apart from the yield stress of the gel, two factors can also support the denser layer:

(1) The first factor is the friction between the colloids and glass wall. Gravity induces not only compressive stresses in the bulk of a gel, but also shear stresses near adhesive vertical walls of the container. The shear leads to friction. A colloid at the vertical glass wall is pressed onto the wall by two pressures. The first one is the pressure resulting from depletion force F_d (Eq. 8.2). The depletion pressure between a colloid and a wall is:

$$p_\mathrm{dep} = \frac{F_\mathrm{d}}{\pi a^2} = k_\mathrm{B}T\varphi_\mathrm{p}^\mathrm{free}\frac{3}{\pi a R_\mathrm{g}^2} \ . \tag{8.5}$$

$p_\mathrm{dep} = 0.5 \sim 1$ Pa for the large PMMA gels. The second pressure comes from the gel structure. J. Condre *et al.* [61] suggested that the compressive pressure of the gel structure can be partially re-directed to the horizontal direction $\sigma_\perp$ ($\perp$ denotes that the stress is perpendicular to gravity and the walls). $\sigma_\perp$ pushes the colloids onto the wall. Notice that, the re-directed pressure $\sigma_\perp$ is lower than the yield stress of the gel ($\sim 10^{-2}$ Pa).

It is worth mentioning an interesting result that reported in S. Meeker's thesis [67]. By varying 'container quality', e.g. wall smoothness, the delay time of a rapid collapse gel alters: optical-quality cells (both square cross-section cuvette and cylindrical cuvette) gave high τ_{d}, whereas a measuring cylinder and sample jar gave low τ_{d} [67]. This result could be related to the friction between colloids and the wall. It can also have other origins. Or, it can be an artefact as suspected by the author. Altering the friction between colloids and the glass walls in a more controllable way can test this hypothesis. One possible way is to coat the glass wall with PHSA, the stabiliser on the PMMA surface.

(2) Before the gel interface detaches from the base of a meniscus, the depletion force holding colloids at a meniscus has non-zero vertical component, i.e. $F_{\mathrm{d}}^{\parallel} \neq 0$, see figure 8.2. $F_{\mathrm{d}}^{\parallel}$ can also partially support the weight of the denser layer. This factor may be important for low φ_{c} gels, because their denser layer still attaches to the meniscus before the rapid collapse.

To allow the stress at the wall and meniscus to support the gel, the structure should be able to transmit such stresses through the bulk. This means the following two assumptions are important. The first assumption is that the integrity of the gel structure is mostly maintained. The assumption is true especially for a gel with high colloidal volume fraction. The second one concerns how far the network can transmit a stress. R. Evans showed that stress can only be transmitted through a certain length-scale [81]. To transmit the stress at the wall through the bulk, the stress transmission length of a gel should be larger than half of the container width. To test the second assumption, more investigations with large cuvettes are required.

8.2 Solvent Droplets

In Chapter 6, I reported that the solvent droplets can be found rising in intermediate and high φ_{c} gels, figures 6.5, 6.7 and 6.9. As the solvent droplet reaches the gel interface, a volcanic eruption can be observed. Droplets play an important role in releasing the solvent from a collapsing gel. What is a solvent droplet in a gel? How are they formed? In this section, I report a preliminary investigation into these questions.

One possible first step to study the formation of the droplets is to find out where they are formed. For a gel with high φ_c, the volcanic eruptions at the gel interface suggest that there should be solvent droplets deep inside the gel. In Sec. 8.2.1, I will report a preliminary investigation into the volcanoes at the gel interface. Taken together with the result published in previous studies, I conclude that the spatial distribution of volcanoes cannot reflect the formation position of droplets. However, it offers a possible way to study the heterogeneity of the gel structure. In Secs. 8.2.2 and 8.2.3, I will report two special ways of forming a droplet, which can shed some light on speculating the general formation mechanism of the droplet. Finally, a general discussion of solvent droplets will be given in Sec. 8.2.4.

8.2.1 Spatial Distribution of Volcanoes

In this section, I report preliminary observations on the spatial distribution of volcanoes at the gel interface. To investigate the volcanoes at the gel interface, one may observe the collapse of a gel from the top. However, the existence of a meniscus makes this kind of observation difficult. Hence, a setup was designed wherein there is no meniscus. Here, I report results from two systems: a collapsing gel and a creaming gel. The results show that the distribution of volcanoes depends on the geometry of the container.

8.2.1.1 Collapsing Gel

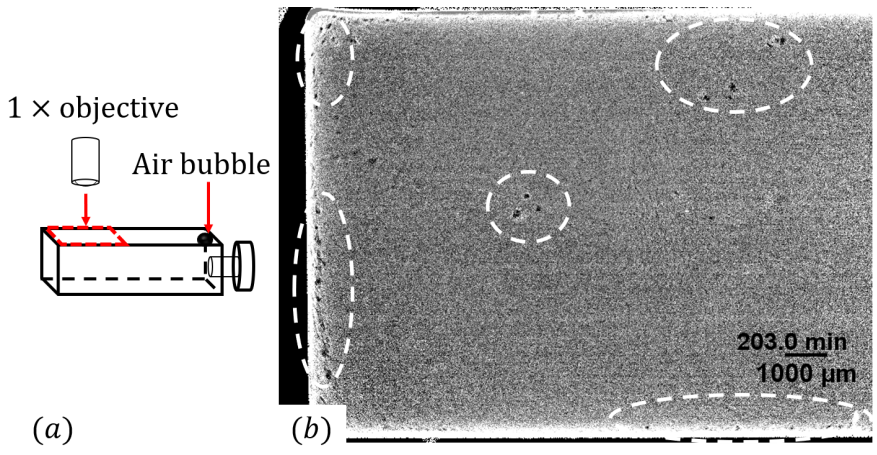

Figure 8.8 *(a) Sketch of geometry $\mathbb{D}$. The air bubble is located in the corner, while the top view of the gel is taken on the other side of the cuvette. (b) The processed image of the top of gel β at $t = 198.5$ min. Volcanoes are indicated by white dashed circles.*

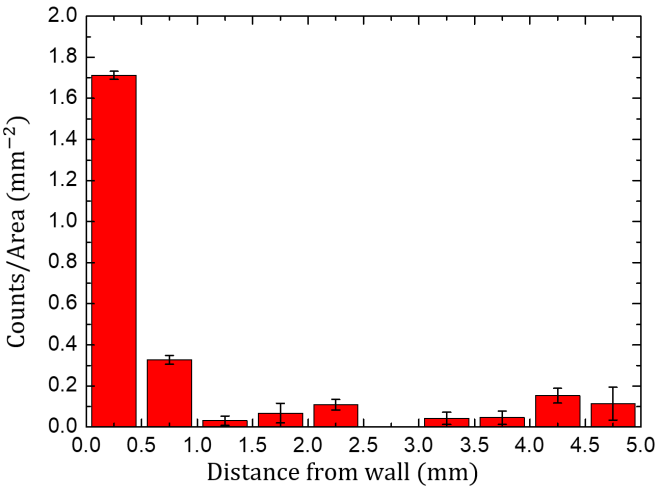

Figure 8.9 *The areal density of the volcanoes plotted against the distance to the nearest wall. With a flat top, most volcanoes are found near the glass walls.*

In a gel that collapses, one may observe the gel interface in geometry $\mathbb{D}$ from top-view, as shown schematically in figure 8.8(a). The side-view images of gel β ($\varphi_c = 0.24$, $\varphi_p^{free} = 0.565$) in geometry $\mathbb{D}$ are reported in Sec. 7.3.1.4. In this section, gel β in geometry $\mathbb{D}$ is observed from its top using a 1× objective. The time interval of imaging is 0.5 min.

Figure 8.8(b) shows the top view of gel β in geometry $\mathbb{D}$. The earliest volcanoes were found at the corner of the cuvette. Debris came out from volcanoes. This suggests that solvent droplets erode the gel structure as they travel through a gel. Later volcanoes erupted with more debris compared to early ones. Here, the criterion for 'early' is the time before the first volcano that erupts at the crater of a previous volcano. Therefore, only the spatial distribution of early volcanoes may be related to the bulk properties of the gel.

When a solvent droplet just reaches the gel interface, the resulting volcano has a clear contour. Hence, the position of (the centre of) a volcano is measurable. The distance between a volcano and the nearest wall is measured. The areal density of volcanoes is plotted against the distance from a wall, see figure 8.9. With a flat top and bottom geometry, most volcanoes are along the glass walls.

8.2.1.2 Creaming Gel

Based on the need for a flat top to a gel to enable volcano observation, a creaming gel was prepared. As the gel structure creams, solvent droplets descend from the bulk and reach the gel interface creating volcanic eruptions. Notice that the gel

interface, in this case, is at the bottom of the sample, see figure 8.10(a). In other words, the process in the collapsing gel is turned upside-down so that the volcanic eruption can be investigated at the bottom.

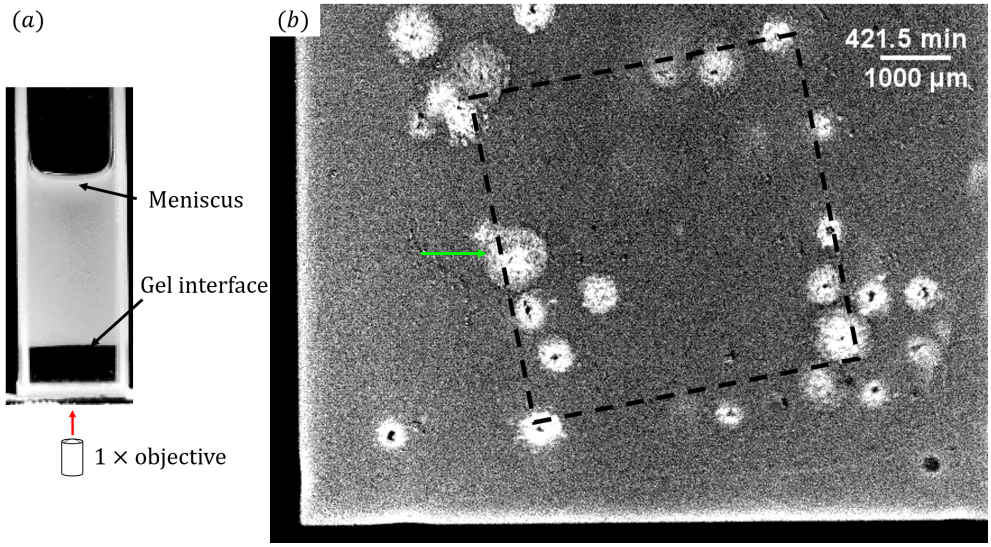

Figure 8.10 *(a) A sideways image of the creaming gel. The meniscus and the gel interface are as indicated. (b) Bottom-view image of the creaming gel in a cuvette, showing the distribution of volcanoes at the interface. The dashed square is a guide for the eyes.*

The creaming gel studied here is the same PMMA + PS mixture as described in Chapter 4, except that it is suspended in a density over-matched solvent mixture. The solvent mixture consists cyclohexyl bromide (CHB) and *cis*-Decalin. The density of the solvent mixture is $\rho_s = 1.2354 \pm 0.0001$ g/ml. The resulting density difference is $\Delta\rho = 0.057$ g/ml so that the gel will cream. A gel with $\varphi_c = 0.25$ and $c_p = 3$ mg/ml was prepared. The radius of gyration $R_g^\theta \approx 0.028\sqrt{M_w}$ =55 nm [77]. Thus, the size ratio $\xi \approx 0.06$, close to that of the collapsing gel. Two types of container are used: a $10 \times 10 \times 45$ mm^3 cuvette with a transparent bottom and a bottom-cut cylindrical vial (with an outer diameter of 1.1 mm) sealed with glass slice. In a cuvette, the sample height is 21.5 mm; in a bottom-cut vial, about 6 mm. A 1× objective was used to image the bottom of samples. The resulting images were processed as described in Sec. 3.2.3. The sideways imaging result of such creaming gel in a cuvette is presented in Appendix A.8. The result shows that the creaming gel is a rapid collapse gel with solvent droplets descending in skewed trajectories.

Figure 8.10(b) shows the bottom-view image of the creaming gel in a cuvette at

$t = 421.5$ min. The first volcano is found about 3 mm away from the wall as indicated by the green arrow. Volcanoes seem to concentrate around a skewed square as indicated in figure 8.10(b).

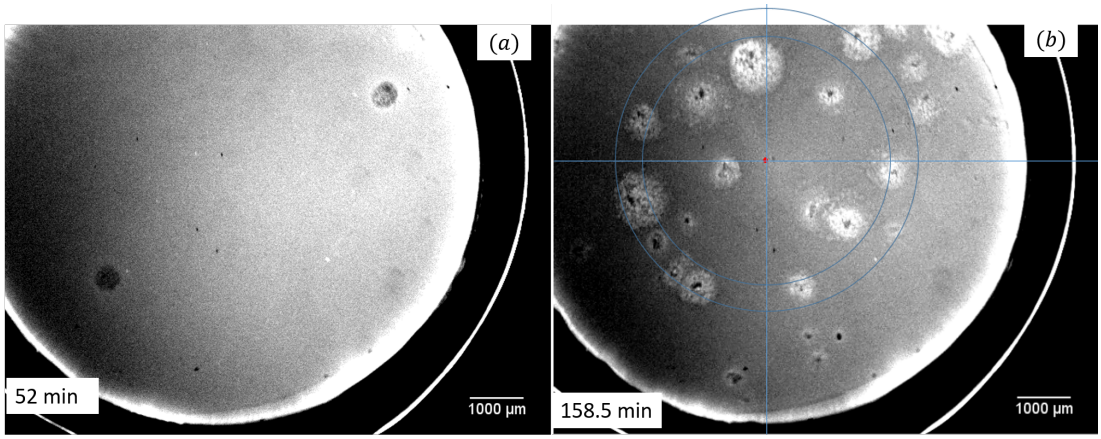

Figure 8.11 *Volcanoes of the creaming gel in a cylindrical vial. (a) Bottom-view at $t = 52$ min. The droplet that just reaches the gel interface produces a clear edge. The debris brought by the solvent can also be seen in the middle of craters. (b) Debris comes out from the volcanoes continuously and forms craters. The red dot indicates the centre of the cross section. Two circles indicate 2.5 and 2.8 mm away from the centre, respectively.*

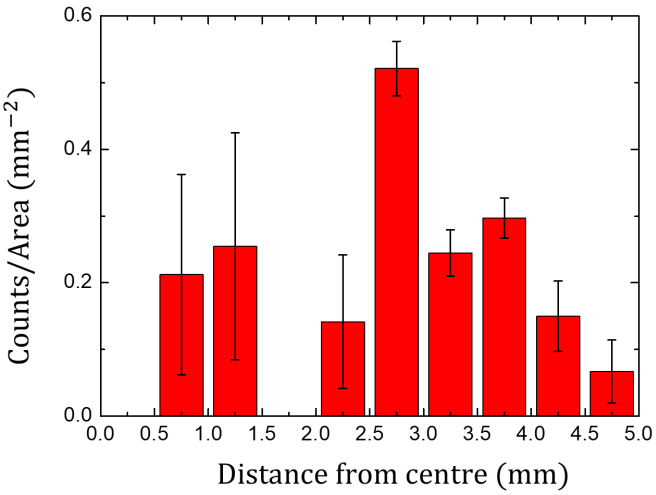

Figure 8.12 *Radial distribution of volcanoes in a bottom-cut vial.*

In a bottom-cut vial, the first two volcanoes erupted at $t \approx 52$ min, as shown in figure 8.11(a). Volcanoes concentrate around the centre of the cross section (figure 8.11(b)). The radial distribution of volcanoes is plotted in figure 8.12. The number of volcanoes is normalised by the area of the corresponding ring. Due to the normalisation, the peak at low distance subjects to high noise and

should be neglected. Therefore, from figure 8.12, the early volcanoes concentrate around 2.7 mm away from the centre.

8.2.1.3 Discussion of Volcanoes

The trajectories of droplets are skewed, as shown in Appendix A.8. This is coincident with dark field imaging result [53]. Therefore, the spatial distribution of volcanoes does not tell where droplets are formed (in the horizontal plane).

The spatial distributions of volcanoes are different in three geometries shown in figures 8.8, 8.10 and 8.11. With flat top and bottom, the majority of volcanoes are found near the walls, figure 8.8. With a flat top, a curved bottom and a square cross section, volcanoes concentrate around a square, see figure 8.10. With a flat top, a curved bottom and a circular cross section, volcanoes concentrate around a circle. It shows that distribution of volcanoes is sensitive to the geometry of the container. I suspect that the spatial distribution of the volcanoes is related to the stress distribution of the gel network. Therefore, preliminary result presented here suggests a way to study the heterogeneity of the gel.

It is important to point out some issues with the creaming gel. First, in density-over-matched solvent, PMMA particles are charged due to the presence of CHB, leading to a long-range repulsion [89, 90]. This varies the interaction for nominally identical systems [19]. Second, with CHB, the radius of gyration of PS shrinks noticeably with increasing polymer concentration [91]. The attraction strength cannot be directly estimated from R_{g}^{θ}. These two factors combined suggest that the inter-particle interaction of the creaming gel is very different from that of the collapsing gel. Furthermore, the absolute value of the density difference of the creaming gel is much smaller than that of the collapsing gel. All these three noticeable differences between the creaming and collapse gels restrict the comparison of their results to be only qualitative.

8.2.2 From Crack to Droplet

In the following two sections, I report close inspections on the solvent droplets. Two special ways of generating solvent droplets will be reported. In this section, I will present droplets that are generated from cracks in the gel near the glass wall. This phenomenon will help us to speculate a general formation mechanism of solvent droplets.

A 2× objective is used to investigate the solvent droplets in detail. Figure 8.13 shows images of the early solvent droplets in a slow collapse gel with $\varphi_c = 0.39$, $\varphi_p^{free} = 0.6$. The original image at $t = 41.0$ min (instead of the first image) was used as a reference image for the imaging process. Because at $t = 41.0$ min, all air bubbles were outside the experimental window while the gel remained homogeneous. In this way, the processed images are clear for viewing.

Figure 8.13 shows an elongated tear-drop-shaped solvent droplet (indicated by the white dashed circle). It was generated from a crack indicated by the white arrow. Figure 8.13 shows how this droplet evolves. The crack indicated by the white arrow emerged gradually after $t = 98.0$ min. At $t \approx 150$ min, the solvent in the crack formed a droplet (with a width about 100 µm) that rose upwards. The speed of this droplet was 2.73 ± 0.03 µm/s. A track was left as it rose. This mechanism of generating solvent droplets is reminiscent of the nucleation of droplets in an elastic network [92, 93]. It can also be observed in gel δ ($\varphi_c = 0.46$ and $\varphi_p^{free} = 0.382$) in geometry $\mathbb{A}$. In gel δ, a crack (at ~ 4.5 mm above the bottom of gel and ~ 1.4 mm away from the edge) generated 9 droplets between $t = 50.0$ and 845.0 min. Most of these droplets zigzagged upwards instead of rising along a straight trajectory. Here, I term these phenomena as solvent droplet, track and crack in line with the nomenclature of Ref. [80]. Cracks are narrower and grow slowly in both vertical and horizontal direction. Also, they do not carry debris. The origin of cracks is unclear. It may be related to the inhomogeneity of the gel and the surface condition (e.g. scratches or dirt) of the wall, which is analogous to heterogeneous nucleation [92].

Interestingly, the opposite process of a crack creating droplets can also be observed. Figure 8.14 shows a droplet that was squeezed back into gel δ. At about $t = 12500.0$ min, no solvent droplet can be found rising in gel δ; however, one droplet (radius of 70 µm) is stuck on the wall. At this time, the average colloidal volume fraction of the sediment is about 0.57. When the lower half of the sample δ was imaged, similar evidence can be found at an earlier time ~ 7000 min. These results show that the solvent can be squeezed back to a gel through the porous structure. This result also implies that the formation of solvent droplet is a nucleation process, see Sec. 8.2.4.3.

In figure 8.13, the droplet indicated by the red dashed circle came from below the

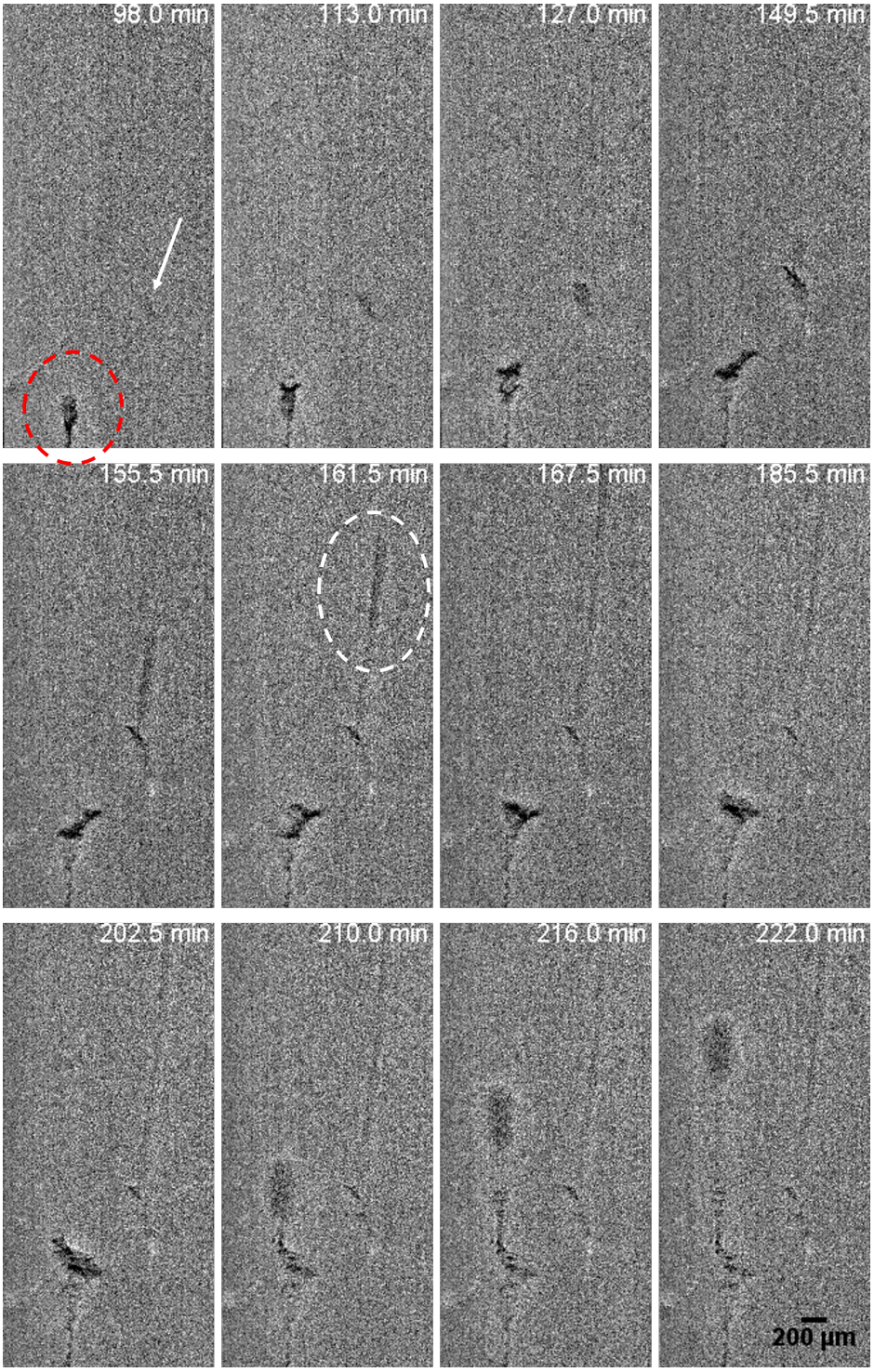

Figure 8.13 *Micrographs of a slow collapse gel ($\varphi_c = 0.39$, $\varphi_p^{free} = 0.600$) observed using a 2× objective. The solvent droplet which attaches to the wall appears irregular shape and zigzag slowly upwards (red dashed circle). The solvent droplet in white dash circle is near but without touching the wall. It appears an elongated tear-drop. The white arrow points at the crack that generates the droplet in the white circle.*

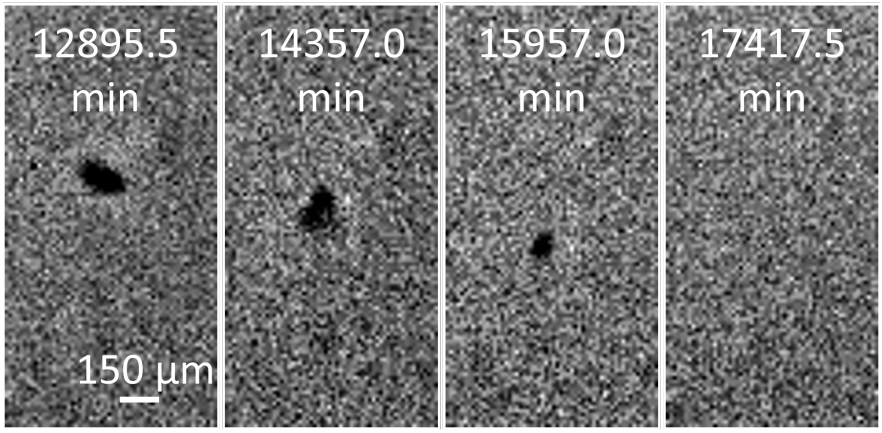

Figure 8.14 *In sample δ, a solvent droplet can be found stuck on the wall and squeezed back into the gel.*

experimental window. It has a high-curvature shape. It zigzags upwards with a speed of $v = 0.07 \pm 0.01$ µm/s in a direction dictated by gravity. At $t = 210.0$ min, this droplet detaches from the wall and becomes more tear-drop-shape and turbid. After it detached, it rises much faster, with a speed of $v = 1.55 \pm 0.01$ µm/s. This is an important observation that can help us to understand the behaviour of solvent droplets. I will come back to this in Sec. 8.2.4, together with the solvent droplets that are generated by cracks.

8.2.3 From Air Bubble to Droplet

In slow collapse gels with high polymer concentration, air bubbles take much longer time to escape from the suspension compared to those in a rapid collapse gel. For a gel with $\varphi_c = 0.46$ and $\varphi_p^{free} = 0.624$, it takes more than 160 min for all visible air bubbles to be released; by contrast, for sample γ, the most extreme case of rapid collapse gels, it takes about 40 min. Here, I report observations of solvent droplets that are generated from the wakes of air bubbles. Discussion directly related to the results will be given in this section; however, general discussion of droplet formation will be given in Sec. 8.2.4.

In a slow collapse gel with higher φ_p^{free}, air bubbles (around the time scale shown in figure 8.15) can create short dark wakes, see the dashed circles in figure 8.15. As an example, the air bubble indicated by black dash circle in figure 8.15(a) is ~ 30 µm in radius at $t = 29.5$ min. As it rose through the gel, it shrank from $R = 60$ µm at $t = 7.0$ min until disappeared at $t = 31.0$ min; its wake elongated from ~ 220 µm at $t = 8.0$ min to ~ 1230 µm at $t = 31.0$ min. As the air bubble disappeared, a solvent-rich wake was left. A solvent droplet can be generated from

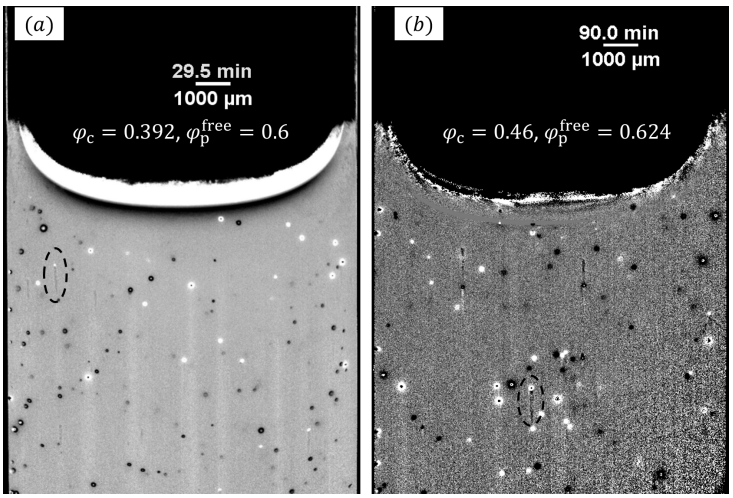

Figure 8.15 *In slow collapse gels with high φ_p^{free}, some air bubbles create wakes as they rise through the gel. The air bubbles appear as bright white circles with a black dot in the centre. The black circles (some with a white dot in the centre) are the air bubbles in the first image of the experiment. Indicated by the black dashed circles are dark wakes created by later air bubble.*

this wake. Figure 8.16 shows a solvent droplet which was generated from the dark short wake of an air bubble indicated by the black dashed circle in figure 8.15(a). The air bubble (bright sphere in the first image) disappeared leaving the wake in the bulk of the gel. In about 60 min, the wake gradually transformed into a low-curvature shape. By assuming the wake at $t = 29.5$ min and the droplet at $t = 59.5$ min has axial symmetry, their volume can be roughly estimated to be $2 \times 10^6\,\mu m^3$ (wake) and $11 \times 10^6\,\mu m^3$ (droplet), respectively. This suggests that the wake accumulated solvent as it transformed. At around $t = 90$ min, the wake rose upwards as a solvent droplet.

This kind of droplet forming mechanism can also be found in small particle gels, see figure 6.15(e). Observations of gel δ in geometry $\mathbb{C}$ suggest that the generation of solvent droplets is related to the existence of air bubbles as well. In two experiments with no air bubble rising, solvent droplet and volcano at the gel interface are absent, see figures 7.14 and 7.15. In contrast, with air bubble rising through the gel, solvent droplets can be found, see figure 7.16.

A similar observation has been reported by G. G. Glasrud *et al.* when studying the settling of Iron Oxide suspensions [94]. They found that the solvent (oil in their case) fills the voids left by the departed air. As the solvent reaches the interface, volcanic eruptions can be observed.

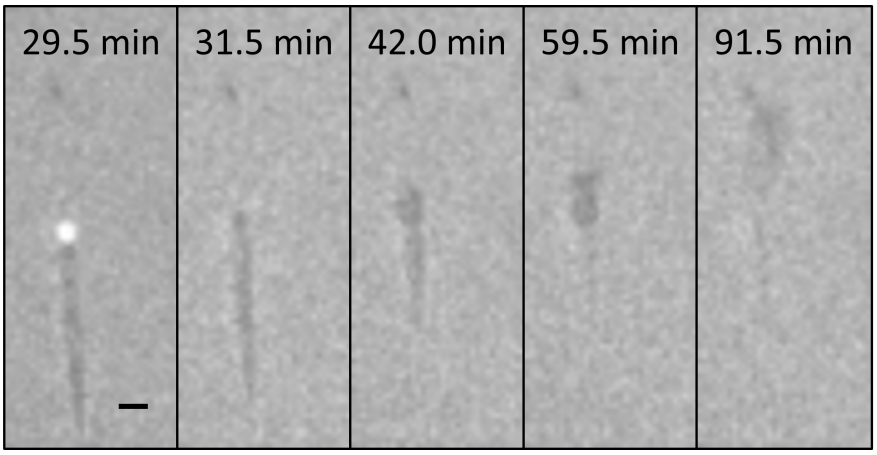

Figure 8.16 *A solvent droplet generated from the wake of an air bubble. The bright sphere in the first left panel is the air bubble. The darker wake transforms gradually into a solvent droplet and rise. The scale bar in the first left panel denotes 100* µm.

The short wakes are darker, suggesting they are solvent-rich. As the air bubble rises, the length of dark short wake increases with time, suggesting the gel structure needs longer time to heal. It is expected since the gel structure is maturing and the relaxation time increases correspondingly.

How does the air bubble in figure 8.16 suddenly disappear? The disappearing of the air bubble is not a result of out of the depth of view. Going out of view, an air bubble should dim as it shrinks. It is possible that the air bubble was dissolved back into the solvent, considering that the air bubble is small.

The largest air bubble that generated droplet was found to be ~ 90 µm in radius. Why do larger air bubbles ($R > 100$ µm) not show dark wakes in the image? In fact, they may create small dark wakes but the imaging method used here cannot resolve these. As an air bubble creates a dark wake, the colloids originally in the wake are compressed into the surrounding structure. For a large air bubble, the layer of compacted colloids that are close to the wall can reduce the contrast so that the wake hidden behind cannot be resolved. However, one may also argue that large air bubbles rise more quickly and can be released shortly after the sample is mounted. The gel is not formed within such a short timescale. The gel structure can rearrange and 'heal' the wake. Hence, to answer this question, detailed study of air bubbles in a gel and the formation time of the gel is required.

8.2.4 Discussion of Solvent Droplets

8.2.4.1 Comparison to Previous Findings

L. Starrs *et al.* studied the collapse of gels formed by small PMMA colloids ($a = 186$ nm) using dark field imaging (DFI) [53]. Their results showed cracks and channels in gels before the delay time. Cracks propagate mainly horizontally; while channels more upwards. The channels appear as bright objects in dark field because the surrounding gel network is broken. DFI results show that the channels can start at various heights that are close to the walls of the sample. They suggested that the channels may nucleate on small inhomogeneities on the inner wall. Also, the channels were bent towards the centre of the gel. They also observed that channels transported materials. When a channel broke through the gel interface, volcano-like structure was observed.

Reported in Sec. 8.2.2, the micrograph (figure 8.13) shows that droplets can be generated from cracks at the glass wall. Also, the trajectories of solvent droplets are skewed. As a droplet reaches the interface, a volcanic eruption can be observed. Debris can be found coming out from the volcanoes.

Comparing the DFI results with the imaging results in this work, I argue that the channel in DFI is the track created by the solvent droplet. As a solvent droplet rises, a gel yields locally so that the gel structure along the droplet track is broken as observed in DFI. To understand why a track or a channel can be observed by DFI after the rising of a droplet, let us consider the droplet 1 and 2 in gel β (figure 6.5(c)) as examples. Their radius and rising speed are 90 ± 1 µm, 5.2 ± 0.1 µm/s and 113 ± 2 µm, 5.9 ± 0.1 µm/s, for droplet 1 and 2, respectively. A droplet forces the gel structure above it to yield; and it shears the surrounding gel structure as it rises. The shear rate created by droplet 1 and 2 is $\dot{\varepsilon} = v_{\text{droplet}}/R_{\text{droplet}} \approx 0.06\ \text{s}^{-1}$. For colloids around the droplet, the shear-induced structure changes can be attributed to the balance between the shear and the depletion force. This balance can be estimated by a modified Peclét number Pe_{dep}, which reflects the ratio of shear to depletion attraction [83, 95]:

$$\text{Pe}_{\text{dep}} = \frac{F_{\text{shear}}}{F_{\text{dep}}} = \frac{6\pi\eta_{\text{s}} a\dot{\varepsilon} a}{U_{\text{dep}}(2a)/2R_{\text{g}}} = \frac{12\pi\eta_{\text{s}} a^2\dot{\varepsilon} R_{\text{g}}}{U_{\text{dep}}(2a)} \ , \tag{8.6}$$

where the depletion potential is approximated by a ramp potential and $U_{\text{dep}}(2a) = 16.4 k_{\text{B}}T$ is the depth of depletion potential for gel β. The viscosity of PS solution

was measured to be $\eta_s = 0.0105 \pm 0.0001$ Pa $\cdot$ s. Hence, for the shear created by the rising of droplet 1 and 2, $\mathrm{Pe}_{\mathrm{dep}} \approx 0.01 \ll 1$. Consider the speed and size of the channels and the attraction strength in DFI result, the modified Peclét number $\mathrm{Pe}_{\mathrm{dep}}$ is also much smaller than 1 in their case. $\mathrm{Pe}_{\mathrm{dep}} \ll 1$ suggests that the colloids around the droplets are strongly affected by the inter-particle attractions. Previous rheo-confocal studies showed that, with high shear rate (i.e. high $\mathrm{Pe}_{\mathrm{dep}}$), the shear breaks a gel completely into single particles. Therefore, after the cessation of the shear, a gel can be reformed. With low shear rate, the shear cannot break the gel completely. Instead, it creates large compacted clusters. The shear-induced rearrangement almost stops after the cessation of the shear, i.e. the resulting compacted gel structure has a long relaxation time [83]. In our case, the shear rate induced by the rising of the droplet is low. Hence, the gel structure around the droplet needs a long time to 'heal'. It leads to the formation of observable channels after the droplet rises.

8.2.4.2 What is a Solvent Droplet?

Let us re-examine the question of what a solvent droplet is? In the confocal image shown in figure 2.6, solvent fills the voids in the gel network. Even though the solvent can flow through these voids, the voids in the gel network are not solvent droplets. In contrast, the confocal images shown in Appendix A.9 is in line with the common impression of a droplet, which is almost tear-drop shaped. Generally speaking, a solvent droplet should be able to locally break the gel above it and maintain its integrity (to some extent) as it travels through the gel.

The yield stress of the gel is 10^1 to 10^2 mPa. The critical size of a droplet that is capable of yielding a gel can be evaluated by $R = 3\sigma_y/4\Delta\rho g$, where $\Delta\rho = \rho_{\mathrm{gel}} - \rho_{\mathrm{solution}} = (\rho_{\mathrm{PMMA}}\varphi_c + (\rho_{\mathrm{IM}} + c_p)(1 - \varphi_c)) - (\rho_{\mathrm{IM}} + c_p) \approx 0.1$ g/ml. Hence, the critical radius of a droplet is $10^1 \sim 10^2$ µm. The smallest solvent droplet that can be identified is found in a rapid collapse gel with $\varphi_c = 0.34$ and $\varphi_p^{\mathrm{free}} = 0.468$, which is ~ 30 µm in radius. The width of this droplet corresponds to 6 pixels in the image. It is close to the resolvable length scale of this setup, see Sec. 3.2.2. It can be seen because it left a track behind as it rose. There can be smaller solvent droplets rising in the gel, although they cannot be resolved in the images, and hence we cannot know for certain what the critical radius is.

As I proposed, a solvent droplet should be able to force the gel above it to yield locally and rise. However, complexity is added when considering a blob of solvent

at the wall. Figure 8.13 suggests that, at the wall, apart from the yield stress of the gel, a blob of solvent needs to overcome more resistance to be able to rise upward. The additional resistance comes from the friction between colloids and glass walls. As discussed in Sec. 8.1.2, colloids at the wall are pushed onto the wall by depletion pressure (p_{dep}) and re-directed stress ($\sigma_{\perp}$), resulting in the friction between colloids and wall. This friction can slow down a droplet; while the fractal structure of the gel leads to the zigzag motion of the droplet.

I also proposed that, a solvent droplet is generally required to maintain its integrity as it rises. At the wall, solvent droplets zigzag upward slowly; they can also merge or split. In this case, the distinction between a droplet and a crack is ambiguous. However, in the result of gel δ (figure 6.9), it is appropriate to term those zigzagging blobs as droplets, considering that their shape has a lower curvature than that of a narrow crack.

Low curvature implies the existence of surface tension. As the droplet rises, it shears the gel structure locally. Colloids can be rearranged to form a low curvature interface that lowers the surface energy. In contrast, the high curvature shape of droplets at the wall suggests anisotropic resistance. In fact, away from the wall, the structure of a gel is also heterogeneous on the length scale of a droplet, see confocal images of droplets in Appendix A.9. The shape of a droplet changes as it travels through a gel, and the surface of a droplet is not smooth. In contrast, the solvent droplets formed in a polymer gel are smoother [93]. This is understandable considering the size of droplets in polymer gel is 3 orders of magnitude larger than the mesh size of the network. The heterogeneity of the gel network is negligible on the length scale of such a large droplet. However, in our colloidal gel, the droplet is $10^1 \sim 10^2$ µm in size while the mesh size is 10^1 µm estimated from figure 2.6 and void volume reported in Ref. [83]. Hence, on the length scale of a droplet, the heterogeneity of the colloidal gel is not negligible.

8.2.4.3 The Formation of Solvent Droplets

A possible first step to understanding the formation of solvent droplets is to observe where solvent droplets can be formed. I reported the spatial distribution of the volcanoes at the gel interface in Sec. 8.2.1, hoping to infer the generation position of droplets in the horizontal plane. However, the side-view images shown in Appendix A.8 show that the trajectory of a droplet can be skewed. This means the spatial distribution of volcanoes at the interface cannot be directly linked to

the generation position of droplets.

I reported that solvent droplets can be formed from the cracks in the gel. The results shown in figure 8.13 implies that the droplet forming mechanism is a nucleation and growth process. R. Style *et al.* studied the nucleation of solvent droplets in an elastic network [93]. They investigated the de-mixing of two types of liquid in a cross-linked polymer network. In a polymer gel, the classic nucleation process is modified by the presence of elasticity. To grow beyond the mesh size of the network, a nucleus needs to overcome not only the energy barrier set by the balance between interfacial energy and bulk free energy, but also the restraining pressure set by Young's modulus of the gel as it deforms the network [92, 93]. In their case, the driving force of nucleation is liquid-liquid phase separation due to changes in temperature [93]. The polymer gel is merely a constraint. In our gels, I suggest that the driving force is spinodal decomposition. As a gel forms, the spinodal decomposition leads to the colloids to aggregate, resulting in a negative pressure that force the solvent to form voids. These voids together with defects on glass walls and wakes of air bubbles serve as active nuclei or seeds for droplet growth. When a droplet is smaller than the minimum size of a stable nucleus which is set by the interfacial tension and the elasticity of the gel network, it will be "re-dissolved" back to the gel. The droplet shown in figure 8.14 could be this case. When a droplet grows large enough, it forces the gel to yield and rises. In other words, the formation of the colloidal gel is the driving force, while the resulting gel is the constraint.

8.3 Conclusion

In this chapter, I discussed the two key features during the onset of the collapse, i.e. the denser layer and the solvent droplets.

In Sec. 8.1, based on the observations that gels start collapsing at the vertical part of a meniscus, I speculated that the steep slope of the meniscus leads to an unbalanced force so that the gel in such region is unstable to gravity compared to other parts of the sample. The colloids at a frictionless meniscus slide downwards due to the tangential component of the buoyancy force. Hence, the surrounding gel network is dragged down through inter-particle attraction or hydrodynamic interaction. The fact that gels start collapsing around an air bubble in nearly-filled cuvette supports this force balance hypothesis. Also, a cone geometry in

which a gel curved upwards was designed to test this hypothesis. The imaging results show that the gel initially collapsed to one side and created a strong back flow in the centre, which is expected from the force balance hypothesis.

The mass of a section of a denser layer was estimated and compared to the yield stress of the gel in Sec. 8.1.2. The result shows that the denser layer accumulated more mass than it needs to force the gel to yield. Two factors were speculated to partially support the denser layer. One is the friction between the colloids and the glass walls; the other is the depletion force that pushes colloids towards the meniscus. It suggests that the container with frictional inner walls can potentially prolong the delay time. However, further study is required.

In Sec. 8.2, to study the formation of the solvent droplets, the spatial distribution of volcanoes at the gel interface of collapsing and creaming gels were investigated. The results suggest that the distribution is geometry dependent, which can be related to the stress distribution of the gel network. However, because the trajectories of solvent droplets are skewed in vertical planes, the spatial distribution of the volcanoes cannot imply the generation position of solvent droplets.

I reported that solvent droplets can be formed from cracks at the glass walls and wakes of air bubbles. These results imply that the formation of solvent droplets is a nucleation and growth process. The spinodal decomposition leads to a negative pressure that aggregates solvent to form voids in the gel network. These voids, defects on glass walls and wakes of air bubbles are active nuclei or seeds for droplet growth. When a droplet grows large enough, it forces the gel to yield and rises.

Chapter 9

Conclusion and Future Work

In this thesis, the gravitational collapse of the colloidal gel with short-range depletion attraction has been studied. The main interest of this work is the onset of the collapse. As highlighted in Sec. 2.5, for our model system, the falling of the denser layer and the expulsion of the solvent are two of the key processes in the collapse. To investigate these two processes, the onset of the collapse is observed using microscopic time-lapse imaging. The application of the fluorescence microscopy enables the observation of detail phenomena before and after the macroscopic collapse of gels. Here, I summarise main findings in this work.

As presented in Chapter 6, the interplay between these two key processes leads to an evolution of collapse mechanism. At very low φ_c, a gel cannot support the stress exerted by a single particle. It collapses straightforwardly with very short delay time. At low φ_c, finger-like clusters form and fall through the gel prior to the avalanche of the denser layer. At intermediate φ_c, the denser layer accumulates more mass. Solvent droplets can be found rising through the gel before the falling of finger-like clusters. Solvent droplets interact with fingers. At higher φ_c, a gel can support more mass at its top so that the falling of finger-like clusters can no longer be observed. The denser layer collapses as large blocks. Increases the φ_c even further, a gel can support the mass of denser layer; only solvent droplets can be observed. A gel collapses without fast sedimentation. Generally, a gel can support more weight at its top as φ_c increase. This result can potentially help with shortening the product development cycle by predicting the type of collapse in the early stage.

In Chapter 6, the imaging results show that the mass source of the denser layer comes mainly from the colloids at the corner (vertical part) of the meniscus. In Chapter 7, by removing most of the curved meniscus and leaving only a small air bubble in the sample, the delay time of a rapid collapse gel can be prolonged. This confirms that the air-gel interface is crucial for the formation of a denser layer. In Sec. 8.1, the mechanism of denser layer formation was speculated. Colloids at the air-gel interface are pressed toward the interface by the depletion force. However, the component of the depletion force that balances the buoyancy force decreases at the vertical part of the air-gel interface. Therefore, compared to at the bottom of the meniscus and in the bulk, the gel at the corner is more unstable under gravity. As these colloids fall down and accumulate at the top of the gel, where a denser layer can be formed. When such layer is heavy enough, it falls down as finger-like clusters or as big blocks. The falling of the denser layer creates large-scale recirculation and triggers the rapid collapse. Therefore, reducing the vertical part of the air-gel interface can retard the mass accumulation of the denser layer, hence, postpones the rapid collapse.

The evolution of collapse mechanism seems to support the scenario that the collapse of the denser layer is a yielding event. In Chapter 8, a preliminary test of the scenario of a denser layer breaking a gel suggests that the denser layer accumulates more mass than it needs to force a gel to yield. On the other hand, in the investigation of the solvent droplets at the glass wall, results show that these droplets exhibit high-curvature shapes and zigzag motions. I speculate that the friction between colloids and the glass wall may partially support the denser layer at the top and act as an extra resistance for the solvent droplets at the wall. Such friction is induced by pressures that push the colloids onto the wall, including the depletion pressure and redirected pressure of the gel network.

In Chapters 6 and 7, the imaging results also show that the solvent can be expelled from the gel as rising solvent droplets. As a droplet rises, a track (or channel) is left allowing the solvent to be released more quickly. Also, the rising of droplets damages the gel structure. The solvent flow erodes the surrounding gel structure as it flows through the track. When a droplet reaches the gel interface, a volcanic eruption can be observed. Debris brought with the solvent flow comes out from the volcanoes forming craters. This debris also contributes to the mass accumulation of the denser layer, especially when a curved meniscus is far away. In Sec. 8.2, I reported that solvent droplets can be formed from cracks at the

glass wall and from the wakes of air bubbles. However, the general mechanism of the droplets generation is not clear. I suggest that the formation of droplets is a nucleation and growth process. In our model system, a gel is formed by arresting the spinodal decomposition. Such a decomposition process leads to a negative pressure that aggregates the solvent to form voids. These voids together with defects on the walls and the wakes of air bubbles act as active nuclei or seeds for droplet growing. When a droplet grows big enough, it forces the gel network to yield and rise upwards.

The results presented here highlight the important role of hydrodynamics in the collapse of a gel. During the initial stage of collapsing, the solvent flows through the network, counteracts the compression of the gel network. In this case, the hydrodynamic force supports the gel structure. On the other hand, the solvent flow can erode the gel structure locally. In this case, the hydrodynamics is a damaging effect instead of a supportive one. Moreover, the falling of a denser layer leads to a large-scale recirculation. Such recirculation can also propagate across a gel breaking the gel structure. In this case, the hydrodynamics affects the collapse in the length-scale of the whole sample.

This study is mainly about exploring the onset of collapse. Some observations lead to open questions for future work. The first question is about the generation of the finger-like clusters. In our model system, fingers collapse leading to the avalanche of the denser layer that brings down the gel. However, for some gels, this is not the case. For example, a gel formed by colloids in nematic liquid crystal starts collapsing at the corner of the meniscus; however, the resulting denser layer is stuck at the meniscus while the network breaks in the middle of the sample and collapses without the layer at the top. This kind of partial collapse may be undesirable in many products. Therefore, understanding the collapse of the fingers and hence the denser layer is important. Imaging results (figures 6.3 and A.10 as examples) show that the fingers have similar width (for a given gel). It is reminiscent of the bulk elastic fingering instability [96, 97]. Envision a denser viscous fluid is placed on top of a less dense gel, the interface is unstable. Any fluctuation of density will lead to the destabilization of the interface, leading to the formation of fingers. However, such an interface is ill-defined in the micrographs. Base on the discussion of the denser layer formation (Sec. 8.1.1), this interface can be revealed from the difference in colloidal volume fraction or colloidal mobility. Once this interface is observed, one can compare

the collapse of fingers with the fingering instability.

The second is the formation of solvent droplets. The nucleation of solvent droplets in a polymer gel has been studied qualitatively[93]. The general argument may be applicable for droplets in colloidal gels. However, in a colloidal gel, the gelation is the driving force for the nucleation of droplets and the resulting gel becomes the constraint. It is interesting to investigate further the nucleation of droplets in a colloidal gel. Images deep inside a gel are desired. This can be potentially achieved by applying selective plane illumination microscopy [98]. In this technique, only the focal plane of the detection optics is illuminated. It yields images similar to that from a confocal laser scanning microscopy, but has a larger field of view with higher axial resolution. Preliminary study suggests that the concentration of fluorophore should be reduced significantly to illuminate deep inside a gel.

Third, it would be fruitful to study the collapse of gel in simulations taking hydrodynamics into account. It may provide insight into the role that hydrodynamics plays related to the delay time of the gel and the interface speed of the collapse. Especially, it may answer why a slow collapse gel exhibits a constant interface speed when the meniscus is mostly removed.

Moreover, this work demonstrates the crucial role of a curved meniscus and the friction at the walls during gel instability. Therefore, instead of designing gels by changing compositions, altering the surface property of a container can be a new direction to extend the shelf life of a gel product. For example, a 90° contact angle and frictional inner walls may be beneficial.

Appendix A

Supplementary Observations

A.1 Shape of a Meniscus

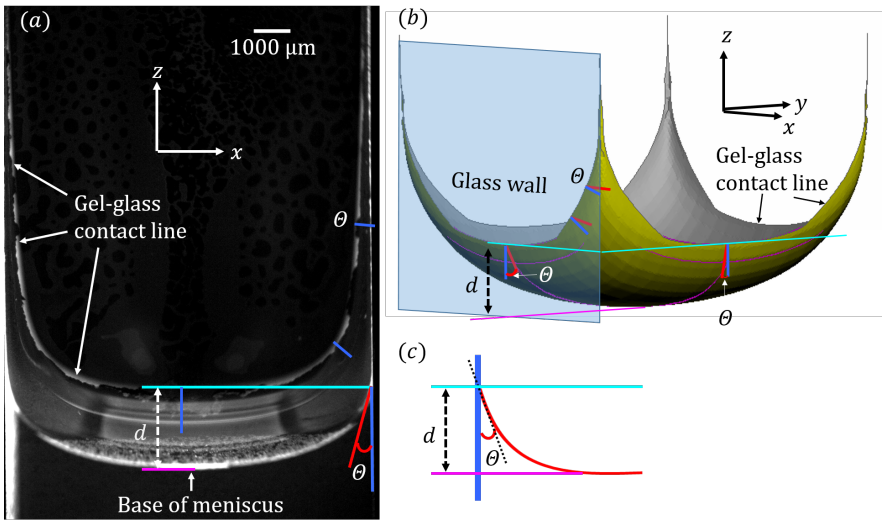

Figure A.1 *(a)The micrograph shows the meniscus of a sedimented gel in a cuvette. (b) A 3D illustration of the meniscus, in which only one of the glass walls are presented in the image. (c) Sketch of a cross section at the bottom of a contact line showing the contact angle* Θ*. The cyan lines indicate the bottom of gel-glass contact lines. Red lines are on the meniscus and perpendicular to the contact line. Their projection on glass walls are indicated by the blue lines. Therefore, the angle between blue and red lines are the contact angle of the gel* Θ*. The distance d is between the bottom of a contact line and the base of the meniscus.*

The shape of a meniscus is important in understanding the effect of a meniscus in gel collapse, especially for the discussion in Sec. 8.1. Here, I present a 3D illustration of the meniscus of the gels studied in this work to help picturing its shape. However, calculating the shape of the meniscus in our case is complicated

and is out of the scope of this work [99, 100].

Figure A.1(a) shows the meniscus of a sedimented gel in a cuvette. At the edge of a cuvette (each side of the image), the 'gel', it is in fact the PS solution in this image, touches two glass walls that perpendicular to each other. On each wall, the contact angle Θ should be the same. In our gels, Θ is acute. Therefore, the contact line bends upwards, due to capplilary force. In an ideal case, where $\Theta = 90°$, the contact line will not bend. It will be perpendicular to the edges of a cuvette so that two glass walls and the flat meniscus are three mutually perpendicular planes.

To help picturing the shape, in figure A.1(a), at the bottom of contact lines (indicated by the cyan lines), the contact angle Θ is indicated at two locations: in the centre (the blue line) and on the right-hand side (the angle) of the image. Correspondingly, these two cases are represented in figure A.1(b). Note that red lines are on the meniscus and blue lines are their projections on a glass wall. Similarly, at a corner of the meniscus in figure A.1(a) and (b), the contact angle is indicated at two more locations.

Now, let us estimate the contact angle of the gel in a glass cuvette. Figure A.1(c) sketchs a cross section at the bottom of a contact line showing the contact angle Θ. From the imaging result, this cross section can only be seen after a gel is collapsed. Therefore, to estimate the contact angle of a gel, I will first estimte that of the PS solution from the image. Then, I will show that it agrees with the result measured directly on a glass slice.

The cuvette is assumed to be wide enough so that the air-gel interface approaches the ambient level far from the flat wall. Hence, the air-gel interface can be modeled as meniscus at a flat wall. In this case there is no capillary effect and the contact angle Θ can be estimated from the height at the wall d by [101]:

$$\Theta = \arcsin(1 - \rho g d^2/2\alpha) \ , \tag{A.1}$$

where α and ρ are the surface tension and density of the solvent. In our gel, the IM solvent consists 81% of *cis*-decalin. Hence, for estimation, these properties of *cis*-decalin are used, which are $\alpha = 0.03$ N/m [102] and $\rho = 0.8964$ g/ml. $d = 2253 \pm 6$ µm was measured from figure A.1(a) giving $\Theta = 14°$. To verified this estimation, the contact angle of 4 mg/ml PS in IM solution on a glass slice

was measured using Krüss EasyDrop tensiometer, which is $\Theta = 14.45 \pm 0.13$. This result agrees well with the estimated value in a cuvette, considering that the PS solution in figure A.1(a) is not devoid of PMMA particles. My result also agrees with the previous observation of a monodispersed colloids in decalin, which is $\Theta \approx 15°$ [103]. Therefore, the contact angle of a gel is taken as the value measured on a glass slice which is $\Theta \approx 20°$ from Ref. [103].

A.2 Height Profiles from Macro- and Micro-scopic Imaging

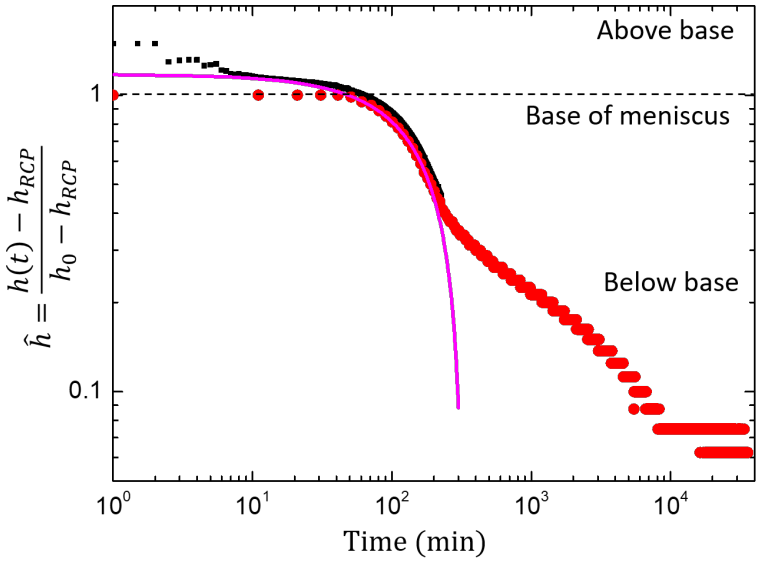

Figure A.2 *Scaled height profiles $\hat{h}(t)$ vs. time of the rapid collapse gel α ($\varphi_c = 0.19$, $\varphi_p^{free} = 0.557$, see figure 6.1) in standard geometry obtained from ■: microscopic time-lapse imaging with 0.5 min time interval; and ●: long-time macroscopic time-lapse imaging with 10 min time interval. For the macroscopic result, the magenta solid line is linear fit to the rapid collapse.*

The scaled height profiles $\hat{h}(t) = \frac{(h(t)-h_{RCP})}{(h_0-h_{RCP})}$ *vs.* time of gel α ($\varphi_c = 0.19$, $\varphi_p^{free} = 0.557$, see figure 6.1) obtained from macro- and micro- scopic imaging are compared in figure A.2. Only one result from each method is shown for clarity. All (scaled) height profiles are calculated using the original images (see Chapter 3).

Notice that the delay time τ_d from microscopic imaging is larger than that from macroscopic imaging. The difference is about 17% of τ_d from microscopic imaging. By repeating macroscopic time-lapse imaging with 1 min time interval,

the average delay time is $\tau_{\mathrm{d}}^{25} = 53 \pm 0.7$ min at 25 °C and $\tau_{\mathrm{d}}^{23} = 54 \pm 1.1$ at 23 °C. The variances of τ_{d} are close to the resolution (time interval) of the experiment. The microscopic imaging was operated at $T = 23 \pm 0.5$ °C with time interval of 0.5 min. The average delay time $\tau_{\mathrm{d}} = 63.6 \pm 0.6$ min. The variance is also close to the resolution of the experiment. In each experiment, the measurement of τ_{d} can be well reproduced. Also, the temperature difference does not affect the measurements significantly. Hence, the τ_{d} measured in macro- and micro- scale experiments are different significantly for other reasons. One possible source of the difference is the vibration cause by the fan in macro-imaging chamber. The vibration exerted on the gel may lead to low τ_{d}.

The interface speed during the rapid collapse period v_{i} can be measured by linearly fit to the height profile. At 23 °C, macroscopic results yield $v_{\mathrm{i}} = 769 \pm 2$ nm/s. Microscopic result yields $v_{\mathrm{i}} = 767 \pm 3$ nm/s. Hence, v_{i} is well reproduced with both methods.

The large variation of τ_{d} suggests that the onset of the rapid collapse is sensitive to the environment (i.e. initial condition). On the other hand, v_{i} is not sensitive to the environment. More importantly, within the range of the temperature variance, all qualitative observations can be well reproduced.

A.3 The Interface Speed of Rapid Collapse

The interface speed of rapid collapse v_{i} can be calculated by fitting the linear region of the height profile during the rapid collapse. v_{i} is plotted against colloidal volume fraction φ_{c} in the inset of figure A.3. The error of v_{i} is less than 0.01 µm/s for all rapid collapse gels. v_{i} does not vary with c_{p} significantly. This is understandable. For a fix φ_{c}, changing c_{p} can vary the local structure of the gel (cluster-like or string-like) [104]. After the onset of rapid collapse, the gel structure is broken into clusters. The structural information of the original gel will not be retained in the resulting clusters due to the rearrangement of clusters under the strong shear coursed by the large-scale recirculation. Hence, the interface speed of rapid collapse is dominated by the φ_{c} rather than c_{p}.

The interface speed is normalised by the single particle sediment speed v_{s} and plotted against φ_{c} with different polymer concentration in figure A.3. $v_{\mathrm{s}} =$

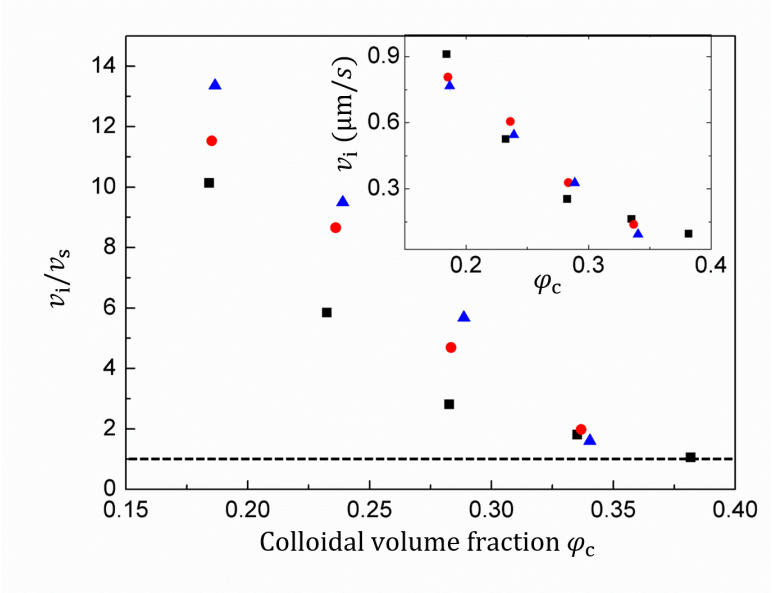

Figure A.3 *The normalised interface speed v_i/v_s of rapid collapse is plotted against colloidal volume fraction φ_c with different polymer concentrations. The inset plots v_i vs. φ_c. Polymer concentration c_p are ■: 3 mg/ml; ●: 4 mg/ml; and ▲: 5 mg/ml.*

$2\Delta\rho g a^2/9\eta$, where η is the viscosity of the PS solution and $\Delta\rho$ is the density difference between colloids and the PS solution. v_i/v_s increases with c_p. This is because higher polymer concentration leads to higher solution viscosity η, therefore, lower single particle sedimentation speed v_s. On the other hand, v_i decrease with increasing colloidal volume fraction φ_c. As φ_c increases, v_i approaches to v_s. Why this should be is not clear.

A.4 The Onset Height of Rapid Collapse

As shown in figure 6.2, the onset of rapid collapse can be defined by fitting the linear section of sedimentation during pre-collapse and rapid collapse. The x-coordinate of the intersecting point is the onset time of the rapid collapse (τ_o); the y-coordinate is the onset height of the rapid collapse Δh_o, which is the distance between the gel interface and the base of the meniscus at the onset of the rapid collapse.

Δh_o is plotted against φ_c in figure A.4. Most of our samples start rapid collapse before the gel interface detaches the meniscus, i.e. $\Delta h_o > 0$ in most cases. From figure A.4, a positive correlation between Δh_o and c_p can be seen at low φ_c and there exists a maximum Δh_o, i.e. Δh_o does not always decrease with φ_c. This

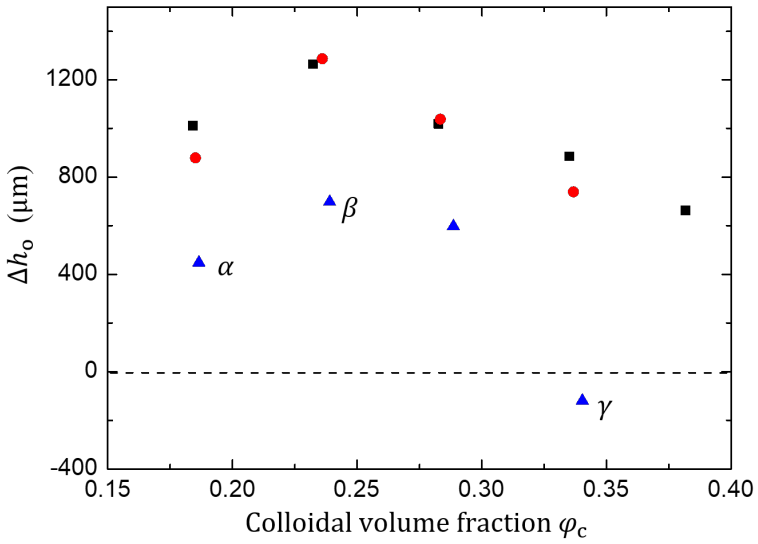

Figure A.4 *The onset height (Δh_o) of rapid collapse vs. colloidal volume fraction with different polymer concentration.* $c_p = 3\,\mathrm{mg/ml}$ *(■),* $4\,\mathrm{mg/ml}$ *(●); and* $5\,\mathrm{mg/ml}$ *(▲). The onset heights of sample α, β and γ are indicated.*

may not be what one expects. Because, the extra mass of the denser layer comes from the meniscus above Δh_o. Follow the idea of the yielding of the gel by the denser layer, one may expect the onset height of the rapid collapse (Δh_o) should decrease both with φ_c and c_p, because higher φ_c or c_p leads to higher yield stress σ_y, so that the denser layer requires more mass to yield the gel.

Without knowing the volume above Δh_o, no quantitative explanation can be made why Δh_o behaves in this way. To speculate the reason, we first notice that the shape of the menisci of gels may change with φ_c, because the contact angle Θ is composition dependent. Second, the colloidal volume fraction above the base of meniscus is assumed to be the same as that of the bulk. Considering that the increment of φ_c can lead to higher mass accumulation. This suggests, at low φ_c, the increment of φ_c leads to higher yield stress; at the same time, it also leads to more mass at the top of gel, which is needed to yield the gel. This may be responsible for the decrease of Δh_o as φ_c increases from 0.18 to 0.23. On the other hand, solvent droplets can also bring debris to the top. However, at low φ_c, solvent droplet is rare. The mass accumulation of low φ_c will mainly rely on the colloids above Δh_o. This may also be responsible for the existence of the maximum of Δh_o.

A.5 The Delay Time

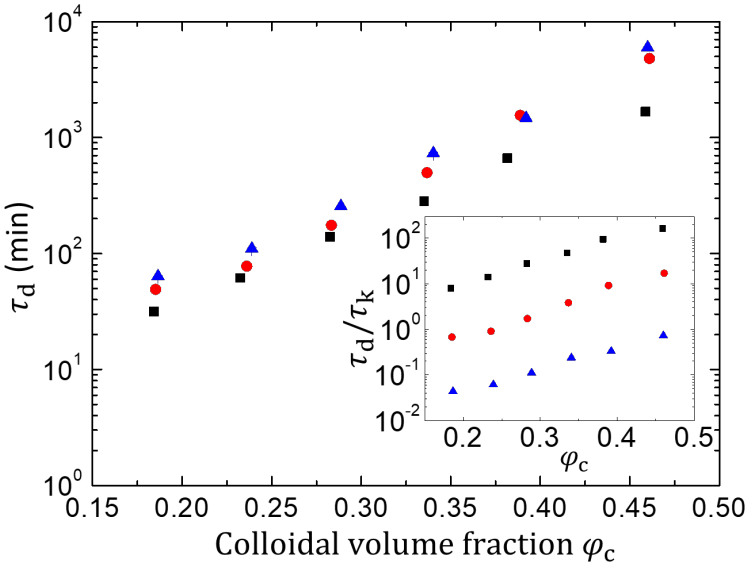

Figure A.5 *Delay time τ_d of large-colloid gels with varying colloidal volume fraction φ_c and polymer concentration c_p. The inset plots τ_d/τ_k against φ_c. c_p =* 3 mg/ml *(■), 4 mg/ml (●); and 5 mg/ml (▲).*

The delay time of gels with varying colloidal volume fraction φ_c and polymer concentration c_p are plotted in figure A.5. Generally, higher φ_c and/or c_p leads to longer delay time.

In a gel system formed by long-range depletion attraction, P. Bartlett *et al.* have studied the origin of the delay time. They found that the delay time is proportional to the Kramers escape time of a single-particle bond τ_k (hence, τ_d/τ_k is close to a constant) for a wide range of c_p [54]. τ_k is the escape time for a particle to break a bond due to thermal fluctuation. They proposed that the spontaneous thermal fluctuations is crucial in determining the delay time of the gel with long-range attraction.

Here, I apply the same analysis to our system. To obtain analytic expression for τ_k, the depletion potential is approximated by a ramp potential of the same depth and width. The Kramers escape time τ_k is given by [105]:

$$\tau_k = \frac{\Delta^2}{D_s} \frac{\exp(-U_{dep}(2a)/k_BT) - (1 - U_{dep}(2a)/k_BT)}{(U_{dep}(2a)/k_BT)^2} , \qquad (A.2)$$

where $\Delta = 2R_g$ is the width of the potential, D_s is the self-diffusion coefficient of

the particle inside the well, $U_{\mathrm{dep}}(2a)$ is the depth of the potential. To estimate τ_{k} we need the diffusion coefficient D_{s} for particles confined to each others' potential wells. For a hard-sphere suspension, P. N. Segrè *et al.* [106] found that $D_{\mathrm{s}} = kD_0$, where k is a coefficient that depends on the (local) colloidal volume fraction, and D_0 is the free-particle diffusion coefficient that varies with the viscosity of the PS solution (therefore c_{p}). To estimate the local colloidal volume fraction φ_{local}, the average surface-to-surface distance is assumed to be twice the thickness of the depletion zone, i.e. $2R_{\mathrm{g}}$. Therefore, $\varphi_{\mathrm{local}} = \varphi_{\mathrm{RCP}} \times a^3/(a + R_{\mathrm{g}})^3 \approx 0.55$. Hence, from Ref. [106], we have $D_{\mathrm{s}} = 0.2D_0$. $\tau_{\mathrm{d}}/\tau_{\mathrm{k}}$ is plotted in the inset of figure A.5.

In our gels, $\tau_{\mathrm{d}}/\tau_{\mathrm{k}}$ decreases with increasing polymer concentration. This may come from the fact that the depletion potential $U_{\mathrm{dep}}(2a)$ is calculated assuming the radius of gyration of the polymer R_{g} in all concentration is the same. However, the R_{g} may decrease due the the solvent is a good solvent for polystyrene. This leads to a smaller $U_{\mathrm{dep}}(2a)$ at higher c_{p}, thus a lower τ_{k}. This means the $\tau_{\mathrm{d}}/\tau_{\mathrm{k}}$ curves in the inset of figure A.5 may be shifted vertically. Hence, the result here cannot test if $\tau_{\mathrm{d}}/\tau_{\mathrm{k}}$ is a constant for varying c_{p}.

$\tau_{\mathrm{d}}/\tau_{\mathrm{k}}$ also increase with φ_{c}. The effect on $U_{\mathrm{dep}}(2a)$ with increasing φ_{c} should have been mostly compensated by Eq. 2.1. Considering that the $\tau_{\mathrm{d}}/\tau_{\mathrm{k}}$ at high φ_{c} is one order of magnitude higher than that at lowest φ_{c}, this trend should not be attributed to the way $U_{\mathrm{dep}}(2a)$ was estimated. The result that $\tau_{\mathrm{d}}/\tau_{\mathrm{k}}$ increase with φ_{c} is expected. The escape time τ_{k} accounts for a single bond. With increasing φ_{c} colloids are bonded with more neighbours. The time needed for a colloid to break the cage increases with φ_{c}. Therefore, if the spontaneous thermal fluctuation is crucial as proposed in Ref. [54], $\tau_{\mathrm{d}}/\tau_{\mathrm{k}}$ is expected to increase with φ_{c}.

The onset time of the rapid collapse τ_{o} has been defined in figure 8.7. Figure A.6 plots τ_{o} against colloidal volume fraction φ_{c} with different polymer concentration c_{p}. τ_{o} is reasonably well re-produced when repeating the experiments. The errors of τ_{o} are $\approx 10\%$. The dependency of τ_{o} on φ_{c} is exponential-like for 3 mg/ml gels. With higher c_{p}, the dependency deviates from exponential-like at low φ_{c}. Generally, higher φ_{c} and/or c_{p} leads to longer τ_{o}.

It is reasonable to consider the onset of rapid collapse as the beginning of the delayed collapse, i.e. taking τ_{o} as the delay time. With this assumption, $\tau_{\mathrm{o}}/\tau_{\mathrm{k}}$ is plotted in the inset of figure A.6. Similar to $\tau_{\mathrm{d}}/\tau_{\mathrm{k}}$, $\tau_{\mathrm{o}}/\tau_{\mathrm{k}}$ increases with increasing

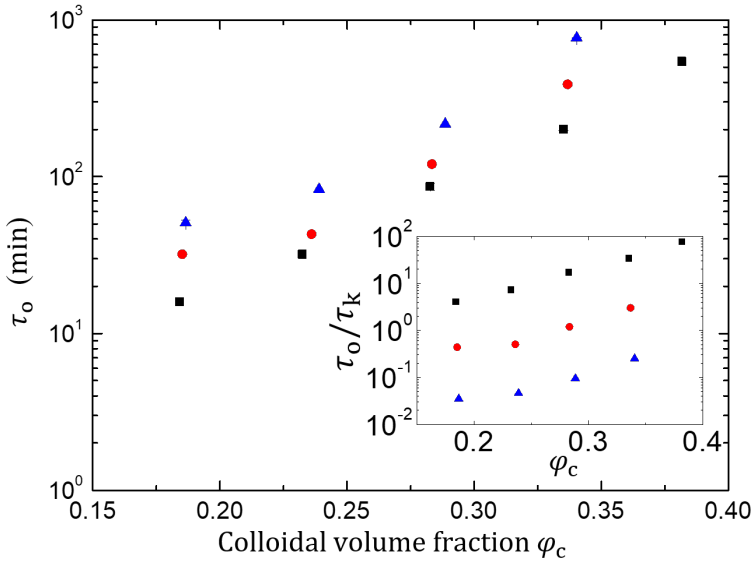

Figure A.6 *Onset time of rapid collapse τ_o of large particle gels with varying colloidal volume fraction φ_c and polymer concentration c_p. The inset plots τ_o/τ_k against φ_c. $c_p = 3\,\mathrm{mg/ml}$ (■), $4\,\mathrm{mg/ml}$ (●); and $5\,\mathrm{mg/ml}$ (▲).*

φ_c and decreases with increasing c_p.

Similar to the discussion in previous part, the τ_o/τ_k may be shifted due to the variance of R_g. Also, the increase of τ_o/τ_k with φ_c is reasonable.

A.6 Propagation of the Onset of Rapid Collapse

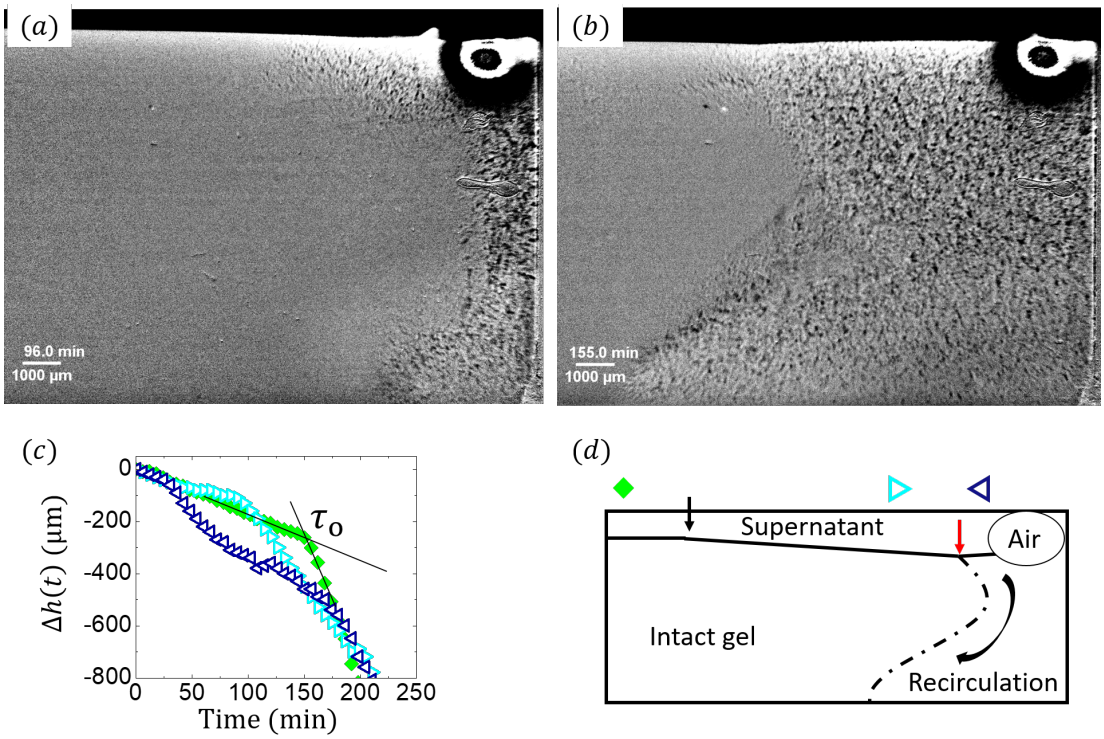

Figure A.7 *(a) and (b): Micrographs of gel β ($\varphi_c = 0.24$, $\varphi_p^{free} = 0.565$) in geometry $\mathbb{D}$, showing the propagation of onset of rapid collapse and the recirculation. (c): Height profiles of gel β in geometry $\mathbb{D}$ are re-plotted from figure 7.9. (d): Key features in the propagation of onset of rapid collapse in geometry $\mathbb{D}$. The gel interface that separates the supernatant and the gel is bended as indicated by the black arrow. A trough (red arrow) can also be found near the air bubble. The curved arrow indicates the recirculation of the colloids. The dash-dotted line denotes the front of the recirculation. Symbols indicate the measure-positions of the height profiles in (c).*

With large width of sample, gel β ($\varphi_c = 0.24$, $\varphi_p^{free} = 0.565$) in geometry $\mathbb{D}$ clearly shows a propagation of the recirculation from the air bubble side to the opposite side, figure A.7(a) and (b). The height profiles measured at 3 locations (near the air bubble ◁, near the middle of the sample width ▷ and far away from the air bubble ◆) also suggest that the onset of the rapid collapse commences around the air bubble and propagates to the opposite side, see figure A.7(c). Figure A.7(d) illustrates the key features during this two propagations. A clear sharp gel interface separates the supernatant from the settling gel. Near the air bubble, the gel structure is broken by the recirculation, while the gel structure far away remains intact. A front of recirculation encroaching the intact gel can be seen, as schematically represented in figure A.7(d) by the dash-dotted line.

Since the onset of the rapid collapse propagates across the sample, the interface is expected to be bended at the location where the rapid collapse just commences, for example, the location indicated by the black arrow in figure A.7(d). Left to this location, the gel still settles slowly; while right to this location, the gel already settles rapidly. To test this hypothesis, the shape of the gel interface is extracted from the micrographs and plotted with varying time in figure A.8. By comparing the shape of the interface with the height profiles, the bending of the interface as indicated by the black arrows can be correlated to the onset of the rapid collapse. Such bending position (indicated by the black arrows) moves leftwards with a speed about 2 µm/s as the onset of the rapid collapse propagates.

Interestingly, after $t = 96$ min, a trough (indicated by the red arrows in figure A.8) can also be seen in the gel interface which also propagates leftwards. Comparing to the micrographs, such troughs correspond to the falling of the denser layer at the top, i.e. it is related to the large-scale recirculation, see figure A.7(d).

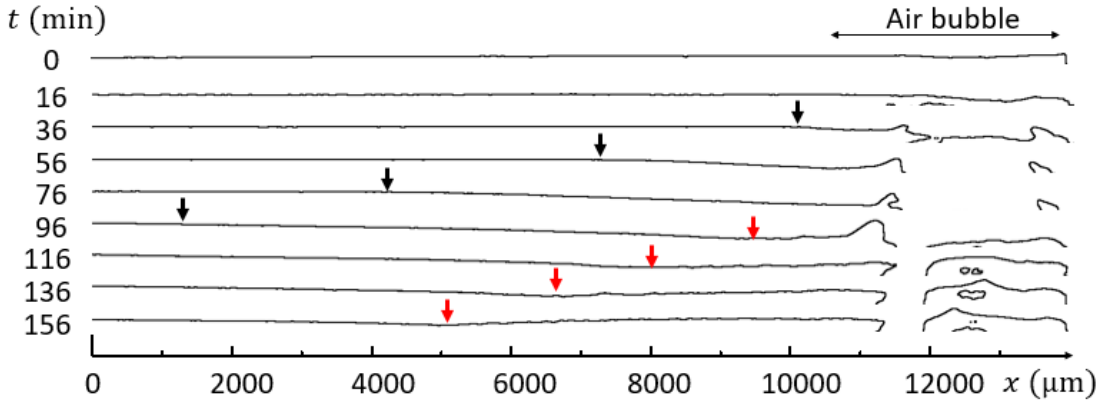

Figure A.8 *Shape of the gel interface of gel β changes with time in geometry $\mathbb{D}$. The gel interface is bended at two locations (indicated by the black and red arrows, respectively.*

In geometry $\mathbb{D}$, once the rapid collapse is triggered, it propagates much faster than the recirculation. The result shown here suggests that the propagation of the rapid collapse is not due to the recirculation in the gel. However, the mechanism of this propagation is unclear at the moment. When the rapid collapse is triggered around the air bubble, the rest of the gel remain intact. Presumably, the gel on the left is pulled down by the colloids on the right through the network so that the onset of the rapid collapse is propagated, figure A.7(d). I speculate that slowing down this propagation may retard the delay collapse even further.

A.7 Verification of the Postponement of the Rapid Collapse

To verify the key observations made from gel β ($\varphi_c = 0.24$, $\varphi_p^{free} = 0.565$) in Sec. 7.3, a gel with $\varphi_c = 0.23$, $\varphi_p^{free} = 0.338$ was also studied in the four geometries shown in figure 7.1.

The sample preparation in each geometries is described in Sec. 7.2; however, in geometry $\mathbb{C}$ and $\mathbb{D}$, the radius of the air bubble is about 3 mm, which is much larger than that of gel β. Also, in geometry $\mathbb{C}$ and $\mathbb{D}$, the sample was sealed with a Teflon stopper and warped with PTFE and Parafilm. The height profiles in different geometries are plotted in figure A.9.

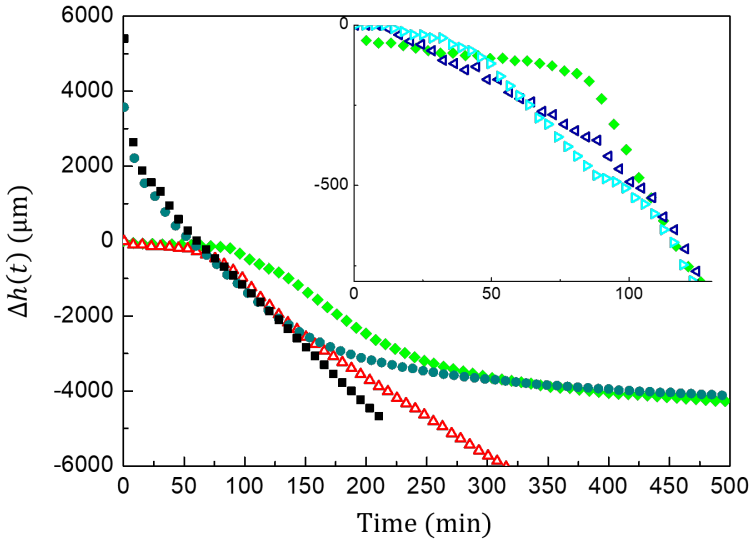

Figure A.9 *Height profiles of a rapid collapse gel ($\varphi_c = 0.232$, $\varphi_p^{free} = 0.338$) in geometry $\mathbb{A}$, $\mathbb{B}$, $\mathbb{C}$ and $\mathbb{D}$. The inset expose the details of the same data to show the initial stage of the collapse in geometry $\mathbb{D}$. The symbols correspond to those used in figure 7.1 along with the illustration of the geometries.*

A.7.1 Geometry 𝔸

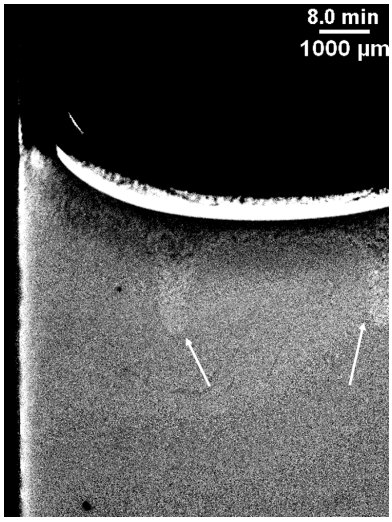

Figure A.10 *Microscopic image of gel* $\varphi_c = 0.23$, $\varphi_p^{free} = 0.338$ *in geometry* 𝔸. *White arrows indicate the finger-like clusters.*

In geometry 𝔸, as the colloids fall from the corner of meniscus, finger-like clusters can be found generating at the top of gel at $t \approx 8$ min, figure A.10. The falling of denser layer creates a strong back flow, which triggers the rapid collapse. The onset time of rapid collapse is $\tau_o = 32$ min, the delay time is $\tau_d = 61.5$ min, and the interface speed of rapid collapse is $v_i = 526 \pm 1$ nm/s. No solvent droplet can be found.

A.7.2 Geometry 𝔹

In geometry 𝔹, the gel collapses with the same mechanism as in geometry 𝔸. As shown in figure A.11, finger-like cluster can be found falling through the gel. Also, in geometry 𝔹, no solvent droplet can be found before the onset of rapid collapse. The height profile is plotted as ● in figure A.9. The onset time of rapid collapse is $\tau_o = 28$ min, about 13% shorter than that in geometry 𝔸; the delay time $\tau_d = 56.5$ min, 8% shorter than that in that in geometry 𝔸; and $v_i = 490 \pm 1$ nm/s, about 7% slower than that in geometry 𝔸. Hence, the gel in geometry 𝔹 starts collapsing slightly earlier than but very close to that in geometry 𝔸.

Figure A.11 *Microscopic image of gel* $\varphi_c = 0.23$*,* $\varphi_p^{free} = 0.338$ *in geometry* $\mathbb{B}$*. White arrow indicates the finger-like cluster.*

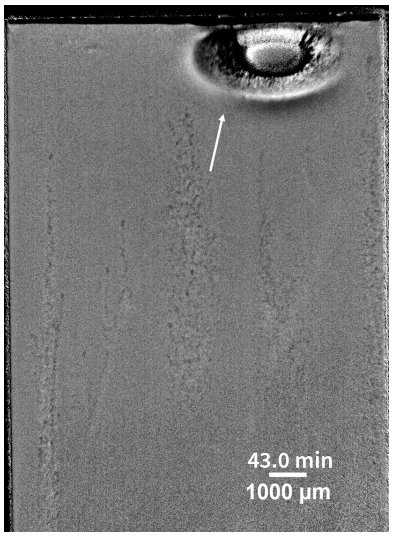

Figure A.12 *Microscopic image of gel* $\varphi_c = 0.23$*,* $\varphi_p^{free} = 0.338$ *in geometry* $\mathbb{C}$*. White arrow indicate a forming cluster. Solvent droplets can be found rising both at the edge and in the centre of the image.*

A.7.3 Geometry $\mathbb{C}$

$\mathbb{C}$

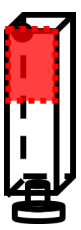

In geometry $\mathbb{C}$ only the face with air bubble (the red dashed square in figure 7.1) was imaged. The height profile measured at the edge that far away from the air bubble is plotted in figure A.9 as △. Not only clusters, but also solvent droplets were observed, figure A.12. The solvent droplets interact with the falling cluster. The onset time of rapid collapse is $\tau_o = 73$ min, which is longer than τ_o but close to τ_d in geometry $\mathbb{A}$ and $\mathbb{B}$. Hence, for this gel, geometry $\mathbb{C}$ does not yield a prolonged rapid collapse. Also notice that, after about 140 min, the interface

speed decrease from 519 ± 5 nm/s to 344.3 ± 0.6 nm/s. At $t \approx 140$ min, the gel interface detached from the air bubble. When the experiment was repeated, the gel interface speed also decrease as it detached from the air bubble. Hence, this speed change may be related to the detachment from the air bubble. Interestingly, in geometry $\mathbb{C}$, solvent droplets were observed both at the edge of cuvette and in the centre of the image. Therefore, the key process observed in figure 7.5 is reproduced, i.e. clusters fall from the air bubble and solvent droplets rise.

A.7.4 Geometry $\mathbb{D}$

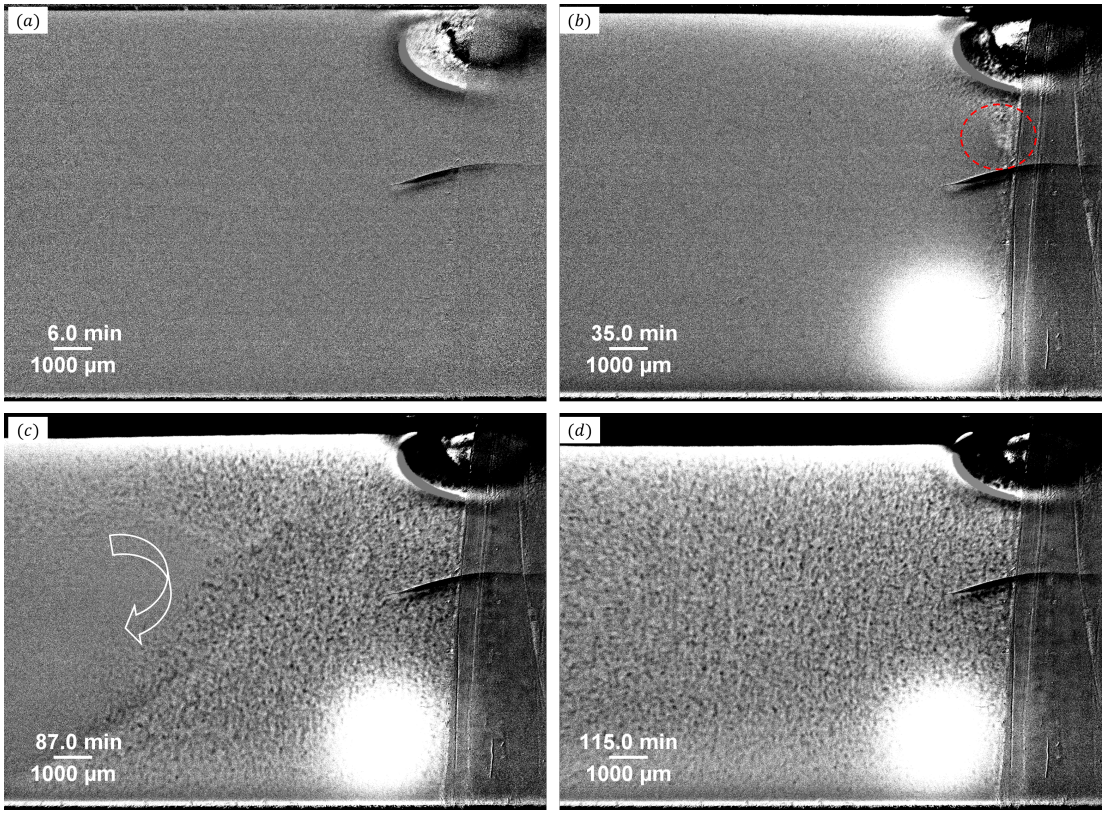

Figure A.13 *Microscopic image of gel* $\varphi_c = 0.23$, $\varphi_p^{free} = 0.338$ *in geometry* $\mathbb{D}$ *at air bubble side. Red dashed circle indicate a finger-like cluster. The large bright spot at the bottom right of the images figure A.13(b) - (d) is due to an LED light in the environment that shifted on 14 min after the time-lapse was started. The strip-like object on the left of the images is the Parafilm that wraps the cuvette. It become more visible because the illumination of the sample is changed by the extra LED light, so that the imaging process fails to remove it. However, the main observation reported here is not affected.*

In geometry $\mathbb{D}$, the faces with and without air bubble were imaged simultaneously as illustrated in figure 7.1.

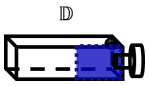

Near the air bubble Figure A.13 shows the images of gel $\varphi_c = 0.23$, $\varphi_p^{free} = 0.338$ at the air bubble side. At $t = 35$ min, a cluster was found falling from the air bubble. Around this time, the settling of the gel interface near air bubble speeds up, ◁ in figure A.9, and rapid collapse commences at this point. From the height profiles measured at different locations, the propagation of the rapid collapse can be seen, see the inset of figure A.9. Also, the falling of clusters created large-scale recirculation that propagated towards the other end of cuvette, figure A.13(b) - (d).

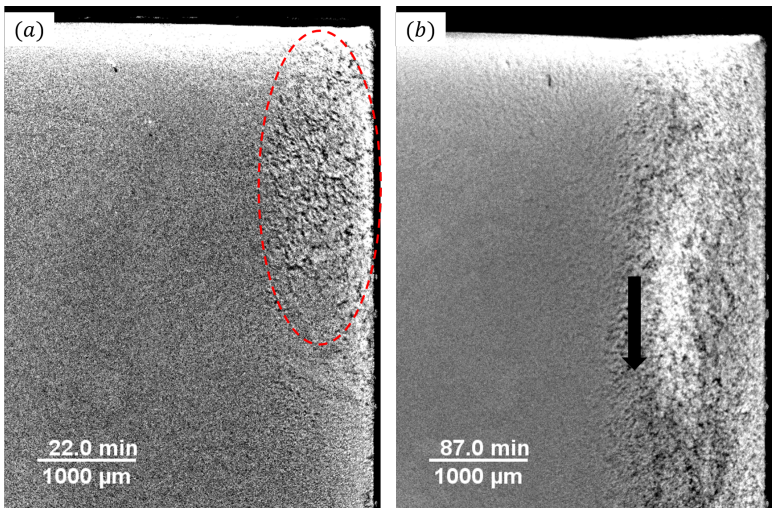

Figure A.14 *Microscopic image of gel $\varphi_c = 0.23$, $\varphi_p^{free} = 0.338$ in geometry $\mathbb{D}$ far away from the air bubble. The red dashed circle indicates solvent droplets close to the edge of the cuvette. The black arrow indicates the falling of bright debris.*

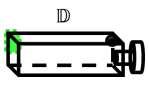

Far from air bubble At the other end of cuvette (the green dashed square in figure 7.1), the gel was imaged using a 2× objective. The images are shown in figure A.14. Solvent droplets can be found rising close to the edge of cuvette, as indicated by the red dashed circle in figure A.14(a). At $t = 87.0$ min, a stream of bright debris can be found falling from the top of gel, as indicated by the black arrow in figure A.14(b). Around this time, the settling speed of the gel interface in the centre of the image suddenly increases, ◆ in the inset of figure A.9. The rapid collapse is therefore triggered. This result is similar to the second observation of gel β in geometry $\mathbb{D}$. Notice that, from figure A.9, geometry $\mathbb{D}$ can prolong the delay time.

A.7.5 Summary

Generally, the results of gel with $\varphi_c = 0.23$, $\varphi_p^{free} = 0.338$ reproduce the key observations of gel β in different geometries. Interestingly, by eliminating most of the meniscus, the collapse mechanism of the gel $\varphi_c = 0.23$ and $\varphi_p^{free} = 0.338$ shifts from clusters falling (D1 behaviour) to clusters and solvent droplets interacting (D2 behaviour).

The height profiles in figure A.9 show that the postponement of collapse is not significant especially in geometry $\mathbb{C}$, compared to the result shown in figure 7.12. This may be due to the large air bubble that covers more than half of the top of cuvette in geometry $\mathbb{C}$ for the gel $\varphi_c = 0.23$, $\varphi_p^{free} = 0.338$. Compared to the full size meniscus in geometries $\mathbb{A}$ and $\mathbb{B}$, the large air bubble does not reduce significantly the mass that can contribute to the formation of denser layer. Therefore, the rapid collapse is prolonged only slightly.

A.8 Micrographs of a Creaming Gel

Here, I report the 'collapse' of the creaming gel in a cuvette that is reported in Sec. 8.2.1.2.

Figure A.15 shows the height profile $\Delta h(t)$ *vs.* t of the creaming gel $\varphi_c = 0.25$ and $c_p = 3$ mg/ml in a cuvette. The height of the gel interface is defined with respect to the bottom of the cuvette (as indicated by the white dashed line in the inset of figure A.15). The creaming gel detaches from the bottom of the cuvette at $t = 185.0$ min. After the detachment, the interface speed v_i gradually accelerates for about 700 min and reaches a constant speed of $v_i = 161 \pm 1$ nm/s. It suggests that the creaming gel is a rapid collapse gel. The final compression started at about $t = 1200.0$ min. The height profile of the creaming gel is qualitatively similar to that of gel β in geometry $\mathbb{C}$ which is a rapid collapse with a (mostly) flat top, see the inset of figure 7.3.

Figure A.16 shows the microscopic side-view image of the creaming gel in a cuvette. The black edges on the left and the bottom of figure A.16(a) are the glass of the cuvette. Figure A.16(a) shows that the gel was homogeneous at $t = 2.0$ min. At $t = 200.0$ min, cracks can be found in the gel. Also, the first solvent droplet in the experimental window reached the gel interface (at the

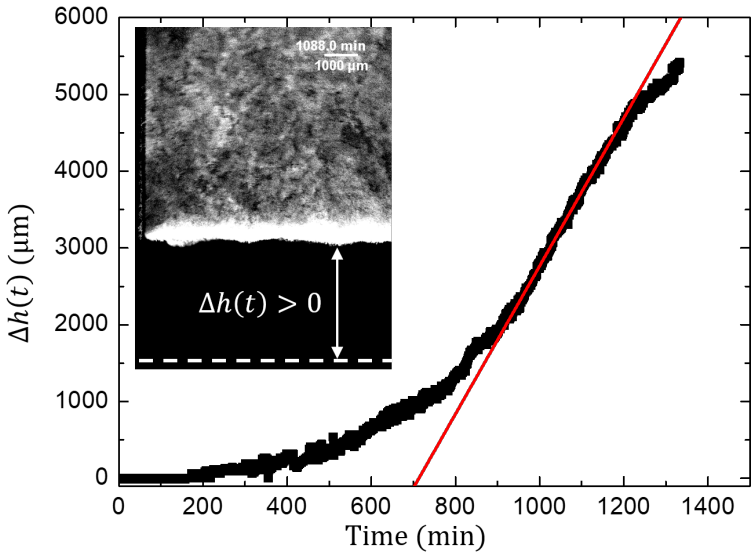

Figure A.15 *Height profile of the creaming gel* $\varphi_c = 0.25$ *and* $c_p = 3$ mg/ml *in a cuvette. The red line is a linear fit to the rapid sedimentation. The inset shows a processed micrograph of the creaming gel. The white dashed line indicates the bottom of the cuvette. The height of the gel interface* $\Delta h(t)$ *is as defined.*

bottom of the creaming gel). This was after the gel detached from the bottom glass. The speed of the first droplet in gravitational direction was about 2.5 µm/s. From figure A.16(b) and (c), solvent droplets descended from the bulk of the gel in skewed trajectories. No sign of the falling of finger-like cluster can be found in this creaming gel.

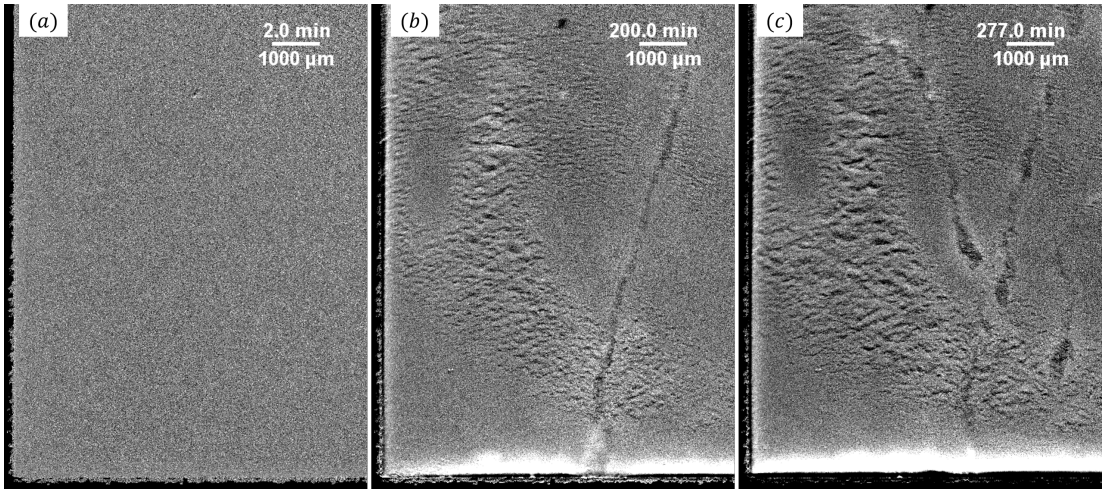

Figure A.16 *Micrographic side-view images of the creaming gel* $\varphi_c = 0.25$ *and* $c_p = 3$ mg/ml *in a cuvette. (a) The gel was homogeneous at* $t = 2.0$ *min. (b) Cracks can be found in the gel. The first solvent droplet in the experimental window reached the gel interface after the gel detached from the glass. (c) More solvent droplets can be found descending from the top. Solvent droplets did not descend vertically.*

A.9 Solvent Droplets in Laser Scanning Confocal Microscopy

The creaming gel (reported in Sec. 8.2.1 and Appendix A.8) was studied using laser scanning confocal microscope Zeiss LM700. The creaming gel was transferred in to a bottom-cut vial that was sealed with a cover slice. The sample height was about 6 mm. The sample was shaken by hand before each experiments. The room temperature was 23 ± 0.5 °C. The 3D stacks with size of $640\,\mu m \times 640\,\mu m \times 1200\,\mu m$ were taken using a 20× objective (Zeiss, NA=0.4). The pixel size in xy-plane is 5 µm/pixel. The pixel size in z-axis is 7.5 µm/pixel, which is scaled by the focus shift in the paraxial limit $k(n) = n_1/n_2$, where $n_1 \approx 1.5$ and $n_2 \approx 1$ are the refractive index of the solvent in the sample and the mediate between the lens and the sample, respectively [107]. The first image of each 3D stack ($z = 0$ image) was taken about 10 um beneath the cover slice. Time interval between two 3D stacks is 2 min.

Figure A.17 shows the confocal image of a solvent droplet at $t = 260$ min. The observation position was about 1 mm away from the edge of the sample. The corresponding position of three orthogonal planes are indicated by the yellow lines in the images. The gravitational direction is indicated for each planes. The position of the glass slice can be identified after the gel detaches, because some of the PMMA particles still attach to the glass. The gel interface is much brighter and deep inside the gel is darker. Because the excitation light is scattered by the colloids and absorbed by the dye, the laser can not penetrate deep inside the gel. As the solvent droplet approaches the gel interface, colloids at the surface of the droplet deep inside of the gel can be illuminated, for example, the colloids as indicated by the red circle in xz-plane in figure A.17. The droplet is darker, because it is solvent-rich. The confocal image provides a close view of the tear-drop shape of the droplet. The droplet is ~ 350 µm wide. From xy-plane image, the droplet does not exhibit axial symmetry. From vertical-plane images, the interface between the droplet and the gel structure is coarsened. The surface of the droplet is not smooth. It suggests an anisotropic surface tension and heterogeneous gel structure on the length scale of the droplet.

Figure A.18 shows the time-series images in xz-plane. The observation position was about 2 mm away from the edge of the sample. At $t = 2$ min, the gel was homogeneous. At $t = 96$ min, the gel interface detached from the glass slice. At

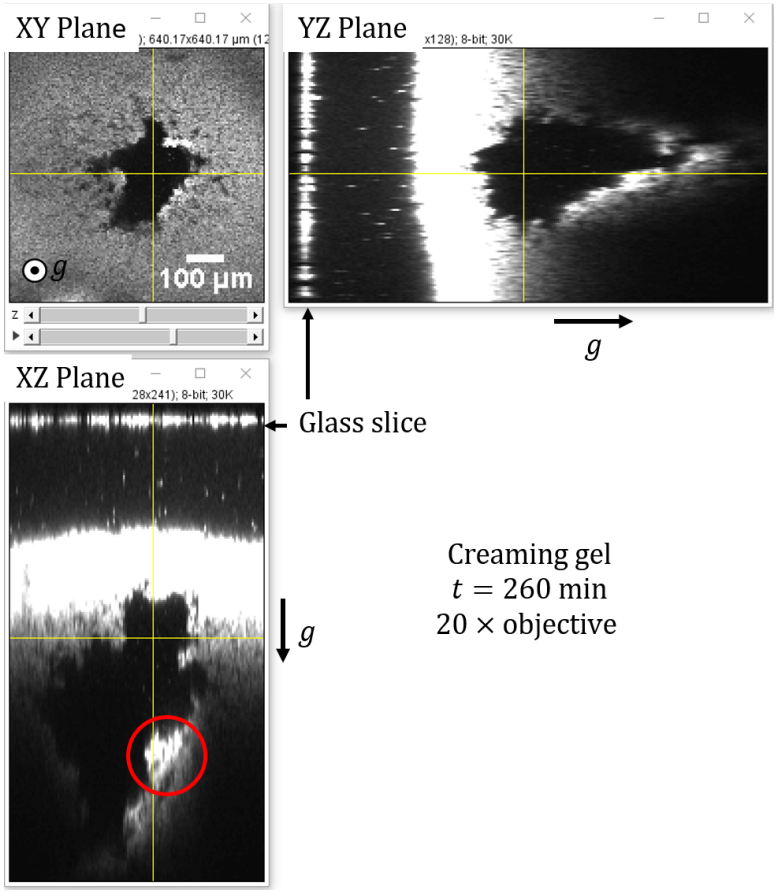

Figure A.17 *Confocal image of a solvent droplet in the creaming gel* $\varphi_c = 0.25$ *and* $c_p = 3$ mg/ml.

$t = 110$ min, the first solvent droplet came into the experimental window. The image of $t = 110$ min shown here is contrast-adjusted for easy-viewing. At about $t = 128$ min, the solvent droplet reached the interface and the volcanic eruption can be seen. As the solvent droplet descended, its shape varied and debris was brought to the interface. However, for the first droplet, no obvious erosion of the surrounding gel structure can be observed as the solvent passes through the track. The second solvent droplet can be found at $t = 152$ min. It was very close to the first one. As it descended, it closed up the track left by the first droplet. More debris came out from the second volcano, $t = 178 \sim 234$ min. Solvent flow eroded the surrounding gel structure was evidenced. The third solvent droplet can be seen at $t = 230$. Its corresponding eruption cannot be viewed directly in this xz-plane; however, the large crater it created can be seen in the image at $t = 234$ min. Debris accumulated at the gel interface and creamed with the gel.

The confocal image shows that the surface of a droplet is coarsened. It suggests that the solvent droplet can detect the anisotropy of the structure. Also, the

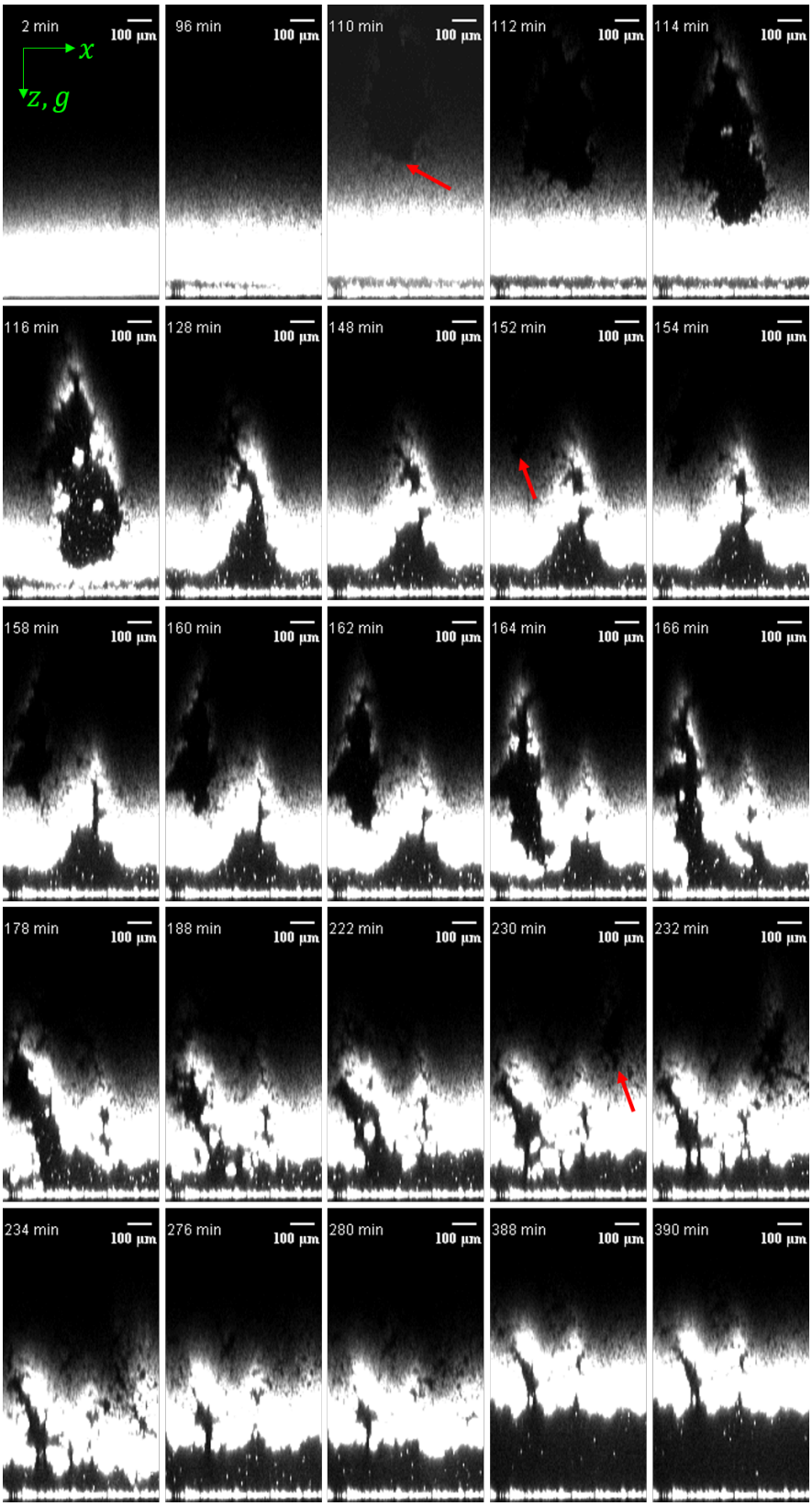

Figure A.18 *Confocal image of volcanic eruptions in the creaming gel* $\varphi_c = 0.25$ *and* $c_p = 3$ mg/ml. *Three eruptions are shown in the images. Red arrows point at the solvent droplets in their first appearing images.*

change of the shape as a solvent droplet travel through the gel suggests that the gel structure is heterogeneous. The skewed trajectory of the droplet observed in side-view micrographs (Appendix A.8) also suggests that the structure of a gel is heterogeneous on the length scale of a solvent droplet.

Appendix B

Rheology Study of Gel γ

The yield stress of the gel γ ($\varphi_c = 0.34$ and $\varphi_p^{free} = 0.586$) was measured using TA-DHR with 40 mm rough plane geometry at 23 °C. High rate steady shear ($\dot{\varepsilon} = 800\ s^{-1}$) was performed followed by a waiting time of typically 500 s before each test. This waiting time was determined by a linear viscoelastic measurement with a strain of $\varepsilon = 0.1\%$ and an angular frequency of $\omega = 1$ rad/s, figure B.1. The gradual increase in storage modulus G' and weakly decrease in loss modulus G'' shows a clear strengthening of the gel with time. After $t \approx 2000$ s, G' slowly decreases. This may be due to the collapse of the gel.

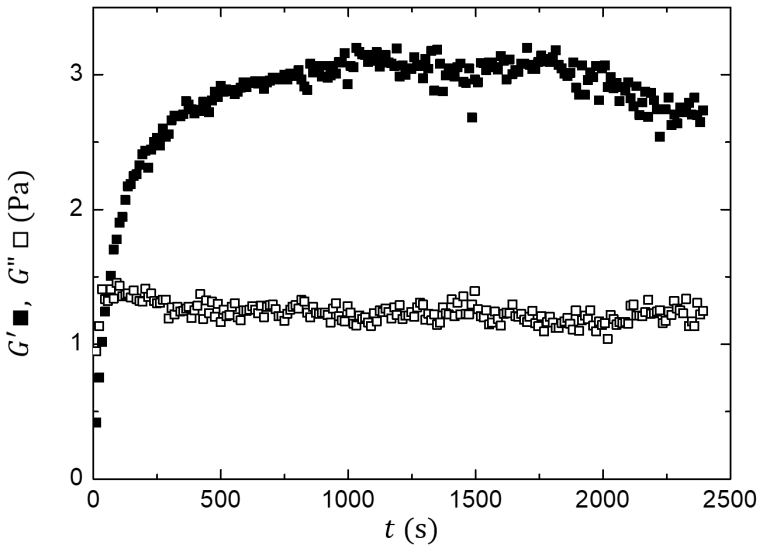

Figure B.1 *Linear viscoelastic measurement for gel γ at $\omega = 1$ rad/s and $\varepsilon = 0.1\%$.*

The frequency respond of gel γ was measured at $\varepsilon = 0.1\%$, figure B.2. The weak

dependence of G' and the minimum of G'' is the typical frequency respond of colloidal glasses and gels [95, 108, 109].

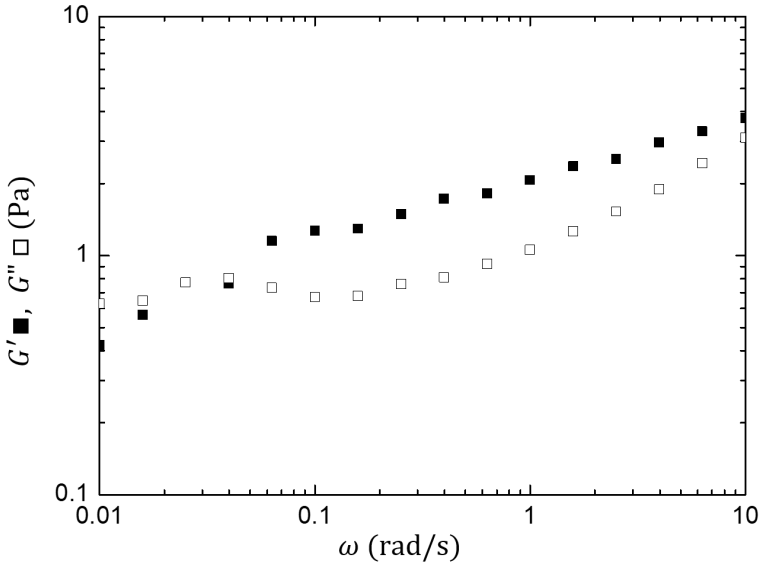

Figure B.2 *Frequency respond of gel γ at $\varepsilon = 0.1\%$.*

Dynamic strain sweep was performed at $\omega = 1$. Figure B.3 plots the storage and loss modulus against the measured strain ε. At low strain, $G' > G''$; the structure is solid-like. As the strain increases, G'' exhibits a broad peak and decreases at high strain. At the same time, G' varies weakly with low applied strain and decreases as the strain increases above $\varepsilon \sim 1$ %. G' decreases faster than G''; they crossover at ε_c.

The peak strain of G'' is close to the size ratio $\xi = 0.05$. It is linked to the breaking of the inter-particle bond [95]. Higher than the crossover strain ε_c, $G' < G''$, suggesting that the gel structure is fluid-like. For gel γ, ε_c is close to strain of bond-breaking. It suggests a rarefied gel structure, so that the sample may melt upon the breakage of some of the inter-cluster bonds which keep the percolating network solid [95]. It is reasonable to define the crossover strain as the yield strain of gel ε_y, although defining the yield strain of a gel itself was demonstrated to be complicated [95, 110, 111].

At high strain, $\varepsilon \approx 10^3$ %, G' decreases more slowly; also G'' ceases decreasing. This phenomenon resembles the cage breaking of a small-colloids gel [95, 112].

Figure B.4 plots G' and G'' *vs* measured stress σ. Corresponding to the yield

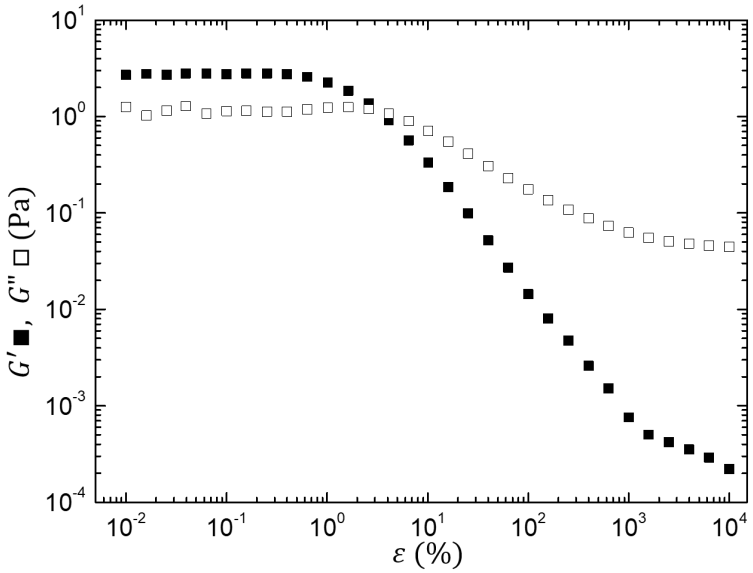

Figure B.3 *Dynamic strain sweep of gel γ at $\omega = 1$. $G'(\blacksquare)$, $G''(\square)$ vs. ε.*

strain, the yield stress of gel σ_y can be defined. For gel γ, $\sigma_y \approx 53$ mPa.

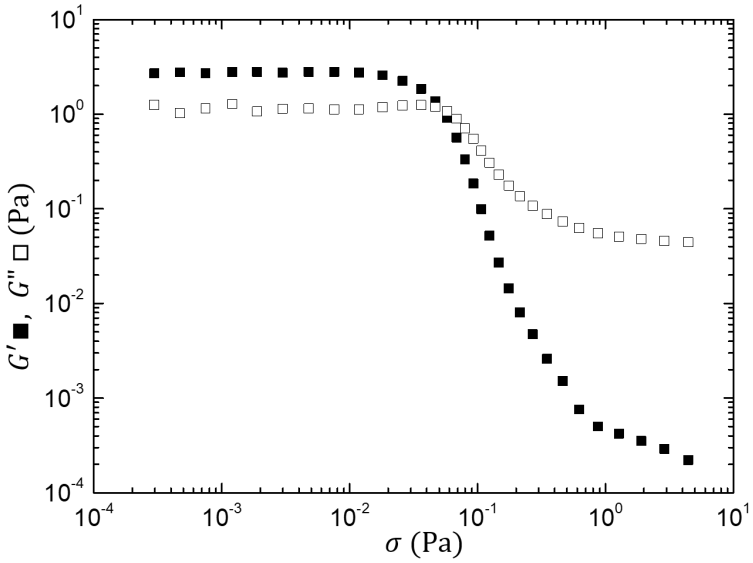

Figure B.4 *Dynamic strain sweep for gel γ at $\omega = 1$. $G'(\blacksquare)$, $G''(\square)$ vs. σ.*

Figure B.5 shows the flow curve of gel γ. The stress σ and the viscosity of gel η_g are plotted against the shear rate $\dot{\varepsilon}$. Above $\dot{\varepsilon} \approx 10$ s^{-1}, $\sigma \sim \dot{\varepsilon}$ and η_g only weakly depends on $\dot{\varepsilon}$, i.e. the sample is fluid-like. Below $\dot{\varepsilon} \approx 0.03$ s^{-1}, the stress reaches a plateau. The sample is solid-like. The plateau value of the stress is ~ 55 mPa, which is close to the yield stress $\sigma_y = 53$ mPa. The stress at lowest $\dot{\varepsilon}$ is slightly smaller, this can be caused by the short waiting time (10 s) before the

data acquisition.

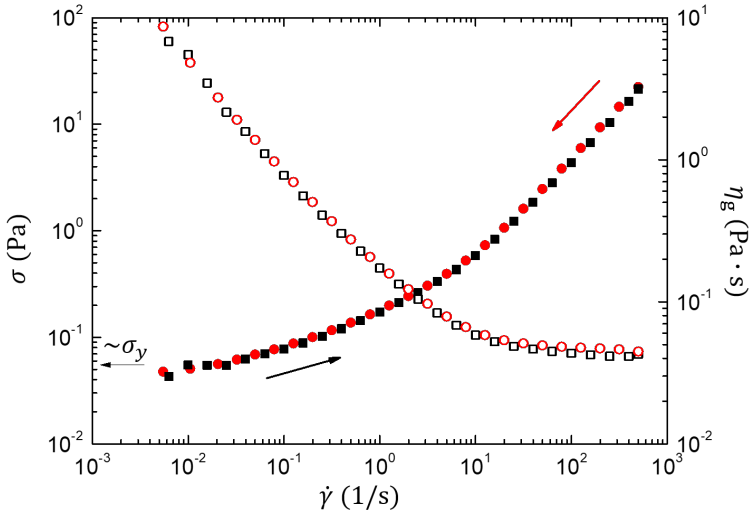

Figure B.5 *Flow curve of gel γ. The stress σ (solid symbol) and the viscosity of gel η_g (open symbol) are plotted against the shear rate $\dot{\varepsilon}$. The colour arrows indicate the direction of the experiment (black squares: increasing shear rate; red circles: decreasing shear rate).*

Bibliography

[1] van Blaaderen, A. & Wiltzius, P. Real-space structure of colloidal Hard-Sphere Glasses. *Science* **270**, 1177 (1995).

[2] Besseling, R., Isa, L., Weeks, E. R. & Poon, W. C. K. Quantitative imaging of colloidal flows. *Advances in colloid and interface science* **146**, 1–17 (2009). URL http://www.ncbi.nlm.nih.gov/pubmed/19012873.

[3] Jenkins, M. C. & Egelhaaf, S. U. Confocal microscopy of colloidal particles: towards reliable, optimum coordinates. *Advances in colloid and interface science* **136**, 65–92 (2008). URL http://www.ncbi.nlm.nih.gov/pubmed/17869203.

[4] Brambilla, G. *et al.* Probing the Equilibrium Dynamics of Colloidal Hard Spheres above the Mode-Coupling Glass Transition. *Physical Review Letters* **102**, 085703 (2009). URL http://link.aps.org/doi/10.1103/PhysRevLett.102.085703.

[5] Laurati, M. *et al.* Structure, dynamics, and rheology of colloid-polymer mixtures: From liquids to gels. *The Journal of Chemical Physics* **130**, 134907 (2009). URL http://scitation.aip.org/content/aip/journal/jcp/130/13/10.1063/1.3103889.

[6] Menzel, A. M. Tuned, driven, and active soft matter. *Physics Reports* **554**, 1–45 (2015). URL http://linkinghub.elsevier.com/retrieve/pii/S0370157314003871.

[7] Poon, W. C. K. & Haw, M. Mesoscopic structure formation in colloidal aggregation and gelation. *Advances in colloid and interface science* **73**, 71–126 (1997). URL http://www.sciencedirect.com/science/article/pii/S0001868697900038.

[8] Sedgwick, H., Egelhaaf, S. U. & Poon, W. C. K. Clusters and gels in systems of sticky particles. *Journal of Physics: Condensed Matter* **16**, S4913–S4922 (2004). URL http://stacks.iop.org/0953-8984/16/i=42/a=009?key=crossref.435903944d6fa77a98282e1014d56d30.

[9] Pusey, P. & van Megen, W. Phase behaviour of concentrated suspensions of nearly hard colloidal spheres. *Nature* **320**, 340–342 (1986). URL http://www.physics.emory.edu/{~}weeks/lab/papers/pusey-nat86.pdf.

[10] Lekkerkerker, H. N. W., Poon, W. C. K., Pusey, P., Stroobants, A. & Warren, P. B. Phase Behaviour of Colloid + Polymer Mixtures. *Europhysics Letters* **20**, 559–564 (1992). URL http://iopscience.iop.org/0295-5075/20/6/015.

[11] Poon, W. C. K. Colloidal Suspensions. In *The Oxford Handbook of Soft Condensed Matter* (eds. Terentjev, E. M. & Weitz, D. A.), chap. 1, 1 (Oxford University Press, 2012).

[12] Hermes, M. & Dijkstra, M. Thermodynamic signature of the dynamic glass transition in hard spheres. *Journal of physics. Condensed matter : an Institute of Physics journal* **22**, 104114 (2010). URL http://www.ncbi.nlm.nih.gov/pubmed/21389448.

[13] Yethiraj, A. & van Blaaderen, A. A colloidal model system with an interaction tunable from hard sphere to soft and dipolar. *Nature* **421**, 513–517 (2003).

[14] Cheng, Z., Zhu, J., Russel, W. B., Meyer, W. V. & Chaikin, P. M. Colloidal hard-sphere crystallization kinetics in microgravity and normal gravity. *Applied Optics* **40**, 4146 (2001). URL http://ao.osa.org/abstract.cfm?URI=ao-40-24-4146http://www.sciencemag.org/lookup/doi/10.1126/science.aan5404https://www.osapublishing.org/abstract.cfm?URI=ao-40-24-4146.

[15] Tuinier, R. & Feenstra, M. S. Second virial coefficient at the critical point in a fluid of colloidal spheres plus depletants. *Langmuir* **30**, 13121–13124 (2014).

[16] Sanz, E. *et al.* Avalanches mediate crystallization in a hard-sphere glass. *Proceedings of the National Academy of Sciences of the United States of America* **111**, 75–80 (2014). URL http://www.pubmedcentral.nih.gov/articlerender.fcgi?artid=3890891{&}tool=pmcentrez{&}rendertype=abstract.

[17] Donev, A., Connelly, R., Stillinger, F. H. & Torquato, S. Underconstrained jammed packings of nonspherical hard particles: Ellipses and ellipsoids. *Physical Review E - Statistical, Nonlinear, and Soft Matter Physics* **75**, 1–32 (2007).

[18] Jones, R. A. *Soft Condensed Matter* (Oxford University Press, 2002).

[19] Royall, C. P., Poon, W. C. K. & Weeks, E. R. In search of colloidal hard spheres. *Soft Matter* **9**, 17 (2013). URL http://xlink.rsc.org/?DOI=c2sm26245b.

[20] Sciortino, F., Mossa, S., Zaccarelli, E. & Tartaglia, P. Equilibrium Cluster Phases and Low-Density Arrested Disordered States: The Role of Short-Range Attraction and Long-Range Repulsion. *Physical Review Letters* **93**,

055701 (2004). URL http://link.aps.org/doi/10.1103/PhysRevLett.93.055701.

[21] Campbell, A., Anderson, V., van Duijneveldt, J. & Bartlett, P. Dynamical Arrest in Attractive Colloids: The Effect of Long-Range Repulsion. *Physical Review Letters* **94**, 208301 (2005). URL http://link.aps.org/doi/10.1103/PhysRevLett.94.208301.

[22] Pusey, P. Liquids, Freezing and Glass Transition: Les Houches Session 80. (1991). URL https://books.google.co.uk/books?id=YC30nwEACAAJ.

[23] Hamaker, H. C. the London–Van Der Waals Attraction Between Spherical Particles. *Physica* **4**, 1058–1072 (1937). URL http://dx.doi.org/10.1016/S0031-8914(37)80203-7.

[24] Napper, D. H. & Netschey, A. Studies of the steric stabilization of colloidal particles. *Journal of Colloid And Interface Science* **37**, 528–535 (1971). URL http://linkinghub.elsevier.com/retrieve/pii/0021979771903304.

[25] Furukawa, A. & Tanaka, H. Key Role of Hydrodynamic Interactions in Colloidal Gelation. *Physical Review Letters* **104**, 245702 (2010). URL http://link.aps.org/doi/10.1103/PhysRevLett.104.245702.

[26] Varga, Z., Wang, G. & Swan, J. The hydrodynamics of colloidal gelation. *Soft Matter* **11**, 9009–9019 (2015). URL http://xlink.rsc.org/?DOI=C5SM01414J.

[27] Royall, C. P., Eggers, J., Furukawa, A. & Tanaka, H. Probing Colloidal Gels at Multiple Length Scales: The Role of Hydrodynamics. *Physical Review Letters* **114**, 1–5 (2015).

[28] Kamp, S. W. & Kilfoil, M. L. Universal behaviour in the mechanical properties of weakly aggregated colloidal particles. *Soft Matter* **5**, 2438–2447 (2009). URL http://xlink.rsc.org/?DOI=b814975e.

[29] Harich, R. *et al.* Gravitational collapse of depletion-induced colloidal gels. *Soft Matter* **94**, 218302 (2016). URL http://xlink.rsc.org/?DOI=C5SM02651B.

[30] Zhu, J. *et al.* Crystallization of hard-sphere colloids in microgravity. *Nature* **387**, 883–885 (1997).

[31] Poon, W. C. K., Weeks, E. R. & Royall, C. P. On measuring colloidal volume fractions. *Soft Matter* **8**, 21–30 (2012). URL http://xlink.rsc.org/?DOI=c1sm06083jhttp://dx.doi.org/10.1039/C1SM06083J.

[32] Underwood, S., Taylor, J. & Megen, W. V. Sterically stabilized colloidal particles as model hard spheres. *Langmuir* 3550–3554 (1994). URL http://pubs.acs.org/doi/abs/10.1021/la00022a030.

[33] Widom, B. Some Topics in the Theory of Fluids. *J. Chem. Phys.* **39**, 2808 (1963). URL http://scitation.aip.org/content/aip/journal/jcp/39/11/10.1063/1.1734110.

[34] Reiss, H., Frisch, H. L. & Lebowitz, J. L. Statistical Mechanics of Rigid Spheres. *The Journal of Chemical Physics* **31**, 369 (1959). URL http://scitation.aip.org/content/aip/journal/jcp/31/2/10.1063/1.1730361.

[35] Lebowitz, J. L., Helfand, E. & Praestga.E. Scaled Particle Theory of Fluid Mixtures. *Journal of Chemical Physics* **43**, 774—-& (1965).

[36] Lekkerkerker, H. N. W. Osmotic equilibrium treatment of the phase separation in colloidal dispersions containing non-adsorbing polymer molecules. *Colloids and Surfaces* **51**, 419–426 (1990).

[37] Ilett, S., Orrock, A., Poon, W. C. K. & Pusey, P. Phase behavior of a model colloid-polymer mixture. *Physical Review E* **51**, 1344–1353 (1995). URL http://journals.aps.org/pre/abstract/10.1103/PhysRevE.51.1344.

[38] DeHoff, R. *Thermodynamics in Materials Science, Second Edition*. Materials Science Textbooks (Taylor & Francis, 2006). URL https://books.google.co.uk/books?id=bh6ki2FfPoUC.

[39] Poon, W. C. K. *et al.* An experimental study of a model colloid-polymer mixture. *Journal de Physique II* **3**, 1075–1086 (1993). URL http://www.edpsciences.org/10.1051/jp2:1993184.

[40] Pham, K. N. *et al.* Multiple glassy states in a simple model system. *Science (New York, N.Y.)* **296**, 104–106 (2002).

[41] Zaccarelli, E. & Poon, W. C. K. Colloidal glasses and gels: The interplay of bonding and caging. *Proceedings of the National Academy of Sciences of the United States of America* **106**, 15203–8 (2009). URL http://www.pubmedcentral.nih.gov/articlerender.fcgi?artid=2741229{&}tool=pmcentrez{&}rendertype=abstract.

[42] Poon, W. C. K., Pirie, A. D. & Pusey, P. Gelation in colloid–polymer mixtures. *Faraday Discussions* **101**, 65–76 (1995). URL http://pubs.rsc.org/EN/content/articlehtml/1995/fd/fd9950100065.

[43] Rosch, T. W. & Errington, J. R. Fluid phase behavior of a model colloid-polymer mixture: Influence of polymer size and interaction strength. *Journal of Chemical Physics* **129** (2008).

[44] Noro, M. G. & Frenkel, D. Extended corresponding-states behavior for particles with variable range attractions. *The Journal of chemical physics* **113**, 5 (2000). URL http://arxiv.org/abs/cond-mat/0004033.

[45] Vliegenthart, G. a. & Lekkerkerker, H. N. W. Predicting the gas-liquid critical point from the second virial coefficient. *Journal of Chemical Physics* **112**, 5365 (2000).

[46] Lu, P. J. & Weitz, D. A. Colloidal Particles: Crystals, Glasses, and Gels. *Annual Review of Condensed Matter Physics* **4**, 217–233 (2013). URL http://www.annualreviews.org/doi/abs/10.1146/annurev-conmatphys-030212-184213.

[47] Weitz, D. A. & Oliveria, M. Fractal structures formed by kinetic aggregation of aqueous gold colloids. *Physical Review Letters* **52**, 1433–1436 (1984).

[48] Lu, P. J., Conrad, J. C., Wyss, H. M., Schofield, A. B. & Weitz, D. A. Fluids of Clusters in Attractive Colloids. *Physical Review Letters* **96**, 028306 (2006). URL http://link.aps.org/doi/10.1103/PhysRevLett.96.028306.

[49] Buscall, R. & White, L. R. The Consolidation of Concentrated Suspensions. *J. Chem. Soc., Faraday Trans. 1* **83**, 873–891 (1987).

[50] Allain, C., Cloitre, M. & Wafra, M. Aggregation and sedimentation in colloidal suspensions. *Physical Review Letters* **74**, 1478–1481 (1995).

[51] Manley, S., Skotheim, J. M., Mahadevan, L. & Weitz, D. A. Gravitational collapse of colloidal gels. *Physical Review Letters* **94**, 3–6 (2005).

[52] Secchi, E., Buzzaccaro, S. & Piazza, R. Time-evolution scenarios for short-range depletion gels subjected to the gravitational stress. *Soft matter* **10**, 5296–310 (2014). URL http://www.ncbi.nlm.nih.gov/pubmed/24913393.

[53] Starrs, L., Poon, W. C. K., Hibberd, D. J. & Robins, M. M. Collapse of transient gels in colloid-polymer mixtures. *Journal of Physics: Condensed Matter* **14**, 2485–2505 (2002). URL http://iopscience.iop.org/0953-8984/14/10/302.

[54] Bartlett, P., Teece, L. J. & Faers, M. a. Sudden collapse of a colloidal gel. *Physical Review E* **85**, 1–13 (2012).

[55] Blijdenstein, T. B. J. & VanAken, G. A. Scaling Behavior of Delayed Demixing, Rheology, and Microstructure of Emulsions Flocculated by Depletion and Bridging. *Langmuir* **20**, 11321–11328 (2004). URL file:///Users/pspicer/Patrick/References/PDFArticles/1357.pdfpapers2://publication/uuid/D2217236-ED6E-47CA-AF1D-F1743FBEE9CB.

[56] Kim, C. *et al.* Gravitational stability of suspensions of attractive colloidal particles. *Physical Review Letters* **99**, 1–4 (2007).

[57] Senis, D. & Allain, C. Scaling analysis of sediment equilibrium in aggregated colloidal suspensions. *Physical Review E* **55**, 7797–7800 (1997).

[58] Kim, J. M., Fang, J., Eberle, A. P., Castañeda-Priego, R. & Wagner, N. J. Gel transition in adhesive hard-sphere colloidal dispersions: The role of gravitational effects. *Physical Review Letters* **110**, 1–5 (2013).

[59] Biot, M. A. General theory of three-dimensional consolidation. *Journal of Applied Physics* **12**, 155–164 (1941).

[60] Huh, J. Y., Lynch, M. L. & Furst, E. M. Poroelastic consolidation in the phase separation of vesicle-polymer suspensions. *Industrial and Engineering Chemistry Research* **50**, 78–84 (2011).

[61] Condre, J.-M., Ligoure, C. & Cipelletti, L. The role of solid friction in the sedimentation of strongly attractive colloidal gels. *Journal of Statistical Mechanics: Theory and Experiment* **2007**, P02010–P02010 (2007). URL `http://stacks.iop.org/1742-5468/2007/i=02/a=P02010?key=crossref.4b7ecd28122d6ee07b303a728ae51ec9`.

[62] Buzzaccaro, S., Secchi, E., Brambilla, G., Piazza, R. & Cipelletti, L. Equilibrium concentration profiles and sedimentation kinetics of colloidal gels under gravitational stress. *Journal of Physics: Condensed Matter* **24**, 284103 (2012).

[63] Brambilla, G., Buzzaccaro, S., Piazza, R., Berthier, L. & Cipelletti, L. Highly nonlinear dynamics in a slowly sedimenting colloidal gel. *Physical Review Letters* **106**, 1–4 (2011).

[64] Derec, C., Senis, D., Talini, L. & Allain, C. Rapid settling of a colloidal gel. *Physical Review E* **67**, 062401 (2003). URL `http://link.aps.org/doi/10.1103/PhysRevE.67.062401`.

[65] Senis, D., Gorre-Talini, L. & Allain, C. Systematic study of the settling kinetics in an aggregating colloidal suspension. *The European Physical Journal E* **4**, 59–68 (2001). URL `http://link.springer.com/article/10.1007/PL00013683`.

[66] Lindström, S. B., Kodger, T. E., Sprakel, J. & Weitz, D. A. Structures, stresses, and fluctuations in the delayed failure of colloidal gels. *Soft Matter* **8**, 3657 (2012).

[67] Meeker, S. P. *LowShear Rheology and Delayed Sedimentation of Colloidal Systems - Meeker.pdf*. Ph.D. thesis, University of Edinburgh (1998).

[68] Murphy, D. B. *Fundamentals of Light Microscopy and Electronic Imaging* (John Wiley & Sons, Inc., 2002). URL `http://doi.wiley.com/10.1002/9781118382905`.

[69] Semrock. BrightLine® single-band filter set (2017). URL `https://www.semrock.com/SetDetails.aspx?id=3310`.

[70] Karamanide, Z. Light Sheet Fluorescence Microscopy for large samples. Tech. Rep. March, Univeristy of Edinburgh (2017).

[71] Schindelin, J. *et al.* Fiji: an open-source platform for biological-image analysis. *Nature Methods* **9**, 676–682 (2012). URL http://www.nature.com/doifinder/10.1038/nmeth.2019.

[72] Laven, P. MiePlot (2017). URL http://www.philiplaven.com/mieplot.htm.

[73] Zemb, T. & Lindner, P. (eds.). *neutrons x-rays and light scattering methods applied to soft condensed matter* (North-Holland, 2002), 1st edn.

[74] Ballesta, P., Petekidis, G., Isa, L., Poon, W. C. K. & Besseling, R. Wall slip and flow of concentrated hard-sphere colloidal suspensions. *Journal of Rheology* **56**, 1005 (2012). URL http://scitation.aip.org/content/sor/journal/jor2/56/5/10.1122/1.4719775.

[75] Fairhurst, D. *Polydispersity in colloidal phase transitions*. Ph.D. thesis, University of Edinburgh (1999). URL https://www.era.lib.ed.ac.uk/handle/1842/1496.

[76] Leunissen, M. E. *Manipulating colloids with charges and electric fields*. Ph.D. thesis, Utrecht University (2007). URL http://igitur-archive.library.uu.nl/dissertations/2007-0227-200119/UUindex.html{%}5Cnfile:///C:/Users/nogawa/SkyDrive/Mendeley/Leunissen-2007-Manipulatingcolloidswithchargesandelectricfields.pdf.

[77] Berry, G. C. Thermodynamic and Conformational Properties of Polystyrene. II. Intrinsic Viscosity Studies on Dilute Solutions of Linear Polystyrenes. *The Journal of Chemical Physics* **44**, 4550 (1966). URL http://scitation.aip.org/content/aip/journal/jcp/46/4/10.1063/1.1840854.

[78] Rubinstein, M. & Colby, R. H. *Polymer physics* (Oxford University Press, New York, 2003).

[79] Bailey, A. *et al.* Spinodal Decomposition in a Model Colloid-Polymer Mixture in Microgravity. *Physical Review Letters* **99**, 205701 (2007). URL http://link.aps.org/doi/10.1103/PhysRevLett.99.205701.

[80] Starrs, L. *Collapse of transient gels in colloid-polymer mixtures*. Phd thesis, University of Edinburgh (1999). URL http://hdl.handle.net/1842/14483.

[81] Evans, R. M. L. & Starrs, L. Emergence of a stress transmission length-scale in transient gels. *Journal of Physics: Condensed Matter* **14**, 2507–2529 (2002).

[82] Happel, J. & Brenner, H. *Low Reynolds number hydrodynamics*, vol. 1 of *Mechanics of fluids and transport processes* (Springer Netherlands, Dordrecht, 1981). URL http://link.springer.com/10.1007/978-94-009-8352-6.

[83] Koumakis, N. *et al.* Tuning colloidal gels by shear. *Soft Matter* **11**, 4640–4648 (2015). URL http://pubs.rsc.org/en/Content/ArticleLanding/2015/SM/C5SM00411J.

[84] Weon, B. M. & Je, J. H. Capillary force repels coffee-ring effect. *Physical Review E - Statistical, Nonlinear, and Soft Matter Physics* **82**, 1–4 (2010).

[85] Tseng, Q. *et al.* Spatial organization of the extracellular matrix regulates cell-cell junction positioning. *Proceedings of the National Academy of Sciences* **109**, 1506–1511 (2012). URL http://www.pnas.org/cgi/doi/10.1073/pnas.1106377109.

[86] Deegan, R. D. *et al.* Capillary flow as the cause of ring strins from dried liquid drops. *Nature (London)* **389**, 827–829 (1997).

[87] Hu, H. & Larson, R. G. Marangoni effect reverses coffee-ring depositions. *Journal of Physical Chemistry B* **110**, 7090–7094 (2006).

[88] Ryu, S. A., Kim, J. Y., Kim, S. Y. & Weon, B. M. Drying-mediated patterns in colloid-polymer suspensions. *Scientific Reports* **7**, 1–7 (2017). URL http://dx.doi.org/10.1038/s41598-017-00932-z.

[89] Smith, G. N., Hallett, J. E. & Eastoe, J. Celebrating Soft Matter's 10th Anniversary: Influencing the charge of poly(methyl methacrylate) latexes in nonpolar solvents. *Soft Matter* (2015). URL http://xlink.rsc.org/?DOI=C5SM01190F.

[90] van der Linden, M. N. *et al.* Charging of Poly(methyl methacrylate) (PMMA) Colloids in Cyclohexyl Bromide: Locking, Size Dependence, and Particle Mixtures. *Langmuir : the ACS journal of surfaces and colloids* **31**, 65–75 (2015). URL http://www.ncbi.nlm.nih.gov/pubmed/25535669.

[91] Prasad, V. *Weakly Interacting Colloid Polymer Mixtures.* Ph.D. thesis, Harvard University (2002).

[92] Mullin, J. W. *Crystallisation* (Elsevier, Oxford, UK, 2001), 4th edn. URL http://pubs.acs.org/doi/abs/10.1021/op0101005.

[93] Style, R. W. *et al.* Liquid-Liquid Phase Separation in an Elastic Network. *Physical Review X* **8**, 11028 (2018). URL http://arxiv.org/abs/1709.00500http://dx.doi.org/10.1103/PhysRevX.8.011028.

[94] Glasrud, G. G., Navarrete, R. C., Scriven, L. E. & Macosko, C. W. Settling behaviors of iron oxide suspensions. *AIChE Journal* **39**, 560–568 (1993).

[95] Koumakis, N. & Petekidis, G. Two step yielding in attractive colloids: transition from gels to attractive glasses. *Soft Matter* **7**, 2456 (2011). URL http://xlink.rsc.org/?DOI=c0sm00957a.

[96] Saintyves, B., Dauchot, O. & Bouchaud, E. Bulk elastic fingering instability in hele-shaw cells. *Physical Review Letters* **111**, 1–5 (2013).

[97] Biggins, J. S., Saintyves, B., Wei, Z., Bouchaud, E. & Mahadevan, L. Digital instability of a confined elastic meniscus. *Proceedings of the National Academy of Sciences* **110**, 12545–12548 (2013). URL `http://www.pnas.org/cgi/doi/10.1073/pnas.1302269110`.

[98] Huisken, J. Optical Sectioning Deep Inside Live Embryos by Selective Plane Illumination Microscopy. *Science* **305**, 1007–1009 (2004). URL `http://www.sciencemag.org/cgi/doi/10.1126/science.1100035`.

[99] Fowkes, N. D. & Hood, M. J. SURFACE TENSION EFFECTS IN A WEDGE. *The Quarterly Journal of Mechanics and Applied Mathematics* **51**, 553–561 (1998).

[100] Norbury, J., Sander, G. & Scott, C. Corner solutions of the Laplace–Young equation. *The Quarterly Journal of Mechanics and Applied Mathematics* **58**, 55–71 (2005).

[101] Lautrup, B. Surface tension. In *Physics of Continuous Matter: Exotic and Everyday Phenomena in the Macroscopic World*, no. 1, chap. 8, 624 (Institute of Physics Publishing, 2004), 2nd edn. URL `http://www.tandfonline.com/doi/abs/10.1080/00107514.2012.756936`.

[102] U.S. Coast Guard Department of Transportation. *CHRIS - Hazardous Chemical Data. Volume II* (U.S. Government Printing Office, Washington, D.C., 1984).

[103] Weon, B. M. & Je, J. H. Fingering inside the coffee ring. *Physical Review E - Statistical, Nonlinear, and Soft Matter Physics* **87**, 1–6 (2013).

[104] Lee, M. H. *Microstructure and microrheology of colloidal gels*. Ph.D. thesis, University of Delaware (2007).

[105] Smith, P. A., Petekidis, G., Egelhaaf, S. U. & Poon, W. C. K. Yielding and crystallization of colloidal gels under oscillatory shear. *Physical Review E* **76**, 041402 (2007). URL `http://link.aps.org/doi/10.1103/PhysRevE.76.041402`.

[106] Segrè, P. N., Behrend, O. P. & Pusey, P. Short-time Brownian motion in colloidal suspensions: Experiment and simulation. *Physical Review E* **52**, 5070–5083 (1995).

[107] Besseling, T. H., Jose, J. & Blaaderen, A. V. Methods to calibrate and scale axial distances in confocal microscopy as a function of refractive index. *Journal of Microscopy* **257**, 142–150 (2015).

[108] Wyss, H. M. *et al.* Strain-rate frequency superposition: A rheological probe of structural relaxation in soft materials. *Physical Review Letters* **98**, 1–4 (2007).

[109] Prasad, V. *et al.* Universal features of the fluid to solid transition for attractive colloidal particles. *Faraday Discussions* **123**, 1–12 (2003). URL `http://xlink.rsc.org/?DOI=b211107c`.

[110] Kobelev, V. & Schweizer, K. S. Nonlinear elasticity and yielding of depletion gels. *Journal of Chemical Physics* **123**, 164902 (2005).

[111] Pai, V. B. & Khan, S. A. Gelation and rheology of xanthan/enzyme-modified guar blends. *Carbohydrate Polymers* **49**, 207–216 (2002).

[112] Laurati, M., Egelhaaf, S. U. & Petekidis, G. Nonlinear rheology of colloidal gels with intermediate volume fraction. *Journal of Rheology* **55**, 673 (2011).